UNIVERSITY OF LIVERPOOL

INVESTIGATING THE FATE AND IMMUNOLOGY OF INTRAVENOUSLY INJECTED MESENCHYMAL STROMAL CELLS IN MICE

Thesis submitted in accordance with the requirements of the

University of Liverpool for the degree of Doctor in Philosophy

By

Francesco Amadeo

August 2022

INVESTIGATING THE FATE AND IMMUNOLOGY OF INTRAVENOUSLY INJECTED MESENCHYMAL STROMAL CELLS IN MICE

FRANCESCO AMADEO

ABSTRACT

Introduction: Mesenchymal stromal cells (MSCs) are multipotent cells showing great promise in pre-clinical studies and currently used in many clinical trials. The regenerative potential of MSCs is mediated, at least in part, by direct and indirect immunomodulatory mechanisms through the secretion of paracrine molecules. However, the mechanism of action behind the beneficial effect of these cells is not fully understood yet, and there are still concerns about possible undesired negative effects associated with the administration of living cells. Bioluminescence imaging (BLI) is widely used in preclinical models to investigate the biodistribution and safety of injected MSCs by monitoring the fate of luciferase-expressing cells following administration.

Aims: The present study was performed to (i) compare the short term biodistribution of umbilical cord (UC), bone marrow (BM) and adipose (A) MSCs, (ii) assess the long-term fate and safety of UC-MSCs in immunocompromised animals and (iii) investigate the mobilisation of different immune cells following the *in vivo* administration of UC-MSCs.

Methods: To generate luciferase-expressing MSCs so that the cells could be visualised *in vivo*, a lentiviral transduction protocol was optimised by testing different polycations, and then used to investigate the use of two possible reporter genes, Firefly Luciferase (FLuc) or a novel luciferase called AkaLuc. An IVIS Spectrum system was used to characterise the two BLI systems *in vitro* and to assess their sensitivity *in vivo*, via the imaging of FLuc and AkaLuc UC-MSCs intravenously (IV) administrated to C57BL/6J albino mice. Because the FLuc was selected as the optimal reporter gene, lentiviral vectors were used to generate FLuc-expressing UC, BM and A-MSCs. The *in vivo* short term biodistribution was assessed via the imaging of C57BL/6J albino mice up to 7 days post IV administration of $FLuc^+$ MSCs. Severe combined immunodeficient (SCID) and non-obese diabetic (NOD)/SCID mice were used to evaluate the long-term safety of $FLuc^+$ UC-MSCs up to 31 days from their administration. Flow cytometry was used to compare the percentage of innate and adaptive immune cells in the blood, the lungs, the bone marrow, and the spleen of C57BL/6 albino mice 2h and 24h following the administration of UC-MSCs. A multiplex analysis performed on the plasma of

the animals was used to evaluate the levels of different cytokines, chemokines, soluble receptors, and growth factors directly associated with the immune system.

Results: The *in vivo* comparison of FLuc and AkaLuc showed that the signal intensity of cells expressing AkaLuc was not stronger than FLuc when standard substrate doses were used (30 mM Akalumine-HCl and 47 mM D-Luciferin). By increasing the D-luciferin dose to 144.5 mM, it was possible to increase the light output obtained with the FLuc system, which was then 4.5-fold stronger than AkaLuc. The AkaLuc system was associated with scar formation under the skin of the animals at the site of subcutaneous injection of the substrate, AkaLumine-HCl. For these reasons FLuc was selected as the optimal reporter for subsequent experiments.

$FLuc^+$ UC, BM and A-MSCs were entrapped in the lungs of C57BL/6 albino mice after IV administration. Most of the cells (>90% of the UC, ≥94% of the BM and ≥85% of the A) died in the first 24h post administration and almost no signal was detected by day 3. UC-MSCs administered to immunocompromised mice were also entrapped in the lungs and showed a reduction in the signal in the first 24h similar to that observed in immunocompetent animals. Around 25% of the SCID and 45% of the NOD/SCID animals displayed detectable signal up to day 14. One NOD/SCID mouse showed weak signal up to day 31. Following the administration of UC-MSCs in C57BL/6 albino mice, flow cytometry analysis revealed an increase in the percentage of neutrophils in the lungs, the blood and the spleen 2h after the administration of the cells. Neutrophil chemoattractants (CCL2, CCL7, Gro-α and IP-10) were also upregulated in the plasma of the animals 2h after the administration of the MSCs.

Conclusions: The characterisation of the biodistribution of the cells and the involvement of the immune system show that although MSCs are short-lived in mice they still result in an immunological response that might contribute to a therapeutic effect.

DECLARATION

I declare that all the experiments and the data shown in this thesis have been performed and obtained by me, the author of this thesis, unless otherwise indicated. All results here presented are original and have never been presented for the qualification of another degree.

Francesco Amadeo

ACKNOWLEDGMENTS

It has been more than 3 years since I arrived in Liverpool. It looked such a long journey to finish the project, but here we are now, faster than a blink of an eye. This was an interesting chapter of my life as I realised I kind of like research more than I expected. And I wish to thank all the supportive and helpful people that, for a reason or another, helped me or were with me (physically or spiritually) during these 3 years.

I would like to start by thanking Dr. Vivien Hanson for giving me the opportunity to do this PhD and to work at the NHSBT for the past 3 years. Despite Covid, I think I learned a lot about industrial workplaces. I also want to thank Prof. Patricia Murray for supervising my work at the University and for always helping me in solving problems that popped up. Special thanks to Dr. Arthur Taylor, for your guidance, your diligence, and your help during these 3 years.

To all the friends I met during these years in Liverpool, for all the good time we had. Thank you, Giuliana, Katherine, Gianmarco and Medina, I think we all enriched our *cuisine* knowledge by sharing great meals! And special thanks to you Jid, for all the Sunday lunches and parties and movies and for successfully introducing me to the gym!

To all my friends in Italy, particularly to Silvio, Anto, Towa, Pigo, Carbo for all the nice, intense, and refreshing gaming sessions we had and for the stupid memes we shared on daily basis. Special thanks to my best friends, Tia and Tutto, for existing. We probably don't chat quite often, but it is always the same. Thank you all for always finding the time to meet me when I spend some time in Italy.

To my family, for always supporting me and for sending me food regularly from Italy. I could not survive without regular supplies of parmesan, actually. Thank you for your support and for helping me!

And finally, to my partner Gaia. Thank you for following me here and for sharing all this together. Thank you for your support, your words and for your smiles for all this time. I love you.

PUBLICATIONS AND PRESENTATIONS

1. Publications
   - *DEAE-Dextran enhances the lentiviral transduction of primary human mesenchymal stromal cells from all major tissue sources without affecting their proliferation and phenotype.* **Amadeo F**, Vivien V, Murray P, Taylor A. Molecular Biotechnology. Doi: 10.1007/s12033-022-00549-2.
   - *Mesenchymal stromal cells: what have we learned so far about their therapeutic potential and mechanisms of action?* **Amadeo F**, Trivino Cepeda K, Littlewood J, Wilm B, Taylor A, Murray P. Emerg Top Life Sci. 2021 Oct 29;5(4):549-562. Doi: 10.1042/ETLS20210013.
   - *Firefly luciferase offers superior performance to AkaLuc for tracking the fate of administered cell therapies.* **Amadeo F**, Plagge A, Chacko A, Wilm B, Hanson V, Liptrott N, Murray P, Taylor A. Eur J Nucl Med Mol Imaging. 2022 Feb;49(3):796-808. Doi: 10.1007/s00259-021-05439-4. Epub 2021 Jul 27.
2. Poster Presentations
   - *A Look into the Fate and Immunology of MSCs in Rodents*. **Amadeo F**, Liptrott N, Wilm B, Hanson V, Murray P, Taylor A. Poster presented at Renal ToolBox International Conference, 2022 Apr 6-7; Liverpool, UK.
   - *In Vitro and In Vivo Bioluminescence Imaging of Mesenchymal Stromal Cells Expressing a Luciferase Analogue*. **Amadeo F**, Plagge A, Murray P, Chacko A, Hanson V, Taylor A. Poster presented at World Molecular Imaging Congress, 2020 Oct 7-10. Online congress.
3. Collaborations
   - *Comparison between optical tissue clearing methods for detecting administered mesenchymal stromal cells in mouse lungs*. Hernandez Pichardo A, **Amadeo F**, Wilm B, Lévy R, Ressel L, Patricia Murray P, Sée V (Submitted).

TABLE OF CONTENTS

ABSTRACT i

DECLARATION iii

ACKNOWLEDGMENTS iv

PUBLICATIONS AND PRESENTATIONS v

TABLE OF CONTENTS vi

INDEX OF FIGURES xii

INDEX OF TABLES xv

ABBREVIATIONS xvi

CHAPTER 1 General Introduction 1

1.1 Kidney Structure and Function[1] 1

1.1.1 Kidney macroscopic anatomy 1

1.1.1.1 The renal corpuscle 4

1.1.1.2 The renal tubule 6

1.1.1.3 The collecting duct 7

1.1.1.4 The juxtaglomerular apparatus 8

1.2 Acute and Chronic Kidney Diseases 8

1.2.1 Acute kidney injury 8

1.2.2 Chronic kidney disease 10

1.2.3 Current therapies 11

1.3 Regenerative Medicine 14

1.3.1 Cell therapies 15

1.4 Mesenchymal Stromal Cells 16

1.4.1 Clinical use of MSCs and importance of understanding the mechanism of action..... 17

1.4.2 MSC immunoregulatory function 18

1.4.3 Apoptosis and phagocytosis of infused MSCs 20

1.4.4 Exosomes 22
1.4.4.1 AKT, ERK and MAPK axis 22
1.4.4.2 WNT/β-Catenin signalling pathway 23
1.4.4.3 Exosomes and immunomodulation 23
1.4.5 MSCs in renal treatment 24
1.4.6 MSCs: possible limitations and importance of conducting proper pre-clinical studies..... 25
1.5 MSCs live imaging 27
1.5.1 Bioluminescence 28
1.6 Introduction Summary and Aims of the Thesis..... 33
CHAPTER 2 General Materials and Methods 35
2.1 Cell Culture..... 35
2.1.1 Cell isolation..... 35
2.1.1.1 Umbilical cord derived mesenchymal stromal cells..... 35
2.1.1.2 Bone marrow derived mesenchymal stromal cells..... 36
2.1.1.3 Adipose derived mesenchymal stromal cells..... 36
2.1.2 Cell culture procedures..... 36
2.1.3 Cryopreservation and thawing of the cells 37
2.1.4 Proliferation and doubling time calculation 38
2.2 Generation of Reporter Cell Lines..... 38
2.2.1 Plasmids 39
2.2.2 Lentiviral particle production..... 39
2.2.3 Concentration of lentiviral particles 40
2.2.4 Virus titration 40
2.2.5 MSC transduction protocol 41
2.3 Flow Cytometry and Imaging Techniques..... 41
2.3.1 Cell preparation for flow cytometry 41
2.3.2 Bioluminescence imaging 43

2.3.2.1 In vitro BLI experiments 43
2.3.2.2 In vivo BLI experiments 44
2.4 Animal Experiments 44
2.4.1 Cell preparation and *in vivo* administration 45
CHAPTER 3 Optimisation and Characterisation of a Lentiviral Transduction Protocol for the Generation of Mesenchymal Stromal Cells Expressing Reporter Genes 46
3.1 Introduction 46
3.2 Materials and Methods 47
3.2.1 MSCs characterisation 47
3.2.1.1 Proliferation and doubling time 47
3.2.1.2 MSC markers 47
3.2.2 Optimisation of a lentiviral transduction protocol 48
3.2.2.1 Transduction efficiency 48
3.2.2.2 ATP assay 49
3.2.2.3 Flow cytometry based on the ZsGreen expression 50
3.2.2.4 Validation of the optimised transduction protocol 50
3.2.3 Establishing and characterising MSCs expressing the reporter gene FLuc_ZsGreen 51
3.2.3.1 Assessing the effects of lentiviral transduction on the properties of MSCs…….. 51
3.2.3.2 Determining bioluminescence properties in vitro 52
3.2.4 Statistical analysis 53
3.3 Results 53
3.3.1 Characterisation of MSCs from different sources 53
3.3.2 Optimisation of a lentiviral transduction protocol 56
3.3.2.1 Umbilical cord-derived mesenchymal stromal cells 56
3.3.2.2 Bone marrow-derived mesenchymal stromal cells 59
3.3.2.3 Adipose derived mesenchymal stromal cells 62

3.3.3 Validation of the selected protocol: DEAE-dextran in static condition 65

3.3.4 Characterisation of the MSCs transduced with the DEAE-dextran static protocol..... 68

3.3.4.1 Umbilical Cord Mesenchymal Stromal Cells 68

3.3.4.2 Bone marrow mesenchymal stromal cells 71

3.3.4.3 Adipose derived mesenchymal stromal cells..... 73

3.3.4.4 BLI characterisation in vitro 76

3.4 Discussion..... 78

3.5 Appendix to Chapter 3 – Supplementary Information 82

CHAPTER 4 Optimisation of Transduction Protocol for Mesenchymal Stromal Cells and Characterisation of Transduced UC-MSCs Both *In Vitro* and *In Vivo*. 83

4.1 Introduction 83

4.2 Materials and Methods..... 84

4.2.1 MSC transduction protocol 84

4.2.2 MSC marker expression determined by flow cytometry 84

4.2.3 Reporter cell line characterisation..... 85

4.2.3.1 In vitro BLI characterisation 86

4.2.3.2 In vivo BLI characterisation 87

4.2.4 Statistical analysis 91

4.3 Results..... 91

4.3.1 Characterisation of the transduced cells 91

4.3.2 BLI characterisation of AkaLuc and FLuc cells *in vitro*..... 93

4.3.3 BLI characterisation of AkaLuc and FLuc cells *in vivo*..... 98

4.3.3.1 In vivo kinetics following SC administration of Akalumine-HCl and D-Luciferin..... 98

4.3.3.2 AkaLuc and FLuc system comparison in vivo following SC administration of substrates..... 100

4.3.3.3 In vivo kinetics following IP administration of Akalumine-HCl and D-Luciferin.. 102

4.3.3.4 AkaLuc and FLuc system comparison in vivo following IP administration of substrates 104
4.3.3.5 AkaLuc and FLuc system unspecific signal in vivo 105
4.3.4 Akalumine-HCl *in vivo* reabsorption in the site of injection 107
4.4 Discussion 108
CHAPTER 5 Investigating the Fate, the Safety and the Interaction of MSCs with the Host Immune System 112
5.1 Introduction 112
5.2 Materials and Methods 113
5.2.1 *In vivo* short term biodistribution analysis 113
5.2.2 Biodistribution of MSCs from different sources in an *in vivo* model of ischemia reperfusion injury (IRI) 114
5.2.3 *In vivo* long term biodistribution in immunocompromised mice 115
5.2.4 Analysis of the BLI signal 115
5.2.5 Flow cytometry analysis of immune cells from different tissues following MSC administration 116
5.2.5.1 Whole blood collection and preparation for staining 116
5.2.5.2 Lungs harvesting and digestion to obtain single-cell suspensions 116
5.2.5.3 Bone marrow harvesting and preparation for staining 117
5.2.5.4 Spleen harvesting and digestion 117
5.2.5.5 Staining for flow cytometry analysis 117
5.2.6 Evaluation of circulating cytokines in the blood of mice administered with UC-MSCs 120
5.2.7 Statistical analysis 121
5.3 Results 121
5.3.1 Almost all the administered MSCs die in the first 24 hours *in vivo* 122
5.3.2 The presence of an IRI does not affect the lung entrapment of MSCs 124
5.3.3 UC-MSCs are also short-lived in immuno-compromised animals 127

5.3.4 Flow cytometry analysis reveals an upregulation of the circulating neutrophils.... 131

5.3.5 Multiplex analysis of the plasma of mice receiving UC-MSCs 134

5.4 Discussion..... 137

CHAPTER 6 Final Discussion and Summary..... 144

6.1 Conclusions 152

REFERENCE LIST 153

INDEX OF FIGURES

Figure 1.1| Longitudinal section of the kidney to illustrate the main structural features. The components of the kidney are described in the text. 2

Figure 1.2| Nephrons and the collecting duct system. 3

Figure 1.3| Renal corpuscle and juxtaglomerular apparatus. 5

Figure 1.4| Number of adult patients on the kidney only UK transplant list on the 31st of March* each year between 2012 and 2021.. 12

Figure 1.5| Post registration outcome for the 3426 new adult kidney-only registrations made in the UK between the 1st of April 2017 and the 31st of March 2018. 14

Figure 1.6| Summary of the potential mechanisms of action by which MSCs might act. 19

Figure 3.1| Lentiviral vector backbones. 49

Figure 3.2| UC, BM and A-MSCs display similar morphology but different proliferation rates. 54

Figure 3.3| Flow cytometry analysis of MSC markers in UC, BM and A-MSCs. 55

Figure 3.4| Effect of polycations and spinoculation on UC-MSC transduction. 57

Figure 3.5| Static DEAE-dextran and spinoculation Ps are valid alternatives to Pb for the transduction of umbilical cord mesenchymal stromal cells.. 58

Figure 3.6| Effect of polycations and spinoculation on BM-MSCs transduction. 60

Figure 3.7| DEAE-dextran following the application of either the static or spinoculation protocol and spinoculation Ps are valid alternatives to the Pb for the transduction of bone marrow MSCs. 62

Figure 3.8| Effect of polycations and spinoculation on A-MSCs transduction. 63

Figure 3.9| DEAE-dextran following the application of the static protocol is a valid alternative to the Pb for the transduction of adipose derived MSCs. 64

Figure 3.10| The application of the DEAE-dextran static protocol increases the transduction efficiency of all types of MSCs with all the lentiviral particles tested. 67

Figure 3.11| Application of the DEAE-dextran protocol to transduce MSCs with four different lentiviral particles 68

Figure 3.12| FLuc_ZsGreen UC-MSCs display similar proliferation to untransduced cells. .. 69

Figure 3.13| Morphological characterisation of transduced UC-MSCs. 70

Figure 3.14| FLuc_ZsGreen BM-MSCs display similar proliferation potential to untransduced cells. 72

Figure 3.15| Morphological characterisation of transduced BM-MSCs. 73

Figure 3.16| FLuc_ZsGreen A-MSCs display similar proliferation potential to untransduced cells. 74
Figure 3.17| Morphological characterisation of transduced A-MSCs. 75
Figure 3.18| Light output as a function of cell density..... 77
Figure 4.1| AkaLuc and FLuc transduced cells retain characteristics of untransduced UC-MSCs..... 92
Figure 4.2| Emission spectra of AkaLuc and FLuc systems with Akalumine-HCl and D-Luciferin. 94
Figure 4.3| The AkaLuc and FLuc reporters saturate at different substrate concentrations in vitro. 95
Figure 4.4| AkaLuc and FLuc systems in vitro saturation curves applying the 660, the 680 and the 700 nm filters..... 96
Figure 4.5| Light output as a function of cell density for the AkaLuc and FLuc reporter systems. 97
Figure 4.6| FLuc and AkaLuc BLI system kinetics in vivo following SC administration of D-Luciferin and Akalumine-HCl. 99
Figure 4.7| Evaluation of FLuc and AkaLuc cells overtime distribution in vivo following SC injection of D-Luciferin and Akalumine-HCl. 101
Figure 4.8| FLuc and AkaLuc BLI system kinetics in vivo following IP administration of D-Luciferin and Akalumine-HCl. 103
Figure 4.9| Evaluation of FLuc and AkaLuc cells overtime distribution in vivo following IP injection of D-Luciferin and Akalumine-HCl. 105
Figure 4.10| In the absence of cells Akalumine-HCl generates a non-specific signal from the liver region when administered IP. 106
Figure 4.11| Macro analysis performed at day 10 of the substrate injection sites. 107
Figure 5.1| All MSCs are entrapped in the lungs and are short-lived following IV administration. 123
Figure 5.2| MSCs are entrapped in the lungs of healthy and IRI-induced animals and do not migrate to the site of injury. 126
Figure 5.3| Administered UC-MSCs die similarly in immunocompetent and immunocompromised mice. 128
Figure 5.4|SCID and NOD/SCID mice displayed a weak but detectable signal even from 5 days post administration of UC-MSCs. 129
Figure 5.5| Images of the NOD/SCID animal administered with donor 2, which showed reduced cell death after day 5. 130

Figure 5.6| Distribution of innate immune cells in the mouse blood, bone marrow, lungs and spleen, 2h and 24h after the administration of UC-MSCs. 132
Figure 5.7| Distribution of adaptive immune cells in the mouse blood, bone marrow, lungs and spleen, 2h and 24h after the administration of UC-MSCs. 133
Figure 5.8| Plasma concentrations of cytokines and chemokines after IV infusion of UC-MSCs. 135
Figure 5.9| Plasma concentrations of cytokines and chemokines after IV infusion of UC-MSCs. 136
Figure 6.1| Graphical abstract of the main finding achieved in this thesis. 144
Supplementary Figure 3.1|ATP assay of transduced and untransduced MSCs. 82

INDEX OF TABLES

Table 1.1: Stages of Acute Kidney Injury following the Kidney Disease: Improving Global Outcomes (KDIGO) clinical practice guidelines..... 9

Table 1.2: Chronic kidney disease classification according to glomerular filtration rate and albuminuria following KDIGO guidelines 11

Table 1.3: Luciferase-luciferin pairs, divided in ATP-dependent and independent groups. The emission peak is specified..... 32

Table 2.1: Details of the antibodies used to investigate the expression of MSC markers. ... 43

Table 3.1: UC, BM and A-MSCs samples and the respective passages at which they were transduced, sorted, cryopreserved and used in animal experiments. 51

Table 3.2: Percentage of cells positive for negative (CD11b, CD19, CD34, CD45 and HLA-DR) and positive (CD44, CD73, CD90 and CD105) MSC markers listed by donor ID 56

Table 3.3: Impact of the polycations (poly.), the spinoculation (spin.), the transduction (tran.) and their combinations on the ATP production of MSCs. 59

Table 3.4: Percentage of FLuc_ZsGreen cells expressing the ZsGreen protein and percentage of untransduced controls and transduced cells positive to CD44, CD45, CD73, CD90 and CD105. FLuc = FLuc_ZsGreen. 71

Table 4.1: Experimental set up to evaluate the kinetics of the two BLI systems. 88

Table 4.2: Experimental set up to evaluate the signal following SC administration of the substrates..... 89

Table 4.3: Experimental set up to evaluate the signal following IP administration of the substrates..... 90

Table 4.4: Experimental set up to evaluate the background signal of D-Luciferin and Akalumine-HCl. 90

Table 5.1: Cell markers used to identify different immune cell populations. 119

Table 5.2: The antibodies employed for the analysis. 119

Table 5.3: Details of the analytes. The relative bead regions are shown in brackets. 121

Table 5.4: Number of SCID animals displaying detectable signal..... 130

Table 5.5: Number of NOD/SCID animals displaying detectable signal 130

ABBREVIATIONS

A

A: Adipose

AKI: Acute Kidney Injury

AKIN: Acute Kidney Injury Network

AMP: Adenosine Monophosphate

APC: Allophycocyanin

APCs: Antigen Presenting Cells

ATP: Adenosine Triphosphate

B

BAFF: B Cell Activating Factor

BLI: Bioluminescence Imaging

BM: Bone Marrow

BRET: Bioluminescence Resonance Energy Transfer

BSA: Bovine Serum Albumin

C

CBR: Click Beetle Red Luciferase

CCD: Charge Couple Device

CCL: Chemokine (C-C motif) Ligand

CD: Cluster of Differentiation

CDt: Collecting Duct

CKD: Chronic Kidney Disease

CNT: Connecting Tubule

COX2: Cyclooxygenase2

CSF: Colony Stimulating Factor

CTR: Control

CTZ: Coelenterazine

CU: Circular Unit

CXCL: Chemokine (C-X-C motif) Ligand

D

DC: Dendritic Cell

DEAE: Diethylaminoethyl

DMEM: Dulbecco's Modified Eagle Medium

DMSO: Dimethyl Sulfoxide

DTZ: Diphenylterazine

E

EDTA: Ethylenediaminetetraacetic Acid

ENA: Epithelial-derived Neutrophil-activating Peptide

ESL: Endothelial Surface Layer

ESRD: End Stage Renal Disease

ERK: Extracellular Receptor Kinase

EV: Extracellular Vesicle

F

FACS: Fluorescence Activated Cell Sorting

FBS: Foetal Bovine Serum

FITC: Fluorescein Isothiocyanate

FLuc: Firefly Luciferase

FMNH2: Reduced Flavin Mononucleotide

FP: Foot Process

FZ: Furimazine

G

GBD: Global Burden of Diseases

GBM: Glomerular Basement Membrane

GCSF: Granulocyte Colony Stimulating Factor

GFP: Green Fluorescent Protein

GFR: Glomerular Filtration Rate

GLuc: *Gaussia Princeps* Luciferase

GMCSF: Granulocyte Macrophage Colony Stimulating Factor

GMP: Good Manufacturing Practice

GVHD: Graft-Versus-Host Disease

H

Hb: Haemoglobin

HEK293T: Human Embryonic Kidney Cells expressing SV40 T antigen

HEPES: (4-(2-hydroxyethyl)-1-Piperazineethanesulfonic Acid

HLA: Human Leukocyte Antigen

HPL: Human Platelet Lysate

HSC: Hematopoietic Stem Cell

HSV1-tk: Herpes Simplex Virus 1 – thymidine kinase

I

IA: Intraarterial

IC: Intracranial

IDO: Indoleamine-pyrrole 2,3-Dioxygenase

IFN-γ: Interferon- γ

IL: Interleukin

IMC: Immature Myeloid Cell

IP: Intraperitoneal

IP-10: Interferon-γ-induced Protein 10

IRI: Ischemia Reperfusion Injury

IV: Intravenous

IVC: Individually Ventilated Cage

IVIS: In Vivo Imaging System

K

KDIGO: Kidney Disease Improving Global Outcomes

L

LIF: Leukaemia Inhibitory Factor

LLOQ: Lower Limit of Quantification

LV: Lentiviral Vector

M

MAPK: Mitogen-Activated Protein Kinase

MCP: Monocyte Chemoattractant Protein

MDC: Myeloid Dendritic Cell

MEMα: Minimum Essential Medium Eagle alpha

MHC: Major Histocompatibility Complex

MIP: Macrophage Inflammatory Protein

MoA: Mechanisms of Action

MOI: Multiplicity of Infection

MRI: Magnetic Resonance Imaging

MSC: Mesenchymal Stromal Cell

N

NF-kB: Nuclear Factor Kappa-light-chain-enhancer of activated B cells

NHS-BT: National Health Service Blood and Transplant

NK: Natural Killer Cell

NO: Nitric Oxide

NOD: Non-obese Diabetic

NT5E: Ecto-5'-nucleotidase

O

O_2: Oxygen

OA: Osteoarthritis

OLuc: *Oplophorus Gracilirostris* Luciferase

OOR: Out of Range

P

Pb: Polybrene

PBS: Phosphate-Buffered Saline

PDC: Peripheral Dendritic Cells

PD-L1: Programmed Death-Ligand 1

PE: Phycoerythrin

PET: Positron Emission Tomography

PGE2: Prostaglandin E2

PI3K: Phosphatidylinositol 3-Kinase

PP: Primary Process

Ps: Protamine Sulphate

R

R: Receptor

RANKL: Receptor Activator of Nuclear Factor kappa-B Ligand

RANTES: Regulated on Activation, Normal T cell Expressed and Secreted

RET: Resonance energy transfer

RIFLE: Risk, Injury, Failure, Loss and ESRD

RLuc: *Renilla Reniformis* Luciferase

ROI: Region of Interest

RRT: Renal Replacement Therapy

S

SC: Subcutaneous

SCID: Severe Combined Immunodeficient

SCr: Serum Creatinine

SPECT: Single-Photon Emission Computerized Tomography

SPION: Superparamagnetic Iron Oxide Nanoparticle

STZ: Selenoterazine

T

TGF-β: Transforming Growth Factor-β

Th: T Helper Cell

TLR. Toll-like Receptor

TNF-α: Tumour Necrosis Factor-α

Treg: Regulatory T Cell

TU: Transducing Units

U

UC: Umbilical Cord

V

VEGF: Vascular Endothelial Growth Factor

CHAPTER 1 GENERAL INTRODUCTION

1.1 KIDNEY STRUCTURE AND FUNCTION[1]

Kidneys are parenchymatous organs found in vertebrates. Together with two ureters, the bladder, and the urethra, they constitute the urinary system, responsible for blood filtration and for the removal of metabolic waste products.

1.1.1 Kidney macroscopic anatomy

In humans, the kidneys are a pair of bean-like shaped organs located behind the peritoneum, on the right and left sides of the vertebral column. The right kidney is positioned a bit lower than the left kidney. Above each kidney there is an adrenal gland. On the median surface of each kidney there is a fissure, called the *hilum*, through which pass the arterial, venous, and lymphatic vessels, the nerves, and the ureter. Each kidney receives blood from a renal artery, a branch of the abdominal aorta. In the resting condition, the two kidneys receive 20% of the cardiac output. This level of perfusion is very important for renal function, not only for nutrient supply, but also for their role in blood filtration and clearance. The blood exits the kidney through the renal vein, connected to the inferior vena cava.

A frontal section of a kidney (Figure 1.1) reveals two main regions: an outer cortex, and an inner medulla. The medulla is further divided into an outer medulla and an inner medulla, and the outer medulla is subdivided into an outer and an inner stripe. The medulla is organised into conical areas called renal pyramids. The base of each pyramid faces the cortex, while the apex ends in the renal papilla, which is surrounded by a minor calyx. Each renal papilla empties urine into a minor calyx. All the minor calyces converge into two or three major ducts, called major calyces, which, in turn, merge together to form a single funnel-shape duct called the renal pelvis. This is connected to the initial tract of the ureter.

[1]Two books, *Principles of Renal Physiology* (2012, Springer-Verlag New York, Christopher J. Lote) and *Comprehensive Clinical Nephrology* (2019, Elsevier, John Feehally) provided the information for this section, unless otherwise referenced.

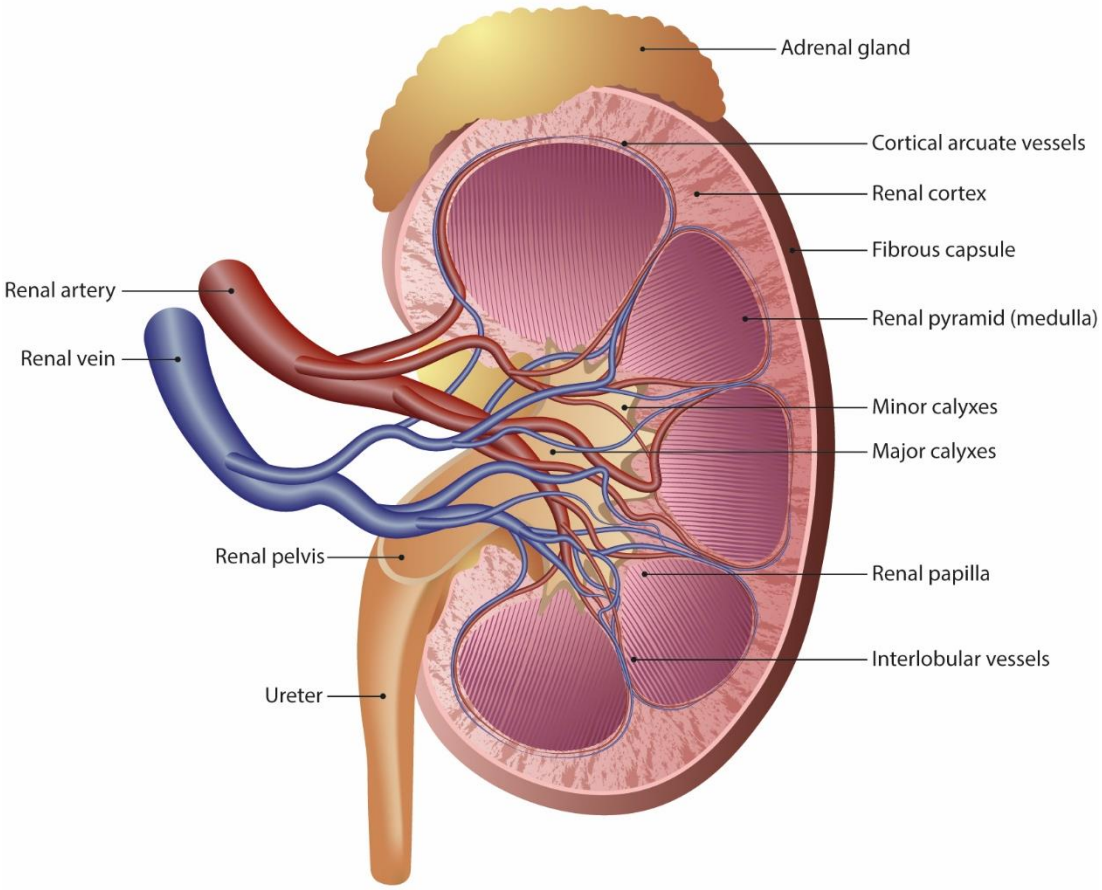

Figure 1.1| Longitudinal section of the kidney to illustrate the main structural features. The components of the kidney are described in the text. Figure produced by Glaze Art for Science.

The functional unit of the kidney is the nephron. Each nephron filters blood and produces urine. Each kidney can contain approximately 1 million nephrons, although the exact number can vary among people. The number of nephrons is established during prenatal development: the genesis of new nephrons stops around the 32° week of gestation and through life new nephrons cannot form, and lost ones cannot be replaced. A nephron (Figure 1.2) is composed of a renal corpuscle, which produces the renal filtrate, and a renal tubule, which drains the filtrate into a collecting duct (CDt). The renal corpuscle, divided into a glomerulus and a Bowman's capsule, is in the cortex, and three types of nephrons can be distinguished on its position: cortical (renal corpuscle in the outer part of the cortex), midcortical and juxtamedullary (renal corpuscle in the inner part of the cortex, close to the medulla) nephrons. The renal tubule consists of a proximal (convoluted and straight parts) and a distal tubule (convoluted and straight portions), both connected by the loop of Henle. The length of the loop of Henle identifies two types of nephrons: those with long loops and those with short. Short loops turn back in the outer medulla or even in the cortex and are

usually those descending from cortical nephrons (Figure 1.2). Long loops turn back in the inner medulla and are usually those from juxtamedullary nephrons.

The CDt is formed in the renal cortex from several nephrons and a connecting tubule separates each nephron from the CDt. The CDts then descend within the medullary rays of the cortex. After entering the inner medulla, they fuse together and open on a minor calyx.

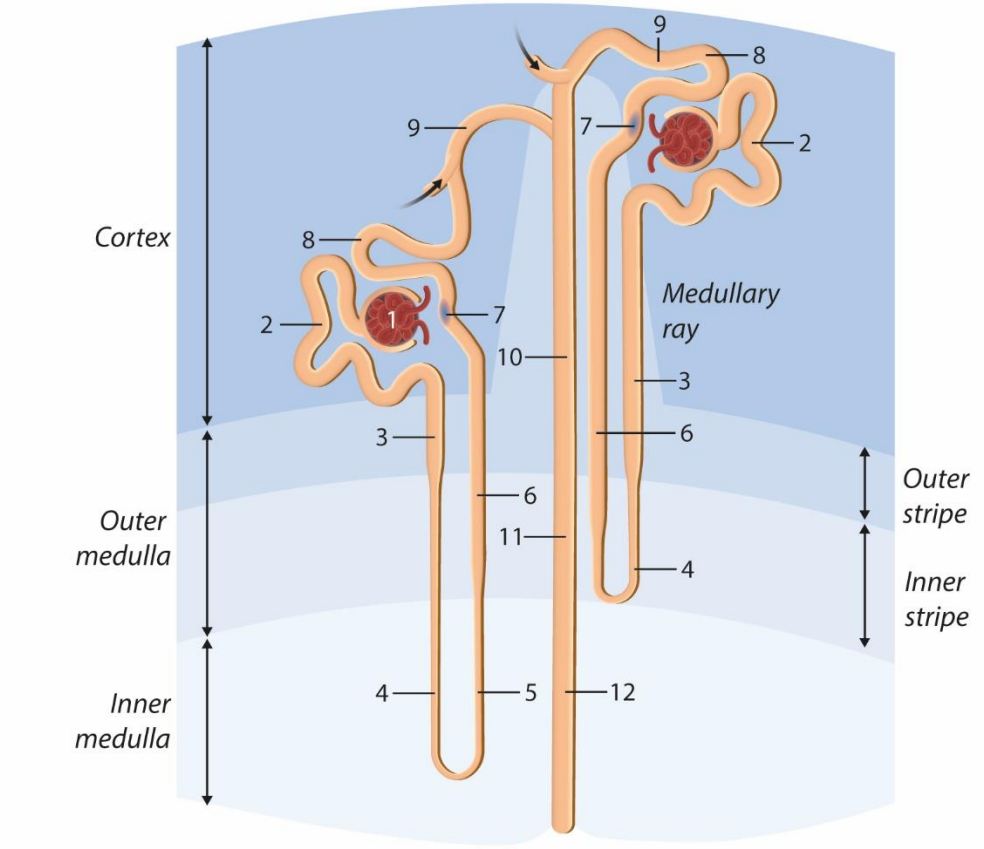

1. Renal corpuscle
2. Proximal convoluted tubule
3. Proximal straight tubule
4. Descending thin limb
5. Ascending thin limb
6. Distal straight tubule (thick ascending limb)
7. Macula densa
8. Distal convoluted tubule
9. Connecting tubule
10. Cortical collecting duct
11. Outer medullary collecting duct
12. Inner medullary collecting duct

Figure 1.2| Nephrons and the collecting duct system. The figure shows the main structure of short- and long-looped nephrons, together with a collecting duct system. Arrows represent the confluence of further nephrons in the same CDt system. The main components are described in the text of the figure. Figure produced by Glaze Art for Science.

1.1.1.1 The renal corpuscle

The glomerulus is an intricate specialised capillary network, surrounded by the Bowman's capsule, which is connected to the renal tubule (Figure 1.3). The capillary network is supported by the mesangium, made of intraglomerular mesangial cells and mesangial matrix. Glomerular capillaries are a unique type of vessel, composed only of highly fenestrated endothelial cells. The main feature of these capillaries is the presence of pores with a diameter between 50 and 100 nm lacking diaphragms bridging the pores [1]. This allows only water and small molecules to pass through the fenestrae. Moreover, the luminal side of the endothelial cells is covered by a negatively charged hydrated structure known as the endothelial cell surface layer (ESL) [1]. This applies a further restriction to the type of molecules that can pass the barrier depending on their charge. The glomerular capillaries and the mesangium are covered by epithelial cells (podocytes) forming the visceral epithelium of the Bowman's capsule. The glomerular basement membrane (GBM) develops at the interface between the side of capillaries and mesangium and the layer of podocytes. The GBM has a trilaminar structure and is mainly composed of collagen type IV, laminin, and heparan sulphate proteoglycans. While collagen composes the main structure, laminin provides mechanical strength and flexibility, and proteoglycans create a meshwork that is well hydrated and can absorb loading forces [2, 3]. These components give the GBM structural function with mechanical resistance to hydrostatic pressure. Mesangial cells have many processes extending from the body toward the GBM and are anchored to it by the mesangial matrix. Together with mesangial cells, the mesangial matrix supports the GBM. On the other side of the GBM, there is a layer of podocytes. Differentiated podocytes are unable to replicate, therefore in adults, lost podocytes cannot be replaced [4-6]. Podocytes have a voluminous cell body, from which different large primary processes (PPs) emanate. The PPs further divide into foot processes (FPs) which fix the podocytes to the capillaries, on the other side of the GBM. The FPs of neighbouring podocytes interdigitate, leaving filtration slits in between. These slits are bridged by a complex extracellular structure, the slit diaphragm, forming pores with a maximum radius of 4 nm. This complex structure that adheres to the GBM is homogenous and creates a uniform cover that represents another size-specific barrier to macromolecules. The main function of the glomerulus is to produce ultra-filtered plasma and the endothelial cells, the podocyte layer and the GBM comprise the glomerulus filtration barrier. As a result of the properties of the components described above, the barrier is freely permeable to water, solutes, and small molecules. The size and the charge of the molecules influence filtration restrictions [1].

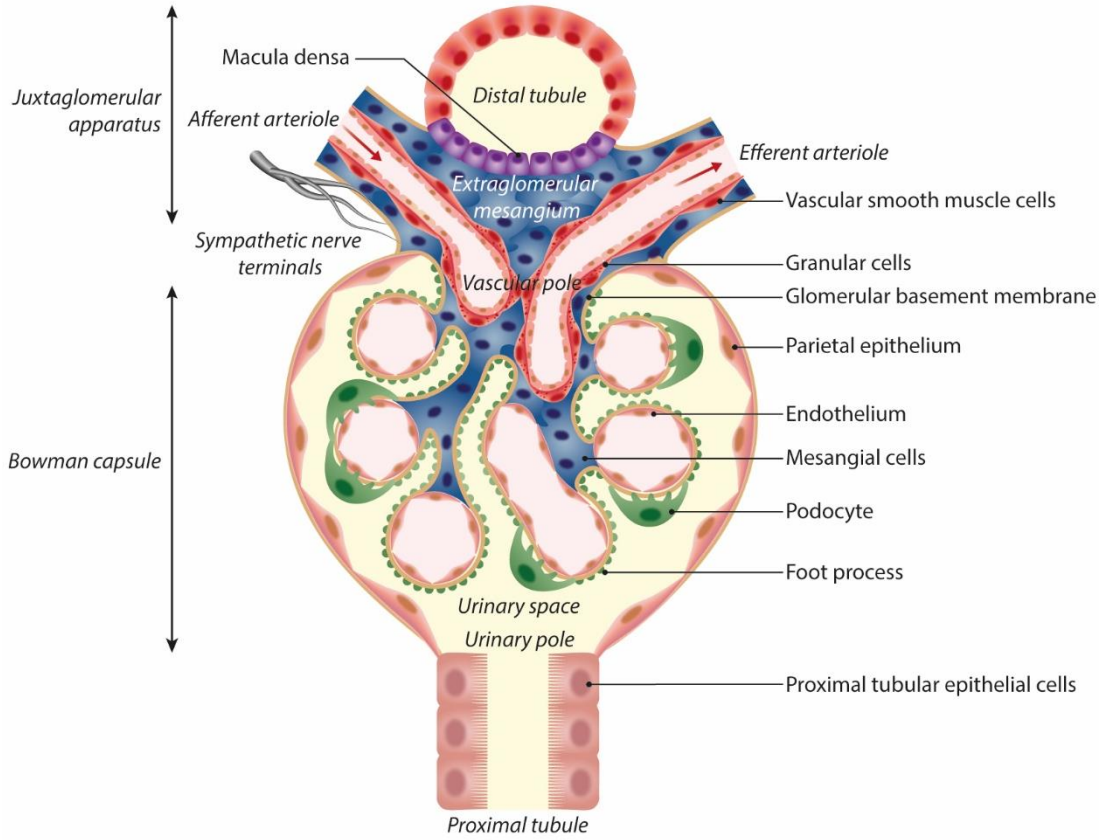

Figure 1.3| Renal corpuscle and juxtaglomerular apparatus. The components of the renal corpuscle are described in the text of the figure. Figure produced by Glaze Art for Science.

The filtration occurs in the following way. The blood flows through an afferent arteriole to the glomerular capillaries. There, part of the plasma is filtered through the Bowman's capsule in a process called glomerular filtration. The blood is then drained through the efferent arteriole and can re-enter the circulation. The hydrostatic pressure of the blood in the capillaries regulates the filtration of water and solutes through the glomerular filtration barrier. The barrier shows high permeability for water, small molecules (e.g. glucose, amino acids, and urea) and ions (e.g. sodium and potassium), whereas it is very selective for macromolecules, depending on their size, shape, and charge. Uncharged macromolecules up to an effective radius of ~1.8 nm can freely pass through the barrier [7]. Larger molecules are increasingly restricted up to an effective radius of 4 nm, above which the passage is completely blocked by the slit diaphragm. Plasma albumin has an effective radius of 3.6 nm, but its passage through the barrier is further obstructed by its negative charge, so only a minimal amount manages to pass into the glomerular filtrate [8-10]. Almost all of it will be reabsorbed, mainly in the proximal tubule, resulting in very low excretion of albumin in the urine of healthy individuals [11-13].

1.1.1.2 The renal tubule

The renal tubule connects the nephron to the CDt and is divided into different segments: the proximal tubule (convoluted and straight), an intermediate tubule, known as the loop of Henle, a distal tubule (straight and convoluted), and a connecting tubule (CNT). The CNT connects the nephron to the CDt system. The renal tubules are characterised by a single layer of epithelial cells attached to a basement membrane. These cells have multiple transport functions and show distinctive adaptations for this role. On the apical side, adjacent cells are stuck together by tight junctions and connected by desmosomes. On the basal side, there is a space between adjacent cells, the lateral intercellular space. As a result, two pathways can be identified: a transcellular pathway, including transport across the transluminal and basolateral cell membranes, and a paracellular transport, across the junction complexes and the cellular interspace [14]. The transcellular transport depends on the channels and transporters located on the transluminal and basolateral cell surfaces. Cells spread across the renal tubule differ in terms of membrane transporter and channel composition. As a direct consequence, the various segments of the tubule display different properties.

The liquid filtered in the Bowman capsule enters the initial part of the renal tubule, called the proximal convoluted tubule, and continues to the proximal straight tubule, which can also be considered as the thick descending limb of the loop of Henle. The proximal tubule reabsorbs protein, amino acids, glucose, macromolecules such as albumin, and most of the water and ions. The proximal tubule can be divided into three segments, that differ in cellular organisation and, consequently, in function [15]. S_1 is the initial short part of the convoluted segment; S_2 is composed by the other part of the convoluted segment and the initial portion of the proximal straight tubule; and S_3 is the medullary segment of the proximal straight tubule. Generally, the epithelium of the proximal tubule is composed of cuboidal cells with a luminal surface enriched in microvilli, forming the brush border. The brush border highly increases the surface area available for re-absorption of tubular fluid. On the basolateral membrane, epithelial cells are rich in mitochondria that supply ATP (adenosine triphosphate) to the Na^+/K^+-ATPase [16]. This machinery is responsible for the activation of many other transporters based on the movement of Na^+, such as the reabsorption of the filtered glucose via a sodium-glucose cotransporter [17]. Most other solutes are also reabsorbed in the proximal tubule (e.g. 60% of calcium, 50% of urea). The apical and the basolateral membranes are also rich in aquaporin 1 channels, making the proximal tubule highly permeable to water [18]. Moving from the Bowman's capsule to the end of the proximal

tubule, the cells change shape. The cells of the straight part of the proximal tubule are flatter and have a less dense brush border than the cuboidal cells of the convoluted part.

The proximal tubule continues into the loop of Henle, a U-shaped loop composed of a thin descending limb, a thin ascending limb, and a thick ascending limb. The descending tract goes deep in the renal medulla, while the ascending limb goes in the direction of the cortex. The cells of the thin descending and ascending parts of the loop of Henle are squamous (very thin and flattened) and structurally very similar, even though they display some important functional differences. The thin descending limb is highly permeable for water, but impermeable to solutes, whereas the thin ascending limb is impermeable to water, but highly permeable to ions [19]. The thick ascending limb of the loop of Henle is a cuboidal epithelium highly impermeable to water. On the other hand, these cells are enriched of the Na-K-Cl symporter (NKCC2 isoform) in the luminal membrane and can reabsorb a high amount of sodium and chloride [20]. The thick ascending limb of the loop of Henle goes back in the direction of the cortex and becomes the straight distal tubule.

Like the proximal tubule, the distal tubule is divided into a straight and a convoluted section. The straight portion has the same structure and function as the ascending part of the loop of Henle, with high reabsorption of sodium and chloride. This portion of the nephron continues in the cortex and at the point where it meets the distal convoluted tubule, the *macula densa* can be observed. The *macula densa* adheres to the glomerulus of the same nephron and is part of the juxtaglomerular complex. The cells of the convoluted distal tubule are responsible for the removal of the remaining sodium using a specific Na-Cl-cotransport system (NCC) [21]. Finally, the produced liquid, which is now a concentrated urine, made of excess water enriched in nitrogenous waste products, flows through the CNT to the collecting duct.

1.1.1.3 The collecting duct

Liquid from renal tubules from different nephrons converge into the same CD. In the cortex, each CDt receives about six connecting tubules and, as the ducts enter the medulla, they join with each other to finally form a papillary duct, which drains into a renal calyx. Most of the cells of the CDt are cuboidal and increase in size toward the apex of the papilla. These cells contain a shuttle system for aquaporin 2 under the control of vasopressin and can switch the water permeability from zero/very low to permeable, further concentrating the urine. Moreover, these cells can increase the expression of sodium channel on the apical surface under the control of aldosterone. Thanks to this, the CDs are the final regulators of fluid and electrolyte balance.

1.1.1.4 The juxtaglomerular apparatus

The juxtaglomerular apparatus comprises the *macula densa*, the extraglomerular mesangium, the granular cells of the terminal portion of the afferent arteriole, and the initial portion of the efferent arteriole (Figure 1.3). The granular cells are assembled in clusters and replace ordinary smooth muscle cells of the afferent arteriole. These cells are rich in cytoplasmatic granules containing renin and are densely innervated by sympathetic nerve terminals. The main function of the juxtaglomerular apparatus is to control the release of renin, which, through the renin-angiotensin-aldosterone system, can act on the volume of extracellular fluid and arterial vasoconstriction to regulate the blood pressure.

1.2 ACUTE AND CHRONIC KIDNEY DISEASES

The global burden of diseases (GBD) study analysed data from 1990 to 2017 on death and disability associated with over 350 different diseases [22]. It revealed that kidney disease, including acute kidney injury (AKI) and chronic kidney disease (CKD), is a major health problem worldwide, affecting over 750 million persons [23].

1.2.1 Acute kidney injury

AKI is defined by a rapid and unexpected decrease in kidney function, characterised by both structural damage and impairment in glomerular filtration rate (GFR) and urine output [24]. It is usually a silent condition, since it does not cause pain or any specific signs or symptoms, except for urinary tract obstruction. AKI is an important complication among hospitalised patients, affecting 10-15% of all hospitalisations, and is even more frequent in patients admitted to intensive care units, where its prevalence can exceed 50% [25]. It can affect both paediatric and adult patients and is associated with serious and short-term complications, including increased mortality [26]. A single episode of AKI can potentially lead to the development of CKD or end stage renal disease (ESRD) [27]. AKI can be caused by many different aetiologies, and most cases of AKI are multifactorial [28]. The pathogenesis is characterised by an intense inflammatory response, endothelial dysfunction, altered microcirculation and tubular injury [24], and is often associated with the presence of sepsis [29, 30], ischemia [31] and nephrotoxicity [32]. Furthermore, many patients have a mixed clinical picture, where AKI often coexists with many other syndromes, making it very difficult to recognise and properly treat [25, 28].

The term “acute kidney injury” was used for the first time by William MacNider in 1918 [33, 34]. Over the years, many different definitions of AKI and its characteristics have been

proposed. To standardise the definition and the different stages of this pathology, an international interdisciplinary group coined the RIFLE system in 2002 [35]. This system categorises AKI stages into three severity grades, **R**isk, **I**njury and **F**ailure, and two outcome classes, **L**oss and **E**nd stage renal disease (RIFLE). In 2007 this system was optimised by the Acute Kidney Injury Network (AKIN), with the aim to increase the sensitivity of AKI diagnostic criteria [36]. The most recent classification for AKI injury follows the Kidney Disease: Improving Global Outcomes (KDIGO) guidelines [37], which is based on the previous two systems. The KDIGO guidelines classify AKI into 3 stages, based on the level of serum creatinine (SCr) and urine output (Table 1.1).

Table 1.1: Stages of Acute Kidney Injury following the Kidney Disease: Improving Global Outcomes (KDIGO) clinical practice guidelines [37].

Stage	Serum Creatinine	Urine Output
1	1.5-1.9 times baseline *Or* ≥ 0.3 mg/dL (≥ 26 μM) increase within 48 hours	< 0.5 mL/kg/h for 6-12 h
2	2.0-2.9 times baseline	< 0.5 mL/kg/h for ≥ 12 h
3	3.0 times baseline *Or* ≥ 4.0 mg/dL (≥ 352 μM) increase *Or* Initiation of renal replacement therapy (RRT) *Or* Decreased in estimated GFR < 35 mL/min/1.73 m^2 in patients younger than 18 years old	< 0.3 mL/kg/h for ≥ 24 h *Or* Anuria for ≥ 12 h

The acute renal insult that follows an AKI event leads to the damage of several kidney cell populations and structures within the kidney. These can include a tubular injury, the activation of endothelial cells, a tubular obstruction, a vascular injury or the recruitment of inflammatory cells [38]. All these can contribute to different levels of injury, as indicated above. However, a variety of repair processes are promptly activated following an AKI event, all contributing to the repair of kidney function. This process is called adaptive repair and involves an active proliferation of local kidney cells [39]. Multiple renal injury events can enhance cell ageing and increase the chances of differentiation toward a profibrotic phenotype [39]. This process is called maladaptive repair and can be triggered by several pathophysiological processes [38]. Maladaptive repair can occur in different renal

compartments (tubular, vascular, and interstitial) and can directly contribute to the progression from AKI to CKD [25, 28].

1.2.2 Chronic kidney disease

The GBD study [22] included the analysis of CKD and revealed an increase in the prevalence of this disease between 2007 and 2017, which amounted to 28.2% among females, and 25.4% among males [40]. Furthermore, a forecast analysis conducted in 2018 revealed that the number of deaths due to chronic kidney disease will increase from 1.2 million in 2016 to approximately 3.1 million in 2040 [41]. Albeit the GBD study has important limitations (*e.g.* considerable assumptions are required for countries with sparse data, or difficulties in identifying CKD), it reveals the growing global impact of CKD, highlighting the importance of improvement in prevention and in the development of novel treatments for this pathology [42].

CKD is defined as a pathological change in the kidney function or structure affecting the health of an individual for more than 3 months. Diabetes [43, 44], obesity [45] and hypertension [43, 46, 47] are leading causes [48, 49] of CKD development and progression. Other risk factors that might contribute to the pathology are age [50], previous or current AKI episodes [51], smoking [52, 53] socioeconomic status [54], and gender [55]. As AKI, there are different stages of CKD classified following the KDIGO clinical practice guidelines [37]. The different stages indicate the contribution of GFR, albuminuria and, more infrequently, the leading cause of CKD (Table 1.2).

Decreased GFR is defined by a value less than 60 mL/min per 1.73 m^2, which, together with albuminuria ≥ 30 mg/g, represent CKD. CKD can lead to ESRD and increased cardiovascular morbidity and mortality and there is no specific treatment for CKD, although it is possible to pharmacologically act on some comorbidities (*e.g.* hypertension and cardiovascular diseases). Currently, the main interventions to slow the progression towards a more advanced stage is by acting on lifestyle (*e.g.* no smoking, reduction in sodium and protein intake, weight management, and increased physical activity) [49]. At its final stage (stage 5/ESRD), CKD necessitates the use of dialysis or renal transplantation.

Table 1.2: Chronic kidney disease classification according to glomerular filtration rate and albuminuria following KDIGO guidelines [37]. How GFR and albuminuria interact to influence the risk to progress to kidney failure is represented from lowest to highest by green, yellow, orange, and red.

			Persistent albuminuria categories description and range		
			A1	A2	A3
			Normal to mildly increased	Moderately increased	Severely increased
GFR categories (mL/min/1.73 m^2) description and range			< 30 mg/g < 3 mg/mmol	30-300 mg/g 3-30 mg/mmol	> 300 mg/g > 30 mg/mmol
G1	Normal or high	≥ 90			
G2	Mildly decreased	60-89			
G3a	Mildly to moderately decreased	45-59			
G3b	Moderately to severely decreased	30-44			
G4	Severely decreased	15-29			
G5	Kidney failure	< 15			

1.2.3 Current therapies

When AKI stage 3 or ESRD has developed, the patient is no longer able to properly filter their own blood and a renal replacement therapy (RRT) is required. RRT are therapies capable of replacing and mimicking renal blood filtration and include various forms of dialysis, hemofiltration, and renal transplantation. Since their development, their use has increased progressively due to the growing number of patients. In 2010 the number of people receiving RRT was estimated to be around 2.6 million worldwide [56].

The rationale of dialysis is to maintain homeostasis (electrolyte, acid-base and volume) and to remove waste products of nitrogen metabolism that can accumulate in the blood (uraemia). Unfortunately, dialysis is not able to substitute other kidney functions, like hormone regulation and activation of vitamin D. Indeed, patients undergoing dialysis typically experience disorders associated with the hypothalamic-pituitary-gonadal axis, with impairments of synthesis and clearance of many hormones [57]. Furthermore, patients undergoing haemodialysis are usually required to go to dialysis centres two or three times a week for 3-4 hours per session. Similarly, peritoneal dialysis, even if it can be performed at home or at work, needs to be performed several times per day (every 4-5 hours), or

continuously during the night (8-10 consecutive hours), requiring specific equipment [58]. Either option can influence both the professional and personal life of the patient and can have a huge impact on mental and psychological health [58]. Furthermore, despite the advancements in clinical dialysis management, the mortality and morbidity rates of these patients remains high [59].

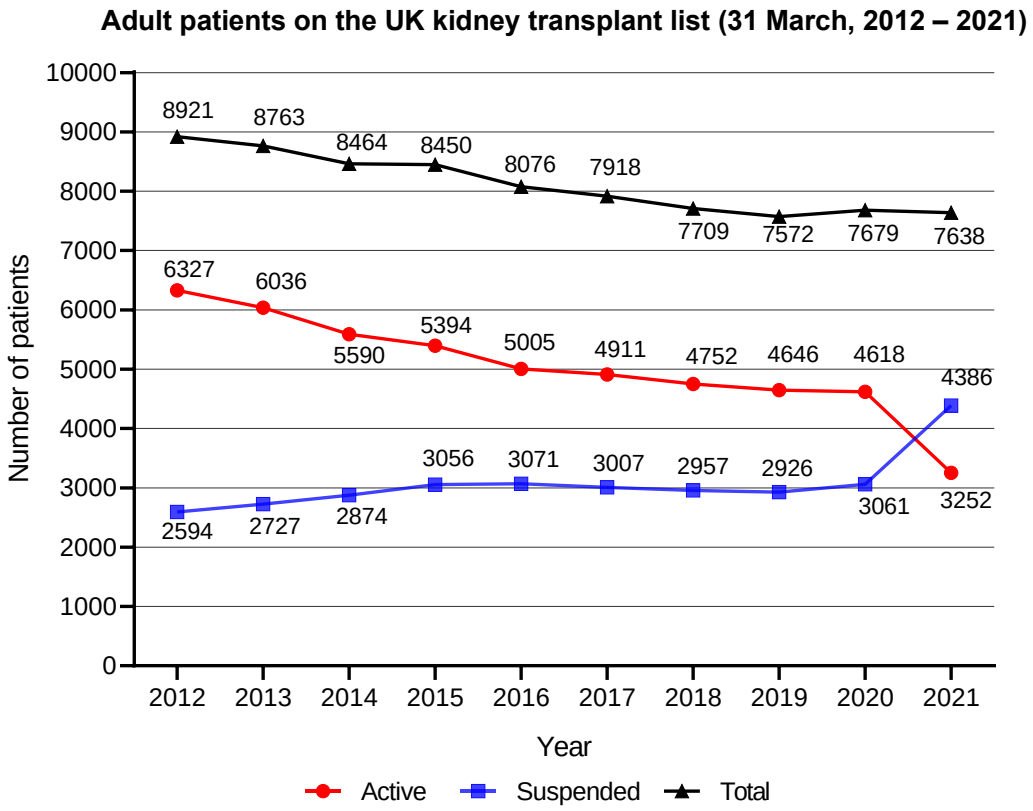

Figure 1.4| Number of adult patients on the kidney only UK transplant list on the 31st of March* each year between 2012 and 2021. Active patients are shown in red, while the suspended patients are displayed in blue. The total number of patients waiting for a kidney transplant in the UK is shown in black. *2020 data are shown on the 29th of February due to the ongoing pandemic. Figure adapted from the "Annual report on kidney transplantation 2020/2021 (1 April 2011 – 31 March 2021)" [60].

Life expectancy and quality of life are typically greater after transplantation. In particular, pre-emptive kidney transplantation is associated with better patient outcomes and organ survival than transplantation after dialysis has begun [61]. Despite the evident advantages, performing this type of surgery requires the immediate availability of a donor kidney and the recipient capable to remain stable off dialysis while all the analysis required by the transplantation program are performed [62]. However, it is important to know that transplantation may not be feasible for all patients. The general health condition of the patient, their ability to undergo a major surgery or to sustain the immunosuppressive therapy

which follows the transplantation can all be limiting factors. Furthermore, there can also be complications associated with the surgery itself. Indeed, the transplanted kidney undergoes an ischemia reperfusion injury that can irreversibly damage the organ. But the major limitation to kidney transplantation is the lack of donors. The number of adult patients registered in the waiting list for a kidney transplantation in UK has declined gradually from 2012 to 2021 (The number of patients actively waiting for a kidney transplant in the UK decreased from 6633 in 2012 to 4618 in 2020, Figure 1.4) [60]. It is important to notice that the waiting list from the 31st of March 2020 does not accurately reflect the need for kidney transplantation due to the COVID-19 pandemic, which had an unprecedent impact on the number of suspensions, leading to the drop of active waiting donors to 3252 in 2021 (Figure 1.4). Indeed, on the 31st of March 2021 many patients were still suspended due to the impact of the pandemic. Because of that, the data from the last year should be interpreted with caution [60]. Anyway, an analysis of the 3426 adult patients registered between the 1st of April 2017 and the 31st of March 2018 revealed that only 36% of them received a transplant within one year (Figure 1.5). Furthermore, three years after listing, only 66% of the patient has received a transplant (Figure 1.5) [60]. Regardless the impact of the pandemic in the last two year, the gradual reduction identified in the last decade is also partly due to the expansion of the donor pool by including older donors (60-69 and >70 year group) in the UK kidney donation guidelines [63]. Despite being well know that older donors are associated with higher risk of graft loss [64], it has also been recently revealed that the quality of kidneys from ≥70 year old donors (2007-2016) improved to the level of kidney from 60 to 69 year old donor of the previous decade (1997-2006) [65].

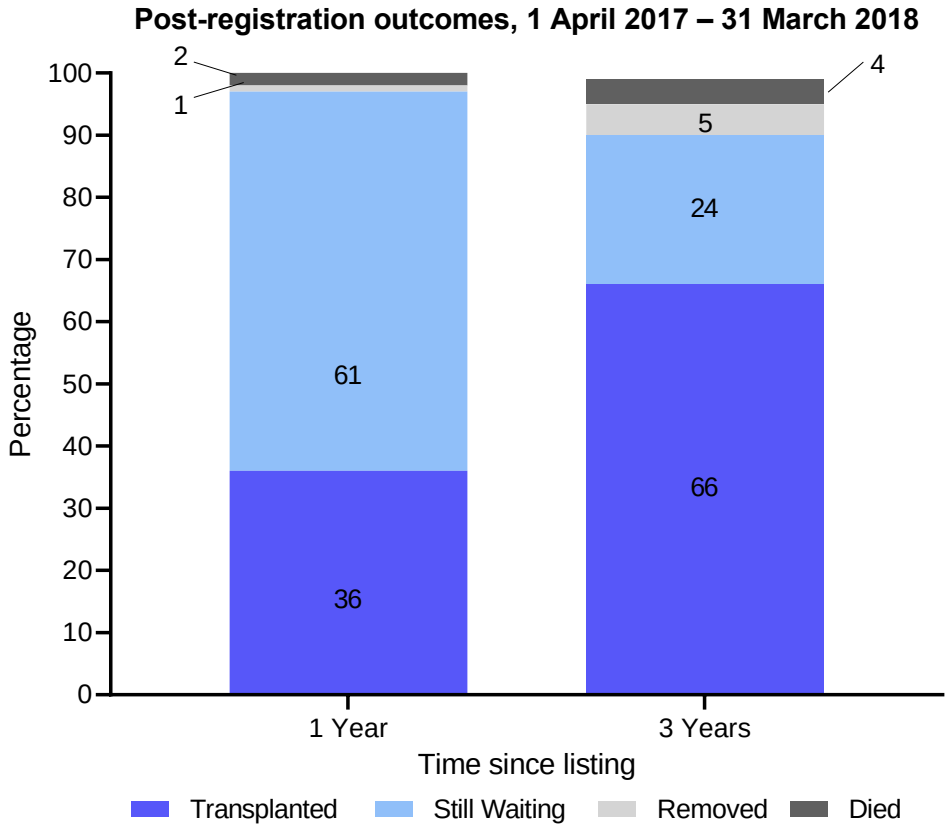

Figure 1.5| Post registration outcome for the 3426 new adult kidney-only registrations made in the UK between the 1st of April 2017 and the 31st of March 2018. The graph shows the proportion of transplanted patients (blue) or still waiting (light blue) one and three years after joining the list in the UK. It also shows the proportion of removed (grey) patients from the list and those died (black) while on it. Figure adapted from the "Annual report on kidney transplantation 2020/2021 (1 April 2011 – 31 March 2021)" [60].

Summarising, the poor quality of life of patients doing dialysis while waiting for a transplantation [66, 67], the lack of donors and the average waiting time before surgery [60] and the several conditions that can prevent the access of some patients to transplantation (e.g. age, other clinical conditions that can affect the outcome of the surgery, immunological compatibility) are all significant limitations of current RRT. All these underlines the need for novel therapies for kidney disease capable to act at the different stages of AKI, CKD and ESRD.

1.3 Regenerative Medicine

Regenerative medicine is a branch of medicine which studies novel methods to repair, regrow or replace cells, tissues and organs damaged by age, trauma, diseases, or congenital defects [68]. Regenerative medicine includes cell therapy, tissue engineering and the production of artificial organs.

Regenerative medicines are necessary because there are some acute and chronic pathologies for which there are no treatments capable of stopping and/or reverting the disease. The only therapies for those pathologies are currently mainly based, where possible, on organ replacement by transplantation. Unfortunately, this option suffers from huge limitations due to a restricted number of donors, possible immunological responses, and complications associated with the clinical procedures themselves. Regenerative medicine aims to overcome these limitations using two main strategies: fully replacing a damaged tissue with a new one having the same structural and functional properties of the original healthy tissue or, contributing to tissue healing (regeneration and repair) [68].

1.3.1 Cell therapies

The goal of cell therapy is to repair or replace damaged tissue or organ by infusion of viable cells [69]. The potential of this approach has been tested for many different diseases, including cardiovascular conditions [70], solid [71] and blood associated tumours [72, 73], neurological impairments [74], kidney associated diseases [75] and others. Bone marrow transplantation is one of the most well-known and widespread cell therapy in clinical practice and it was successfully performed in the first time in 1956 [76]. Cells for regenerative medicine can be basically distinguished between progenitor cells, including hematopoietic stem cells (HSC) and mesenchymal stromal cells (MSCs), and differentiated cells (*e.g.* T cells) [69]. In respect to the source of the cells, they can be derived from the patient (autologous cells) or from a donor (allogeneic cells) [77]. The choice between the two depends on many factors and is associated with specific strengths and weaknesses:

a) Autologous cells: the cells come from the patient themself, so there is no possible immune reaction against them. This is the main advantage of using these cells. Still, there are several drawbacks. The cells need to be harvested and expanded, a procedure that can be time-consuming and is not certain to yield enough cells at the end of the process. The harvest of the cells also requires specific equipment, which will depend on the tissue of origin. Moreover, for some pathologies it might be risky or difficult to get and use them (*e.g.* for blood related tumours, the autograft may be contaminated with clonogenic tumour cells that can contribute to relapse) [77, 78].
b) Allogeneic cells: the cells come from a donor, so they can be expanded, screened, and stored in liquid nitrogen (-180° C) long before they need to be used. This can be performed in specific well-equipped centres. Then, the cells can be shipped and

distributed to small centres where the cells can be easily thawed and administered to the patient [77, 78].

The cells can be administered to the recipient using different routes and methods, and the optimisation of cell delivery is essential to maximise the therapeutic effect of the cells. There are two main routes of cell administration [69]:

a) Systemic administration: cells can be intravenously (IV) or intraarterially (IA) injected. This route of administration has the advantage of being minimally invasive and to theoretically allow the cells to reach every tissue in the body. Nevertheless, intravenous administration of cells is usually associated with lung entrapment in animal models [79].
b) Local transplantation: the cells are delivered directly to the tissue of interest. Because of that, this route of administration can be more invasive than a systemic one and it is not feasible for all types of tissues. Anyway, there has been limited evidence that following local transplantation the cells can enter the circulation and reach different tissues [79].

Following cell administration, two different possible mechanisms of action have been proposed to take place [69]:

a) Engraftment of the administered cells followed by replacement of diseased cells.
b) Release of cytokines and/or growth factors from the injected cells, which are then capable of inducing endogenous tissue healing.

Cell therapy is a promising field for the treatment of different diseases. In particular, MSCs have raised the interest of the scientific community for their characteristics and potentiality.

1.4 MESENCHYMAL STROMAL CELLS

MSCs were isolated for the first time from the bone marrow (BM) in 1968 by Friedenstein and colleagues, who reported an adherent, fibroblast-like, clonogenic non-hematopoietic cell population with a high replicative capacity *in vitro* [80, 81]. Since then MSCs have been found in and isolated from many other sources, including adipose tissue [82], umbilical cord blood [83] and Wharton's Jelly [84], synovial membrane [85], tooth pulp [86] and other tissues [87]. [87]Three minimum common criteria have been set up by The International Society for Cellular Therapy to determine whether a cell can be considered a MSC: plastic adherence, trilineage (adipogenic, chondrogenic, osteogenic) differentiation potential *in vitro* and expression of CD73, CD90 and CD105, together with the absence of haematopoietic

markers such as CD45 and major histocompatibility complex (MHC) class II human leukocyte antigen (HLA)-DR [88].

In addition to trilineage potential, there are also many claims that they have the ability to (trans-)differentiate into cells of all three germ layers (e.g. pancreatic-like cells [89], neural-like cells [90], hepatocytes-like [91, 92], and others [93]), though the evidence for this is not very strong and lacks rigorous scientific support [94]. Moreover, in addition to having low immunogenicity, MSCs also have immuno-regulatory capacity [95]. All these properties have made MSCs a promising tool for cell therapy and tissue regeneration.

1.4.1 Clinical use of MSCs and importance of understanding the mechanism of action

MSCs were infused for the first time in human as a clinical agent in 1995 by Lazarus and colleagues [96]. Here, autologous bone marrow MSCs were collected from patients with hematologic malignancies in complete remission, expanded *in vitro* and reinfused intravenously with the aim to evaluate the feasibility of collecting, expanding and injecting human MSCs [96]. The first clinical trial was completed in 2000 by Koc and co-workers [97], who evaluated the positive impact of human autologous BM-MSCs on peripheral blood progenitor cells after the co-infusion of this cells in advanced breast cancer patients that had received high-dose chemotherapy [97]. Now, the use of stromal cell-based therapies in clinical applications is rapidly growing. Currently, there are over 3700 MSC-based clinical trials active or in recruitment world-wide (clinicaltrials.gov). However, despite their promising properties, little is known about how they might exert beneficial effects in disease and possible limitations associated with their use. In order to understand their potential mechanisms of action (MoA), better knowledge on the *in vivo* biodistribution and fate of exogenously administered MSCs is fundamental. In turn, a better comprehension of the MoA will allow optimal dosing regimens and targeting strategies to be established.

A recent report investigating the trends in MSC clinical trials undertaken from 2004 to 2018, revealed that among the multiple routes of MSC administration, IV injection is the most commonly used method for delivering MSCs to patients, accounting for 43% of trials [98]. For this reason, in most preclinical studies involving small animals, the selected route of administration is IV, typically through the tail vein of rodents [99, 100]. However, it is now well recognised that, at least in animal models, the IV-infused MSCs are subjected to a “first-pass” effect where they get trapped in the microcapillary network of the lungs, with no migration to other body sites [99, 101-104]. Moreover, they display a short-term survival, with most cells disappearing in the next few hours [99, 103, 105]. Therefore, one of the main

questions about MSCs is: how can these cells exert their therapeutic function if, after IV injection, they get stuck in the lung and die after a few days? On the other hand, preclinical studies conducted with locally injected MSCs revealed a prolonged survival of the cells at the site of injection [106], so understanding which mechanisms are involved in the clearance of infused cells is also something of a major interest.

1.4.2 MSC immunoregulatory function

Accumulating evidence suggests that MSCs exert their therapeutic potential by modulating the immune system instead of replacing local damaged cells themselves. Various *in vitro* and *in vivo* studies have shown the ability of MSCs to regulate both the innate and adaptive immune responses by suppressing natural killer cell proliferation and function [107, 108], inhibiting dendritic cell maturation [109], reducing B and T cell activation [110, 111], inducing an anti-inflammatory polarisation of the macrophages and by increasing the differentiation of T cells toward a regulatory phenotype [108]. MSCs have been reported to be able to secrete many soluble factors capable of mediating the immunomodulatory effects (Figure 1.6), including transforming growth factor-β1 (TGF-β1), involved in the regulation of lymphocyte proliferation, differentiation and survival, and in migration and survival of many innate immune cells; indoleamine-pyrrole 2,3-dioxygenase (IDO), an enzyme involved in the degradation of the essential amino acid tryptophan required for T cell activity; nitric oxide (NO), which attenuates T cell responsiveness; interleukin-10 (IL-10), a potent anti-inflammatory cytokine able to block immune responses at different levels by acting directly and indirectly on both the innate and adaptive immune systems; and prostaglandin E2 (PGE2), which suppresses the effector functions of macrophages, neutrophils and dendritic cells, but promotes Th2, Th17, and Treg responses [112-114]. Nevertheless, even if the modulatory effect is well documented, the therapeutic benefit is not yet well defined. Therefore, in the following paragraphs some novel insights into MSC-mediated immunomodulation and the role of the primed immune cells in mediating the therapeutic effects of MSCs will be introduced (Figure 1.6).

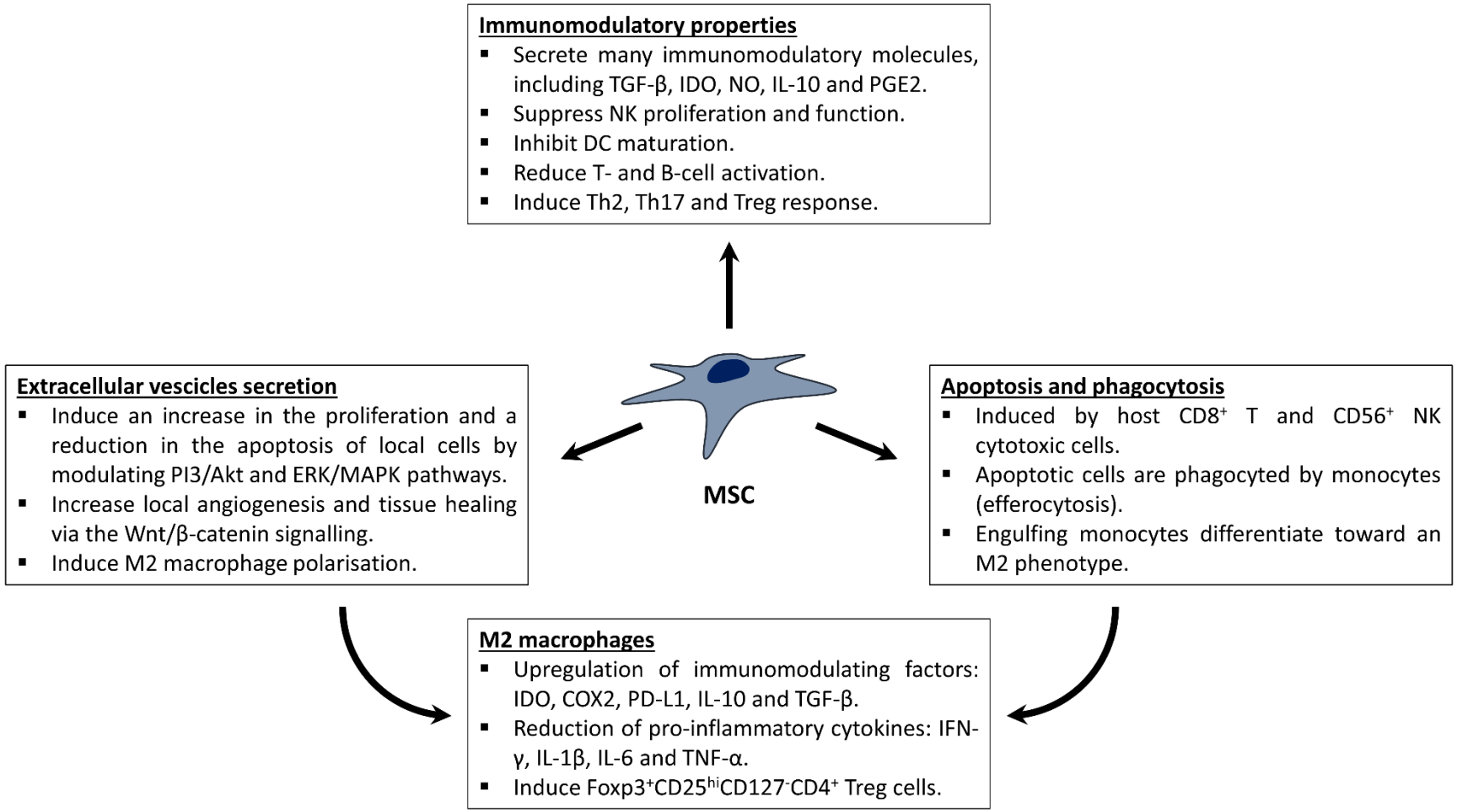

Figure 1.6| Summary of the potential mechanisms of action by which MSCs might act. This figure summarises some of the well know and documented mechanisms of action of MSCs and some novel ones recently proposed. Figure from Amadeo et al [115].

1.4.3 Apoptosis and phagocytosis of infused MSCs

Recognition and engulfment of apoptotic cells by phagocytic cells have an important role in tissue homeostasis, immunomodulation, and regulation of inflammation. When a cell undergoes apoptosis, it is cleared by local macrophages, which can then polarise toward different phenotypes depending on the stimulus. Apoptosis of IV-injected MSCs in the lungs followed by phagocytosis of the resultant debris by host macrophages has been recently proposed as a mechanism involved in MSC-mediated immunomodulation [102, 113, 116, 117]. This hypothesis has been tested in a mouse model of graft-versus-host disease (GVHD) by Dazzi and co-workers [113]. This group found that, although IV-administered human bone marrow-derived MSCs (BM-MSCs) rapidly underwent extensive caspase activation and apoptosis in the lung, this did not affect their ability to mediate immunosuppression. Apoptosis of the MSCs was mediated by the release of granzyme B and perforin by host $CD56^+$ Natural Killer and $CD8^+$ T cytotoxic cells [113]. Interestingly, the recognition of the MSCs was not triggered or mediated by the human leukocyte antigen (HLA) class I or class II and did not require the formation of an immunological synapse. Thus, the mechanism by which infused MSCs are recognized by cytotoxic cells has not yet been clarified. However, this same study further confirmed the role of apoptosis in mediating immunomodulation by infusing apoptotic MSCs (apoMSCs) and obtaining the same immunomodulatory effect. Furthermore, by labelling and tracing the apoMSCs, among several phagocytic populations investigated, the authors detected a $CD11b^{high}CD11c^{intermediate}$, a $CD11b^{high}CD11c^-$ and a $CD11b^-CD11c^+$ population responsible for MSC engulfment and clearance in the lungs, a process called efferocytosis [113]. To clarify the role of apoMSCs engulfment in exerting MSC function, Dazzi's group conducted a further study where they found a reduction in the T-cell response mediated by monocytes co-cultured with apoMSCs [118]. Interestingly, these monocytes exhibited a functional and molecular immunosuppressive phenotype, with a significant upregulation of immunomodulatory molecules, including IDO, cyclooxygenase2 (COX2) and programmed death-ligand 1 (PD-L1), together with an increased secretion of PGE2 and interleukin-10 (IL-10), and a reduction of tumour necrosis factor-α (TNF-α). Moreover, the study showed how the upregulation of PD-L1, IDO and IL-10 was mediated by the COX2/PGE2 axis, identifying it as a key effector of apoMSC-induced immunosuppression [118]. Indeed, only monocytes that had engulfed the apoMSCs displayed this phenotype, linking the *in vivo* MSC apoptosis with their immunomodulatory function [118]. This result agrees with a recent study published by Witte et al [102], where human umbilical cord MSCs (UC-MSCs) labelled with the lipophilic dye PKH26 were infused in mice. As expected, the cells got trapped in the

lungs and, after 24h, the PKH26 dye was mostly found in $CD11^+$ cells, suggesting the phagocytosis of the UC-MSCs from local host innate-immune cells. Witte and colleagues confirmed these results *in vitro* by mixing PKH26-labelled MSCs with $CD14^+$monocytes derived from peripheral blood mononuclear cells: nearly all monocytes became positive for PKH26 within 24 hours. Interestingly, this co-culture also revealed a shift of the monocytes, with increased expression of CD163 and CD206, markers associated with an immune regulatory function. Furthermore, these primed monocytes were added to mixed lymphocyte reactions resulting in the upregulation of the level of $Foxp3^+CD25^{hi}CD4^+$ regulatory T (Treg) cells [102]. A similar phagocytosis mechanism was reported by Braza et al [117], who reported that IV infused PKH26-labelled BM-MSCs were cleared in the lungs by monocytes/macrophages within 24h. PKH26 positive macrophages were reported to display an anti-inflammatory M2 phenotype, with an increase in TGF-β and IL-10 secretion. This result is corroborated by *in vitro* experiments performed by Ghahremani et al [119], who showed the induction of an anti-inflammatory-like phenotype in macrophages after the efferocytosis of adipose derived MSCs (A-MSCs), with an upregulation of IL-10 secretion, and a reduction of TNF-α and NO production.

A possible mechanism to explain the macrophage-mediated phagocytosis of MSCs was proposed by Gavin et al [116], who revealed that live MSCs can be phagocytised by monocytes via a complement-mediated opsonization. The complement system is made up of a large spectrum of different plasma proteins that can react with each other to opsonise pathogens and trigger a series of inflammatory responses. After exposing BM-MSCs to human plasma, an enrichment of C3 complement protein on the surface of the cells was detected [116]. Interestingly, Gavin et al reported an increase in monocyte phagocytosis of MSCs pre-treated with plasma, and a significant reduction of this effect by inhibiting the C3 protein, suggesting a direct role of complement opsonization in the clearance of the infused cells [116].

Taken together, these results suggest a direct involvement of the immune system in the clearance of IV-infused MSCs and in mediating their function. Apparently, after MSCs get trapped in the lungs, they are quickly killed and opsonised by local cytotoxic cells and macrophages, respectively. Then, the phagocytosis triggers the polarization of the macrophages to a M2 anti-inflammatory phenotype, which can increase the secretion of immunomodulatory factors, such as IDO, IL-10 and TGF-β, and the upregulation of Treg cells. Nevertheless, even if the involvement of phagocytosis and MSC clearance after IV infusion is

becoming quite clear, how this mechanism can mediate the final therapeutic process still remains uncertain.

1.4.4 Exosomes

Another potential mechanism for the therapeutic effect of MSCs is the paracrine secretion of tropic factors, with exosomes being of special interest. These nano-sized membrane vesicles are able to carry several types of molecules, including proteins, nucleic acids, and lipids, some of which could possibly mediate the beneficial effects of MSCs. Indeed, during the last few years, exosomes derived from different sources of MSCs were found to have a therapeutic effect in many disease models, such as myocardial ischemia/reperfusion injury [120-122], kidney disease [123, 124], wound healing [125], hepatic disease [126-128], and more recently, cartilage and bone regeneration [129-132] and neurological disease [133]. In particular, many studies have reported an increase in local cell proliferation and reduction of apoptosis and inflammation after exosome infusion or transplantation [134-136], and different molecular mechanisms have been investigated. Interestingly, exosomes can be released by the administered cells, or can be collected *in vitro* and administered directly into the subject, avoiding the need of injecting cells and all the possible negative effects that can be related to that.

1.4.4.1 AKT, ERK and MAPK axis

A molecular pathway that has recently emerged to be mediated by MSC-released exosomes and to have a role in the regulation of proliferation and apoptosis is the protein kinase B (also known as Akt), extracellular receptor kinase (ERK) and mitogen-activated protein kinase (MAPK) axis [131, 132, 136, 137]. The phosphatidylinositol 3-kinase (PI3K)/Akt pathway and the MAPK/ERK signalling cascade are both composed of a group of downstream effectors important for regulating cell growth and proliferation, survival and apoptosis, mobility and invasion [138, 139] . In a recent study involving both an *in vitro* and an *in vivo* model of osteoarthritis (OA), Zhang et al [132] demonstrated that exosomes purified from human embryonic stem cell-derived MSCs could reduce inflammation and restore matrix homeostasis by acting through adenosine receptor-mediated Akt and MAPK/ERK phosphorylation on local chondrocytes. As a direct consequence of the involvement of this pathway, Zhang and colleagues reported an enhancement in local proliferation, with a reduction in apoptosis and fibrosis [132]. Furthermore, Zhang et al have previously reported that activation in chondrocytes of these two pathways was mediated by the ecto-5'-nucleotidase (NT5E) activity of CD73 carried by the exosomes [136]. Indeed, CD73 can

convert extracellular adenosine monophosphate to adenosine, which in turn can interact with adenosine receptor and modulate the Akt and MAPK/ERK signalling [140, 141]. These results were confirmed by Chew and colleagues, who demonstrated the involvement of this mechanism in the enhancement of periodontal regeneration mediated by MSC-derived exosomes [131].

1.4.4.2 WNT/β-Catenin signalling pathway

Another possible molecular mechanism for the role of exosomes in tissue regeneration is the Wnt/β-catenin signalling pathway. Since this mechanism plays a key role in tissue homeostasis and cell fate [142], it has become a major field of interest in the last years. This mechanism was investigated and reported to be involved in wound healing by Zhang and colleagues, who found that human UC-MSC-derived exosomes could promote angiogenesis and wound healing when injected subcutaneously into second degree burns [143-145]. After Wnt4 knockdown, the beneficial effects induced by the exosomes were reduced, suggesting an involvement of this pathway in exosome mediated angiogenesis in cutaneous wound healing [144]. The involvement of Wnt/β-catenin was also recently revealed in a model of myocardial ischemia-reperfusion injury by Cui and colleagues [122], who reported an increased activation of the pathway in rat myocardium, associated with anti-apoptotic and pro-survival effects on local cardiomyocytes, after the IV administration of A-MSC derived exosomes [122]. Nevertheless, there are some controversial results about the role of exosomes in the activation or inhibition of this pathway. Ron et al recently published a paper where they claimed BM-MSC derived exosomes reduced liver fibrosis through the inhibition of the Wnt/β-catenin pathway [146]. So, how this mechanism is regulated by exosomes remains unclear and further analysis are required to elucidate whether the exosomes are really able to mediate it and if this has any therapeutic relevance.

1.4.4.3 Exosomes and immunomodulation

Immunomodulation is another function that can be exerted by exosomes, and this has become a major field of interest. A novel metabolomic study published by Showalter and colleagues [147] revealed how the correct priming of MSCs can increase the packaging of molecules and lipid membrane components inside the exosomes that have been directly associated with immunomodulation, including M2 polarization *in vivo*. Several studies have indeed reported the increase of M2 macrophage infiltration and anti-inflammatory cytokine upregulation, such as IL-10, with a parallel decrease in M1 macrophages and inflammatory cytokines, including interferon- γ (IFN-γ), IL-1β, IL-6, and TNF-α following the administration

of MSCs-derived exosomes [121, 136, 148]. Apparently, the function exerted by exosomes and the macrophage M2 polarisation are strictly related mechanisms, both involved in MSC-mediated wound healing. Indeed, in support of this hypothesis, studies have shown that the depletion of macrophages can reduce and delay the wound healing exerted by infused MSCs [121, 149]. Likewise, inhibition of exosome release also results in a reduction of macrophage polarisation toward a M2 phenotype both *in vitro* and *in vivo* [149].

Macrophages have displayed polarisation towards an M2 phenotype after exposure to MSC-derived exosomes in multiple studies [121, 136, 150-153] and different factors have recently been proposed to be involved in this. Lan, et al revealed how the incorporation of protein inside the exosomes can exert effects that the free form of the same protein cannot do [148]. They discovered that the incorporation into MSCs exosomes of Metallothionein-2, a critical regulator of numerous cell activities (including immunomodulation), mediates the upregulation of macrophages anti-inflammatory ability, while the free form of this protein has no effect on them [148]. Many research groups are focusing their attention to investigate the role of the population of miRNA contained inside exosomes and to clarify any possible role in their immunomodulatory capacity. Let-7a, miR-23a, miR-25b [150] and miR-182 [121] have already been identified as miRNAs able to act on and downregulate the Toll-Like receptor 4 (TLR4)/NF-kB signalling pathway within macrophages, which in turns increases the activation of the PI3K/Akt signalling pathway, leading to M2 macrophage polarisation [121].

Even if there is no clarity yet on whether there is a polarisation of the local macrophages or just a recruitment of these cells, all these results support the active role of immunomodulatory macrophages in mediating the therapeutic effect of MSCs, and the involvement of MSC-derived exosomes in this process. However, the *in vivo* biodistribution, pharmacokinetics and the specific mechanisms of action of exogenously administered exosomes are still to be further elucidated.

1.4.5 MSCs in renal treatment

Transplantation of autologous and allogeneic MSCs have been shown to improve kidney injury in different animal models [154-156], and the use of these cells as a possible therapeutic agent is now being extensively tested in different clinical trials. The potential application of MSCs in kidney disease have been explored taking different aspects into account.

The secretion of a pool of different trophic factors and the immunomodulatory properties of these cells have been considered and evaluated to enhance the natural regenerative process

of AKI [157-159]. In preclinical studies, MSC-derived exosomes have been reported to ameliorate kidney injury in terms of renal cell survival, reduction of epithelial cell apoptosis, decrease of inflammation and immune response, improvement of the structure of the extracellular matrix [154, 160]. The same effect can also be obtained with other types of MSCs derived vesicles. As described previously, vesicle secreted by MSCs are rich in molecules and miRNA and their use have been extensively investigated for a possible therapeutic effects in models of AKI [155, 156], where their use was reported to reduce renal cell apoptosis and increase their proliferation [156]. In a mouse model of induced AKI, the administration of MSC-derived microvesicles accelerated functional recovery by inducing the proliferation of tubular cells [157]. A similar effect was also reported in a rat model of renal ischemic reperfusion injury: the extracellular vesicles improved the tubular injury and protected renal function by modulating the activity of NK cells [158].

The immunosuppressive effect of MSCs has also been investigated in kidney transplants. In a rat model of allogeneic kidney transplantation, infusion of allogeneic BM-MSCs reduced infiltration of CD8 T cells and monocytes into the transplanted kidney and helped reduce the incidence of graft rejection [161]. A kidney transplantation study performed using a mouse model revealed that the administration of MSCs 24 hours before kidney transplantation was associated with an increase in the pool of regulatory T cells and an increased survival of the graft [162]. On the other hand, some studies have shown no beneficial effect of MSCs on renal transplantation. A recent Chinese study reporting on the outcome of a clinical trial where 21 recipients received allogeneic UC-MSCs immediately prior to transplantation, revealed no statistically significant differences with the controls in terms of renal function, rejection or survival of the kidney transplant one year post-transplantation [163]. Moreover, an experimental study conducted in Germany revealed adverse effects following MSC infusion in a rat model of kidney transplantation. The intravenous administration of BM-MSCs four days before kidney transplantation was associated with a more severe cellular and humoral rejection and worse graft function [164]. This is another example of how it is necessary to have a good understanding of the mechanisms of action before moving forwards with clinical studies.

1.4.6 MSCs: possible limitations and importance of conducting proper pre-clinical studies

Besides the importance of understanding the mechanism of action of MSCs to determine whether the cells or their derived products such as extracellular vesicles or apoptotic bodies exert the therapeutic function, there are many other concerns relating to the applicability of

MSCs-based regenerative medicine therapies to the clinic. As stated previously in 1.4.1, MSCs are currently being used in many clinical trials. For this reason, collecting adequate pre-clinical data relating to the safety, the biodistribution, and the fate of the cells is crucial before moving to clinic. Some cases of misconduct have already been reported, such as what has happened with a surgical procedure for replacing parts of the trachea using a tissue engineering construct. The substitute was developed by growing mesenchymal stromal cells on a synthetic scaffold and subsequently implanted into nine patients without doing any pre-clinical analysis. Seven out of those nine patients died within two years after the surgery [165]. Another example of the importance of proper preclinical studies is the case of a patient affected by the neurodegenerative hereditary disorder ataxia telangiectasia and administered with human neuronal stem cells derived from embryonic stem cells [166]. Four years after the first treatment the patient was diagnosed with a multifocal brain tumour caused by the implanted cells [166].

The only way to effectively minimise this risk is to obtain robust data from pre-clinical trials before moving to the clinic. Questions that need to be addressed include:

a) Undesired differentiation: uncontrolled proliferation or differentiation of infused MSCs can be a major concern related to their clinical use. BM-MSCs used to treat a model of myocardial infarction in mice has been reported to lead to the formation of calcified tissue close to the infarcted area [167, 168]. However, no cases of uncontrolled proliferation have been reported so far in humans.
b) Possible tumorigenicity [169]: this is directly related to the previous point. Due to their differentiation and proliferation abilities, MSCs could potentially develop a tumour in the site of engraftment. Also, genetic manipulation and long-term *in vitro* cultures can be associated to genetic instability and chromosomal aberration [169]. Additionally, MSCs can also be implanted in chemotherapy or radiotherapy patient, with a compromised immune system, and this can also be associated with a risk of tumorigenesis [170].
c) Furthermore, MSCs can contribute to the growth of a pre-existing tumour in different ways. MSCs immunomodulatory properties can enhance tumour survival and growth [171] and, additionally, MSCs can enhance the formation of novel vascular structures and, again, facilitate tumour survival, growth and metastasis [172].
d) Embolism: the administration of MSC through the cardiovascular system can lead to the blockage of a vessel. The formation of micro-occlusion following intra-arterial MSCs infusion have been reported and have been revealed to be associated on the

infusion modalities. In particular, cell dose and infusion velocity seem to influence the risk of embolism [173]. Also, Jung et al reported lung embolisms and infarcts in three patients who received multiple intravenous infusions of autologous adipose MSCs [174].

e) Immunogenicity: despite the immunomodulatory potential of MSCs, using allogeneic cells can be a risk to trigger an adverse undesired immunological reaction and it must be considered when moving toward the clinic [175].

f) Efficacy: the evaluation of the efficacy in pre-clinical models should be mandatory, and the cells' therapeutic effect should always be compared with the standard therapies for a specific disease. Each batch of MSCs should be well characterised prior to administration and the development of novel *in vitro* assays looking into the therapeutic potency of the cells can help into this [176].

It is important to investigate all these aspects in appropriate pre-clinical models before translating into the clinic. Having a complete knowledge of these would also help to better develop a risk-benefit analysis for each clinical scenario.

1.5 MSCs LIVE IMAGING

The development of non-invasive pre-clinical imaging methods to monitor the fate and the biodistribution of infused cells into various animal models at different time points can help to generate a better understanding of the efficacy and the safety of MSC-based therapies [177]. Cells can be tracked either by labelling the cells with specific molecular probes or by genetically engineering them to overexpress a specific reporter gene. Labelling probes need to be taken up by the cells and, because of this, it is important to underline that the signal is not directly related to the cells and to its viability, but just to the presence of the probe itself, which can also be released from the labelled cells and lead to misleading false positive results [178, 179]. Furthermore, when a cell labelled with this kind of probes divides, the probe is distributed between the two new cells, resulting in a progressive signal dilution [179]. This type of probes includes fluorescent quantum dots for optical imaging [180], superparamagnetic iron oxide nanoparticles (SPIONs) or paramagnetic metal chelates for magnetic resonance imaging (MRI) [181], radioisotopes for positron emission tomography (PET) and single-photon emission computerized tomography (SPECT) [182] or gold nanorods for photoacoustic imaging [183].

On the other side, reporter genes can be integrated into the cell genome using viral or non-viral methods. Once integrated, they can be transcribed and transduced into a final protein.

This technique can include genes encoding for fluorescent probes for optical imaging [184], iron homeostasis proteins (e.g. ferritin [185]), reporter enzymes [186] and chemical exchange saturation transfer [187] for MRI, reporter genes encoding either for protein capable to phosphorylate a specific PET probe, or for a receptor or a transmembrane protein specific for a PET probe [188], and genes encoding for enzyme capable of oxidising a specific bioluminescent substrate resulting in the emission of light (bioluminescence imaging) [189]. The last technique in particular requires the administration of a specific molecule (substrate) capable of interacting with the protein (enzyme) encoded by the reporter gene to obtain a signal coming from the cell [177]. Reporter genetic probes have the great advantages of not losing or diluting the signal when the cells divide and to be directly associated to the cells, with no release in the surrounding environment for most of the reporter genes used [178]. On the other hand, they have one major limitation, which is the genetic manipulation of the cells and can represent a safety issue. Further limitations include substrate distribution or enzyme turnover [177, 178], or background uptake and clearance of the substrate. Also, some reporter genes, such as the herpes simplex virus 1 – thymidine kinase (HSV1-tk) [188] or the Firefly luciferase (FLuc) [190], have been associated to an increased immune response in the host toward the genetically modified cells.

Bioluminescence is a gene reporting imaging technique widely used to track the biodistribution of infused cells in small animal models. In the next section the principles of bioluminescence and its use for live imaging will be described.

1.5.1 Bioluminescence

Bioluminescence is a natural phenomenon occurring in many groups of organisms, from bacteria and protists to animals (e.g. fish and insects) [191]. The production of light is a result of a biochemical reaction, during which the oxidation of a substrate (e.g. luciferin) is catalysed by an enzyme (e.g. luciferase). Unlike fluorescence, there is no need of incident radiation to emit light. This allows the signal to glow on a dark background, resulting in an increase in the sensitivity of the system. Furthermore, luminescence does not share the disadvantages of fluorescence associated with the necessity of an incident light source, like cytotoxicity, autofluorescence of the sample, quenching of the signal or bleaching of the fluorochrome [192]. All these properties make luminescence a good candidate for non-invasive imaging in living animals. Consequently, its use has increased greatly in the past two decades and BLI is now a standard technique for quantitative non-invasive live imaging that can be used to monitor different mechanisms, such as gene expression [193], cell

biodistribution [99], tumour growth [194], and protein-protein interaction [195], in animal models at different intermediate time points without killing the animal [196].

Different bioluminescence systems, composed of a specific enzyme and a related substrate, have been identified in nature. Bioluminescence systems widely used in research can be divided into two major groups, based on consumption of adenosine triphosphate (ATP). The first group of enzymes, mostly derived from insects, generates light through a two-step oxidative biochemical reaction. The substrate is initially adenylated by ATP to generate an adenosine monophosphate (AMP)-substrate intermediate. This is subsequently oxidised by molecular oxygen (O_2) leading to the formation of an excited oxy-intermediated from which photons can be emitted with a specific wavelength [197]. The second group of enzymes includes ATP-independent luciferases cloned from luminous marine organisms [191]. ATP-independent luciferase commonly used in laboratories are derived from the sea pansy *Renilla reniformis* (RLuc), the marine copepod *Gaussia princeps* (GLuc), or the deep-sea shrimp *Oplophorus Gracilirostris* (OLuc). A substrate shared by many of these marine luciferases is coelenterazine (CTZ). CTZ can react with O_2 in presence of its luciferase pair and form an oxidized intermediate, which can emit light following CO_2 loss [191]. It is also important to mention that, whilst most of the luciferases are intracellular enzymes, the GLuc is actually secreted [198].

The most commonly used ATP-dependent system used in research is composed by the Firefly Luciferase (FLuc) from *Photinus Pyralis* and its specific substrate, the D-Luciferin. Luciferases from other organisms have also been cloned and are used in research, but not as widely [199].

In vivo bioluminescence imaging (BLI) is the result of light emitted by the reporter system exceeding the light absorbed and scattered by the animal tissues [200]. Thus, even though bioluminescence has the great advantage of a dark background because there is no spontaneous light emission from the tissue, these can reduce the signal intensity at the surface by absorption [201]. Endogenous chromophores present in the body are responsible for this phenomenon. Within the visible spectrum (from 400 to 760 nm) haemoglobin is the main chromophore responsible for light absorption in the tissues, together with melanin in the skin if the animal is pigmented [201]. As a direct consequence of light attenuation by tissues, light sources closer to the surface of the animal give a stronger signal when compared to those that are deep-seated.

Haemoglobin (Hb) absorbs mainly in the blue and green part of the visible spectrum, displaying some differences depending on its form (oxyhaemoglobin or deoxyhaemoglobin) [202]. However, it has a low absorption of wavelength longer than 600 nm, allowing the transmission of red light through the tissues [201]. Therefore, the spectral properties of the luminescence system can have a significant impact on imaging, and systems that emit red light are optimal when transmission through tissues is concerned. The oxidation of D-Luciferin catalysed by FLuc yields the emission of photons with a peak wavelength of ∼560 nm. On the other hand, oxidation of CTZ in the presence of natural marine luciferases produces photons at ∼480 nm [196]. Because of its long-wavelength emission, FLuc and D-luciferin system have been widely preferred to other luciferases systems. Nonetheless, part of the light emitted during the oxidation of D-luciferin is still absorbed. Therefore, many strategies have been studied and developed to generate red-shifted light.

Both ATP-dependent and independent luciferase systems have been extensively engineered to improve signal output. Table 1.3 summarises some luciferase reporters and the associated substrates. The gene encoding for the original FLuc, for example, was optimised for mammalian expression (e.g. luc2 gene). In addition to the enzyme, substrates have also been engineered. For instance, D-Luciferin analogues have been developed and synthetized [203], although most of them did not result in an increase of signal intensity when compared to FLuc/D-Luciferin. Only a few D-Luciferin analogues, such as CycLuc1 [204] or Akalumine [205], are claimed to have improved *in vivo* performance under particular conditions. Engineering of FLuc/D-luciferin system has also been used for other purposes, not only to increase the signal. Prescher and colleagues [206] synthetized a series of D-Luciferin analogues and screened them for different FLuc mutants able to discriminate among the D-Luciferin analogues. This resulted in a series of FLuc/D-luciferin-derived pairs that can be used to perform multiple BLI analysis in the same animal at the same time [207]. Furthermore, to date, more than 30 luciferases able to oxidise D-luciferin have been discovered from different species. Among all of these, click beetle luciferases such as CBR and ELuc are reporters commonly used because of their thermal stability and ability to emit different colours from 540 nm to 615 nm following D-luciferin oxidation [208]. Those luciferases have been modified to optimise the signal as well. Recently, Hall et al [209] reported an engineered mutant of the CBR, CBR2opt, which showed a maximum emission at 745 nm in presence of a naphthyl-luciferin analogue, NH2-NpLH2, although the sensitivity *in vivo* was not better than CBR2opt paired with D-luciferin (617 nm emission peak) [209].

As mentioned before, RLuc, GLuc and OLuc are ATP-independent luciferase commonly used in laboratories. Different luciferases have been derived from these, to increase the wavelength of emission. It is important to notice that CTZ and some other substrates for marine luciferases display poor water solubility [210, 211], something that can hinder and reduce their *in vivo* application [211]. So, in the same way, many analogues of CTZ have been synthesized [212] (Table 1.3). Some of the newly developed luciferases have revealed to have *in vitro* properties even better than FLuc. For example, a derivate of OLuc, the NanoLuc, in presence of furimazine (FZ), a CTZ analogue, has revealed a signal ∼100-fold brighter than FLuc *in vitro* [213]. Unfortunately, NanoLuc, as many other ATP-independent luciferases and their derivates, displays a blue emission peak at ∼460 nm, resulting in poor tissue penetration and thus are not well-suited for *in vivo* imaging. A derivate of NanoLuc, teLuc, was recently engineered [214]. In the presence of diphenylterazine (DTZ), a synthetic substrate, teLuc displays an emission peak at ∼502 nm, with a good emission of photons at wavelength longer than 600 nm [214]. A recent study has reported novel FZ-derived substrates for NanoLuc able to shift the emission to nearly 600 nm, although the bioluminescence intensities were low [215]. Another strategy adopted to red shift the signal from this category of luciferase is the Bioluminescence Resonance Energy Transfer (BRET). Resonance energy transfer (RET) is a photophysical phenomenon occurring between two chromophores. An excited donor chromophore may transfer its energy to an acceptor chromophore via a nonradiative dipole-dipole coupling process [192]. Basically, a photon emitted by the excited chromophore has the right wavelength to excite the second chromophore, which will emit a photon with a second wavelength. This energy transfer can happen only if the two chromophores are in close contact. When the light source required to excite the second chromophore is the results of a bioluminescence reaction, this phenomenon is called BRET [192, 216]. Although BRET is a useful method for monitoring different biological process, like protein-protein interactions [217], it can also be used to generate a red-shifted signal, evading tissue absorption [218-220]. This has been achieved, for example, by fusing NanoLuc or teLuc with CyOFP1, a fluorescence protein with an emission peak at 590 nm, to generate two BRET systems called Antares [218] and Antares2 [214], respectively.

Table 1.3: Luciferase-luciferin pairs, divided in ATP-dependent and independent groups. The emission peak is specified.

	Luciferase	Luciferin	λ_{max} (nm)	References
ATP-Dependent Luciferases	FLuc	D-Luciferin	563	[221, 222]
		CycLuc1	600	[204]
		Akalumine/Akalumine-HCl	675	[223]
	AkaLuc	Akalumine/Akalumine-HCl	650	[205]
	CBR	D-Luciferin	615	[208]
	CBR2opt	D-Luciferin	615	[209]
		NH2-NpLH2	745	[209]
	ELuc	D-Luciferin	538	[224]
ATP-Independent Luciferases	Rluc	CTZ	482	[225]
	RLuc8	CTZ	487	[226]
	RLuc8.6	CTZ	535	[227]
		v-CTZ	590	[227]
	GLuc	CTZ	473	[228]
	GLuc Monsta	CTZ	513	[229]
	GLuc4	CTZ	495	[230]
	OLuc	CTZ	460	[231]
	NanoLuc	FZ	460	[213]
	teLuc	DTZ	502	[214]
	yeLuc	STZ	527	[214]
	Antares (BRET fusion protein)	FZ	590	[218]
	Antares2 (BRET fusion protein)	DTZ	590	[214]

Abbreviations: CBR, click beetle red luciferase; CTZ, coelenterazine; DTZ, diphenylterazine; FLuc, firefly luciferase; FMNH2, reduced flavin, mononucleotide; FZ, furimazine; GLuc, Gaussia luciferase; RLuc, Renilla luciferase; STZ, selenoterazine.

Finally, there are other factors that must be considered when performing BLI. Bioluminescence has a low brightness caused by the slow turnover of the luciferases. Because of this, bioluminescent reporters are mostly used in macroscopic imaging with low spatiotemporal resolution, although recent studies revealed the possibility to perform imaging with a single-cell detection sensitivity [192, 205]. Moreover, several factors influence the detection of the internal light source (sensitivity). These include the level of expression of the luciferase, the amount of substrate delivered to the expressing cells, the depth of the labelled cells within the body, the absorption of the signal from the surrounding tissues, and the sensitivity of the detection system itself [199, 232]. Improvements in the technology of the detection systems have increased the sensitivity and the quality of the acquired images. Emitted photons are detected by a specialised charge couple device (CCD) cameras, which can convert the incident photons into specific electrical signals that can be converted by a dedicated software into the final image [199].

1.6 Introduction Summary and Aims of the Thesis

Summarising, kidneys are important organs involved in waste removal, fluid and blood homeostasis, and secretion of important hormones. Different pathologies, including AKI and CKD, can severely affect kidney function, resulting in patients no longer being able to properly filter their own blood. There are no specific treatments for AKI or CKD and the only available therapies involve replacing renal function, either with dialysis or transplantation.

Regenerative therapies are promising solutions for kidney disease and different cell types, including mesenchymal stromal cells from different sources, have shown beneficial effects in preclinical models and are currently being tested in clinical trials. However, despite being widely studied, the current understanding of the biodistribution, safety and the interaction of MSCs with the host is still not complete. Furthermore, a parallel comparison of the behaviour *in vivo* of different sources of MSCs has not been performed yet. Bioluminescence imaging is a non-invasive preclinical imaging technique that can be used to assess the biodistribution and the safety of MSCs encoding for a BLI reporting gene *in vivo*.

The main goals of this thesis were to:

1. Characterise three different sources of MSCs (umbilical cord, bone marrow and adipose) *in vitro* and optimise a transduction protocol suitable to generate transduced UC, BM and A-MSCs.
2. Evaluate the use of a novel Firefly Luciferase analogue, the Akaluc system, as a possible reporter gene for *in vivo* cell tracking in small rodents.

3. Use the transduced MSCs to explore their short term biodistribution in small rodents when administered intravenously and to investigate whether the presence of an ischemia reperfusion injury can impact on it.
4. Use the transduced UC-MSCs to explore their safety in immunocompromised animals and to investigate the response of the host immune system in the first 24 hours following the administration of the cells.

CHAPTER 2 GENERAL MATERIALS AND METHODS

2.1 CELL CULTURE

Umbilical cord (UC-), bone marrow (BM-) and adipose derived (A-)MSCs are the most used MSCs in clinical trials (clinicaltrials.gov). As part of the RenalToolBox international training network, we had the possibility to share between different sites mesenchymal stromal cells (MSCs) coming from these three different sources (umbilical cord, bone marrow and adipose tissue). The idea was to culture and work with the three most commonly used MSCs using standard conditions shared among the sites to identify any possible difference in the *in vitro* and *in vivo* behaviour of the cells.

2.1.1 Cell isolation

The three types of MSCs were provided by different sites according with their specific regulations.

2.1.1.1 Umbilical cord derived mesenchymal stromal cells

Human UC-MSCs were isolated from umbilical cord tissue donated by 3 healthy volunteers at National Health Service Blood and Transplant (NHS-BT), in Speke, Liverpool. The procurement and processing of the umbilical cords was licensed by the UK's Human Tissue Authority. The cells were isolated according to NHS-BT good manufacturing practice (GMP) procedure: at arrival, the cord tissue was quickly washed with an ethanol solution and moved to the grade A GMP environment. Here, the tissue was halved horizontally, chopped into big pieces, and plated into 150 mm diameter dishes with the inner layers facing the surface of the dish. Then, the cord pieces were covered with 60 mL of GMP-grade Minimum Essential Medium Eagle alpha (MEM-α) supplemented with 10% of GMP-grade human platelet lysate (HPL). After 7 days, during which the cord was cultured untouched, the pieces were removed, and the medium replaced with fresh medium. Then, the cells were passaged, and the process was scaled up to produce the number of cells required for clinical use. When the cells were split from P2 to P3, an aliquot of cells was cryopreserved and shipped to the Department of Molecular Physiology and Cell Signalling of the University of Liverpool in accordance with a Materials Transfer Agreement drawn up by the NHS to cover all the experiments described in this thesis.

2.1.1.2 Bone marrow derived mesenchymal stromal cells

Human BM-MSCs were provided by the University of Galway following isolation from 3 separate donors after being purchased from Lonza (Basel, Switzerland). Briefly, at the arrival of the bone marrow, the tissue was washed twice with phosphate-buffered saline (PBS). Following a centrifugation at 900g for 5 minutes the supernatant was discarded, and the lower phase was suspended in 5 mL of PBS to perform a cell count. The mononucleated cells suspension was then seeded into T-175 flasks with a seeding density between $2.37x10^6$ and $3.39x10^6$ cells/cm^2. The cells were expanded until 80% confluence with regular medium change every 3-4 days. Following passaging, an aliquot of each donor was cryopreserved and shipped to the Department of Molecular Physiology and Cell Signalling of the University of Liverpool, to perform all the experiments described in this thesis.

2.1.1.3 Adipose derived mesenchymal stromal cells

Human A-MSCs were isolated in the University of Mannheim from lipoaspirates donated by 3 healthy donors after obtaining informed consent (Mannheim Ethics Commission; vote number 2006-192NMA). At the arrival of the lipoaspirate, the tissue is digested with a solution of NB4 Collagenase (Serva/Nordmark) dilute in MEMα (0.15 U/mL) for 30 to 45 min, at 37°C with gentle agitation. The digestion is then stopped by adding an equal volume of MEMα and everything is filtered through a 100 µm nylon mesh filter to remove any undigested tissue. The cells are then centrifuged at 1200g for 10 minutes and plated with MEMα supplemented with 10% foetal bovine serum (FBS). After 24h from the seeding the cells are extensively washed to remove any non-adherent and red blood cells. The cells have then been expanded according to the optimal seeding density and an aliquot of cells was cryopreserved and shipped to the Department of Molecular Physiology and Cell Signalling of the University of Liverpool, to perform all the experiments described here.

2.1.2 Cell culture procedures

All MSCs were cultured and expanded at the University of Liverpool according to standard mammalian tissue culture protocols and sterile techniques. In detail, cell culture procedures were performed using aseptic techniques in a class II Biosafety Cabinet. Any solution that entered in close contact with the cells was pre-warmed to 37°C. All the cell lines were cultured at 37°C in a humidified incubator, with 5% CO_2. The different sources of MSCs were cultured with MEM-α already supplemented with GlutaMAX (Gibco, #32561037), with the addition of 10 % FBS (Gibco, #10270-106). All the FBS used was from the same batch to reduce any possible difference associated to the serum production. The FBS was selected

following a serum screening in Galway with the aim was to find out a serum suitable for the MSCs coming from all the different sources. The HEK 293T cell line was cultured in Dulbecco's Modified Eagle Medium (DMEM; Sigma-Aldrich, #D6546-500ML) supplemented with 10% FBS (Gibco) and 2 mM L-glutamine (Sigma-Aldrich, #G7513-100ML). The medium was changed every 3-4 days and the cells were passaged when they reached around 80-90% confluency.

To passage the cells, the medium was removed, the cells washed twice with sterile PBS without Ca^{2+} and Mg^{2+} (Sigma-Aldrich, #D8537-500ML) and detached with trypsin/EDTA [500 mg porcine trypsin and 200 mg EDTA] solution (Sigma-Aldrich, #T4174-100ML) for 3 minutes. Then, trypsin activity was inhibited by adding culture medium supplemented with FBS (10%). The solution containing the detached cells was collected and centrifuged at 400 g for 3 minutes. Following the centrifugation, the supernatant was removed, and the cells were counted and seeded again or frozen down. The seeding density for the three cell types was optimised at the different sites (here for the UC-MSCs, in Galway for the BM-MSCs and in Mannheim for the A-MSCs). After the optimisation, a seeding density of $3x10^3$ cells/cm^2 was agreed for UC and BM cells, while a seeding density of $3x10^2$ cells/cm^2 was agreed for the A-MSCs. The HEK cells were usually split at a ratio of 1:8 or 1:10.

To reduce the risk of contamination, each surface, bottle and/or box of material that entered the Biosafety Cabinet was disinfected with 70% ethanol.

2.1.3 Cryopreservation and thawing of the cells

For cryopreservation of cells, after performing cell detachment and centrifugation, the cells were suspended into a freezing medium containing 90 % complete medium (MEM-α with 10% FBS) and 10 % dimethyl sulfoxide (DMSO; Sigma-Aldrich, #D2650-100ML) at a density between $5x10^5$ and $2x10^6$ cells/mL. Then, the cell suspension was transferred into cryovials (1 mL each), placed into a freezing container filled with 2-propanol and stored at -80°C overnight. The day after, the cells were moved to the liquid nitrogen tank (-180°C). The 2-propanol is required to allow a slow freezing of the cells (1°C/minute circa). DMSO is a cryoprotective agent which reduces the freezing point of the medium and allows a slower cooling rate. Both the slow freezing and the cryoprotection are required to reduce the risk of ice crystals formation during the freezing, which can damage and destroy the cells during the process.

Thawing is a stressful process for the cells. Contrary to freezing, it must be performed rapidly to minimise the shock. Cells were warmed in the water bath at 37°C for less than a minute,

then added gently to 5 mL of fresh medium. The cells were then centrifuged at 400 g for 3 minutes to remove the DMSO, which can interfere with the growing of the cells, and plated with fresh pre-warmed medium as described in the previous section.

2.1.4 Proliferation and doubling time calculation

The cells coming from the three tissue sources were cultured in the same way through the entire thesis. After being passaged or thawed, the cells were plated at their optimal seeding density ($3x10^2$ cells/cm^2 for adipose cells and $3x10^3$ cells/cm^2 for umbilical cord and bone marrow cells) and expanded until 60-90% confluence. The cells were then counted and plated again at each new passage, and the doubling time calculated using the following equation:

$$Td = \frac{t}{Log_2(\frac{N_t}{N_0})}$$

Where Td is the doubling time, N_t is the number of cells at time t and N_0 is the number of cells seeded, from which the number of doublings was calculated based on the time the cells had been in culture.

2.2 Generation of Reporter Cell Lines

Foreign genetic material can be introduced into a host cell by viral and non-viral methods, called transduction and transfection, respectively. The different sources of MSCs have been transduced with lentiviruses to generate stable reporter cell lines for bioluminescence imaging (BLI). Lentiviruses are a genus of the retroviral family, and they can infect both dividing and non-dividing cells. For safety reasons, virus particles for research purpose have been engineered to be replication incompetent; thus, they can infect host cells, but cannot produce new virus particles. The production of virus particles is achieved by using specific cells able to replicate the viral genome, called packaging cells. These cells require the presence of the transfer plasmid together with other plasmids carrying all the genes encoding the replication machinery and for the virus structural components, called packaging plasmids. In this work, the HEK293T packaging cell line was used to produce the lentivirus particles for MSC transduction by transfection with a transfer, a packaging and an envelope plasmid, as described in the next sections.

All the work was performed in accordance with the approval of a risk assessment for the work with genetically modified micro-organisms, in force from the 1st of January 2019 to the 31st of December 2023. The document regulates the production of genetically modified cells for their administration into animal models to investigate their biodistribution, fate and

safety. This regulates the process from the production and isolation of the plasmid to the administration of reporter cells to animals, including the production and storage of lentiviral particles and the generation of genetically engineered cell lines as intermediate steps. In agreement with this, all solutions, materials and surfaces that were in direct contact with the lentiviral particles were disinfected with a 1% (w/v) solution of Virkon.

2.2.1 Plasmids

Different transfer plasmids were used in this work to perform the separate steps of this thesis. The detailed sequence of each lentiviral vector (LV) is specified in the related chapter. All the transfer plasmids used in this thesis are third generation replication incompetent vectors, suitable for second or third generation packaging systems. In this work, a second-generation packaging system was used. This involves the use of 3 different plasmids. In summary, the transfer plasmid, carrying the genes of interest, was cotransfected with the packaging plasmid psPAX2 (Addgene, #12260) and the envelope plasmid pMD2.G (Addgene, #12259) into HEK293T cells. The psPAX2 carries the gag and the pol genes, encoding for a major structural protein of the virus and for the reverse transcriptase respectively, while the pMD2.G encodes for the VSV-G envelope protein.

2.2.2 Lentiviral particle production

The transient transfection into HEK cells of the transfer plasmid together with the packaging and the envelope plasmids was performed using the calcium phosphate transfection kit supplied by Sigma-Aldrich (#CAPHOS). HEK cells were seeded and transduced on the same day, with a 4-5 hours interval between these steps to allow the cells to attach. To produce high titres, $2.5x10^6$ or $7x10^6$ HEK cells were seeded into 100 mm ø or 150 mm ø dishes, respectively. Before starting the transfection, the cells were checked to be properly attached and uniformly distributed on the surface of the dish. To prepare the DNA- calcium chloride solution, calcium chloride ($CaCl_2$) was diluted to a final concentration of 250 mM into a solution containing the plasmids (12 µg for a 100mm ø dish and 32 µg for a 150 mm ø dish) with a mass ratio of 3:2:1 (transfer : packaging : envelope). Then, an equal volume of 2x HEPES (4-(2-hydroxyethyl)-1-piperazineethanesulfonic acid), pH 7.05, was carefully added dropwise to the $CaCl_2$-DNA solution, mixing it lightly while dropping. This leads to the formation of insoluble calcium phosphate, which co-precipitates with the DNA. After a light vortex, the precipitate was allowed to sit for about 10 minutes and added to the cells dropwise. The cells were finally incubated at 37°C for 16 hours. calcium-phosphate-DNA precipitate complexes adhere to the cell membrane and enter the cytoplasm by endocytosis.

Following the overnight incubation, the medium was refreshed, and the cells were cultured under the same condition for 2 days, during which the virus was released into the medium. The medium was collected and centrifuged at 500 g for 5 minutes to pellet cells and large debris. The virus-containing supernatant was then filtered with a 0.45 µm PES filter and prepared to be concentrated via ultracentrifugation.

2.2.3 Concentration of lentiviral particles

To concentrate the lentiviral particles, all the filtered collected medium was pooled together and divided between a maximum of 6 tubes (13.2 mL, 14 mm x 89 mm) for Beckman SW41Ti rotor. The ultracentrifuge tubes were cleaned and sterilised the day before the centrifugation. Up to 8 mL of filtered vector-containing cell culture supernatant was moved into each of the tubes and 1.2 mL of a 20% sucrose solution were gently added to the bottom of each tube. The tubes were then carefully weighted and balanced adding PBS or media until they were within 0.1 g of each other. Subsequently, the tubes were placed into the pre-cooled Beckman SW41Ti rotor and centrifuged at 82700 g for 2 hours at 4°C. At the end of the centrifugation, the tubes were removed carefully to avoid the detachment of the pellets, the supernatant was poured off and the tubes were left inverted on a paper towel for 10 minutes and quickly air dried to allow residual liquid to be removed. To slowly dissolve the pellet, 80 µl of sterile PBS (without Ca^{2+}/Mg^{2+}) was added to each pellet and incubated at 4°C for 2 hours, vortexing every 20 minutes. The tubes were then spun at 500 g for 1 minute before suspending the pellet by gently pipetting. Finally, the virus suspensions from all tubes from a single production cycle were pooled, aliquoted, quickly frozen on dry ice and stored at -80°C until further use.

2.2.4 Virus titration

Determining the virus titre is important to infect the cell using a known number of viral particles per cell, also known as multiplicity of infection (MOI). To determine the virus titration, HEK cells were transduced with increasing amounts of the produced virus to generate a dilution curve.

HEK cells were seeded into 6-well plates at a density of $5x10^4$ cells/well. The cells were transduced in the presence of Polybrene (Pb), a polycation commonly used during transduction, 4-5 hours after the seeding. To determine the virus titre, serial dilutions of the virus stock solution were prepared in fresh medium containing 8 µg/mL of Pb. The volumes of virus ranged from 0.0045 µL to 4.5 µL. The solution was then added to the cells and the HEK cells were incubated at 37°C for 3 days. Then, the cells were detached, and the

percentage of transduced cells was evaluated using the flow cytometry(see flow cytometry paragraph for further details). The titre, in the form of single transducing units (TU)/mL, was determined by evaluating the percentage of transduced cells and calculated using the following equation:

$$\frac{TU}{mL} = \frac{F * N}{V}$$

Where F is the ratio of cells positive for the fluorescent protein (transduced cells), N is the total number of cells at the time of transduction (seeded cells) and V is the volume of virus solution added into each well. A linear relationship should be found between the ratio of fluorescent cells (F) and the volume of virus stock solution used (V). Moreover, F should be less than 40% for accurate calculation (>40% suggests that cells may have more than one infection, leading to underestimation of viral titre).

2.2.5 MSC transduction protocol

A protocol suitable for the transduction of all UC, BM and A-MSCs was optimised in CHAPTER 3, where several transduction procedures where explored. To generate pure transduced MSC populations, cells were seeded at a density of $3x10^3$ cells/cm^2 and transduced the same day. This density was used to transduce also the adipose cells as a preliminary test where the A-MSCs (n = 3) were transduced at $3x10^2$ cells/cm^2 showed poor transduction efficiency, followed by a rapid loss of the expression of the proteins encoded by the transduced genes. After the seeding the cells were allowed to attach for 4-5 hours before being transduced. The transduction was performed using a MOI of 5 in freshly prepared medium containing 6 µg/mL of DEAE-dextran. The cells were incubated with the DEAE-dextran overnight at 37°C in the incubator and the day after the medium was replaced with fresh medium not containing any DEAE-dextran or lentiviral particle. Such transduced cells were then sorted in sterile conditions using a FACSAria II to ensure the selection populations with a percentage of transduced cells above 99%.

2.3 Flow Cytometry and Imaging Techniques

2.3.1 Cell preparation for flow cytometry

Flow cytometry has been used in this work for different purposes: evaluate the presence of specific markers via antibody staining (1), evaluate the expression of fluorescent proteins (2) and sort cells expressing a specific fluorescent protein (3). To perform any of the flow cytometry analysis listed, cells were detached using trypsin as described in the section 2.1.2,

collected and centrifuged at 400 g for 3 minutes. Then, the supernatant was discarded, the cells were washed with 5 mL of PBS without $Ca2^{+}$ and $Mg2^{+}$ and centrifuged again at 400 g for 5 minutes. Then a specific protocol was used to prepare the cells for each analysis:

1. Staining with fluorescence antibodies to detect the expression of specific markers of interest: cells were resuspended into a final volume of 100 µL of PEB (PBS, 5mM EDTA and 0.5% w/v bovine serum albumin) buffer for each marker. Then the cells were divided into an appropriate number of tubes (100 µL/tube) and each antibody was added following the supplier instructions. A maximum of 10^6 cells was used for each tube. Table 2.1 summarises the details (clone, dilution factor, code, fluorochrome) about the antibodies used for the analysis of the mesenchymal stromal cell markers. The cells were vortexed for 2 seconds and incubated with the antibody for 10 minutes in the dark in the fridge (around 4°C). At the end of the incubation step the cells were washed by adding 1 mL of PEB buffer and centrifuged at 300g for 10 minutes. After the supernatant removal the cells were suspended into a proper amount of PEB buffer, transferred into a 5 mL polystyrene round bottom FACS tube (Falcon®, 352054) and analysed using a FACS Calibur (BD Biosciences). This protocol has been used frequently among the thesis to evaluate some common positive (CD44, CD73, CD90, CD105) and negative (CD11b, CD19, CD34, CD45, HLA-DR) MSC markers (Table 2.1). A variation of this protocol was also used in chapter X to stain some defined mouse immune system cells and the samples were analysed using a FACS Canto II (BD Bioscences).
2. Evaluate the expression of a fluorescent protein in transduced cells: cells were suspended into sterile PBS, transferred into a 12 mL FACS tube, and analysed using a FACS Calibur (BD Bioscences). The analysis was based on the excitation-emission spectrum of the expressed fluorescent protein.
3. Sorting of transduced mesenchymal stromal cells: cells were suspended into a solution of PBS and 0.8% FBS and stored in ice. The cells were then moved to the Sorting Facility of the university of Liverpool where the cells were sorted using a FACS Aria (BD Bioscences) based on the expression of a green fluorescent protein. The sorted cells were collected into a sterile tube containing fresh MEMα supplemented with 10 % of FBS and moved back to the sterile Cabinet to be plated and expanded.

Table 2.1: details of the antibodies used to investigate the expression of MSC markers.

Antibody	Fluorochrome	Supplier	Clone	Dilution Factor
CD11b	APC	Miltenyi	M1/70.15.11.5	1:50
CD19	APC	Miltenyi	LT19	1:50
CD34	APC	Miltenyi	AC136	1:50
CD44	APC	Miltenyi	DB105	1:50
CD45	APC	Miltenyi	5B1	1:50
CD73	APC	Miltenyi	AD2	1:50
CD90	APC	Miltenyi	DG3	1:50
CD105	APC	Miltenyi	43A4E1	1:50
HLA-DR	APC	Miltenyi	AC122	1:50

2.3.2 Bioluminescence imaging

The In Vivo Imaging System (IVIS) system (Perkin Elmer) was used to perform the bioluminescence imaging acquisition and analysis. To compare the signal coming from different acquisitions and experimental designs, the data was always normalised to radiance ($p/s/cm^2/sr$), the number of photons (p) per second (s) that leave a square centimetre of tissue (cm^2) and radiate into a solid angle of one steradian (sr).

The dark imaging chamber inside the IVIS allows the housing of plates and small living animals. A heated shelf located at the bottom of the imaging chamber is used to maintain stable the body temperature of the animals and an anaesthesia manifold is directly connected to the isoflurane supplier and can be used to maintain up to 5 animals anaesthetised. The animals can be imaged both in ventral and dorsal position. The instrument allows 3 different types of imaging: fluorescence, bioluminescence, and Cherenkov luminescence. The signal is detected by a CCD camera located at the top of the chamber. In this work the IVIS system was used to investigate both *in vitro* and *in vivo* bioluminescent signals.

2.3.2.1 In vitro BLI experiments

The IVIS system was used to investigate the saturation kinetics and the amount of photon emitted per cell *in vitro* in several chapters of this thesis. Regardless the purpose of the imaging, the *in vitro* imaging was performed immediately after the administration of the substrate to cells expressing a luminescent reporter gene. To test the saturation kinetics, transduced cells were plated into several wells of optical bottom 96-well plate with black walls (#165305, ThermoFisher) at the same density, allowed to attach for around 3-4 hours and treated with rising concentrations of a specific substrate. To evaluate the amount of

photon emitted per cells, rising concentration of transduced cells were treated with the same concentration of the related substrate. All the *in vitro* BLI imaging was performed using a 13.3 field of view, a f-stop of 1, a binning of 8 and a 10 seconds exposure time, unless specified in the specific chapter. The f number refers to the aperture of the hole that regulate the amount of light that hits the CCD camera (from 1, wide open, to 8) and the binning improves the signal-to-noise ratio (8 is a medium setting). Generally, the standard scale was set between $2.0x10^4$ and $5.0x10^6$ p/s/cm^2/sr. Signal was quantified by drawing a region of interest (ROI) around each well or using the 8x12 grid tool specifically designed for 96-well plate.

2.3.2.2 In vivo BLI experiments

The IVIS system was used to perform the saturation kinetics *in vivo* and to evaluate the biodistribution and the long-term persistence of cells following intravenous administration in mice (CHAPTER 4 and CHAPTER 5). Following the administration of the substrate mice were transferred inside the black chamber and located close to the nose cones connected to the anaesthesia manifold. Then, to perform the saturation kinetics of the enzyme-substrate *in vivo* the animals were imaged every minute for 30 minutes using a 22.8 field of view, a binning of 8 and a f-stop of 1. Within each minute of acquisition, the maximum exposure time was set to 45 seconds. To evaluate the biodistribution of the signal and the survival of the cells over different days, the mice were imaged around 18-20 minutes following the administration of the substrate (this was optimised in CHAPTER 4) using a 22.8 field of view, a binning of 8, a f-stop of 1, and 60 to 180 seconds exposure, depending on the day of acquisition (clarified in each specific chapter). The standard scale was set between specifically for each experiment and adjusted to weaker signal to make them more visible. Signal was quantified by drawing a ROI around each animal or around a specific region of the body.

2.4 ANIMAL EXPERIMENTS

Different mouse strains were used to perform the animal experiments described in this thesis. C57 Black-6 (C57BL/6J.Tyr^{c-2J}, from JAX) albino is the strain used for most of the animal experiments. C57BL/6J albino male and female animals were obtained from a colony managed by the Biomedical Service Unit of the University of Liverpool. Severe combined immunodeficient (SCID; CB17/Icr-Prkdc^{SCID}/IcrlcoCrl), Non-obese diabetic SCID (NOD SCID; NOD.CB17-Prkdc^{SCID}/NCrCrl) and Balb/c female mice were purchased from Charles River. All the animals were housed in individually ventilated cages (IVCs) under a 12-hours light/dark cycle and were provided with standard food and water *ad libitum*. Animal purchased from

Charles River were allowed to acclimate for 10 days before performing the actual experiments. All animal procedures were performed under a licence (PP3076489) granted under the Animals (Scientific Procedures) Act 1986 and were approved by the University of Liverpool Animal Ethics Committee. At the end of each experiment the mice were culled following a schedule 1 method, either by a rising concentration of CO_2 or by cervical dislocation, unless a different schedule 1 terminal procedure was applied (specified in the chapter).

2.4.1 Cell preparation and *in vivo* administration

Human UC, BM and A-MSCs were cultured at their optimal seeding density to around 60-90% before being prepared for the *in vivo* administration. When ready, the cells were detached as previously described (2.1.2) and suspended in ice cold PBS at a density of $2.5x10^6$ cells/mL. For each animal a specific tube containing from 130 to 150 µL of the cell suspension was prepared and the tube was kept in ice until injection. Right before the administration, the cells were gently resuspended by pipetting and warmed up to room temperature. 100 µL of the cell suspension (equals to $2.5x10^5$ cells) were loaded into a 0.3 mL syringe with a 30G needle and injected intravenously (IV) through the tail vein of the animal.

CHAPTER 3 Optimisation and Characterisation of a Lentiviral Transduction Protocol for the Generation of Mesenchymal Stromal Cells Expressing Reporter Genes

3.1 Introduction

As mentioned in the introduction to this thesis (1.4.1), several sources of MSCs have already shown considerable therapeutic potential in different preclinical models [233-235] and are currently employed in several clinical trials. Although MSCs isolated from bone marrow are the most commonly used MSCs [236], adipose and umbilical cord derived MSCs are becoming quite attractive sources as they can be collected using less invasive procedures compared to bone marrow harvesting [237-239]. UC, BM and A-MSCs are indeed being used in this thesis to compare their biodistribution and survival *in vivo* in small rodents. To compare the biodistribution, the cells are going to be genetically modified to express a reporter gene for bioluminescence imaging. To make sure that this procedure is not going to impair the properties of the 3 types of cells, it is important to define their properties, in terms of doubling time and expression of different MSC markers. The characterisation of such features and their comparison in UC, BM and A-MSCs can help to identify any difference between the cell sources and to easily assess any change in the properties of the cells following the transduction.

Lentiviral vectors (LV) have been extensively used as gene delivery tools over the last 25 years because of their ability to infect both dividing and non-dividing cells [240]. The interaction between the lentiviral particle and the cell of interest is receptor independent [241] and can be reduced or prevented by the presence of strong electrostatic repulsion between the negatively charged cell and the envelope of the virus [242, 243].

The addition of polycations, positively charged molecules, can reduce the charge of cell membranes, and increase the chance of an interaction between the lentivirus and the cell surface [243]. Polybrene (Pb) is the most commonly used polycation in lentiviral transduction and is associated with a very high transduction efficiency [244, 245]. Nevertheless, it has also been reported to have negative effects on some cell lines [246-248]. In particular, its use during transduction of human endometrium-derived mesenchymal stromal cells has been described to negatively affect their proliferation, migration ability and differentiation potential [248]. Other polycations, such as Diethylaminoethyl-dextran (DEAE-dextran) and

protamine sulphate (Ps) have been successfully used to transduce different cell lines [243, 249].

Another method reported to increase the binding of retroviruses to the surface of the cells is spinoculation [250-252]. Although various mechanisms have been proposed [250, 251], it is still unclear what process is responsible for this enhancement. During spinoculation, the cells are centrifuged at low speed (below 2000g) in the presence of the virus. Importantly, it has been reported that the spinoculation together with the right polycation can further increase the transduction efficiency [249].

In this chapter, the optimisation of a transduction protocol is carried out with the goal of obtaining genetically engineered umbilical cord, bone marrow and adipose-derived MSCs that share the same properties as the unmodified (naïve) cells. The work is divided in broadly three parts (i) characterising MSCs from different tissues and donors, to confirm their stromal cell nature and assess any differences between the tissue of origin (ii) optimising a lentiviral production protocol to efficiently infect these MSCs without affecting their viability and (iii) establishing and characterising MSC populations expressing a bicistronic luminescence/fluorescence reporter gene. The transduced MSC populations are then used in subsequent chapters to determine their biodistribution and fate in mice.

3.2 Materials and Methods

3.2.1 MSCs characterisation

Mesenchymal stromal cells from umbilical cord, bone marrow and adipose tissue were analysed in terms of cumulative doublings, doubling time and expression of common MSC markers to assess any differences associated with the tissue of origin.

3.2.1.1 Proliferation and doubling time

The cells coming from the three tissue sources were plated at their optimal seeding density ($3x10^2$ cells/cm^2 for adipose cells and $3x10^3$ cells/cm^2 for umbilical cord and bone marrow cells) and expanded until 60-90% confluence. The cells were then counted and plated again at each new passage, and the doubling time calculated using equation in 2.1.4.

3.2.1.2 MSC markers

The cells were seeded at their optimal seeding density into a 10 cm diameter dishes and grown to around 60-90% confluence. Then, they were detached and the expression level of different MSC markers was assessed via flow cytometry as described in 2.3.1. Specifically, the

cells were stained with anti-CD11b (APC, #130-113-793, Miltenyi Biotec), anti-CD19 (APC, #130-113-727, Miltenyi Biotec), anti-CD34 (APC, #130-113-738, Miltenyi Biotec), anti-CD44 (APC, #130-113-893, Miltenyi Biotec), anti-CD45 (APC, #130-113-676, Miltenyi Biotec), anti-CD73 (APC, #130-097-945, Miltenyi Biotec), anti-CD90 (APC, #130-117-534, Miltenyi Biotec), anti-CD105 (APC, #130-099-125, Miltenyi Biotec), anti-HLA-DR (APC, #130-113-960, Miltenyi Biotec), IgG1 mouse isotype (APC, #130-113-758, Miltenyi Biotec), or IgG2 mouse isotype (APC, #130-113-831, Miltenyi Biotec) according to the manufacturer's instructions. An extra vial of each cell population was used as unstained control. The data were acquired with a FACScalibur (BD Biosciences) flow cytometer and a minimum of 10^4 events was analysed for each marker.

3.2.2 Optimisation of a lentiviral transduction protocol

Lentiviral particles produced by HEK cells (CHAPTER 2) were used to transduce MSCs and generate luciferase expressing cells. To find the optimal protocol, a LV encoding for the bicistronic expression of firefly luciferase and a green fluorescence protein, ZsGreen (pHIV-Luc2-ZsGreen plasmid, Figure 3.1a) was used.

3.2.2.1 Transduction efficiency

MSCs (UC-, BM- and A-) were seeded at a density of $5x10^3$ cells/cm^2. The seeding and the transduction were performed on the same day, with an interval of 4-5 hours between these steps, to allow the cells to attach. The cells were transduced with pHIV-Luc2-ZsGreen lentiviral particles (the plasmid was a gift from Bryan Welm, Addgene plasmid #3919, Figure 3.1a) with a MOI of 5 in the presence of three different polycations: Pb, Ps or DEAE-dextran. MSCs transduced without any compound served as control of the basal transduction efficiency. To evaluate a possible effect of the polycation themselves on the cells, they were also incubated with either Pb, Ps or DEAE-dextran alone. Finally, MSCs alone were used as control. Summarising, in each plate there were the following conditions:

- Cells alone +/- the viral particles
- Cells with Pb [8 µg/mL] +/- the viral particles
- Cells with Ps [20 µg/mL] +/- the viral particles
- Cells with DEAE-dextran [6 µg/mL] +/- the viral particles

One of the plates was incubated overnight at 37°C in the incubator (from now on, this will be referred to as "static" condition), and the day after, the medium was replaced with medium that did not contain any polycation or lentiviral particle. The other plate was centrifuged for

1 hour at 750 g, incubated for 1 hour at 37°C, following which the medium was replaced and the plate returned to the incubator (this will be referred to as “spinoculation” condition).

Transduction efficiency was assessed with flow cytometry by evaluating the proportion of cells expressing the ZsGreen protein after 7 days of culture (see section 3.2.2.3).

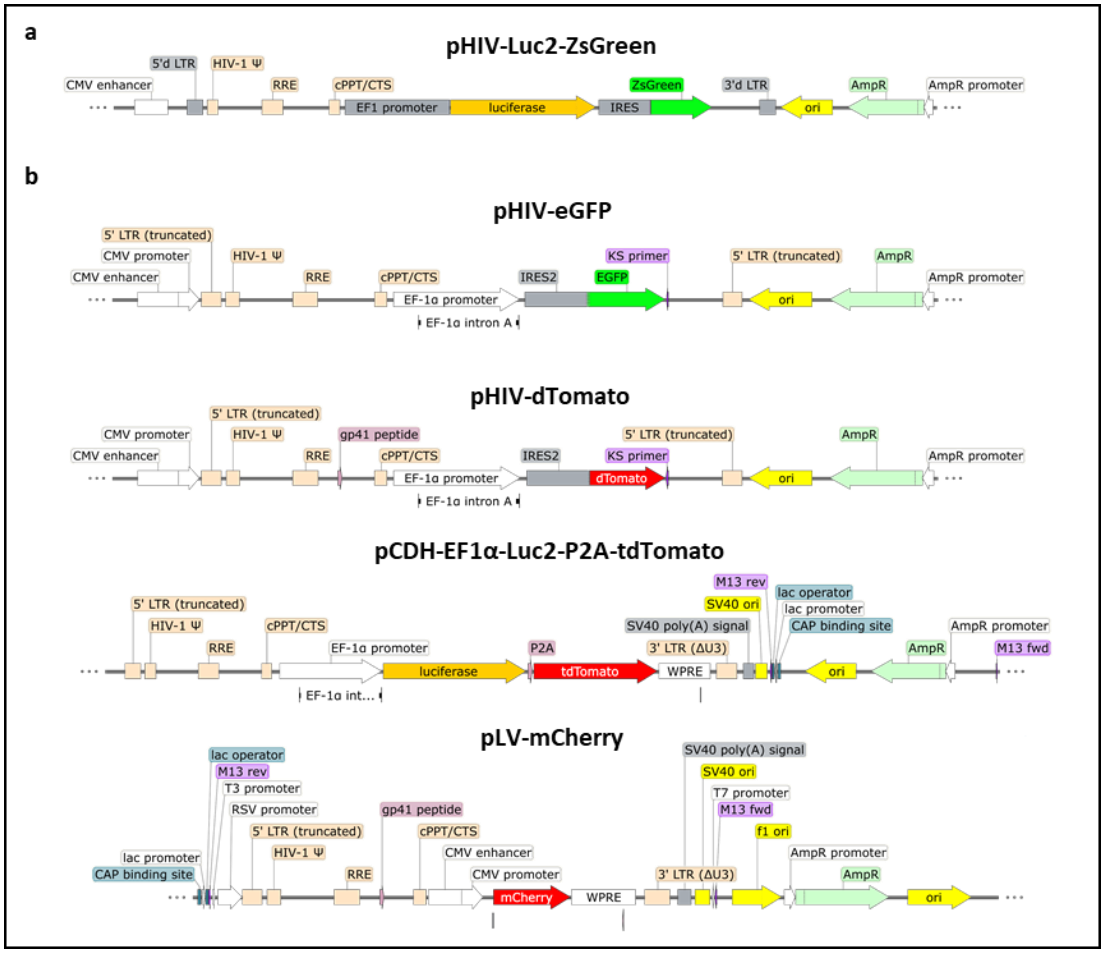

Figure 3.1| Lentiviral vector backbones. (a-b) Schematic representation of the lentiviral vectors used to generate FLuc_ZsGreen cells **(a)** and to perform the validation of the DEAE-Dextran protocol **(b)**.

3.2.2.2 ATP assay

A CellTiter-Glo® Luminescent Cell Viability Assay (Promega, #G7571) was used to evaluate the effect of the transduction method on the viability and the metabolic activity of the cells. Briefly, cells seeded at the same density can grow differently after being exposed to different treatments. A metabolic assay performed post-transduction can give a measure of viable cells. The CellTiter-Glo® Luminescent Cell Viability Assay is based on the oxidation of beetle luciferin catalysed by luciferase in the presence of ATP produced by the cells. Note that this process is intrinsic to the assay and independent of firefly luciferase expression by the cells of interest.

Cells were seeded in 96-well plates at a concentration of $1.5x10^3$ cells/well. The transduction protocol was carried out as described in the previous paragraph. A negative control, where cells were incubated with complete medium with 0.1% Triton X-100, was added. This was used to make sure the ATP assay did not give any false positivity. Each condition was analysed in triplicate to reduce technical errors. At the end of the culture phase the medium was removed from the cells and replaced with 50 µL of fresh medium, and 50 µL of medium were placed in three empty wells to be used as blank. 25 µL of CellTiter-Glo® reagent were then added to each well and the plates were mixed for 2 minutes with a shaker. The plates were then incubated at room temperature for 10 minutes to stabilize the luminescent signal. After that, 70 µL were moved from each well to a corresponding well of a white bottom 96 well plate and the luminescence was recorded with a luminometer. The blank was used to normalise the signal.

3.2.2.3 Flow cytometry based on the ZsGreen expression

MSCs were trypsinised, centrifuged, and resuspended in PBS to remove any residual medium as described in 2.3.1. To evaluate the percentage of MSCs expressing the transgene(s), the cells were suspended into 400 µL of PBS, transferred into a properly labelled FACS tube and analysed with a FACSCalibur cytometer. The green fluorescence was used to evaluate the percentage of the transduced cells.

3.2.2.4 Validation of the optimised transduction protocol

Once the optimal transduction protocol was identified using the Luc_ZsGreen vector, the same protocol was applied for the transduction with 4 other different lentiviral particles. MSCs were seeded at a density of $5x10^3$ cells/cm^2 into 12-well plates. Again, the seeding and the transduction were performed on the same day, with an interval of 4-5 hours between these steps. The cells were then transduced with four different lentiviral particles, listed below and show in Figure 3.1b.:

- pHIV-eGFP (carrying a green fluorescent protein, eGFP; 7686 base pairs)
- pHIV-dTomato (carrying a red fluorescent protein, dTomato; 7680 bp)
- pCDH-EF1α-Luc2-P2A-tdTomato (carrying a red fluorescent protein, tdTomato; 10289 bp)
- pLV-mCherry (carrying a red fluorescent protein, mCherry; 7413 bp)

All transductions were carried out using an MOI of 5 in the presence or absence of optimal polycation, DEAE-dextran [6 µg/mL]. The cells were then incubated overnight at 37°C and the

day after, the medium was replaced with fresh medium that did not contain any polycation or lentiviral particle. Transduction efficiency was assessed via flow cytometry after 7 days of culture as explained above (3.2.2.3). pHIV-EGFP was a gift from Bryan Welm & Zena Werb (Addgene plasmid #21373), pHIV-dTomato was a gift from Bryan Welm (Addgene plasmid #21374), pCDH-EF1-Luc2-P2A-tdTomato was a gift from Kazuhiro Oka (Addgene plasmid #72486) and pLV-mCherry was a gift from Pantelis Tsoulfas (Addgene plasmid #36084).

3.2.3 Establishing and characterising MSCs expressing the reporter gene FLuc_ZsGreen

The MSCs were transduced with the pHIV-Luc2-ZsGreen construct in the presence of 6 µg/mL of DEAE-dextran applying the static protocol. The different donor samples were transduced at the earliest available passage (Table 3.1). Cells were seeded into 10 cm diameter dishes at a density of $3x10^3$ cell/cm^2 and transduced with an MOI of 5 as previously described (3.2.2.1). Following transduction, the cells were cultured up to 60-90% confluence, harvested and sorted via flow activated cell sorting (FACS) to obtain a homogenous population of cells expressing the transgene. For that, they were resuspended in PBS with 0.8% FBS and kept on ice until sorted. The sorting was performed using a FACSAria and was based on the expression of ZsGreen. The transduced cells were then expanded for one passage and frozen down until further use. UC and BM cells were expanded using a density of $3x10^3$ cells/cm^2, while A-MSCs were expanded at $3x10^2$ cells/cm^2.

Table 3.1: UC, BM and A-MSCs samples and the respective passages at which they were transduced, sorted, cryopreserved and used in animal experiments.

Cell type	Donor ID	Transduction Passage	Sorting Passage	Cryopreservation Passage	Passage for *in vivo* studies
UC-MSCs	733S	P5	P6	P7	P8
	735O	P5	P6	P7	P8
	727R	P5	P6	P7	P8
BM-MSCs	BM04	P3	P4	P5	P6
	BM21	P5	P6	P7	P8
	BM42	P3	P4	P5	P6
A-MSCs	LA31	P5	P6	P7	P8
	LA87	P5	P6	P7	P8
	LA96	P5	P6	P7	P8

3.2.3.1 Assessing the effects of lentiviral transduction on the properties of MSCs

The transduced MSCs were compared with untransduced ones in terms of doubling time, expression of common MSC markers and morphology (area, perimeter, and circularity), to ensure that lentiviral transduction did not affect them.

To evaluate the doubling time, the cells were cultured for at least 2 passages. UC and BM MSCs were plated at $3x10^3$ cells/cm^2, while A-MSCs were seeded at $3x10^2$ cells/cm^2. the doubling time calculated using the same equation described in section 3.2.1.1.

Expression of CD44, CD73, CD90 and CD105 and lack of expression of CD45 were evaluated via flow cytometry (3.2.1.2) to assess any difference in the level of common MSC markers.

To assess possible changes in the morphology, the cells were characterised in terms of area, perimeter, and circularity. Transduced and untransduced UC and BM cells were plated at $3x10^3$ cells/cm^2, while A-MSCs were seeded at $3x10^2$ cells/cm^2. The cells were cultured with complete medium overnight. After 16 hours the cells were then fixed with paraformaldehyde (4% w/v in PBS, pH 7) for 20 minutes at room temperature (RT), washed with PBS, permeabilised with 0.1% (v/v) Triton X-100 in PBS and incubated with Alexa Fluor 594 Phalloidin (#A12381, ThermoFisher) [165nM] in PBS with 1% (w/v) bovine serum albumin (BSA) for 1 hour at RT. 4',6 diamidino-2-phenylindole (DAPI) [143 nM] was used as a counter staining for the nuclei. The fluorescence images were acquired with a Leica DM2500 microscope coupled to a DFC350 FX camera. Finally, ImageJ was used to perform the data analysis: the shape of the cells was delineated manually, based on the Phalloidin staining, from which the software was used to calculate the cells' area, perimeter, and circularity.

3.2.3.2 Determining bioluminescence properties in vitro

The IVIS Spectrum system was used to characterise the cells transduced with the FLuc_ZsGreen. The cells were plated at different densities, from 156 to $2x10^4$ cells/well, in optical bottom 96-well plates with black walls (ThermoFisher, #165305) with a technical triplicate. Untransduced cells were used as negative control. The cells were allowed to adhere for 3 hours and then, D-Luciferin was added at a final concentration of 5.12 mM with a final volume of 100 µL per well. The data were obtained with IVIS immediately after the addition of the substrate, acquiring the signal generated using the open filter. The acquired signal was always normalised to radiance (photons/second/$centimeter^2$/steradian) and analysed using the region of interest (ROI) tool of the IVIS software (Living Image v 4.5.2) to obtain the total number of photons emitted in that specific area, also known as total flux (photons/s). The data were then plotted using GraphPad to generate the final graphs displaying the total flux/cell (photons/s/cell).

3.2.4 Statistical analysis

All values in graphs are represented as mean ± standard deviation, unless specified differently in the figure legend. The statistical analysis was performed using the GraphPad Prism software. The type of statistical test and the number of replicates included in the analyses are indicated in the figure legends.

3.3 RESULTS

3.3.1 Characterisation of MSCs from different sources

Umbilical cord, bone marrow and adipose derived MSCs were seeded at their optimal seeding density for comparison of the proliferation and the morphology over time. Representative phase contrast images taken 3 days after the seeding and right before splitting the cells, at different magnifications, are shown in Figure 3.2a. The morphology of the different cell types is fibroblastic and comparable among the cells from different tissue sources. The cumulative doubling analysis performed for the three cell types showed that all the three A-MSC donor samples display similar doublings over the passages (Figure 3.2b). On the other hand, UC- and BM-MSCs revealed a minor variability among the donor samples in terms of cumulative doublings (Figure 3.2b). In parallel, an analysis of the doubling time was carried out to compare each donor sample of the same cell type (Figure 3.2c) and to compare the doubling times of the different cell types (Figure 3.2d). BM-MSCs showed a longer doubling time (95.7 ± 28.0 h) when compared to UC (46.1 ± 9.5 h) and A-MSCs (51.1 ± 1.3 h), while no statistically significant difference was observed between these last two (Figure 3.2d).

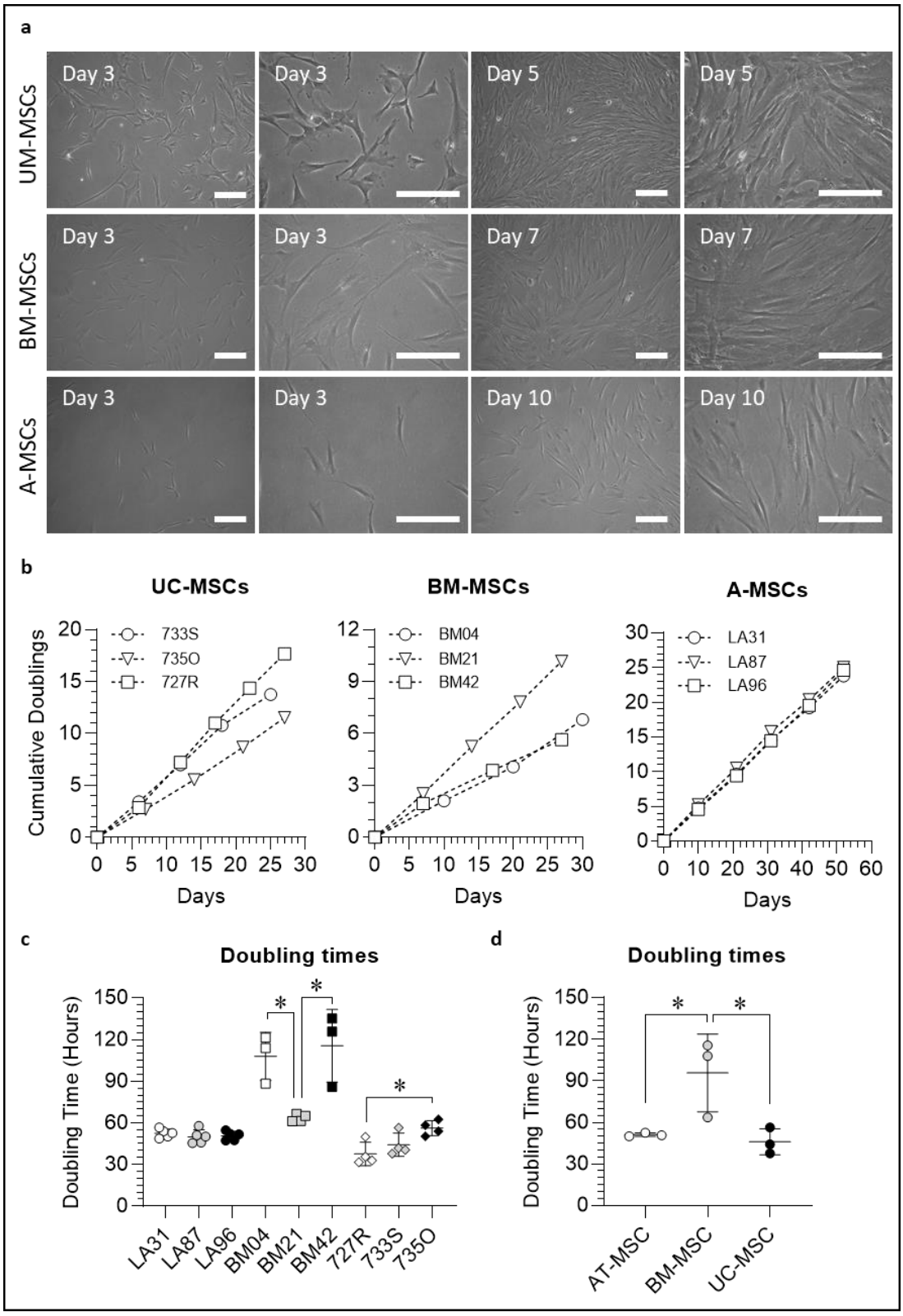

Figure 3.2| UC, BM and A-MSCs display similar morphology but different proliferation rates. (a) Representative phase contrast images of UC, BM and A-MSCs 3 days post seeding and right before being passaged at 2 different magnifications. Scale bar = 200 µm. **(b)** Cumulative doubling analysis of at least 3 passages of UC, BM and A-MSCs. Cumulative doublings are calculated at each passage summing the total doublings performed from up to that point. **(c)** Doubling time analysis of at least 3 passages of UC, BM and A-MSCs sorted by donor sample. Data are displayed as mean ± SD, n ≥ 3.

One-way ANOVA with Tukey's multiple comparison post-hoc test. * $p < 0.05$. **(d)** The average of the doubling times of the different of UC, BM and A-MSCs donor samples. Data are displayed as mean ± SD, n = 3. One-way ANOVA with Tukey's multiple comparison post-hoc test. * $p < 0.05$.

The analysis of the level of expression of positive (CD44, CD73, CD90, CD105) and negative (CD11b, CD19, CD34, CD45, HLA-DR) MSC markers was carried out via flow cytometry. While it was possible to confirm the phenotype of the UC-MSCs samples, with all three showing > 98% positivity to MSC positive markers and < 1% positivity to MSC negative markers (Figure 3.3, Table 3.2), BM- and A-MSCs displayed a small degree of heterogeneity (Figure 3.3). Specifically, all the BM-MSC donor samples displayed a fraction of cells (7.4 ± 6.5%) expressing the major histocompatibility complex class II molecule HLA-DR (Figure 3.3b, Table 3.2), while the A-MSCs (Figure 3.3b, Table 3.2) showed a small percentage of cells positive for CD34 (18.4 ± 11.7%) and CD45 (10.8 ± 7.8%).

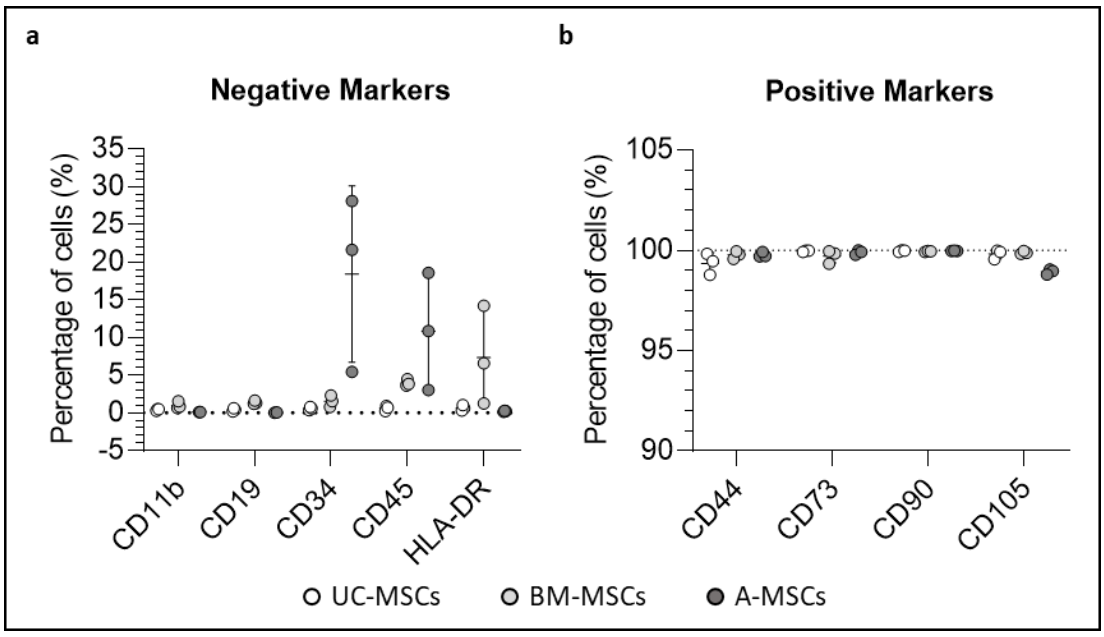

Figure 3.3| Flow cytometry analysis of MSC markers in UC, BM and A-MSCs. (a-b) percentage of cells positive for CD11b, CD19, CD34, CD45 and HLA-DR **(a)** and for CD44, CD73, CD90 and CD103 **(b)**. Data are displayed as mean ± SD, n = 3.

Table 3.2: Percentage of cells positive for negative (CD11b, CD19, CD34, CD45 and HLA-DR) and positive (CD44, CD73, CD90 and CD105) MSC markers listed by donor ID. All data in %.

Donor ID	CD11b	CD19	CD34	CD45	HLA-DR	CD44	CD73	CD90	CD105
727R	0.47	0.39	0.34	0.93	0.62	99.83	99.98	100	99.98
733S	0.28	0.21	0.61	0.24	0.33	98.78	99.98	99.92	99.56
735O	0.49	0.61	0.79	0.68	1.05	99.46	99.92	99.98	99.92
BM04	0.66	1.3	0.79	4.45	1.24	99.79	99.34	99.93	99.82
BM21	0.84	1.22	1.53	3.61	14.2	99.58	99.85	99.97	99.87
BM42	1.54	1.65	2.32	3.82	6.57	99.95	99.96	99.95	99.97
LA31	0.09	0.01	28.13	18.56	0.13	99.7	100	99.97	99.05
LA87	0.12	0.05	5.43	10.85	0.23	99.72	99.78	99.97	98.97
LA96	0.08	0.15	21.63	3.02	0.26	99.93	99.92	99.99	98.8

3.3.2 Optimisation of a lentiviral transduction protocol

In order to optimise the transduction protocol, the effect of different polycations, alone or in combination with a spinoculation step, was tested on UC-MSCs, BM-MSCs and A-MSCs. Cells were infected with a lentiviral particle encoding for firefly luciferase and a green fluorescent protein, ZsGreen, whose expression was used to discriminate between transduced and untransduced cells via flow cytometry. In parallel, an ATP assay was used to investigate the effect of the different protocols on the viability of the cells. Specifically, following the transduction, the cells were cultured for 7-10 days and the level of ATP was measured and compared with the untransduced cells (controls).

3.3.2.1 Umbilical cord-derived mesenchymal stromal cells

Representative phase contrast images of UC-MSCs taken 7 days post-transduction and the respective fluorescence images (green channel) are displayed in Figure 3.4. The images show that cells transduced in the presence of Pb display the highest level of transduction efficiency and a strong level of green fluorescence (Figure 3.4a-b). It is interesting to notice that when the static protocol is applied these cells show a different morphology and a possible reduction in proliferation, as they do not reach the same degree of confluence as the cells in the other conditions do (Figure 3.4a). On the other hand, this effect seems to be reduced following the introduction of a spinoculation step (Figure 3.4b). All the other conditions are associated with cells displaying a normal morphology and confluence levels, although with differences in the degree of transduction efficacy (green fluorescence, Figure 3.4a-b). In particular, cells transduced in the presence of DEAE-dextran, regardless of the incubation

protocol (Figure 3.4a-b), and cells transduced in the presence of Ps following the application of the spinoculation step (Figure 3.4b), display a relatively strong level of green fluorescence.

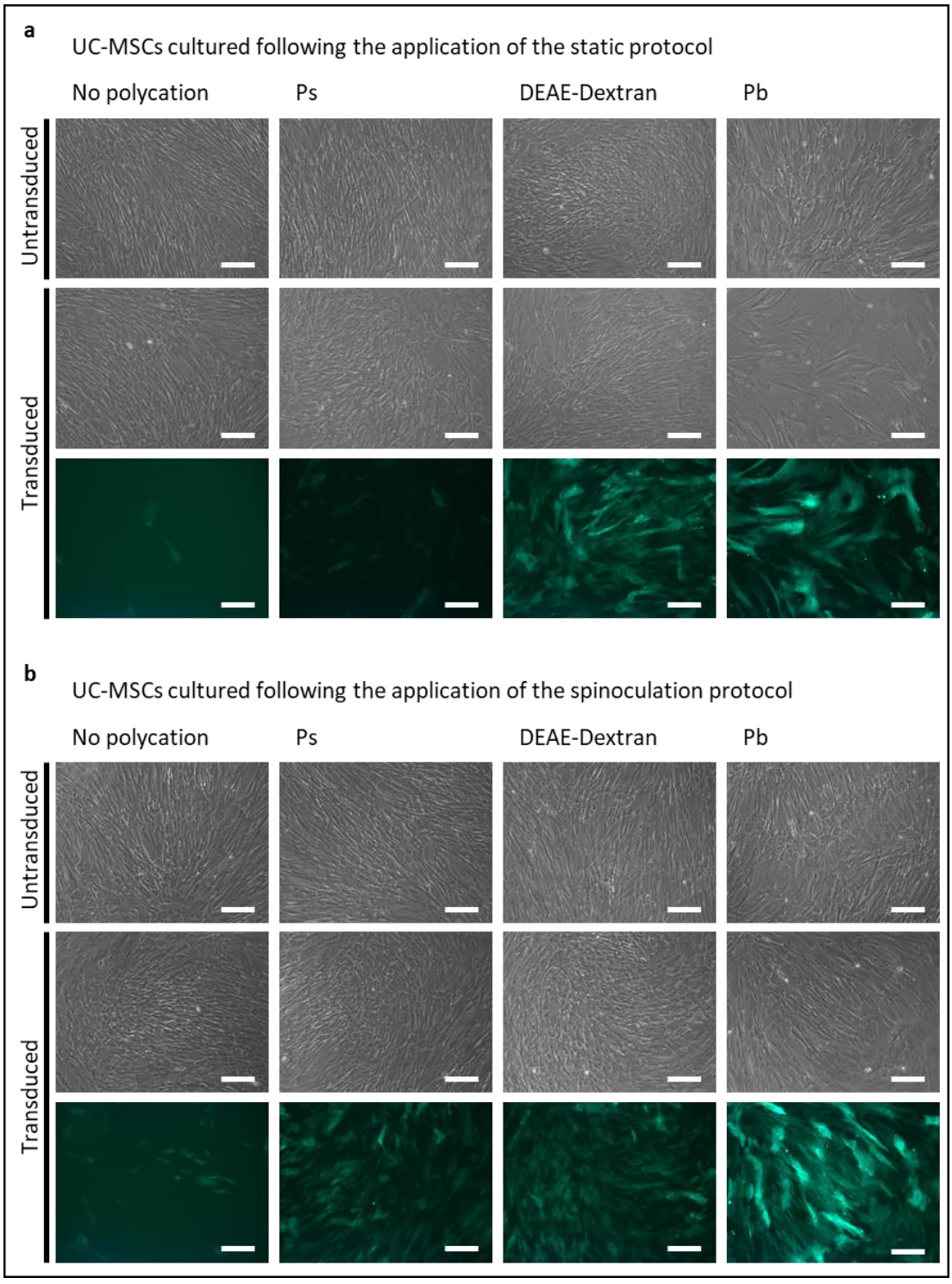

Figure 3.4| Effect of polycations and spinoculation on UC-MSC transduction. (a) Representative phase contrast images of untransduced and transduced UC-MSCs in static condition. The images of the transduced cells are coupled with the green fluorescence channel to show the expression of the ZsGreen protein. Scale bar 200 µm. **(b)** Representative phase contrast images of untransduced and transduced UC-MSCs following the application of the spinoculation protocol. The images of the transduced cells are coupled with the green fluorescence channel to show the expression of the

ZsGreen protein. Scale bar 200 µm. All fluorescence images acquired under the same acquisition conditions.

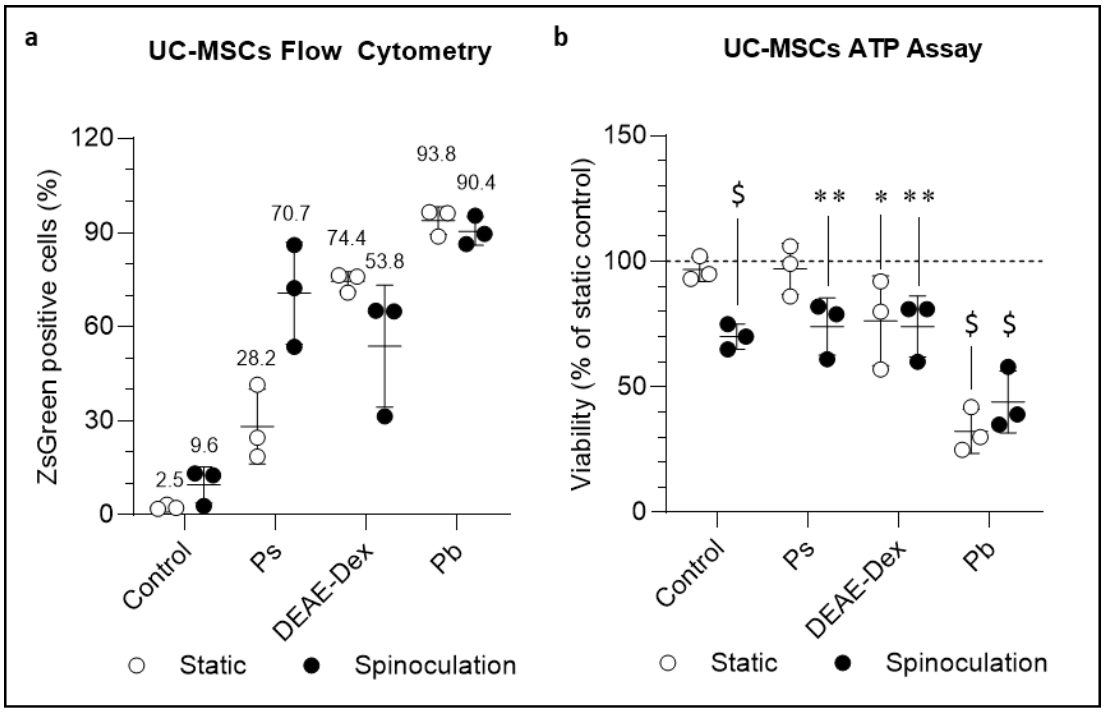

Figure 3.5| Static DEAE-dextran and spinoculation Ps are valid alternatives to Pb for the transduction of umbilical cord mesenchymal stromal cells. The two graphs display the data from transduced cells only. **(a)** Percentage of transduced UC cells expressing the ZsGreen as evaluated via flow cytometry. Data are displayed as mean ± SD, n = 3. **(b)** Levels of ATP produced by transduced UC-MSCs after 7 days of culture following the application of the different protocols. Data are normalised to the control group in static condition and are displayed as mean ± SD, n = 3. Statistical analysis performed on Supplementary Figure 3.1a: Three-way ANOVA with Dunnett post-hoc comparison test against untransduced static control; * p <0.05, ** p < 0.01, $ p < 0.0001.

Flow cytometry and the ATP assay data (Figure 3.5) supported what was observed via microscopy. UC-MSC transduction efficiency in the presence of Pb was high regardless of the application of the static (93.8 ± 4.4%) or the spinoculation (90.4 ± 4.5%) protocol. However, the ATP assay of transduced cells in the presence of Pb revealed a strong reduction in the viability of the transduced cells, which was only 32.3% (± 8.6%) and 44.1% (± 12.5%) of the control in static and spinoculation conditions, respectively (data of untransduced UC-MSCs are shown in Supplementary Figure 3.1a). Cells transduced in the presence of DEAE-dextran resulted in 74.4% (± 3.1%) and 53.8% (± 19.4%) of positive cells (Figure 3.5a) in static and spinoculation conditions and were respectively associated with a viability reduced to 79.3% (± 17.8%) and 74.1% (± 12.2%) (Figure 3.5b). Finally, in the presence of Ps (Figure 3.5a), 28.2% (± 11.9%) and 70.7% (± 16.3%) of the cells were positive for ZsGreen in static and spinoculation conditions, respectively. These conditions were associated with a reduction in viability to 96.9% (± 10.1%) and to 74.0% (± 11.4%) (Figure 3.5b). A three-way ANOVA analysis

was performed on the data displayed in the Supplementary Figure 3.1a to assess the effect of the polycations, the spinoculation and the transduction and the combination of those factors on the viability of the cells. The results reveal that all these conditions and combination had an impact on the viability of UC-MSCs, except for the combination of spinoculation and transduction (Table 3.3).

Table 3.3: Impact of the polycations (poly.), the spinoculation (spin.), the transduction (tran.) and their combinations on the ATP production of MSCs. Results based on three-way ANOVA analysis of Supplementary Figure 3.1.

Cell Type	Poly.	Spin.	Tran.	Poly. X Spin.	Poly. X Tran.	Spin. X Tran.	Poly. X Spin. X Tran.
UC-MSCs	Yes (p=0.0007)	Yes (p=0.09)	Yes (p=0.04)	Yes (p=0.002)	Yes (p=0.005)	No (p=0.23)	Yes (p=0.04)
BM-MSCs	Yes (p<0.0001)	No (p=0.90)	No (p=0.24)	Yes (p=0.0009)	No (p=0.40)	No (p=0.63)	No (p=0.51)
A-MSCs	Yes (p=0.001)	No (p=0.13)	No (p=0.32)	Yes (p=0.006)	No (p=0.08)	No (p=0.29)	No (p=0.84)

3.3.2.2 Bone marrow-derived mesenchymal stromal cells

Representative phase contrast images of transduced BM-MSCs and the respective fluorescence images (green channel) are displayed in Figure 3.6. As observed for the UC-MSCs, the cells transduced with the polybrene display the highest level of transduction efficiency and a strong level of green fluorescence (Figure 3.6a-b). Again, the morphology of these cells and their confluence level looks different from the control (Figure 3.6a), even if the effect was more noticeable for the UC-MSCs (Figure 3.4a-b). All the other conditions are associated with cells displaying a normal morphology and confluence, although with differences in the level of transduction (green fluorescence, Figure 3.6a-b). Similarly to what was observed for the UC-MSCs, the BM cells transduced in the presence of DEAE-dextran, regardless of whether the static or spinoculation protocols were used (Figure 3.6a-b), and the BM cells transduced in the presence of Ps following the application of the spinoculation step (Figure 3.6b), display a relative strong level of green fluorescence.

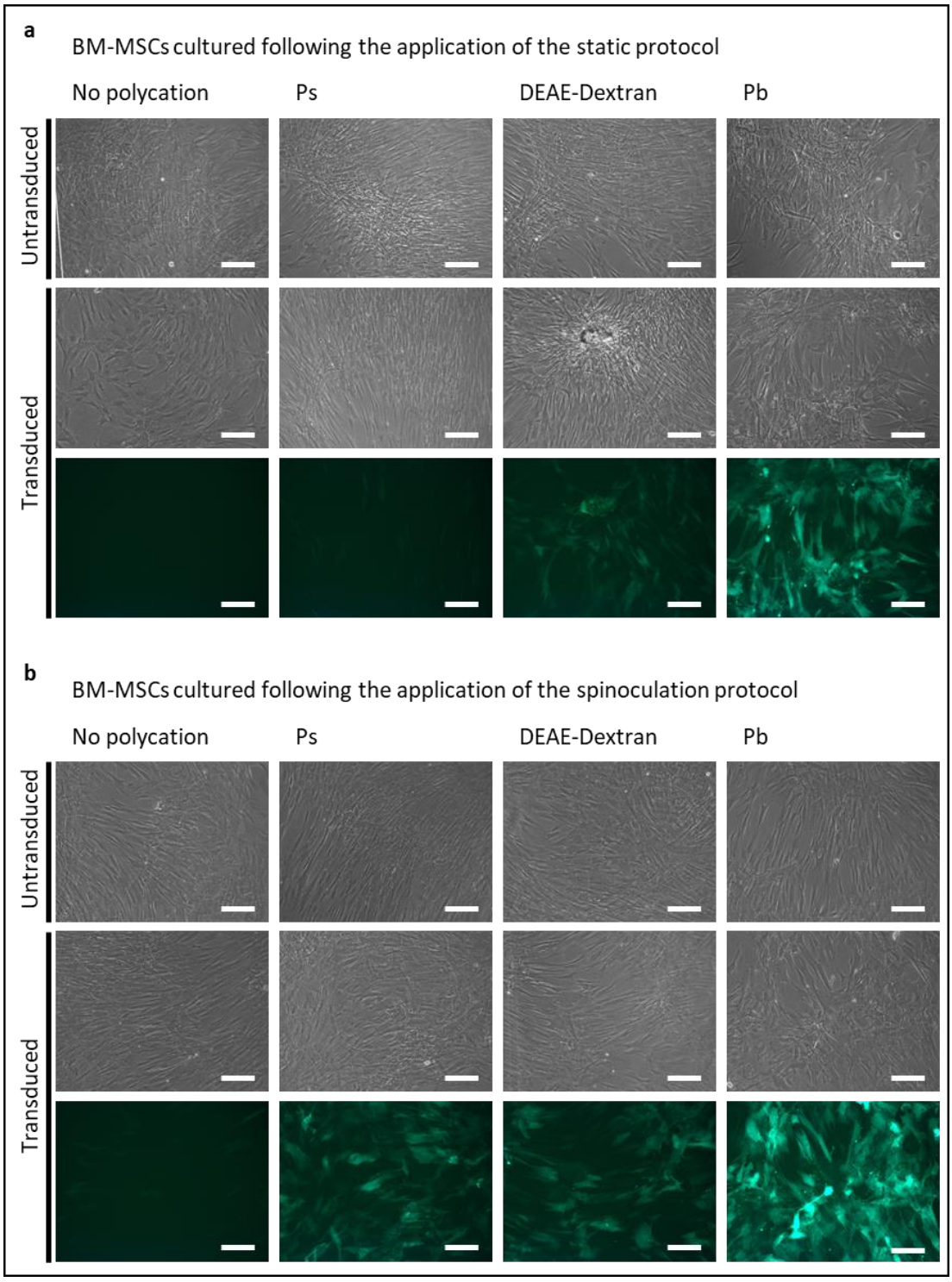

Figure 3.6| Effect of polycations and spinoculation on BM-MSCs transduction. (a) Representative phase contrast images of untransduced and transduced bone marrow MSCs in static condition. The images of the transduced cells are coupled with the green fluorescence channel to show the expression of the ZsGreen protein. Scale bar 200 µm. **(b)** Representative phase contrast images of untransduced and transduced bone marrow derived MSCs following the application of the spinoculation protocol. The images of the transduced cells are coupled with the green fluorescence channel to show the expression of the ZsGreen protein. Scale bar 200 µm.

These results were confirmed by flow cytometry and the ATP assay (Figure 3.7). The transduction in the presence of Pb was associated with 92.3 ± 5.3% and 94.1 ± 3.0% of the cells expressing the ZsGreen protein following the application of the static and the spinoculation protocols, respectively (Figure 3.7a). Again, the presence of Pb resulted in a reduction in the viability of the transduced cells to 72.3 ± 6.0% of the control in static condition but did not really affect the growth of the cells when the Pb was coupled with the spinoculation (94.0 ± 9.5%, Figure 3.7b). Cells transduced in the presence of DEAE-dextran resulted in 80.2% (± 5.1%) and 76.0% (± 11.5%) of positive cells (Figure 3.7a) in static and spinoculation conditions, respectively. Surprisingly, the presence of the DEAE-dextran seems to have increased the viability of the transduced cells to 116.3% (± 10.5%) and to 109.7% (± 2.9%), in static and spinoculation conditions, respectively (Figure 3.7b). This increase in the viability was also observed when the cells were incubated without the lentiviral particles and with the DEAE-dextran only (120.7 ± 10.8% in static and 106.0 ± 3.0% in spinoculation condition, Supplementary Figure 3.1b). Finally, in the presence of Ps (Figure 3.7a), 22.5% (± 10.0%) and 75.8% (± 6.7%) of the cells were positive for ZsGreen in static and spinoculation conditions, respectively. The presence of the Ps was also associated with an increase in viability of transduced cells both in static (128 ± 8.9%) and spinoculation conditions (119.7 ± 3.5%) (Figure 3.7b). The analysis of the impact of spinoculation, transduction and polycations on the viability of the cells revealed that the polycations and their combination with spinoculation had an impact on the viability of the cells ($p < 0.0001$ and $p = 0.0009$ respectively, Table 3.3).

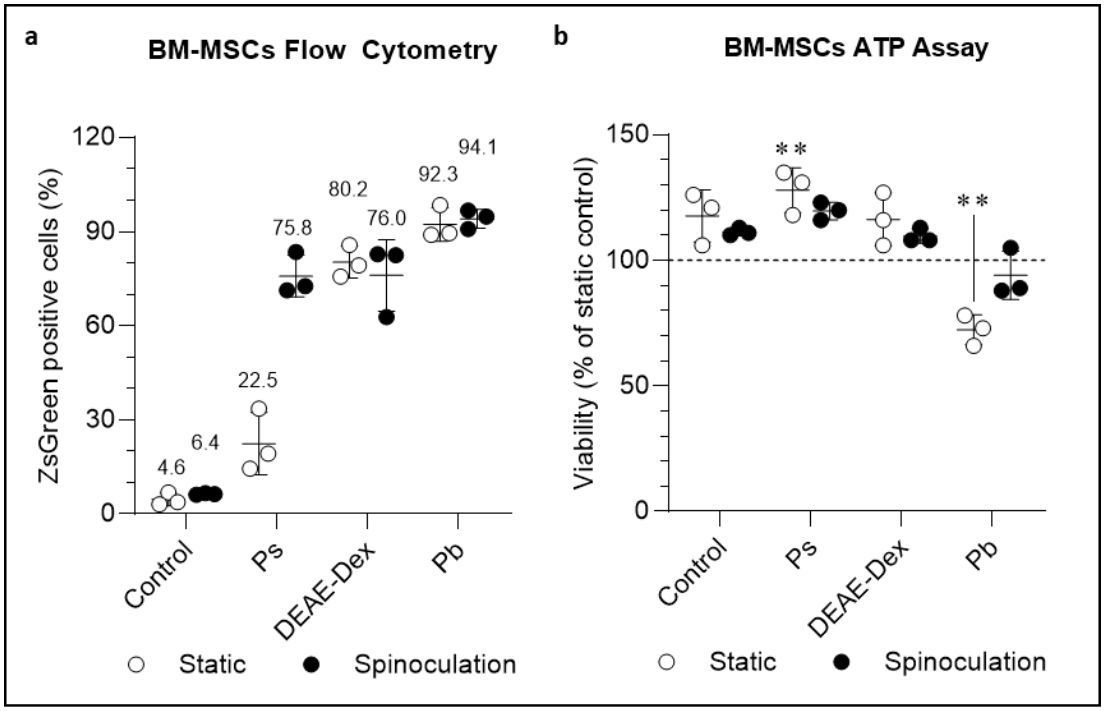

Figure 3.7| DEAE-dextran following the application of either the static or spinoculation protocol and spinoculation Ps are valid alternatives to the Pb for the transduction of bone marrow MSCs. The two graphs display the data from transduced cells only. **(a)** Percentage of transduced BM cells expressing ZsGreen as evaluated via flow cytometry. Data are displayed as mean ± SD, n = 3. **(b)** Levels of ATP produced by transduced BM-MSCs after 10 days of culture following the application of the different protocols. Data are normalised to the control group in static condition and are displayed as mean ± SD, n = 3. Statistical analysis performed on Supplementary Figure 3.1b: Three-way ANOVA with Dunnett post-hoc comparison test against untransduced static control; ** $p < 0.01$.

3.3.2.3 Adipose derived mesenchymal stromal cells

Representative phase contrast images of A-MSCs taken 7 days post-transduction and the respective fluorescence images (green channel) are displayed in Figure 3.8a. Unlike UC- and BM-MSCs, the average transduction efficiency of adipose derived cells appears reduced, even when polybrene is used as the polycation (Figure 3.8). The morphology of the cells look comparable among all the conditions (Figure 3.8), with the only exception being the cells incubated with Pb in static condition, where the cells look more sparse and less confluent (Figure 3.8a).

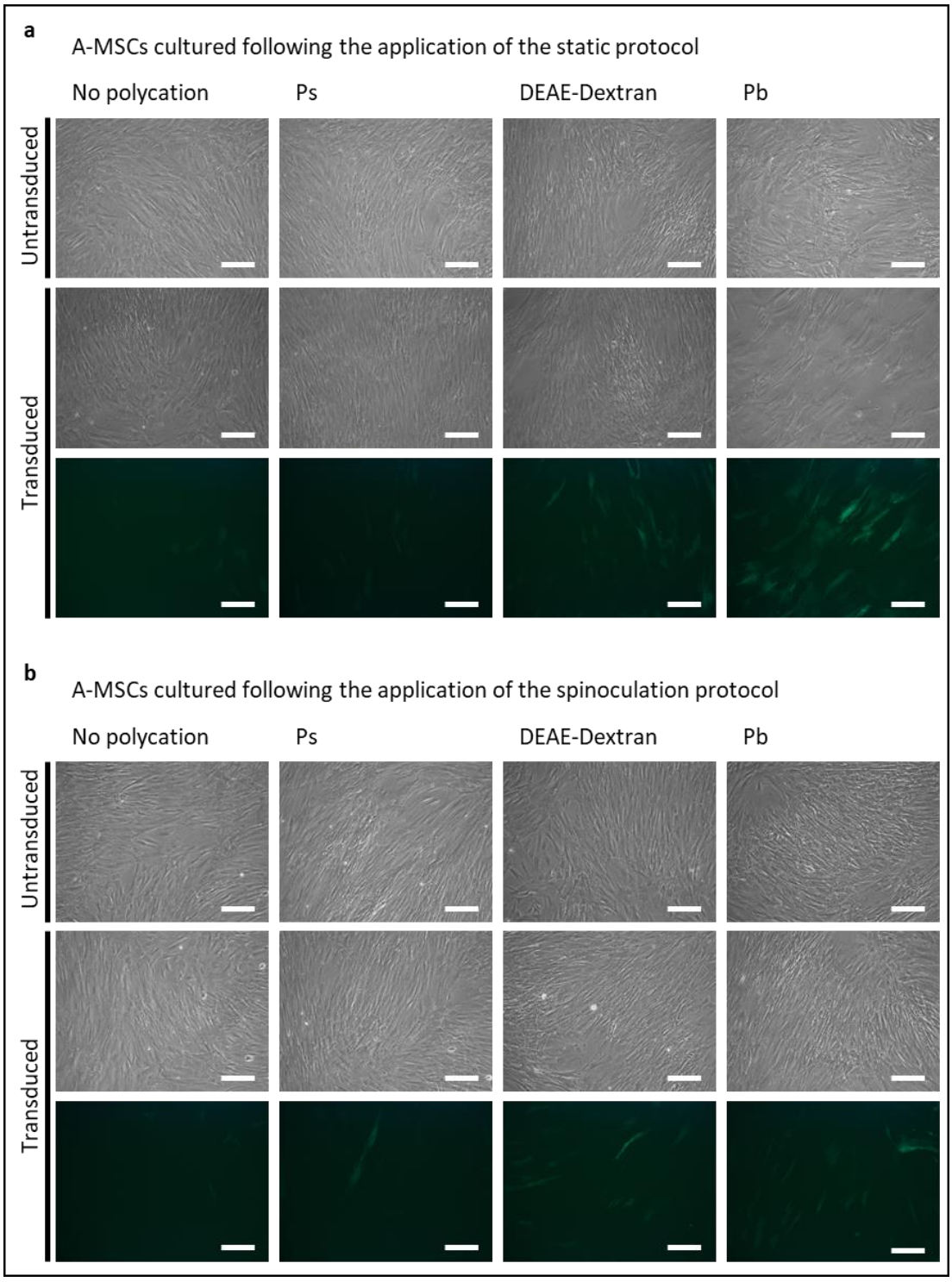

Figure 3.8| Effect of polycations and spinoculation on A-MSCs transduction. (a) Representative phase contrast images of untransduced and transduced adipose derived MSCs in static condition. The images of the transduced cells are coupled with the green fluorescence channel to show the expression of the ZsGreen protein. Scale bar 200 µm. **(b)** Representative phase contrast images of untransduced and transduced adipose derived MSCs following the application of the spinoculation protocol. The images of the transduced cells are coupled with the green fluorescence channel to show the expression of the ZsGreen protein. Scale bar 200 µm.

The flow cytometry analysis revealed that transduction in the presence of Pb in static and spinoculation conditions was associated with only 48.6 ± 7.5% and 19.2 ± 3.8% of cells effectively transduced, respectively (Figure 3.9a). Cells transduced in the presence of DEAE-dextran resulted in 50.0% (± 9.9%) and 12.3% (± 2.8%) of positive cells (Figure 3.9a) in static and spinoculation conditions, respectively. The transduction with Ps resulted in only 8.3% (± 2.3%) and 6.3% (± 1.3%) of positive cells (Figure 3.9a). The ATP assay revealed that the presence of Pb affected the viability of the transduced cells following the application of the static protocol (74.4 ± 6.8%, $p < 0.0001$), while none of the other conditions had an effect on ATP levels (Figure 3.9b, Supplementary Figure 3.1c). The analysis of the impact of spinoculation, transduction and polycations on the viability of the adipose cells revealed that, as for the BM-MSCs, only the polycations and their combination with spinoculation had an impact on the viability of the cells ($p = 0.001$ and $p = 0.006$ respectively, Table 3.3).

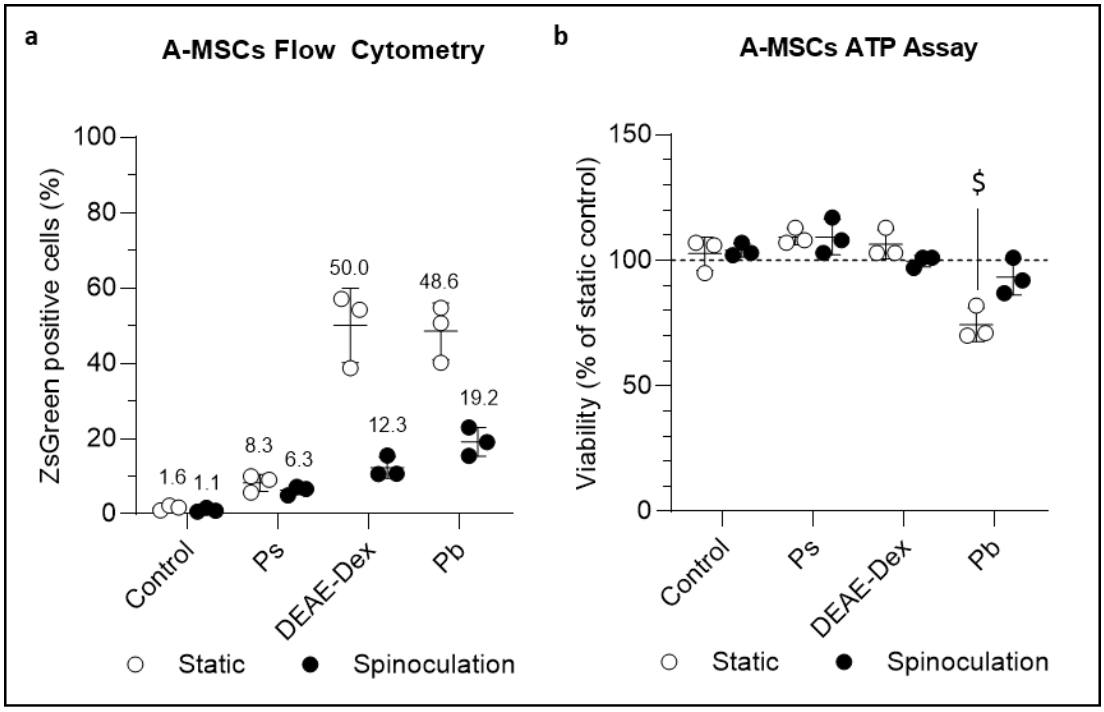

Figure 3.9| DEAE-dextran following the application of the static protocol is a valid alternative to the Pb for the transduction of adipose derived MSCs. The two graphs display the data from transduced cells only. **(a)** Percentage of transduced A-MSCs expressing the ZsGreen as evaluated via flow cytometry. Data are displayed as mean ± SD, n = 3. **(b)** Levels of ATP produced by transduced A-MSCs cells after 7 days of culture following the application of the different protocols. Data are normalised to the control group in static condition and are displayed as mean ± SD, n = 3. Statistical analysis performed on Supplementary Figure 3.1c: Three-way ANOVA with Dunnett post-hoc comparison test against untransduced static control; $ $p < 0.0001$.

3.3.3 Validation of the selected protocol: DEAE-dextran in static condition

The protocol involving DEAE-dextran as the polycation, with an overnight incubation in static conditions was selected as the optimal transduction procedure. This is because it resulted in a good transduction efficiency for all the MSCs tested (74.4% for UC-MSCs, 80.2% for BM-MSCs and 50.0% for A-MSCs) without overtly affecting the viability of the cells. This protocol was then applied to transduce the three types of MSCs with different lentiviral particles to assess how the transduction efficiency could be influenced by the lentiviral construct itself.

Representative fluorescence images of all three MSCs transduced with the four lentiviral particles in the absence or presence of DEAE-dextran are displayed in Figure 3.10. Regardless of the lentiviral particle, all the cell types display a low transduction efficiency when transduced without DEAE-dextran. In contrast, for all four lentiviral particles, the presence of polycation leads to an increase in the number of transduced cells and in the intensity of signal in all three MSCs (Figure 3.10a-c). This increase is particularly remarkable for the pLV-mCherry and for the pHIV-dTomato, while less evident for the pHIV-eGFP and for the pCDH-EF1α-Luc2-P2A-tdTomato (especially for the BM-MSCs, Figure 3.10b).

The fraction of successfully transduced cells for each lentiviral construct was assessed via flow cytometry (Figure 3.11). UC-MSCs displayed a statistically significant increase in the fraction of transduced cells when infected in the presence of the DEAE-dextran for all the lentiviral particles (Figure 3.11a). Specifically, the proportion of cells positive for the transgene increased from 0.3 ± 0.2% to 11.7 ± 4.4% for the pCDH-EF1α-Luc2-P2A-tdTomato (p = 0.0005), from 9.4 ± 2.8% to 61.8 ± 11.6% for the pHIV-dTomato (p < 0.0001), from 10.5 ± 2.7% to 58.7 ± 8.9% for the pHIV-eGFP (p < 0.0001) and from 5.5 ± 2.2% to 72.9 ± 9.2% for the pLV-mCherry (p < 0.0001, Figure 3.11a). A two-way ANOVA analysis also revealed that both the presence of DEAE-dextran and the specific lentiviral construct used have a statistically significant impact on the transduction efficiency (p < 0.01 and p < 0.0001 respectively).

Similar results were obtained with the BM-MSCs (Figure 3.11b), where the proportion of transduced cells increased from 0.49 ± 0.5% to 6.3 ± 1.3% for the pCDH-EF1α-Luc2-P2A-tdTomato (no statistically significant difference), from 13.7 ± 0.9% to 57.8 ± 9.4% for the pHIV-dTomato (p < 0.0005), from 13.2 ± 0.7% to 54.8 ± 17.6% for the pHIV-eGFP (p = 0.0005) and from 11.7 ± 1.1% to 73.2 ± 11.2% for the pLV-mCherry (p < 0.0001, Figure 3.11a). A two-way ANOVA analysis confirmed the statistically significant

effect of the DEAE-dextran and of the lentiviral construct on the transduction efficiency ($p < 0.05$ and $p = 0.0001$ respectively).

Lastly, the adipose derived cells showed a transduction behaviour comparable to the other two MSCs (Figure 3.11c), with an increase in the percentage of transduced cells from 0.8 ± 0.5% to 5.9 ± 2.1% for the pCDH-EF1α-Luc2-P2A-tdTomato (no statistically significant difference), from 6.7 ± 2.6% to 54.0 ± 10.6% for the pHIV-dTomato ($p < 0.0001$), from 5.6 ± 2.4% to 38.1 ± 10.0% for the pHIV-eGFP ($p < 0.0001$) and from 3.2 ± 1.2% to 54.2 ± 13.4% for the pLV-mCherry ($p < 0.0001$, Figure 3.11a). Again, the two-way ANOVA analysis identified a statistically significant impact of the DEAE-dextran and of the type of lentiviral particle on the transduction efficiency ($p < 0.05$ and $p < 0.0001$ respectively).

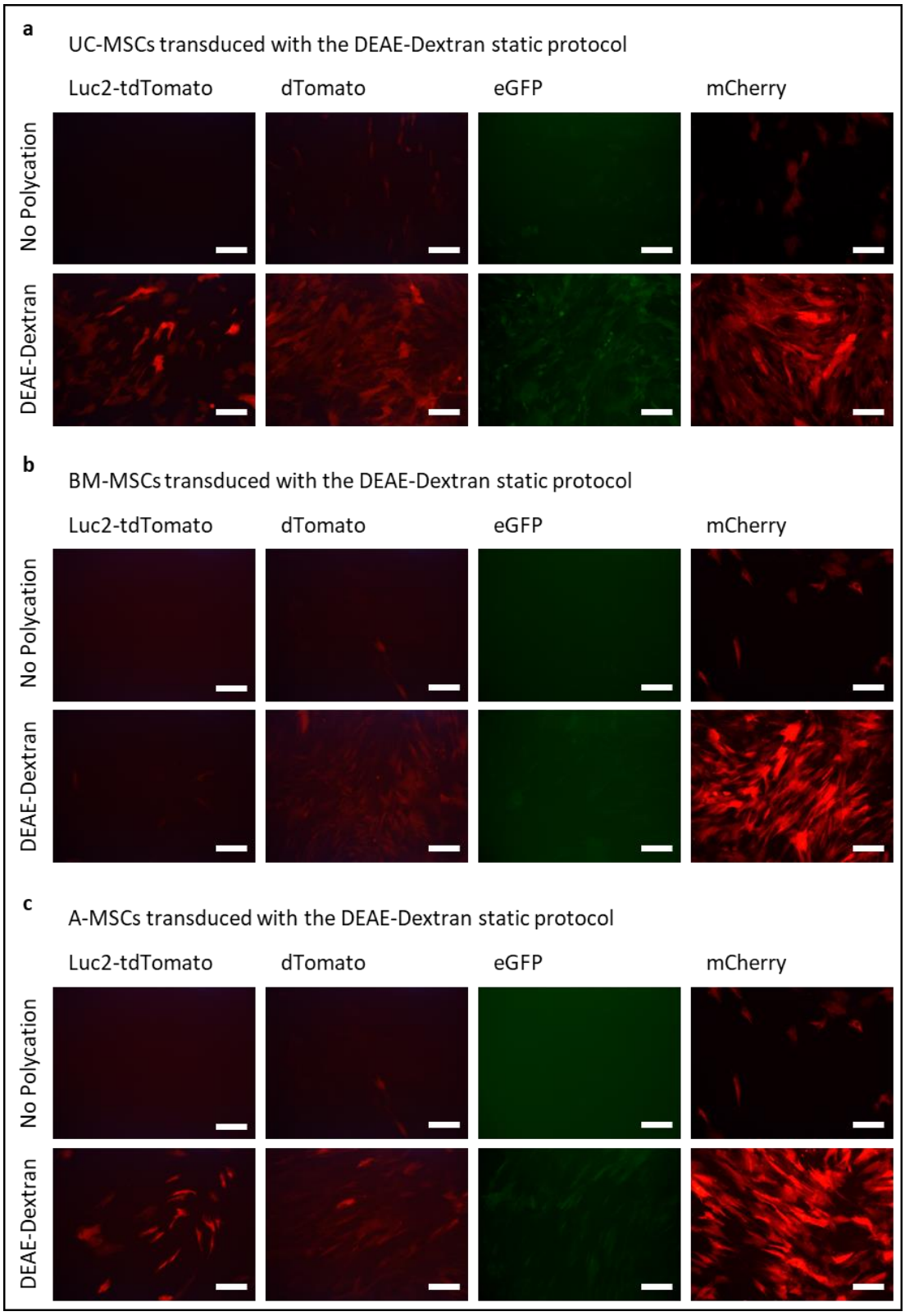

Figure 3.10| The application of the DEAE-dextran static protocol increases the transduction efficiency of all types of MSCs with all the lentiviral particles tested. (a-c) representative fluorescence images of UC- **(a)**, BM- **(b)** and A- **(c)** MSCs transduced with four different lentiviral particles with and without the use of DEAE-dextran as a polycation. Scale bar 200 µm.

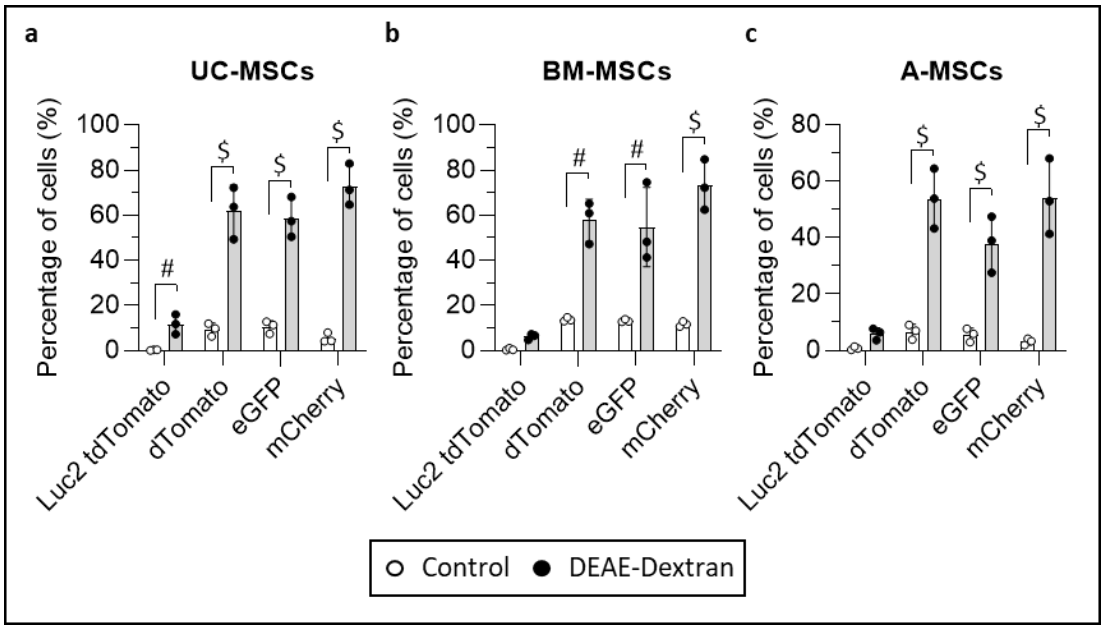

Figure 3.11| Application of the DEAE-dextran protocol to transduce MSCs with four different lentiviral particles. Percentage of transduced and control UC- **(a)**, BM- **(b)** and A-MSCs **(c)** expressing either the tdTomato, the dTomato, the eGFP or the mCherry protein evaluated via flow cytometry. Data are displayed as mean ± SD, n = 3. Two-way ANOVA analysis with Sidak's multiple comparison post-hoc test; $ $p \leq 0.0001$ and # $p \leq 0.0005$.

3.3.4 Characterisation of the MSCs transduced with the DEAE-dextran static protocol

To determine whether the transduction procedure had an impact on the properties of the different MSCs, transduced and untransduced cells were compared in terms of doubling time, expression levels of MSC markers and morphology (area and circularity of the cells). For this study, all MSCs were transduced with the pHIV-Luc2-ZsGreen construct (Figure 3.1a, encoding for ZsGreen and Firefly Luciferase) and sorted to obtain a population 100% positive for the transgenes.

3.3.4.1 Umbilical Cord Mesenchymal Stromal Cells

Representative phase contrast images of control and FLuc_ZsGreen UC cells and the respective green fluorescence images (ZsGreen) after 7 days of culture are shown in Figure 3.12a. The morphology of the different transduced UC cells looks comparable to controls (Figure 3.12a). The analysis of the cumulative doublings from p7 to at least p10 revealed that the transduced cells behaved similarly to the untransduced ones (Figure 3.12b) and no statistically significant difference in the doubling time was observed between transduced and untransduced cells (Figure 3.12c and d).

The flow cytometry analysis of the expression of ZsGreen was performed at P8 (Figure 3.12e) to evaluate any loss of the reporter gene following the expansion after sorting, which was

undertaken at P6. Specifically, 98.62%, 99.08% and 99.36% of 727R, 733S and 735O samples, respectively, are still positive (Table 3.4). Furthermore, the flow cytometry analysis of surface markers revealed a similar level of expression of positive markers (CD44, CD73. CD90 and CD105) and the lack of CD45 negative marker (Table 3.4) in both transduced and untransduced cells.

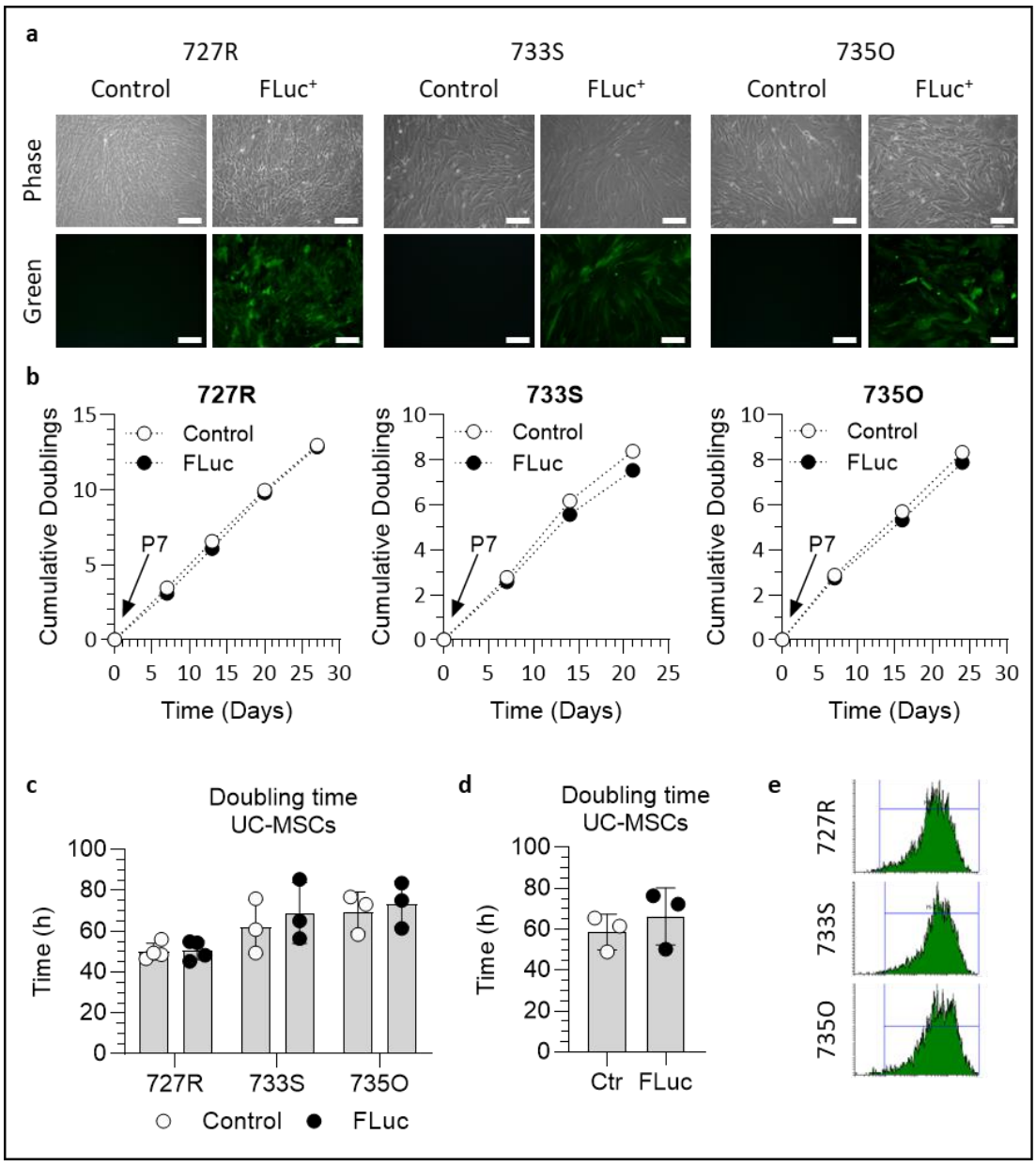

Figure 3.12| FLuc_ZsGreen UC-MSCs display similar proliferation to untransduced cells. (a) Representative phase contrast and green fluorescence images of the 3 UC-MSCs samples after sorting. Scale bar = 200µm. **(b)** Cumulative doubling from p7 to p10-11 for the 3 UC-MSC samples transduced or untransduced. **(c-d)** Average doubling time of transduced and untransduced cells displayed by sample **(c)** and by population **(d)**. Data are displayed as mean ± SD, n ≥ 3. **(e)** ZsGreen expression of transduced cells measured via flow cytometry at p8. FLuc = FLuc_ZsGreen cells.

To perform the morphological analysis, samples were stained with phalloidin to get fluorescent images of the actin filaments and with DAPI to identify the nuclei. Fluorescence images of transduced and untransduced cells at 100x suggested a comparable morphology between the 2 cell populations (Figure 3.13a). Those images were used to perform a quantitative evaluation of the area, the perimeter (used to calculate the circularity), and the circularity of the cells. Only isolated cells, those not in contact with neighbouring cells, were measured to avoid possible errors in detecting their perimeter. The quantitative analysis revealed that for only one of the UC-MSC donor samples was there a statistically significant increase in the area of the cells (Figure 3.13b), with no impact on the circularity (Figure 3.13c). Overall, the average cell area and circularity of transduced and untransduced cells among the three donor samples looked comparable (Figure 3.13d).

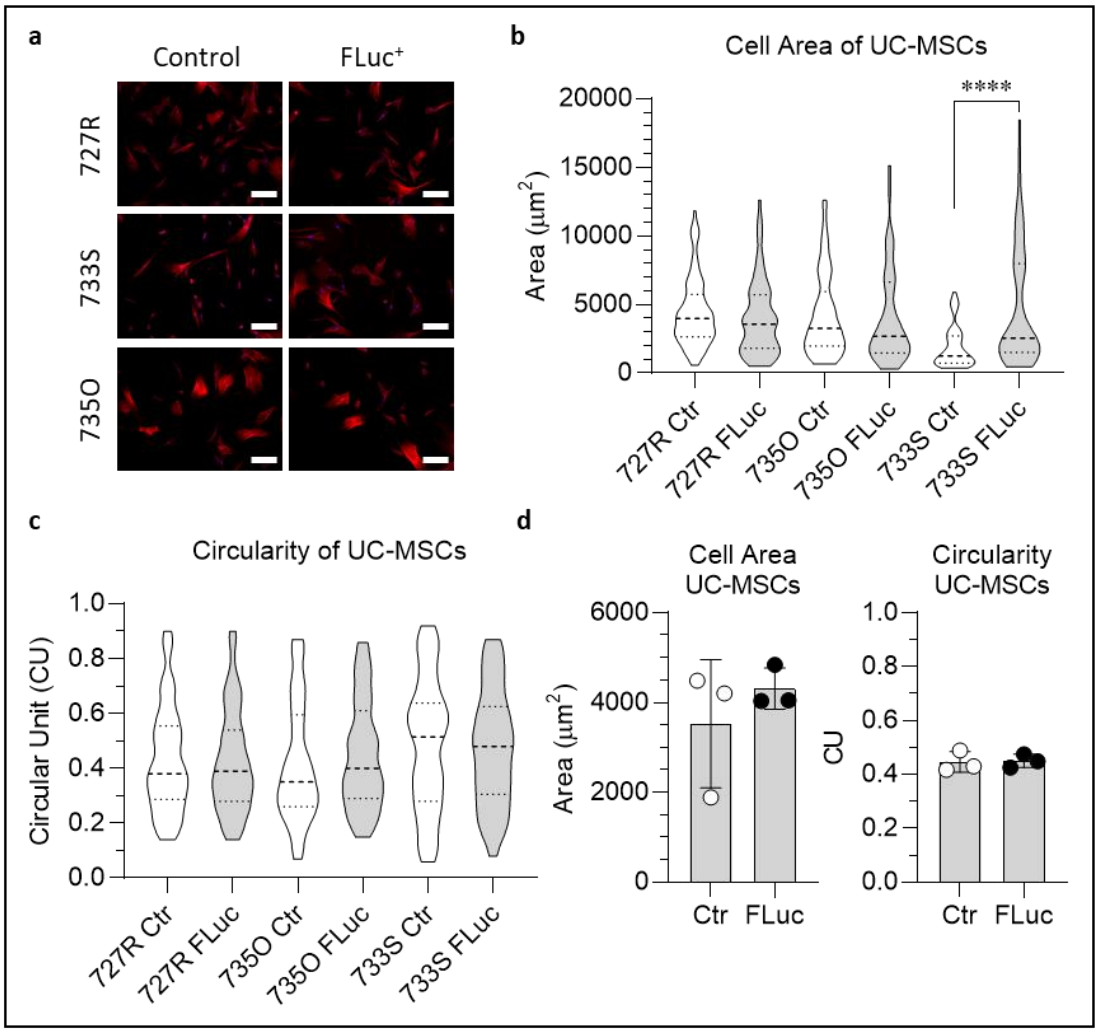

Figure 3.13| Morphological characterisation of transduced UC-MSCs. (a) Fluorescence images of cells 16h after seeding stained with phalloidin (f-actin, red) and DAPI (nuclei, blue) acquired at 100x. Scale bar = 200µm. **(b-c)** Violin plot of the area **(b)** and the circularity **(c)** of the transduced and untransduced cell populations (at least 55 cells from each sample were analysed). The data were plotted into a grouped graph and cleaned from the outliers using the automated GraphPad tool "remove outliers".

A two-way ANOVA was performed on the cleaned data with a Dunn's multiple comparison post-hoc test; $p < 0.0001$. **(d)** Average cell area and circularity of UC-MSCs produced using the data from the 3 donor samples. FLuc = FLuc_ZsGreen cells. Abbreviations: CU = circular unit (1 = perfect circle, 0 = elongated polygon).

Table 3.4: Percentage of FLuc_ZsGreen cells expressing the ZsGreen protein and percentage of untransduced controls and transduced cells positive to CD44, CD45, CD73, CD90 and CD105. FLuc = FLuc_ZsGreen.

Donor ID	Positive cells (ZsGreen)	CD45	CD44	CD73	CD90	CD105
727R Ctr	N/A	1.75%	99.20%	99.88%	99.95%	99.83%
727R FLuc	98.62%	2.68%	99.75%	99.94%	99.95%	99.79%
733S Ctr	N/A	2.96%	99.20%	99.77%	100.00%	99.57%
733S FLuc	99.08%	4.59%	99.65%	99.80%	99.95%	99.49%
735O Ctr	N/A	1.84%	97.37%	99.80%	99.96%	99.95%
735O FLuc	99.36%	5.01%	95.30%	99.74%	99.93%	99.81%
BM04 Ctr	N/A	6.23%	99.85%	96.84%	100.00%	98.49%
BM04 FLuc	99.84%	6.96%	99.97%	99.72%	99.99%	99.64%
BM21 Ctr	N/A	2.17%	99.91%	99.74%	99.83%	97.64%
BM21 FLuc	99.49%	1.98%	99.96%	98.99%	99.86%	93.58%
BM42 Ctr	N/A	1.50%	99.91%	99.90%	99.84%	99.04%
BM42 FLuc	99.86%	1.34%	100.00%	99.88%	99.70%	98.63%
LA31 Ctr	N/A	9.11%	99.81%	99.89%	99.98%	98.82%
LA31 FLuc	99.04%	4.07%	100.00%	99.50%	99.99%	93.79%
LA87 Ctr	N/A	9.28%	99.61%	99.53%	99.99%	98.61%
LA87 FLuc	99.45%	75.52%	99.98%	99.39%	99.98%	99.87%
LA96 Ctr	N/A	12.96%	99.94%	99.84%	100.00%	99.96%
LA96 FLuc	99.40%	11.20%	99.88%	99.65%	99.97%	99.75%

3.3.4.2 Bone marrow mesenchymal stromal cells

Representative phase contrast images of untransduced and transduced BM-MSCs and the respective green fluorescence images (ZsGreen) right before being passaged are shown in Figure 3.14a. The morphology of the transduced and the untransduced cells is similar (Figure 3.14a). The analysis of the cumulative doublings revealed that the FLuc_ZsGreen cells behave similarly to the controls (untransduced) for at least 2 passages (Figure 3.14b). Furthermore, no difference was observed in the doubling time of transduced cells when compared to untransduced controls (Figure 3.14c and d).

The flow cytometry analysis of the expression of ZsGreen was performed 2 passages after the sorting of the cells (Figure 3.14e). Similarly to what was observed for the UC-MSCs, almost all the FLuc_ZsGreen BM-MSCs are positive for the expression of the ZsGreen, with 99.84%, 99.49% and 99.86% of $ZsGreen^+$ cells for BM04, BM21 and BM42 respectively (Table 3.4). The

flow cytometry analysis for the expression of CD44, CD45, CD73, CD90 and CD105 revealed similar levels of expression between transduced and untransduced cells (Table 3.4).

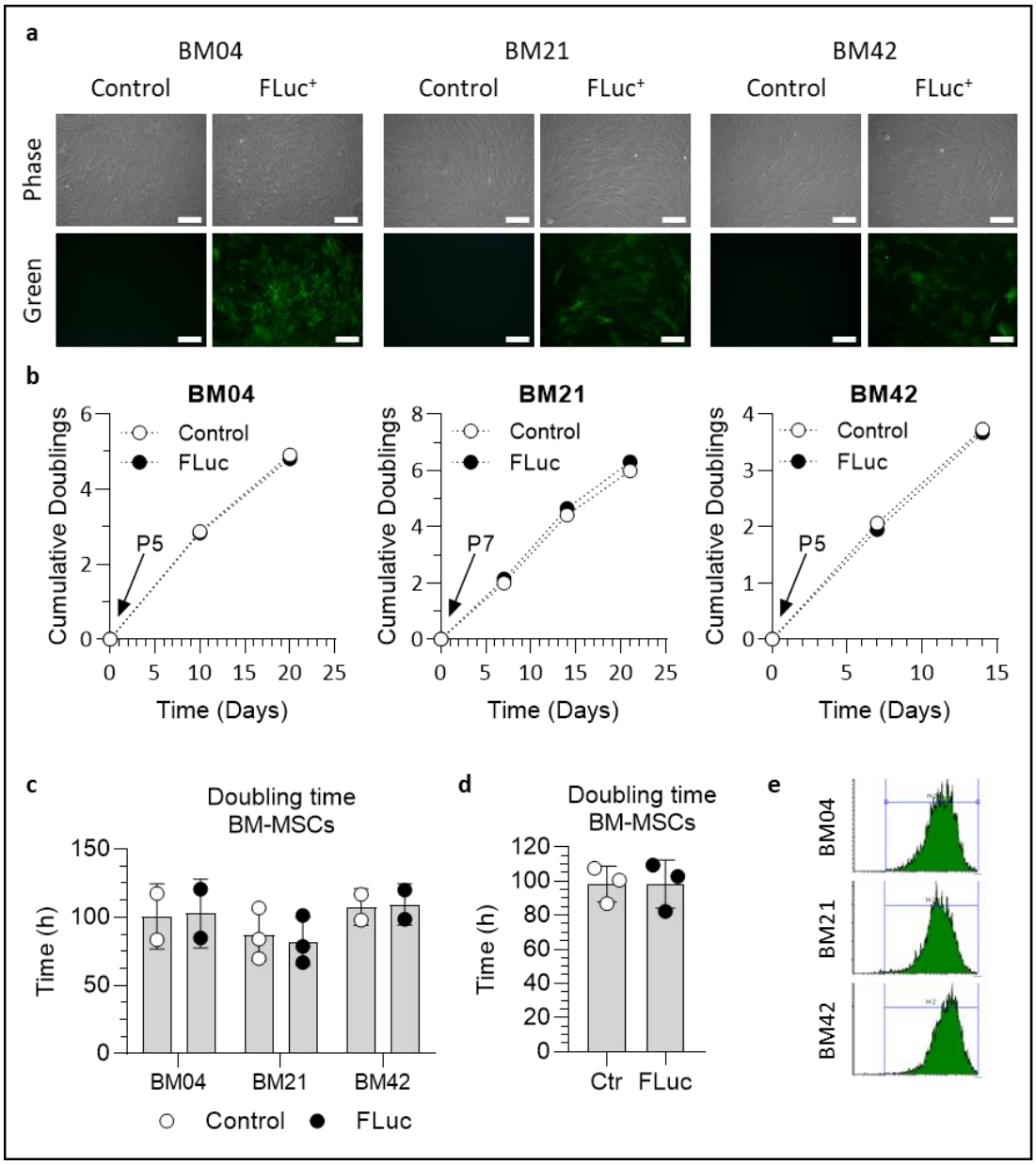

Figure 3.14| FLuc_ZsGreen BM-MSCs display similar proliferation potential to untransduced cells. **(a)** Representative phase contrast and green fluorescence images of the 3 BM-MSCs samples after the sorting. Scale bar = 200µm. **(b)** Cumulative doubling from p5 to p7 (BM04 and BM42) and from p7 to p10 (BM21) of the 3 BM-MSC samples transduced and untransduced. **(c-d)** Average doubling time of transduced and untransduced cells displayed by donor sample **(c)** and by population **(d)**. Data are displayed as mean ± SD, n ≥ 2. **(e)** ZsGreen expression of transduced cells measured via flow cytometry at p6 (BM04 and BM42) and p8 (BM21). FLuc = FLuc_ZsGreen cells.

Representative fluorescent images of transduced and untransduced cells stained with phalloidin and DAPI are shown in Figure 3.15a. The quantitative analysis performed for each donor sample revealed no statistically significant difference between the FLuc_ZsGreen cells

and controls in terms of area and circularity (Figure 3.15b and c). Finally, the average cell area and circularity of transduced and untransduced cells among the three donor samples is comparable without any statistically significant differences (Figure 3.15d).

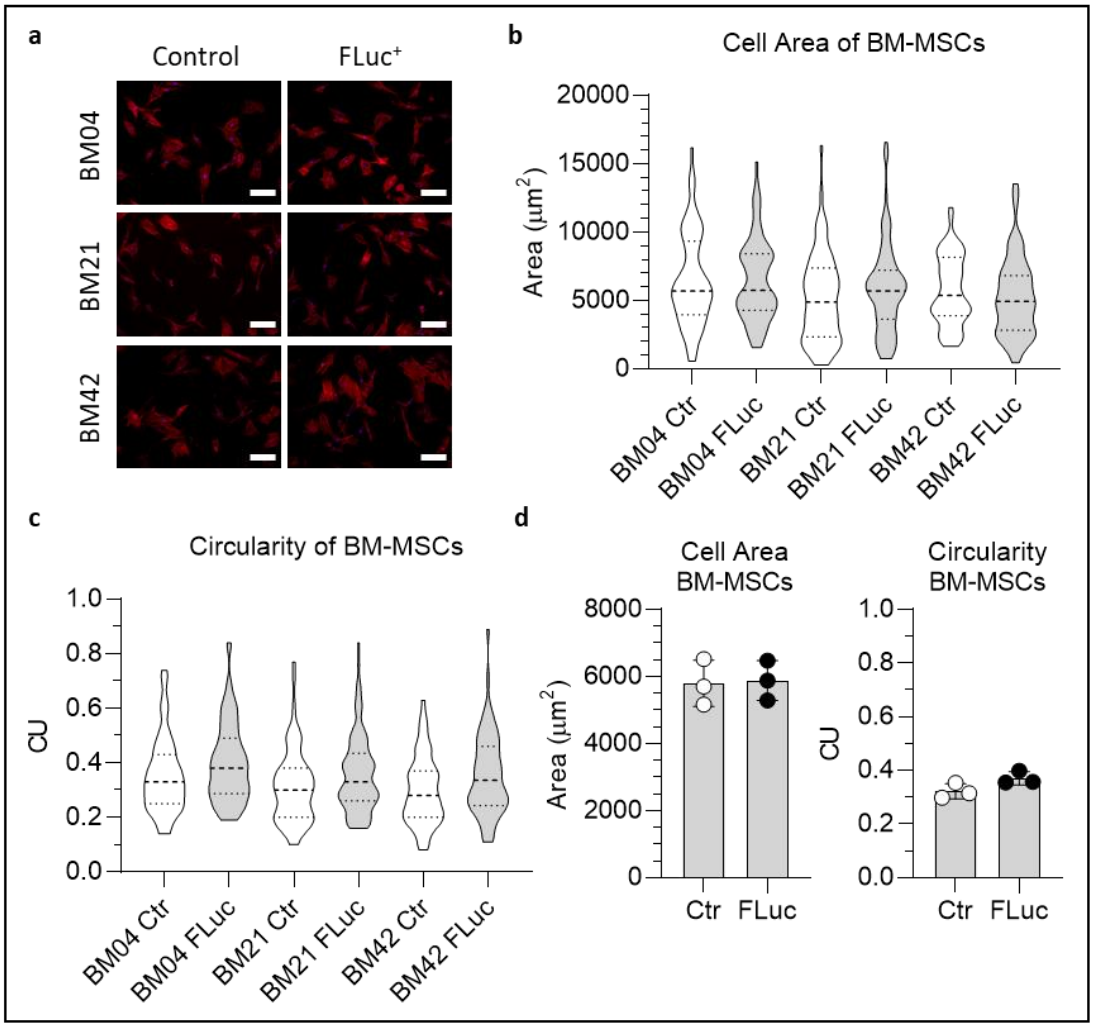

Figure 3.15| Morphological characterisation of transduced BM-MSCs. (a) Fluorescence images of cells 16h after seeding stained with phalloidin (f-actin, red) and DAPI (nuclei, blue) acquired at 100x. Scale bar = 200µm. **(b-c)** Violin plot of the area **(b)** and the circularity **(c)** of the transduced and untransduced cell populations (at least 60 cells for each sample were analysed). The data were plotted into a grouped graph and cleaned by the outliers using the automated GraphPad tool "remove outliers". A two-way ANOVA was performed on the cleaned data with a Dunn's multiple comparison post-hoc test. **(d)** Average cell area and circularity of BM-MSCs produced using the data from the 3 donor samples. FLuc = FLuc_ZsGreen cells. Abbreviations: CU = circular unit (1 = perfect circle, 0 = elongated polygon).

3.3.4.3 Adipose derived mesenchymal stromal cells

Phase contrast images of transduced and untransduced A-MSCs are displayed in Figure 3.16a. From these images, the morphology of the FLuc_ZsGreen adipose cells is comparable to controls (untransduced cells) (Figure 3.16a). The analysis of the cumulative doublings from

p7 to at least p9 revealed that the transduced cells behaved similarly to the untransduced ones (Figure 3.16b) and no difference in the doubling time was observed between the two cell populations (Figure 3.16c and d).

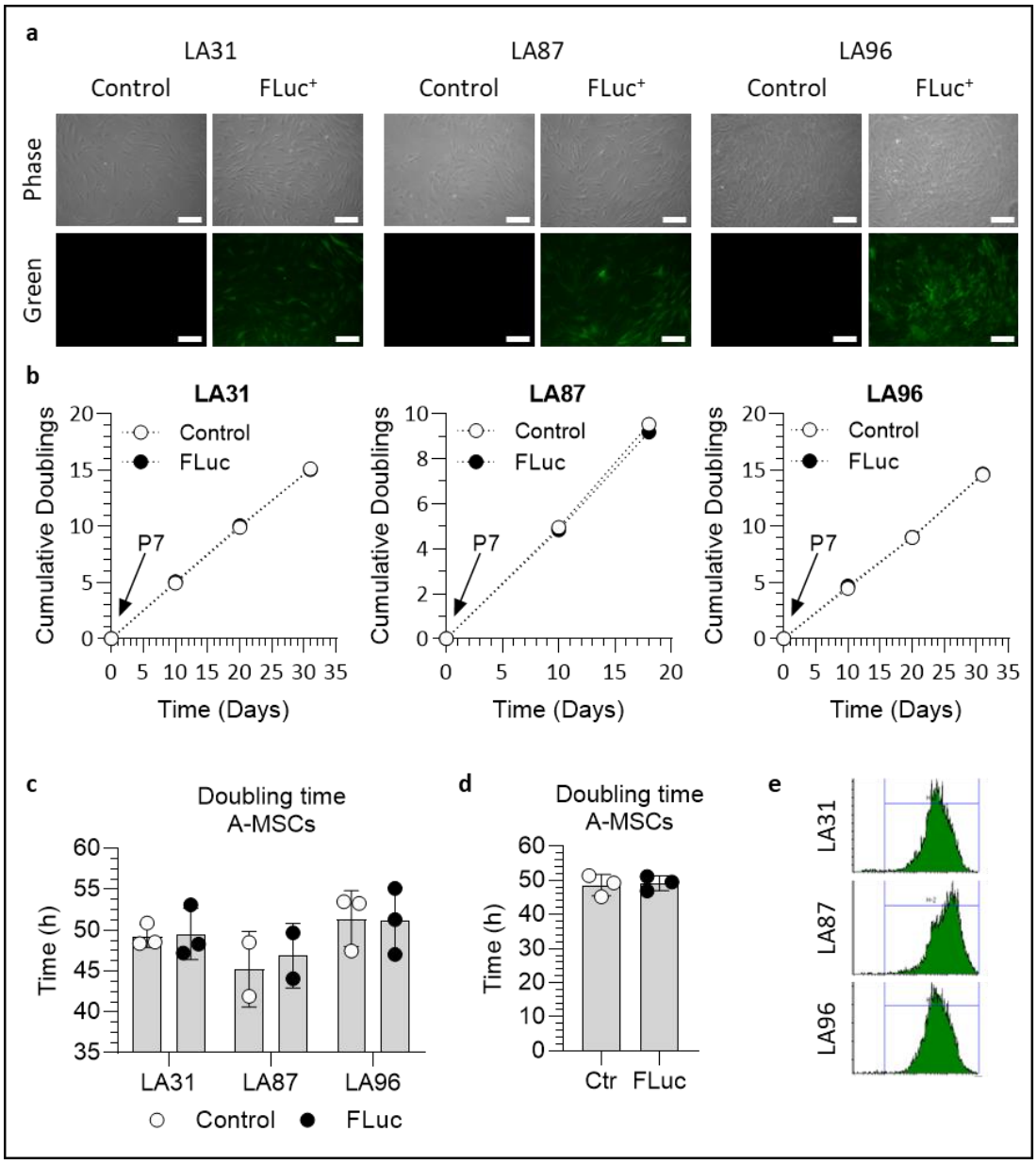

Figure 3.16| FLuc_ZsGreen A-MSCs display similar proliferation potential to untransduced cells. (a) Representative phase contrast and green fluorescence images of the 3 A-MSCs samples after the sorting. Scale bar = 200µm. **(b)** Cumulative doubling from p7 to p9 (LA87) and p10 (LA31 and LA96) of the 3 A-MSC samples transduced and untransduced. **(c-d)** Average doubling time of transduced and untransduced cells displayed by sample **(c)** and by population **(d)**. Data are displayed as mean ± SD, n ≥ 2. **(e)** ZsGreen expression of FLuc_ZsGreen measured via flow cytometry at p8. FLuc = FLuc_ZsGreen cells.

The flow cytometry analysis of the expression of ZsGreen was performed at p8 (Figure 3.16e) to evaluate any loss of expression during the expansion. 99.04%, 99.45% and 99.40% of LA31,

LA87 and LA96 samples are still positive for ZsGreen at this passage (Table 3.4). The levels of expression of positive (CD44, CD73. CD90 and CD105) and negative (CD45) markers is comparable between the transduced and controls populations of LA31 and LA96 (Table 3.4). Surprisingly, for the LA87 sample, transduction resulted in an increase in the percentage of cells positive for CD45, from 9.28% to 75.52% (Table 3.4).

Representative fluorescence images of transduced and untransduced A-MSCs, where the morphology is comparable are shown in Figure 3.17a. The quantitative analysis revealed that only one of the donor samples exhibited a statistically significant increase in circularity (Figure 3.17c), with no impact on the cell area (Figure 3.17b). Overall, the average cell area and circularity of transduced and untransduced cells among the three donor samples is comparable and does not show any statistically significant differences (Figure 3.17d).

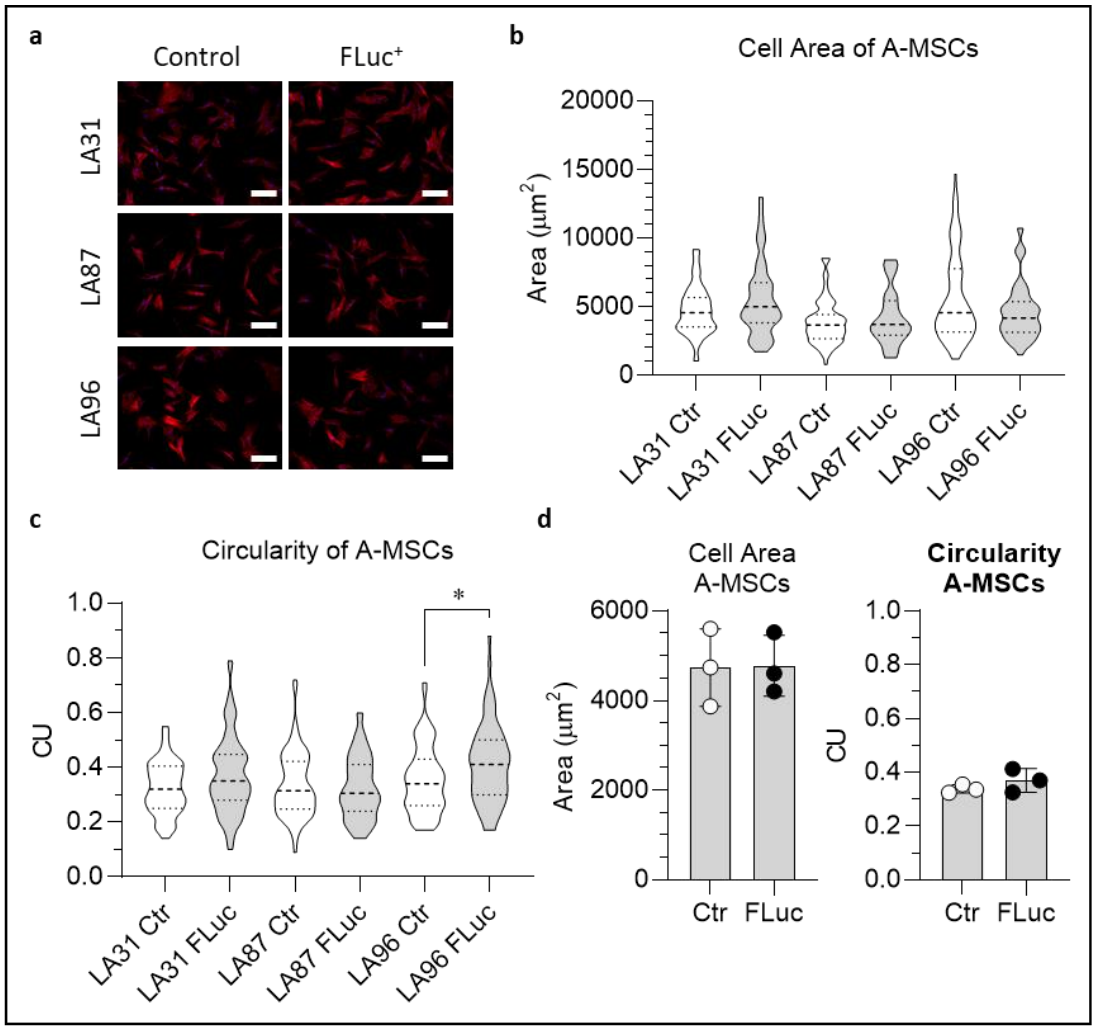

Figure 3.17| Morphological characterisation of transduced A-MSCs. (a) Fluorescence images of cells 16h after seeding stained with phalloidin (f-actin, red) and DAPI (nuclei, blue) acquired at 100x. Scale bar = 200µm. **(b-c)** Violin plot of the area **(b)** and the circularity **(c)** of the transduced and untransduced cell populations (at least 64 cells for each sample were analysed). The data were plotted into a grouped

graph and cleaned by the outliers using the automated GraphPad tool "remove outliers". A two-way ANOVA was performed on the cleaned data with a Dunn's multiple comparison post-hoc test; $p < 0.05$ **(d)** Average cell area and circularity of A-MSCs produced using the data from the 3 donor samples. FLuc = FLuc_ZsGreen cells. Abbreviations: CU = circular unit (1 = perfect circle, 0 = elongated polygon).

3.3.4.4 BLI characterisation in vitro

The total flux emitted by each donor sample was measured to evaluate the quality of the transduction and to identify any difference between the 3 cell types. Cells were plated at various densities from 156 to $2x10^4$ cells/well and subsequently imaged in the presence of the D-Luciferin substrate, at a final concentration of 5.12 mM. The quantification of the flux coming from the wells of each sample was used to build a linear regression curve (Figure 3.18), where the slope corresponds to the flux/cell. The output from the three UC-MSC donor samples was similar ($17.0x10^3$ p/s/cell, $18.7x10^3$ p/s/cell and $19.5x10^3$ p/s/cell for 727R, 733S and 735O, respectively, Figure 3.18a) as it was for the BM-MSCs ($18.6x10^3$ p/s/cell, $15.5x10^3$ p/s/cell and $18.7x10^3$ p/s/cell for BM04, BM21 and BM42, respectively, Figure 3.18b). The output from the A-MSCs revealed one sample displaying higher signal when compared to the other two ($20.8x10^3$ p/s/cell, $30.7x10^3$ p/s/cell and $22.3x10^3$ p/s/cell for LA31, LA87 and LA96, respectively, Figure 3.18c). These values have been averaged and plotted by cell type to evaluate the average flux/cell of the 3 different MSCs (Figure 3.18d). On average, UC and BM-MSCs displayed very similar signal outputs ($18.4x10^3 \pm 1.3x10^3$ p/s/cell and $17.6x10^3 \pm 1.8x10^3$ p/s/cell and $18.7x10^3$ p/s/cell, respectively), while A-MSCs resulted in a stronger signal ($24.6x10^3 \pm 5.3x10^3$ p/s/cell), although no statistically significant difference was observed between MSCs from different tissue sources.

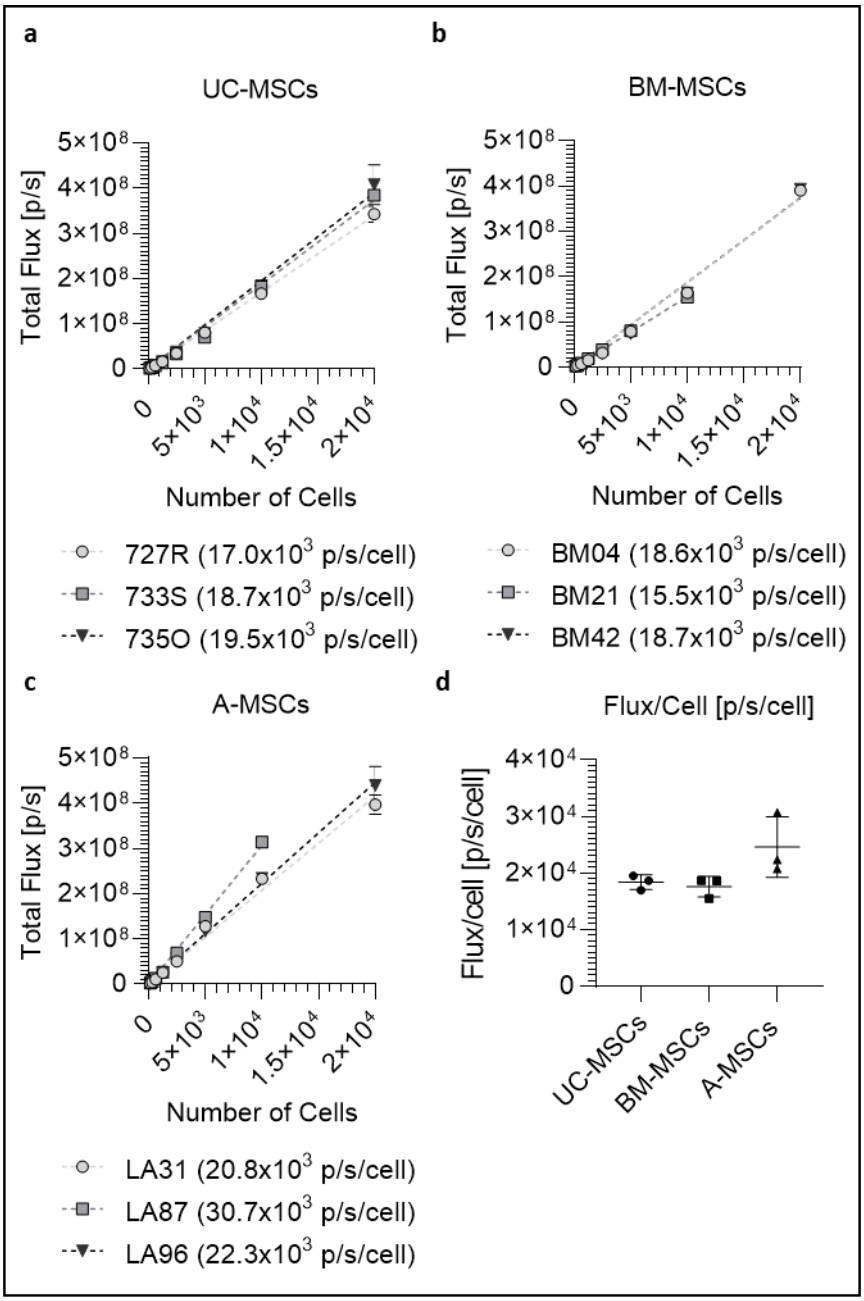

Figure 3.18| Light output as a function of cell density. FLuc_ZsGreen expressing MSCs were seeded at a density of 156 to 2x10^4 cells/well and treated with saturating concentration of D-Luciferin (5.12 mM D-Luciferin. **(a-c)** Light output (flux) as a function of cell concentration, with linear regression curves of UC **(a)**, BM **(b)** and A **(c)** MSCs. The slope of each curve represents the flux/cell and is shown in the legend of the respective graph. Data are displayed as mean ± SD from n = 3. Missing values are due to saturation of the signal (LA87) or unexpected dropping with 2x10^4 cells (BM21). **(d)** Average of the toral amount of photon/second emitted by each cell type following transduction. Data obtained by averaging the samples of each cell type. Data are displayed as mean ± SD from n = 3.

3.4 DISCUSSION

The aim of this chapter was to identify a transduction protocol suitable to infect umbilical cord, bone marrow and adipose MSCs to subsequently generate transduced populations suitable for investigating the biodistribution and the safety of these cells *in vivo*.

Before investigating the actual transduction, the MSCs were compared in terms of doubling time and expression of MSC markers to characterise the cells and identify any difference between the cell sources. The analysis of the proliferation and doubling time revealed some differences between the 3 cell types. While the 3 samples of A-MSCs displayed a very similar and comparable doubling time and the 3 samples of UC-MSCs displayed a small variability between 2 out of the 3 samples, the BM-MSCs showed the greatest variability. In detail, 2 samples resulted in a doubling time that was almost twice the doubling time of the third donor sample. The analysis of the average doubling time of the 3 cell sources also revealed that, while UC and A-MSCs show a comparable growth, the BM-MSCs are significantly slower than the other two sources of cells. The characterisation of doubling time can help to design the actual transduction process, as it is important to know how naïve cells behave and not to grow the cells over confluence. This has been reported to be associated with changes in the proteome of BM-MSCs when compared to cells grown without reaching 100% confluence [253]. In the same way, monitoring the expression of MSC markers is an important indicator of changes in the phenotype of the cells. Positivity to CD44, CD73, CD90 and CD105 and negativity to CD11b, CD19, CD34, CD45 and HLA-DR are widely recognised criteria to validate MSCs. Whilst all the samples showed a positivity of at least 98.7% for all the positive markers, some variability was observed for the negative ones. In particular, A-MSCs showed some positivity to CD34 (18.4 ± 11.7%) and CD45 (10.8 ± 7.8%). This is not unexpected as some previous studies have reported CD34 positivity of A-MSCs [254, 255] and the negativity to that marker is now suggested to be an artifact of cell culture conditions [256]. An atypical expression of CD45 was also already observed in BM-MSCs [257], although the positivity to that marker disappeared by further expanding the cells *in vitro* [257]. Similarly, BM-MSCs showed a small variability in the positivity to HLA-DR (7.4 ± 6.5%). Again, this has also been previously reported by Marta Grau-Vorster [258] who analysed 130 batches of BM-MSCs produced for clinical applications, revealing variability among all those samples and concluding that the absence or presence of HLA-DR do not have an impact on the overall properties of the cells [258]. All these data gave some insight into the proliferation potential of each donor sample and the expression of surface markers before moving to the actual transduction optimisation. Lentiviral transduction can be used to generate stable cell lines

for the expression of a specific gene of interest [259]. However, the transduction with the LV alone is associated with a low transduction efficiency as show in the literature [246, 260] and in this chapter. There are reports showing that several polycations, like Pb [244, 245], Ps [249, 260] and DEAE-dextran [243], and the coupling of those with a spinoculation step [250-252], can be successfully applied to increase the transduction efficiency of different cells. Here a transduction protocol suitable to generating stable Firefly Luciferase expressing MSCs from umbilical cord, bone marrow and adipose tissue was identified.

To optimise the transduction protocol, the impact of different polycations (Pb, Ps and DEAE-dextran) on transduction efficiency and on viability was tested alone or in combination with a spinoculation step. The transduction efficiency in the presence of Pb (8 μg/mL) was high for all the MSCs, with more than 90% of UC and BM cells transduces in both static and spinoculation conditions and with around 50% of adipose cells transduced in static condition. However, viability of cells incubated with the Pb in static condition was significantly reduced in comparison to control cells. This effect was observed not only on the cells incubated with the lentiviral particles (32%, 72% and 74% for UC, BM and A-MSCs respectively), but also on the cells incubated just with the Pb overnight (56%, 69% and 78% for UC, BM and A-MSCs respectively). These results are in line with previous studies [246-248, 260] that reported an association between the presence of polybrene and a reduction in the viability of different cell types. In particular, Lin et al reported, already in 2011, a significant reduction in viability of human bone marrow MSCs with a polybrene concentration of 4 μg/mL, which is half of what was used here [247].

Although it was possible to reduce the negative effect of the Pb on the viability of the BM and A-MSCs following the introduction of the spinoculation protocol, which reduced the exposure to the lentiviral particles to only 2 hours, the impact on UC-MSCs was still substantial. Furthermore, the number of A-MSCs transduced with Pb following the introduction of the spinoculation step dropped from 48.6% to only 19.2%. For these reasons, the Pb protocols were not considered suitable for the transduction of UC, BM and A-MSCs.

As a possible alternative protocol, the DEAE-dextran overnight incubation in static conditions was identified, as it was associated with a good transduction efficiency for all the cell types tested (74.4% for UC, 80.2% for BM and 50.0% for A-MSCs) without overtly impacting the viability of the cells (77% for UC, 116% for BM and 107% for A-MSCs). The superiority of the DEAE-dextran to Pb has been previously shown by Denning et al [243], but their work was focused on the 293FT and the HT-1080 cell lines and not primary MSCs.

A similar analysis where different transduction protocols were tested to optimise the transduction of natural killer (NK) cells was carried out by Malarkannan S. et al [261]. They investigated the transduction efficiency and the impact on cell viability following the lentiviral transduction of primary human and murine NK cells in presence of either Pb (8 μg/mL), Ps (8 μg/mL) or DEAE-dextran (8 μg/mL) [261]. In this study, they combined a 1h spinoculation step at 1000g and an overnight incubation at 37°C [261]. Interestingly they obtained a strong increase in the transduction efficiency by incubating the cells with the DEAE-dextran and almost no transduction with the two other polycations [261].

The data from Denning et al [243] and Malarkannan and co-workers [261] suggest that the type of cells and the lentiviral particle itself might influence the outcome of the transduction and one single protocol might not be suitable for all the cell types and LV constructs. Because of this, the selected protocol was investigated for its ability to transduce the MSCs with four different lentiviruses, characterised by differences in the backbone and in the size of the insert. Regardless of the lentiviral construct used, the DEAE-dextran protocol enabled an increase in the transduction efficiency, when compared to the cells incubated with the LVs alone. However, a difference was identified in the transduction efficiency of the different cells that was directly related to the type of lentiviral vector use. This is something expected, as several factors can influence the transduction efficiency with a specific lentiviral vector. It has been previously shown that efficiency of transduction decreases with an increase in the size of the construct [262]. The results obtained in the present study are in line with those findings, as the longest plasmid, the pCDH-EF1α-Luc2-P2A-tdTomato (10289 bp) was associated with a much lower transduction efficiency than the 3 other plasmids tested, which displayed similar length (7686 bp, 7680 bp and 7413 bp for the pHIV-eGFP, the pHIV-dTomato and the pLV-mCherry, respectively). Furthermore, it was also previously reported that the sequence of the plasmid can affect the lentiviral infection [263] and this can further explain what was observed while applying the DEAE-dextran protocol with 4 different LVs.

Furthermore, the percentage of transduced cells for each lentiviral particle was significantly associated with the origin of the cells, confirming that the type of cell has also a role in the outcome of the transduction. As an example, the percentage of A-MSCs transduced with the pHIV-Luc2-ZsGreen was much lower than the percentage of transduced UC or BM-MSCs.

Finally, a critical aspect of this part of the study was the production of transduced FLuc expressing MSCs that can be used to track their biodistribution *in vivo*. $FLuc^{+}$ cells should be as similar as possible to the naïve, non-genetically modified MSCs in order to replicate their

biodistribution. This was investigated by assessing their proliferation, expression of MSC markers and morphology. A total of 9 donor samples (3 per cell type) were transduced using 6 µg/mL DEAE-dextran and a pHIV_Luc2_ZsGreen LV with an MOI of 5 and sorted following the transduction to obtain pure FLuc expressing populations. It was shown that all the transduced cells display similar properties to their untransduced counterparts in terms of doubling time, proliferation and expression of common MSC markers at the passage they will be used to perform the *in vivo* biodistribution analysis shown in subsequent chapters. Additionally, those 9 donor samples, when genetically modified, exhibited comparable emission of light in the presence of D-Luciferin, underlining the replicability of the methodology. The average flux/cell emitted ranged from 15,531 p/s/cell for one of the BM samples to 30,723 p/s/cell for one of the adipose samples. Such values are quite good, as it has been previously reported that transduction of mouse derived MSCs with the pHIV-Luc2-ZsGreen plasmid in the presence of polybrene resulted in 1508 p/s/cell [264], which is around 10 times lower than the values obtained here.

In summary an overnight incubation with 6 µg/mL DEAE-dextran and a LV with an MOI of 5 can be used to enhance the transduction of umbilical cord, bone marrow and adipose derived MSCs with several lentiviral particles. The characterisation of the transduced cells expressing Luc2_ZsGreen displayed no major effects of the transduction on the properties of the cells. Still, as mentioned previously, the efficiency of transduction is strongly correlated with the LV and with the cell type used. Because of this, it is suggested that several polycations should be tested when optimising a transduction process for a specific cell type.

3.5 APPENDIX TO CHAPTER 3 – SUPPLEMENTARY INFORMATION

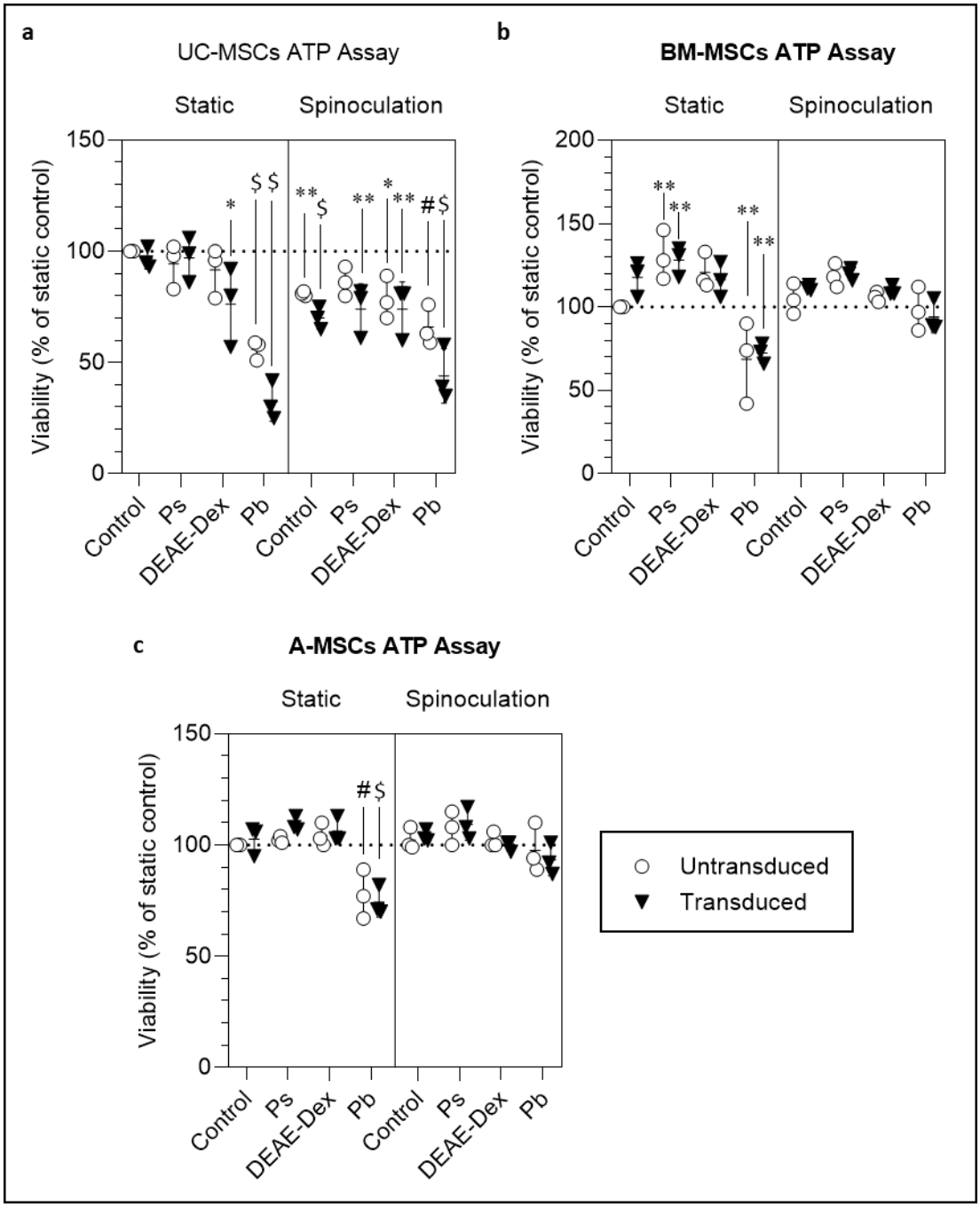

Supplementary Figure 3.1|ATP assay of transduced and untransduced MSCs. (a-c) Data from UC **(a)**, BM **(b)** and A-MSCs **(c)** organised in static and spinoculation protocols. Data are displayed as mean ± SD from n = 3. Statistical analysis performed: three-way ANOVA with Dunnett post-hoc comparison test against untransduced static control; * $p < 0.05$; ** $p < 0.01$; # $p < 0.0005$; $ $p < 0.0001$.

CHAPTER 4 OPTIMISATION OF TRANSDUCTION PROTOCOL FOR MESENCHYMAL STROMAL CELLS AND CHARACTERISATION OF TRANSDUCED UC-MSCS BOTH *IN VITRO* AND *IN VIVO*.

4.1 INTRODUCTION

As described in 1.5.1, bioluminescence imaging (BLI) is widely used in preclinical research studies with the aim to track the biodistribution of cells in living animals. Since photons with a wavelength shorter than 600 nm interact strongly with mammalian tissues, it is usually preferred to use a BLI system with a light output close to the near infrared spectrum (> 650 nm). The light emitted during the oxidation of D-Luciferin catalysed by firefly luciferase (FLuc) peaks at 560 nm, with a significant portion of emission longer than 600 nm [265]. Because of this, the FLuc/D-Luciferin system is still one of the top choices for deep-tissue BLI [214, 265]. Nevertheless, to improve the tissue penetration of the emitted light, many studies have focused on engineering the luciferase enzyme and/or the substrate(s) in order to shift the emission peak to the near infrared section of the spectrum and reduce the amount of light absorbed by tissues [204, 265-269]. Unfortunately, most of the mutated luciferases generated are not able to increase the total output of red light when compared to FLuc/D-Luciferin [266]. In the same way, many of the engineered substrates for FLuc associated with a red shift have not resulted in an increase of light emission when compared to D-Luciferin [265, 267-270]. This is because the shift toward a red wavelength is usually associated with a reduction in the light intensity [265], which means that any gains obtained by less tissue absorption are lost due to poorer emission

Recently, a group from Japan has developed a novel BLI system, composed of a D-Luciferin analogue, the Akalumine-HCl, and a mutated form of the FLuc, the AkaLuc [205, 223]. This BLI system has a light emission peak around 650 nm and has been claimed to provide a light output that is 52-fold stronger than that generated by FLuc when used *in vivo* [205]. Furthermore, they were able to detect light signal from the lungs of mice following intravenous injection of single cell, suggesting a very high sensitivity of the system [205]. All these characteristics make the AkaLuc/Akalumine-HCl (AkaBLI) system very promising for cell tracking. However, to date, this system has not been validated for applications in regenerative medicine.

In this chapter, the use of one of the transduction protocols identified as suitable for the transduction of UC-MSCs following the analysis performed in CHAPTER 3 is applied to generate two UC-MSC populations, each expressing a different luciferase: the FLuc or the AkaLuc. These two populations are then characterised both *in vitro* and *in vivo* to identify the best BLI system among the two to track the biodistribution of UC-MSCs *in vivo*.

4.2 MATERIALS AND METHODS

4.2.1 MSC transduction protocol

Passage 5 (P5) UC-MSCs were transduced with pHIV-Luc2-ZsGreen or pHIV-AkaLuc-ZsGreen in the presence of 20 µg/mL of Ps applying the spinoculation protocol. $3.42x10^5$ cells were seeded into 12 wells of two 6-well plates ($2.85x10^4$ cells per well to be consistent with $3x10^3$ cells/cm^2). Cells in one of the two 6-well plate were transduced with pHIV-Luc2-ZsGreen, while the cells in the other 6-well plate with pHIV-AkaLuc-ZsGreen. Following transduction, the cells were cultured up to confluence, detached and sorted via flow activated cell sorting (FACS) to obtain a homogenous population of cells (P6) expressing the transgene. To separate the transduced cells from the untransduced ones, the cells were harvested, resuspended in PBS with 0.8% FBS and kept in ice until sorted. The sorting was performed using a FACSAria and was based on the expression of the ZsGreen protein. Approximately $5.6x10^5$ FLuc and $6.5x10^5$ AkaLuc expressing cells were obtained following the sorting step. These cells were then expanded up to P7 and frozen down until further use.

4.2.2 MSC marker expression determined by flow cytometry

UC-MSCs were detached, centrifuged, and resuspended in PBS to remove any residual medium, as described in 2.3.1. To evaluate the common MSC markers, the cells were divided into different 1.5 mL vials, with a minimum of 10^5 cells per vial. The cells were then centrifuged for 10 minutes at 300 g and, following surfactant removal, each pellet was suspended with 98µL of PBS with 0.5% of bovine serum albumin (BSA) and 2 µL of anti-CD44 (APC, #130-113-893, Miltenyi Biotec), anti-CD45 (APC, #130-113-676, Miltenyi Biotec), anti-CD73 (APC, #130-097-945, Miltenyi Biotec), anti-CD90 (APC, #130-117-534, Miltenyi Biotec), anti-CD105 (APC, #130-099-125, Miltenyi Biotec), IgG1 mouse isotype (APC, #130-113-758, Miltenyi Biotec), or IgG2 mouse isotype (APC, #130-113-831, Miltenyi Biotec). Following a gentle shaking, the vials were incubated in the dark for 10 minutes at 4°C. An extra vial of cells was used as unstained blank. 500 µL of PBS with 0.5% BSA were added to each vial and they were centrifuged again for 10 minutes at 300 g. Finally, each pellet was

suspended into 400µL of PBS with 0.5% BSA, transferred into a properly labelled FACS tube and analysed with a FACSCalibur. A minimum of 10^4 events was analysed for each marker.

4.2.3 Reporter cell line characterisation

The AkaLuc and FLuc expressing cells have been compared and characterised with untransduced control cells in terms of doubling time and expression of common MSC markers (3.2.1.1). The two sorted populations and the untransduced cells were cultured from P7 to P12 to evaluate the doubling time. The cells were plated at $3x10^3$ cells/cm^2, and the doubling time calculated using equation described in 2.1.4. Furthermore, the level of ZsGreen at P7 and P12 was compared to evaluate the loss of the transduced genes over time.

In order to assess possible morphological changes of the cells due to the transduction and/or the sorting step, the cells were also characterised in terms of area, perimeter and circularity, in the same way performed in CHAPTER 3. Summarising, the cells were plated at $3x10^3$ cells/cm^2 into 8-wells Chamber Slide systems (Nunc Lab-Tek) with complete medium and incubated for 16 hours in the incubator. Then, the cells were washed and fixed with a PFA solution (4% w/v in PBS, pH 7) for 20 minutes at room temperature (RT). After fixation, the cells were washed with PBS and permeabilized with 0.1% (v/v) Triton X-100 in PBS for 15 minutes at RT. Then, the cells were incubated with 100 µL/well of Alexa Fluor 594 Phalloidin (ThermoFisher, #A12381) [165nM] in PBS with 1% (w/v) bovine serum albumin (BSA) for 1 hour at RT. Then, the cells were washed twice with PBS and counterstained with DAPI [143 nM]. Fluorescence images were taken using a Leica DM2500 microscope coupled to a DFC350 FX camera. ImageJ was used to draw and determine the area, the perimeter and the circularity of the cells using the phalloidin channels.

After the morphological and proliferation analysis, the IVIS Spectrum system was used to characterise the two BLI systems, both *in vitro* and *in vivo*. The acquired signal from the different analysis was always normalised to radiance (photons/second/centimeter^2/steradian) and analysed using the Region of Interest (ROI) tool of the IVIS software to obtain the total number of photons emitted in that specific area, also known as total flux (photons/s). The data were then plotted using GraphPad to generate the final graphs.

4.2.3.1 In vitro BLI characterisation

Spectra analysis

The spectra of the light emitted during the oxidation of D-Luciferin by the FLuc cells and during the oxidation of Akalumine-HCl either in the presence of AkaLuc cells or FLuc cells were analysed to check for any shifts in the peak of emitted light.

AkaLuc and FLuc cells were harvested and suspended at a concentration of $5x10^3$ cells into 50 µL inside 0.2 mL vials. The substrates were added to the vials immediately before the acquisition at a final concentration of 160 µM for Akalumine-HCl (Bio-Techne®, #6555) and 640 µM for D-Luciferin (Promega, E1605). Akalumine-HCl was used for both cell populations while D-Luciferin was only used for FLuc cells. To analyse the emission spectra, the IVIS was set -up to acquire the emitted signal every 20 nm from 500 nm to 840 nm.

AkaLuc and FLuc BLI systems kinetics – saturation

A fixed number of AkaLuc and FLuc cells was treated with a rising concentration of the two different substrates to find out the saturating concentrations. The experiment was repeated 3 times, with a technical triplicate each. $1.5x10^3$ cells/well were seeded into an optical bottom 96-well plate with black walls (ThermoFisher, #165305). Untransduced cells were used as negative controls. The cells were allowed to adhere for 3 hours. Then, each compound was tested in triplicate at a final concentration ranging from 2.5µM to 5.12mM, doubling the concentration each time. The final volume per well was 100 µL (50 µL of medium when seeded plus 50 µL of medium with the substrate, which was added just before measurement). The data were acquired with an IVIS Spectrum system immediately after the addition of the substrates using the open filter, to acquire all the signal coming from the cells, and the 660 nm, the 680 nm and the 700 nm filters applied in sequence, to analyse the signal close to peak generated by AkaLuc with Akalumine-HCl. All the possible combinations of substrate-enzyme were tested:

- FLuc cells with D-Luciferin
- FLuc cells with Akalumine-HCl
- AkaLuc cells with D-Luciferin
- AkaLuc cells with Akalumine-HCl

AkaLuc and FLuc BLI systems kinetics – emitted photons per cell

The saturating concentration of each substrate determined in the previous paragraph was used to assess the total flux emitted by each of the cell populations. The cells were plated at different densities, from 156 to $2x10^4$ cells/well. In this way it is possible to build a regression curve where the slope represents the amount of signal emitted per cell. The experiment was repeated 3 times, with a technical triplicate each time. The cells were plated into an optical bottom 96-well plate with black walls (ThermoFisher, #165305). Untransduced cells were used as negative control. The cells were allowed to adhere for 3 hours. Then, Akalumine-HCl and D-Luciferin were added at a final concentration of 160 µM and 5.12 mM, respectively. The final volume per well was 100 µL (50 µL of medium when seeded plus 50 µL of medium with the substrate, which was added just before measurement. The data were obtained with IVIS immediately after the addition of the substrates, acquiring the signal generated using the open filter and the 660 nm, 680 nm and the 700 nm filters applied in sequence. AkaLuc cells were tested only with Akalumine-HCl, while FLuc cells with both substrates. The combination of AkaLuc cells with D-Luciferin was not tested as D-Luciferin is not a substrate for AkaLuc, and this was also confirmed in the previous section.

4.2.3.2 In vivo BLI characterisation

7-9 week old female C57 Black-6 (C57BL/6J.Tyr^{c-2J}, from JAX) albino mice were used for *in vivo* characterisation of the two BLI systems.

In vivo kinetics

The aim of this experiment was to find the best data acquisition window of the BLI systems after the administration of the substrate. This is important because acquiring the data when the signal peaks, it improves the sensitivity of the acquisition.

AkaLuc and FLuc cells were harvested using trypsin/EDTA, centrifuged, suspended in ice-cold PBS at a concentration of $2.5x10^5$ cells/100 µL and kept on ice until being administered *in vivo*. 8-week old female C57BL/6 mice were anaesthetised with isoflurane and intravenously (IV) injected with 100 µL of cell suspension through the tail vein, followed by subcutaneous administration (SC) of the substrate (Table 4.1).

Table 4.1: Experimental set up to evaluate the kinetics of the two BLI systems.

Cells Injected IV	N° of cells	Substrate used	Substrates conc. (mM)	Volume of substrate used SC (µL/g of body weight)	Sites of SC administration	N° of animals
AkaLuc	$2.5x10^5$	Akalumine-HCl	30	Always 100 µL	1	3
FLuc	$2.5x10^5$	D-Luciferin	47	10	1	3
FLuc	$2.5x10^5$	D-Luciferin	144.5	20	2	3

Mice injected with FLuc cells and D-Luciferin 47 mM also received a second SC injection of PBS with a volume equal to the D-Luciferin. This was used to normalise the total volume injected in mice with both high (144.5 mM) and low (47 mM) dose of D-Luciferin. Immediately after the SC injection, the mice were imaged inside the IVIS, with the BLI signal acquired every minute for 30 minutes. The signal was acquired using an open filter, a binning of 8, a f-stop of 1, and 45 seconds exposure. The f number refers to the aperture of the hole that regulate the amount of light that hits the CCD camera (from 1, wide open, to 8) and the binning improves the signal-to-noise ratio (8 is a medium setting). At the end of the acquisition, the mice were allowed to recover and moved back to the cages. The imaging procedure (substrate administration and data acquisition) was repeated the day after the administration of the cells.

AkaLuc and FLuc signal intensity comparison following IV infusion of cells and SC administration of substrates

The aim of this set of experiments was to compare the FLuc and AkaLuc systems and identify the one most suitable for *in vivo* biodistribution experiments. The detachment and the infusion of the cells and the administration of the substrates were carried out as described in the previous section. The experimental details are summarised in Table 4.2. The administration of the substrate and the imaging were performed the day of the injection of the cells and after 1, 3 and 7 days. Furthermore, based on the results from the kinetics experiments, the substrates were administered 20 minutes before imaging the mice in the dorsal position inside the IVIS with the open filter, a binning of 8, a f-stop of 1, and using 15, 30, and 180 seconds exposure time in sequence.

Table 4.2: Experimental set up to evaluate the signal following SC administration of the substrates.

Cells Injected IV	N° of cells	Substrate used	Substrate conc. (mM)	Volume of substrate used SC (µL/g of body weight)	Sites of SC administration	N° of animals
AkaLuc	$2.5x10^5$	Akalumine-HCl	30	Always 100 µL	1	7
FLuc	$2.5x10^5$	D-Luciferin	47	10	1	3
FLuc	$2.5x10^5$	D-Luciferin	144.5	20	2	7

As described in the previous paragraph, mice injected with FLuc cells and the low dose of D-Luciferin also received a second SC injection of PBS with a volume equal to the D-Luciferin solution.

AkaLuc and FLuc signal intensity comparison following IV infusion of cells and IP administration of substrates

The aim of this set of experiments was to compare the FLuc and AkaLuc systems using the same conditions applied by Iwano S. et al [205], where following IV administration of reporter cells, the mice received the substrate intraperitoneally (IP) [205]. Here, the signal generated by AkaLuc and FLuc cells were also evaluated following IP administration of Akalumine-HCl and D-Luciferin. The detachment and administration IV of the cells was carried out as described in the previous sections. The experimental details are summarised in Table 4.3. Again, the administration of the substrate and the imaging were performed on the day of the injection of the cells and 1, 3 and 7 days post administration. Furthermore, on the cell administration day, a kinetic analysis was carried out to identify the signal peaks following IP administration. Immediately after the IP injection, the mice were imaged inside the IVIS, with the BLI signal acquired every minute for 30 minutes. The signal was acquired using an open filter, a binning of 8, a f-stop of 1, with an automatic exposure time set to not exceed the 15 seconds exposure. Based on the results from the administration day, on day 1, day 3 and day 7 the mice were imaged 3, 8, 12, 16, and 20 minutes post IP injection of the substrates using 15, 30, and 180 seconds exposure time in sequence. The mice were imaged in the dorsal position using the open filter. At the end of the sequence of acquisition, the mice were imaged in ventral position as well.

Table 4.3: Experimental set up to evaluate the signal following IP administration of the substrates.

Cells Injected IV	N° of cells	Substrate used	Substrate conc. (mM)	Volume of substrate used IP (µL/g of body weight)	Sites of IP administration	N° of animals
AkaLuc	$2.5x10^5$	Akalumine-HCl	30	Always 100 µL	1	4
FLuc	$2.5x10^5$	D-Luciferin	47	10	1	4
FLuc	$2.5x10^5$	D-Luciferin	144.5	20	1	4

In the previous two paragraphs, the mice injected with FLuc cells and with the low dose of D-Luciferin received also a second SC injection of PBS with a volume equal to the D-Luciferin solution. To keep the volumes consistent with those analysis, in this experiment, the low dose of D-Luciferin was mixed with an equal volume of PBS before being injected IP.

Evaluation of background signal produced following the administration of D-Luciferin and Akalumine-HCl

The aim of this set of experiments was to evaluate the presence or absence of a background signal following the administration of D-Luciferin and Akalumine-HCl alone. The experimental details are summarised in Table 4.4. The mice were imaged in ventral and dorsal position 20 and 24 minutes post administration of the substrates, respectively. Then the mice were culled, and the organs harvested and imaged again. The signal was acquired using an open filter, a binning of 8, a f-stop of 1, and 180 seconds exposure time.

Table 4.4: Experimental set up to evaluate the background signal of D-Luciferin and Akalumine-HCl.

Substrate used	Concentration (mM)	Volume administered (µL/g of body weight)	Sites of administration	N° of animals
Akalumine-HCl	30	Always 100 µL	IP (1 site)	3
D-Luciferin	144.5	20	IP (1 site)	3
D-Luciferin	144.5	20	SC (2 sites)	3

In subsequent sections, the 47 mM and the 144.5 mM doses of D-Luciferin will be referred as low and high doses, respectively. Akalumine-HCl 30 mM will simply be referred to as Akalumine-HCl.

4.2.4 Statistical analysis

All values in graphs are represented as mean ± standard deviation. The statistical analysis was performed using the GraphPad software. The type of statistical test and the number of replicates included in the analyses are indicated in the figure legends.

4.3 RESULTS

4.3.1 Characterisation of the transduced cells

To determine whether the transduction process affected the properties of the UC-MSCs, transduced cells were compared to untransduced ones in terms of the expression levels of MSC markers, doubling time and morphology. The lentiviral vector backbones used to produce the two transduced population are summarised in Figure 4.1a. The structure is the same, only the gene encoding for the Luciferase is different (encoding either for FLuc or for AkaLuc). An example of phase contrast images of confluent control, AkaLuc and FLuc cells and the respective green fluorescence images, showing the expression of the ZsGreen protein, is shown in Figure 4.1b. The morphology of the different cell populations looks very similar and the fluorescence images confirm the expression of the transgene by all cells in the field of view. A cumulative doubling analysis from P7 to P12 (Figure 4.1c), showed that the population doubling time for all three cell populations was almost identical up to P10. After this passage, all populations appear to display a slight decrease in doublings, which is more pronounced for the transduced cells (Figure 4.1c). Flow cytometry analysis of the level of expression of ZsGreen was performed at P7 and P12 to monitor the possible loss of expression of the reporter gene. At P12 the FLuc cells are still all positive for ZsGreen protein, while there was a little reduction in the level of expression of the reporter protein in P12 AkaLuc cells (Figure 4.1d). Furthermore, the flow cytometry analysis of transduced and untransduced cells for the expression of common mesenchymal markers shows a good overlapping of the curves (Figure 4.1e), revealing that the marker expression is not altered, with cells negative for CD45 and positive for the other markers (CD44, CD73. CD90 and CD105) at a similar level (Figure 4.1e).

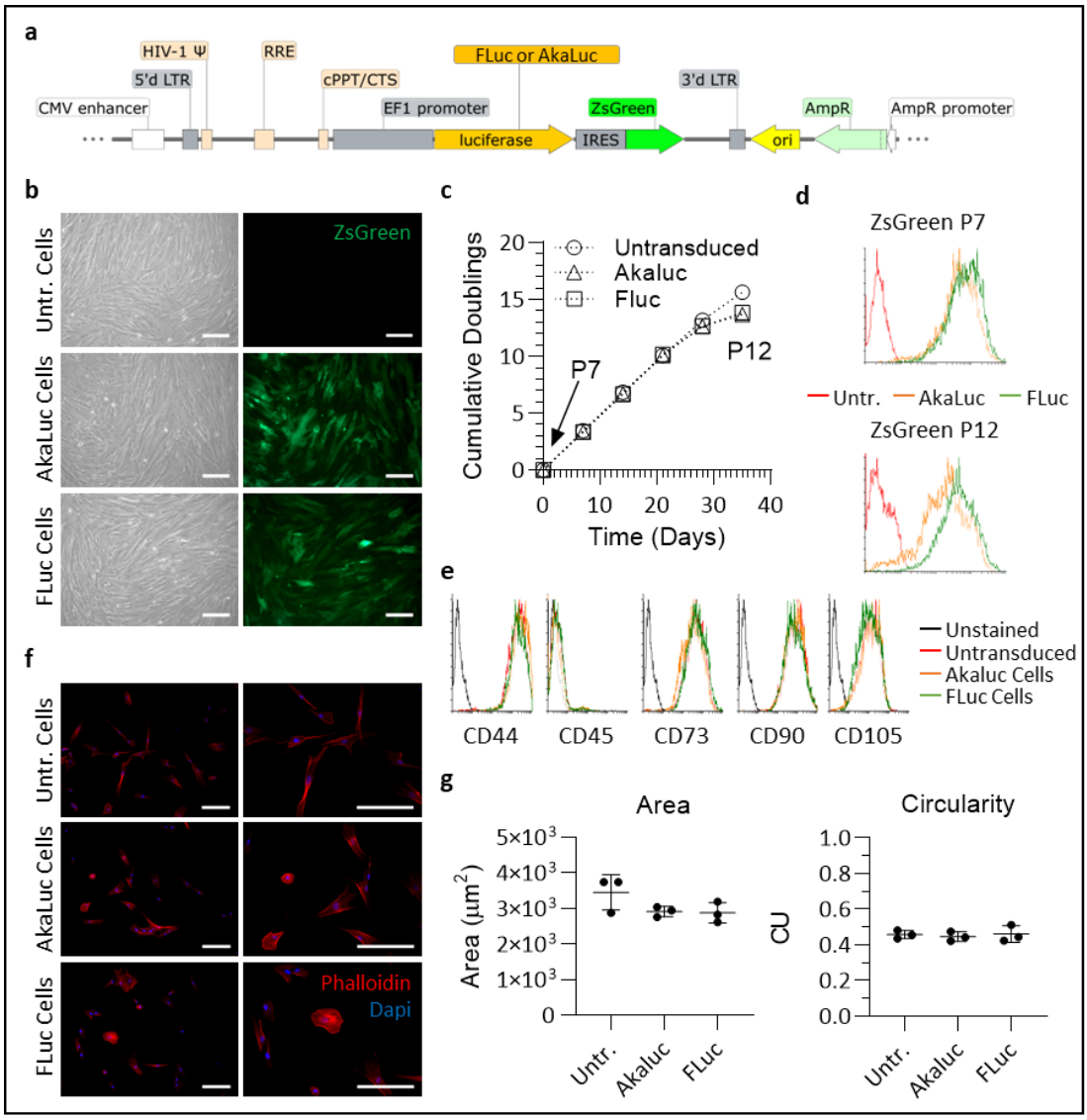

Figure 4.1| AkaLuc and FLuc transduced cells retain characteristics of untransduced UC-MSCs. **(a)** Schematic of the lentiviral vector used the generate FLuc and AkaLuc transduced cell population. The vector was the same, but the gene encoding for the luciferase. **(b)** Representative phase contrast and fluorescence images of untransduced, AkaLuc and FLuc expressing MSCs when fully confluent. ZsGreen expression can be observed in the green channel for the transduced cells. Scale bar = 200 µm. **(c)** Cumulative doubling measured from passages 7 to 12 shows that cells grow at the same rate up to p11. Cumulative doublings are calculated at each passage summing the total doublings performed from the first passage considered (here is p7) to that one. **(d)** ZsGreen expression was measured via flow cytometry at p7 and p12 and untransduced MSCs were used as negative control. The levels of ZsGreen remain largely unchanged, with a slight reduction for AkaLuc cells. The mean fluorescence intensity (MFI) of FLuc population shifted from 1023 AU at p7 to 708 AU at p12, while the MFI of AkaLuc population shifted from 746 AU at p7 to 388 AU at p12. **(e)** Flow cytometry analysis of markers that identify MSCs shows that all populations are positive for CD44, CD73, CD90 and CD105, and negative for CD45. **(f)** Fluorescence images of cells shortly after seeding stained with phalloidin (f-actin, red) and DAPI (nuclei, blue) acquired at 100x and 200x magnification. Scale bar = 200 µm. **(g)** Area and circularity, as measured based on the phalloidin staining of at least 54 cells per replicate, show that MSCs retain their morphology after transduction with either of the reporters. Data are displayed as

mean ± SD from n = 3. One-way ANOVA revealed no statistically significant difference between the three cell populations. Abbreviations: CU = circular unit (1 = perfect circle, 0 = elongated polygon).

To carry out the morphological analysis, AkaLuc, FLuc and untransduced UC-MSCs were stained with 594-phalloidin to get fluorescent images of the actin filaments. Those images were used to draw the shape of the cells on ImageJ to obtain the measures of area, perimeter (data not shown), and circularity of the different cell populations (Figure 4.1f and g; Dapi was used to counterstain the nuclei). An example of fluorescent images of untransduced, AkaLuc and FLuc cells with different magnifications (10x and 20x) is shown in Figure 4.1f. The morphology of the different cell populations looks very similar. To do the quantitative analysis, at least 54 cells were analysed for every condition, and this was repeated 3 times (n=3). Only isolated cells were measured, to avoid possible errors in detecting the perimeter of the cells. The quantitative analysis (Figure 4.1g) confirms that there is no statistically significant difference among area, perimeter, or circularity between all the cell populations.

4.3.2 BLI characterisation of AkaLuc and FLuc cells *in vitro*

The light emission spectra of the two transduced populations are displayed in Figure 4.2. AkaLuc cells displayed a peak at 650 nm following Akalumine-HCl oxidation. This enzyme is unable to catalyse the oxidation of D-Luciferin and no light is emitted with this substrate. Conversely, Firefly luciferase can oxidise both substrates. The oxidation of Akalumine-HCl generates a light peak at 670 nm and the oxidation of D-Luciferin, a peak at 600 nm (Figure 4.2). Emitted light from each source was normalised to the maximum value detected for it, which is 600 nm for FLuc/D-Luciferin, 680 nm for FLuc/Akalumine-HCl and 640 nm for AkaLuc/Akalumine-HCl. The grey area is the absorption of Haemoglobin (Hb) calculated by mediating the absorption of oxy-Hb and deoxy-Hb. Much of the light emitted by the oxidation of D-Luciferin catalysed by FLuc overlaps with the absorption of Hb, which can lead to a loss of sensitivity in *in vivo* imaging. On the other hand, almost all the light emitted by the AkaLuc/Akalumine-HCl system is far from the absorption wavelengths of Haemoglobin (Figure 4.2).

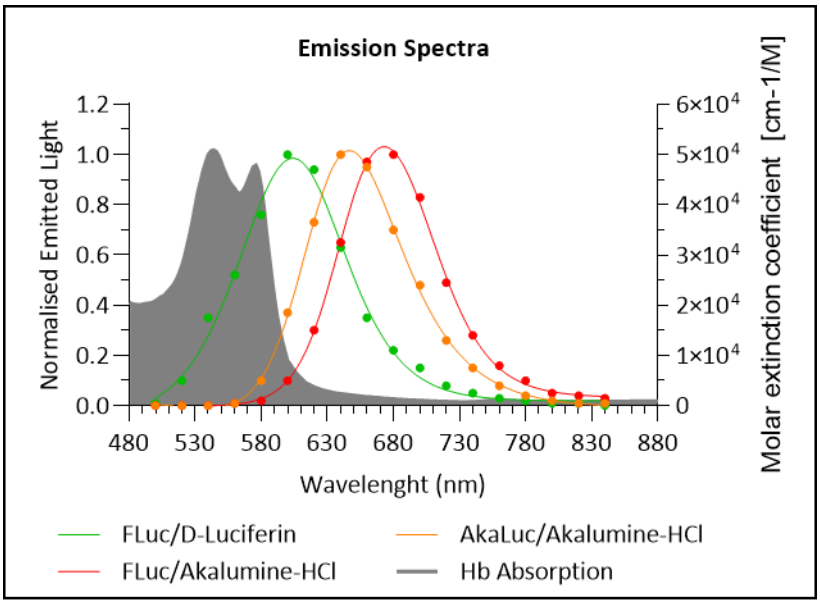

Figure 4.2| Emission spectra of AkaLuc and FLuc systems with Akalumine-HCl and D-Luciferin. Emission spectrum for each enzyme/substrate pair, as measured by acquiring the signal emitted from 500 to 840 nm at 20 nm steps. Data is normalised to the peak value of each condition. The AkaLuc/Akalumine-HCl system displays a peak at 650 nm, whereas FLuc cells display a peak at 600 nm in the presence of D-Luciferin and at 670 nm in the presence of Akalumine-HCl. Haemoglobin (Hb) absorption curve (average of values of oxy-Hb and deoxy-Hb) is plotted in grey (unit of measure: molar extinction coefficient as shown on the right axis).

In order to evaluate the saturating properties of the two BLI systems, the two cell populations were plated at a density of $1.5x10^3$ cells/well and treated with increasing concentrations (from 2.5 µM to 5.12mM) of Akalumine-HCl and D-Luciferin. The two BLI systems revealed different substrate saturation properties (Figure 4.3). Representative BLI images of AkaLuc and FLuc cells incubated with Akalumine-HCl are displayed in Figure 4.3a. As expected, AkaLuc cells incubated with D-Luciferin resulted in signal not distinguishable from the background. Both AkaLuc and FLuc cells in presence of Akalumine-HCl display a peak in signal at very low substrate concentrations, while FLuc cells incubated with D-Luciferin display a slow increase in the signal up to the maximal concentration used. Furthermore, at low concentrations (up to 320 µM), the signal generated by AkaLuc cells with Akalumine-HCl seems to be higher than FLuc cells with either of substrates. However, at higher concentration of the substrates, FLuc cells in presence of D-Luciferin results in a signal intensity stronger than AkaLuc cells with Akalumine-HCl (Figure 4.3a). These results were confirmed by a quantitative analysis of the signal (Figure 4.3b and c). Both FLuc cells and AkaLuc cells get saturated and plateau at a relatively low dose of Akalumine-HCl of approximately 20 µM (Figure 4.3c). At this concentration, the light emitted by AkaLuc cells was 11.8 and 6 times greater than the signal coming from FLuc cells with D-Luciferin or

Akalumine-HCl (Figure 4.3c), respectively. By increasing the dose of the substrates up to 5.12 mM (Figure 4.3b), however, the signal generated by FLuc cells in presence of D-Luciferin keeps rising and is not saturated even at 5.12mM, even if the slope of the curve starts to decrease. Interestingly, the signal from AkaLuc and FLuc cells in presence of Akalumine-HCl 5.12 mM starts to drop (Figure 4.3b). Importantly, the signal produced by FLuc cells with D-Luciferin 5.12mM is 4 times stronger than the signal generated by AkaLuc cells saturated with Akalumine-HCl (Figure 4.3b).

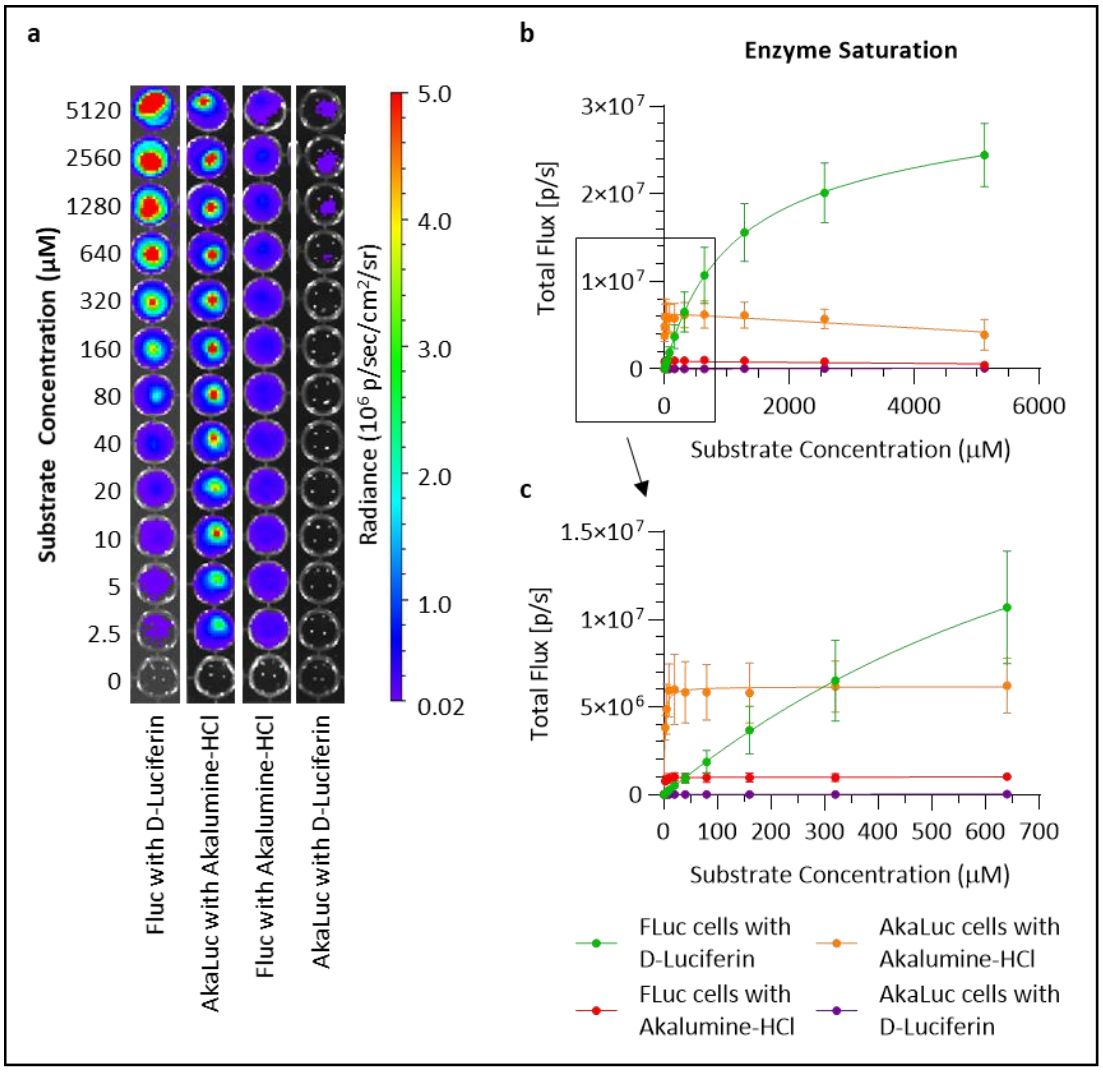

Figure 4.3| The AkaLuc and FLuc reporters saturate at different substrate concentrations in vitro. AkaLuc and FLuc expressing MSCs were seeded at a density of $1.5x10^3$ cells/well and treated with rising concentrations of Akalumine-HCl or D-Luciferin (2.5 µM to 5.12 mM). **(a)** Representative BLI images of a well plate immediately after the substrate addition to the cells. **(b-c)** Light output (flux) as a function of substrate concentration, where (b) shows the signal obtained from 2.5 µM to 5.12 mM and **(c)** from 2.5 µM to 640 µM. Data are displayed as mean ± SD from n = 3. The data were acquired using an open emission filter, a 13.3 field of view (FOV), a f-stop of 1, a binning of 8 and 10 seconds of exposure.

To further compare the *in vitro* behaviour of the signal emitted by the two BLI systems, the saturation curves were also analysed applying the 660 nm (19.57 nm bandwidth), the 680 nm (19.42 bandwidth) and the 700 nm (20.08 bandwidth) filters (Figure 4.4). These wavelengths are outside the Hb absorption spectra (see Figure 4.2) and should give a preliminary idea on the behaviour of the signal generated by the two BLI systems *in vivo*. The signal generated by the two systems was greatest at 660 mm and FLuc is associated with a better performance, where a flux of up to $1.37x10^6$ p/s was obtained with D-Luciferin 5.12 mM, whereas the maximum AkaLuc flux was of $1.08x10^6$ p/s with Akalumine-HCl 640 µM (Figure 4.4a). At longer wavelengths the signal is reduced for all systems (Figure 4.4b/c) and at 700 nm the signal generated by AkaLuc becomes higher than the signal generated by FLuc (Figure 4.4), with a peak of $5.9x10^5$ at 640 µM of Akalumine-HCl and a peak of $4.5x10^5$ at 5.12 mM of D-Luciferin, respectively. Nonetheless, by increasing the acquisition wavelength from 660 nm to 700 nm, the signal generated by the AkaLuc cells have dropped from $1.08x10^6$ p/s (Figure 4.4a) to $5.9x10^5$ (Figure 4.4c).

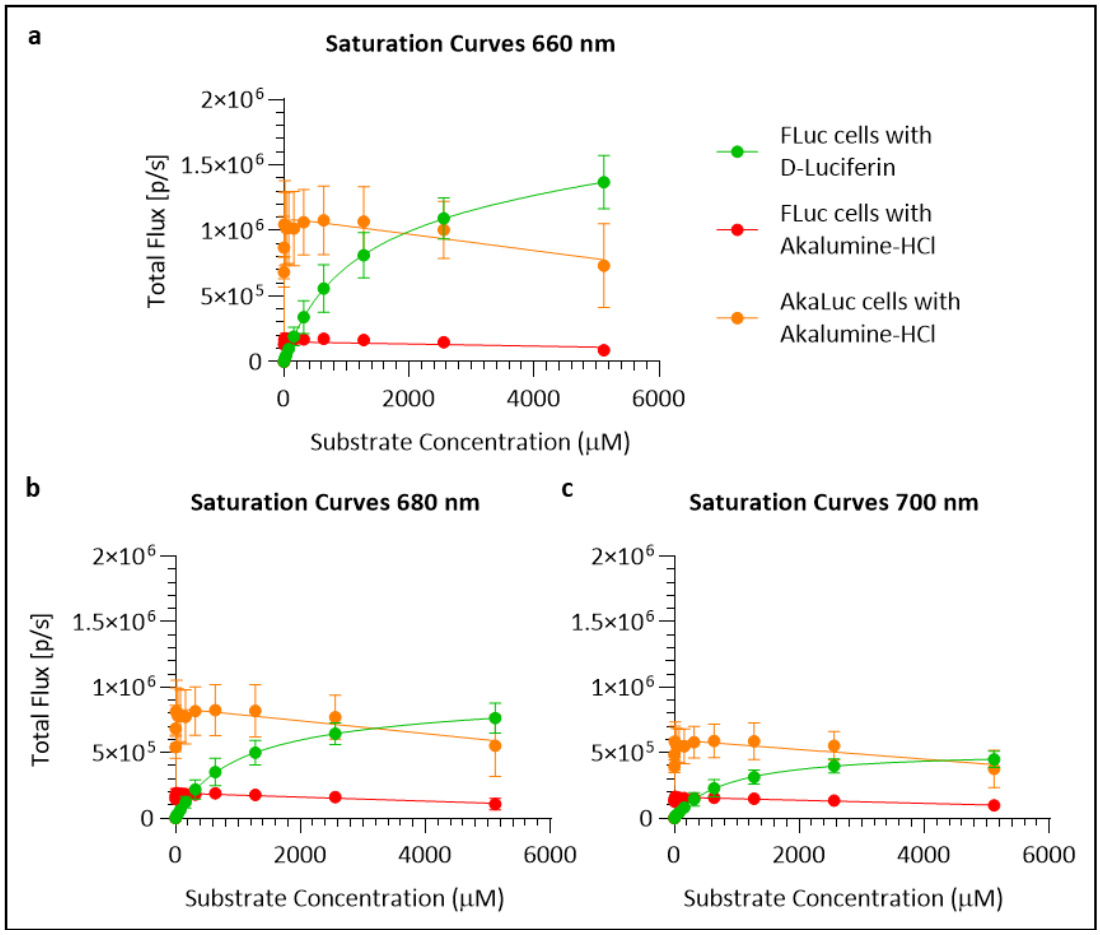

Figure 4.4| AkaLuc and FLuc systems in vitro saturation curves applying the 660, the 680 and the 700 nm filters. AkaLuc and FLuc cells seeded with a density of $1.5x10^3$ cells/well and treated with rising concentration of Akalumine-HCl and D-Luciferin, from 2.5 µM to 5.12mM using different acquisition

filters. AkaLuc cells treated with D-Luciferin did not show any signal above background and are not shown. The graphs display the light output (flux) as a function of substrate concentration using the 660 nm **(a)**, the 680 nm **(b)** and the 700 nm **(c)** filters of acquisition. Data are displayed as mean ± SD from n = 3. The signal was acquired using 10 seconds of exposure.

In order to identify the total flux emitted by the two cell populations, cells were plated at various densities from 156 to 2x10^4 cells/well and subsequently imaged (IVIS) in the presence of Akalumine-HCl and D-Luciferin at a final concentration of 160 µM and 5.12 mM, respectively. To compare the two reporter systems, the light output of the cells was measured with an open filter and with the 660 nm filter (19.57 nm bandwidth), because this includes the emission peak of the AkaLuc-Akalumine-HCl system (650 nm), which is outside the absorption of Hb and should give a preliminary idea of the results *in vivo*. Representative BLI images of AkaLuc cells incubated with Akalumine-HCl 160 µM and FLuc cells incubated with Akalumine-HCl 160 µM and D-Luciferin 5.12 mM are displayed in Figure 4.5a. The quantification of the flux in each well (Figure 4.5b) was used to build a linear regression curve, whose slope indicates the flux/cell. The output of AkaLuc cells (1346 p/s/cell) was nearly 6-fold higher than FLuc cells with Akalumine-HCl (218.5 p/s/cell), but only slightly stronger than FLuc cells with D-Luciferin (1139 p/s/cell, Figure 4.5b).

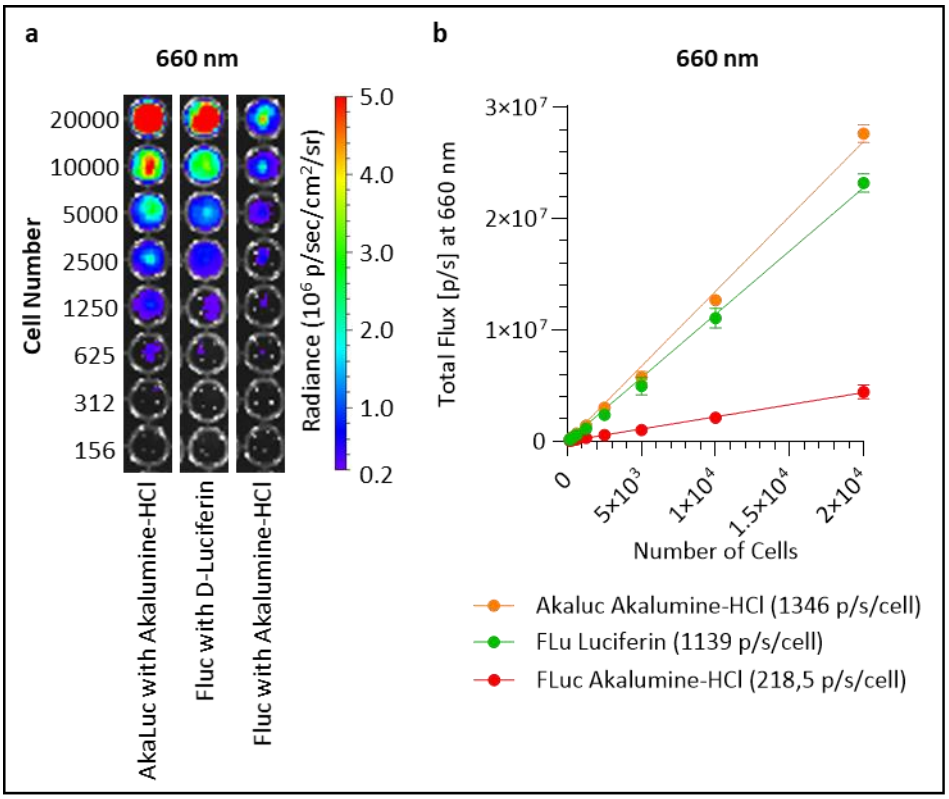

Figure 4.5| Light output as a function of cell density for the AkaLuc and FLuc reporter systems. AkaLuc and FLuc expressing MSCs were seeded at density of 156 to 2x10^4 cells/well and treated with saturating concentration of the substrates (160 µM Akalumine-HCl or 5.12 mM D-Luciferin). AkaLuc

expressing cells were treated with Akalumine-HCl only, whereas FLuc expressing cells were treated with AkaLuc-HCl or D-Luciferin. The signal was acquired using a 660 nm filter, which is close to the emission peak of the AkaLuc system and outside the Hb absorption spectrum. **(a)** Representative BLI images of a well plate immediately after the substrate addition. **(b)** Light output (flux) as a function of cell concentration, with linear regression curves. The slope of each curve represents the flux/cell and is shown in the legend of the graph. Data are displayed as mean ± SD from n = 3. Acquisition parameters: 13.3 cm FOV, f-stop of 1, binning of 8 and 10 seconds of exposure.

4.3.3 BLI characterisation of AkaLuc and FLuc cells *in vivo*

4.3.3.1 In vivo kinetics following SC administration of Akalumine-HCl and D-Luciferin

Mice administered intravenously with cells expressing either of the reporters were imaged every minute for 30 minutes after the subcutaneous injection of the substrates to measure the kinetics of signal generation *in vivo* and to identify the best time window for data acquisition. The analysis was also repeated 24 h post cell administration (Figure 4.6). In both systems and in both measurement days the signal reaches a maximum approximately 18 minutes after the administration of the substrate (Figure 4.6, b and d). Then, the signal coming from FLuc cells stays stable for about 7 minutes and then it starts to decrease. On the contrary, the light output from AkaLuc cells remains stable for a longer period after reaching its maximum (Figure 4.6).

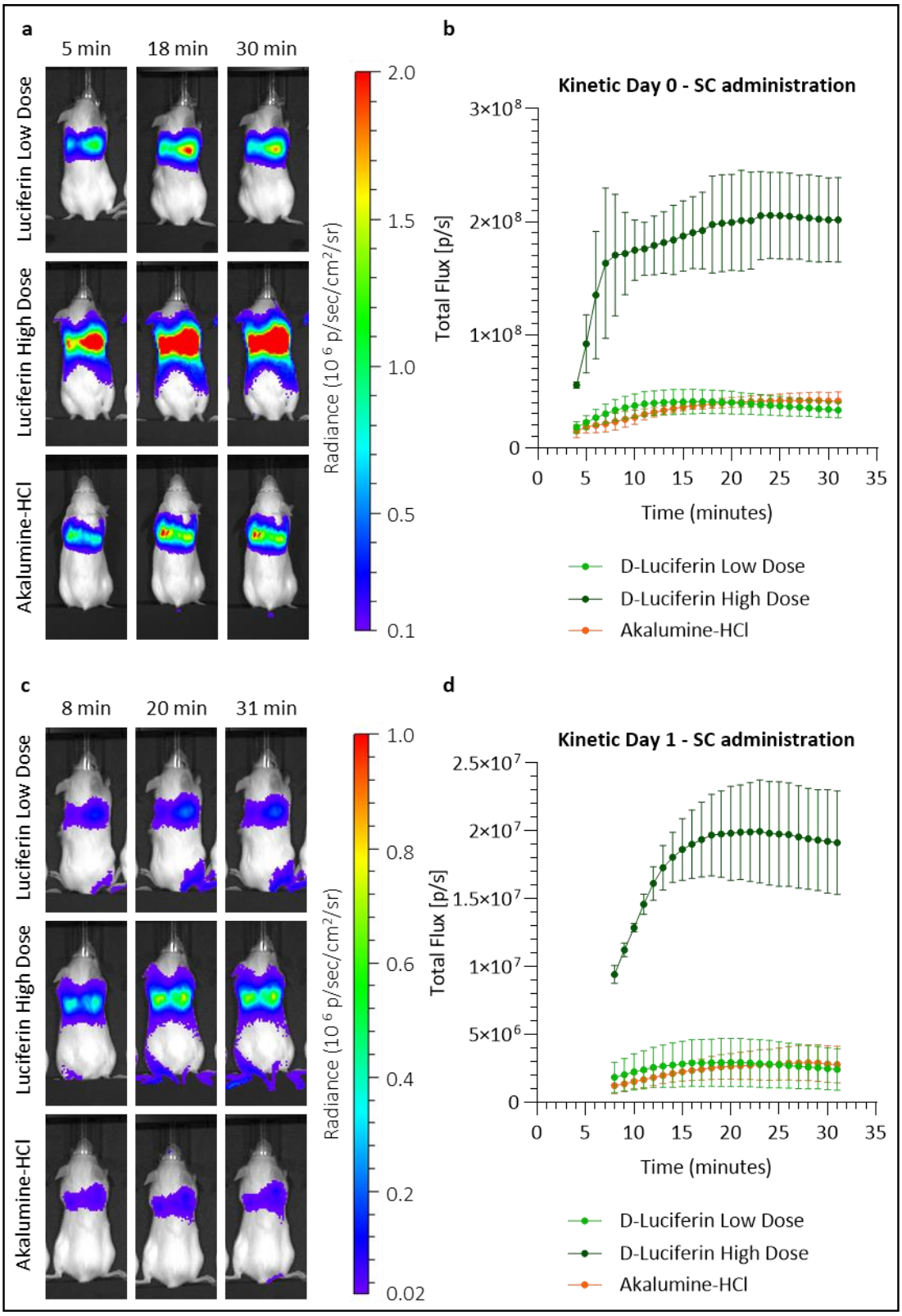

Figure 4.6| FLuc and AkaLuc BLI system kinetics in vivo following SC administration of D-Luciferin and Akalumine-HCl. MSCs ($2.5x10^5$) expressing either AkaLuc or FLuc were administered via the tail vein. The mice then received the substrates subcutaneously, under the same anaesthesia session, after which they were imaged every minute for 30 minutes (kinetic analysis). This kinetics analysis was repeated the day after the administration of the cells, repeating the injection of the substrates. Low dose D-Luciferin = 0.47 mmol/kg; High dose D-Luciferin = 2.89 mmol/kg; Akalumine-HCl = 100 µL of 30

mM solution. **(a)** Representative BLI images of the mice 5, 18 and 30 minutes post SC administration of the substrates on the day of cells injection (radiance scale from $1x10^5$ to $2x10^6$ p/s/cm2/sr). **(b)** Light output (flux) as a function of time, from minute 4 to minute 31. Data are displayed as mean ± SD from n = 3. **(c)** Representative BLI images of the mice 8, 20, and 31 minutes post SC substrate administration the day after cells injection (radiance scale from $2x10^4$ to $1x10^6$ p/s/cm^2/sr). **(d)** Light output (flux) as a function of time, from minute 8 to minute 31, the day after the administration of the cells. Data are displayed as mean ± SD from n = 3. Acquisition parameters: open emission filter, 22.8 cm FOV, f-stop of 1, binning of 8 and maximum exposure of 45 seconds for each point of the curves.

4.3.3.2 AkaLuc and FLuc system comparison in vivo following SC administration of substrates

Based on the results obtained following the kinetics analysis, BLI images of the mice at day 3 and day 7 were acquired 20 minutes post SC administration of the substrates. Bioluminescence imaging showed that IV delivery of UC-MSCs expressing FLuc or AkaLuc resulted in signals exclusively in the lungs (Figure 4.7a). The images were acquired the day of administration of the cells and 1, 3 and 7 days post-administration, imaging the mice 20 minutes after the subcutaneous (SC) administration of the substrates. By looking at the images in panel a, it seems that the cells have disappeared by day 3 and it is only with the quantification of the flux that it is possible to detect a weak signal at day 3 (Figure 4.7b and d). The average signal dropped at least 9-fold from day 0 to day 1 in all conditions (18-fold for Akalumine-HCl). Quantification of the data shows that mice injected with FLuc cells and the high dose of D-Luciferin displayed the highest signal output, with the average light emission being 4.5-fold higher than the signal obtained with FLuc cells with low dose of D-Luciferin, and 3.2-fold higher than the signal acquired with AkaLuc cells (Figure 4.7b). Furthermore, the only condition in which a signal on day 3 can be quantified is the high dose of D-Luciferin (Figure 4.7c), suggesting that some cells are still there but are not detectable using the Akalumine-HCl nor the low dose of D-Luciferin. The quantification (Figure 4.7b and d) revealed that the signal detected was statistically significantly higher than the signal measured in low dose D-Luciferin and Akalumine-HCl mice. These data suggest that the FLuc/D-Luciferin system is more sensitive than the AkaLuc/Akalumine-HCl system following SC administration of the substrates.

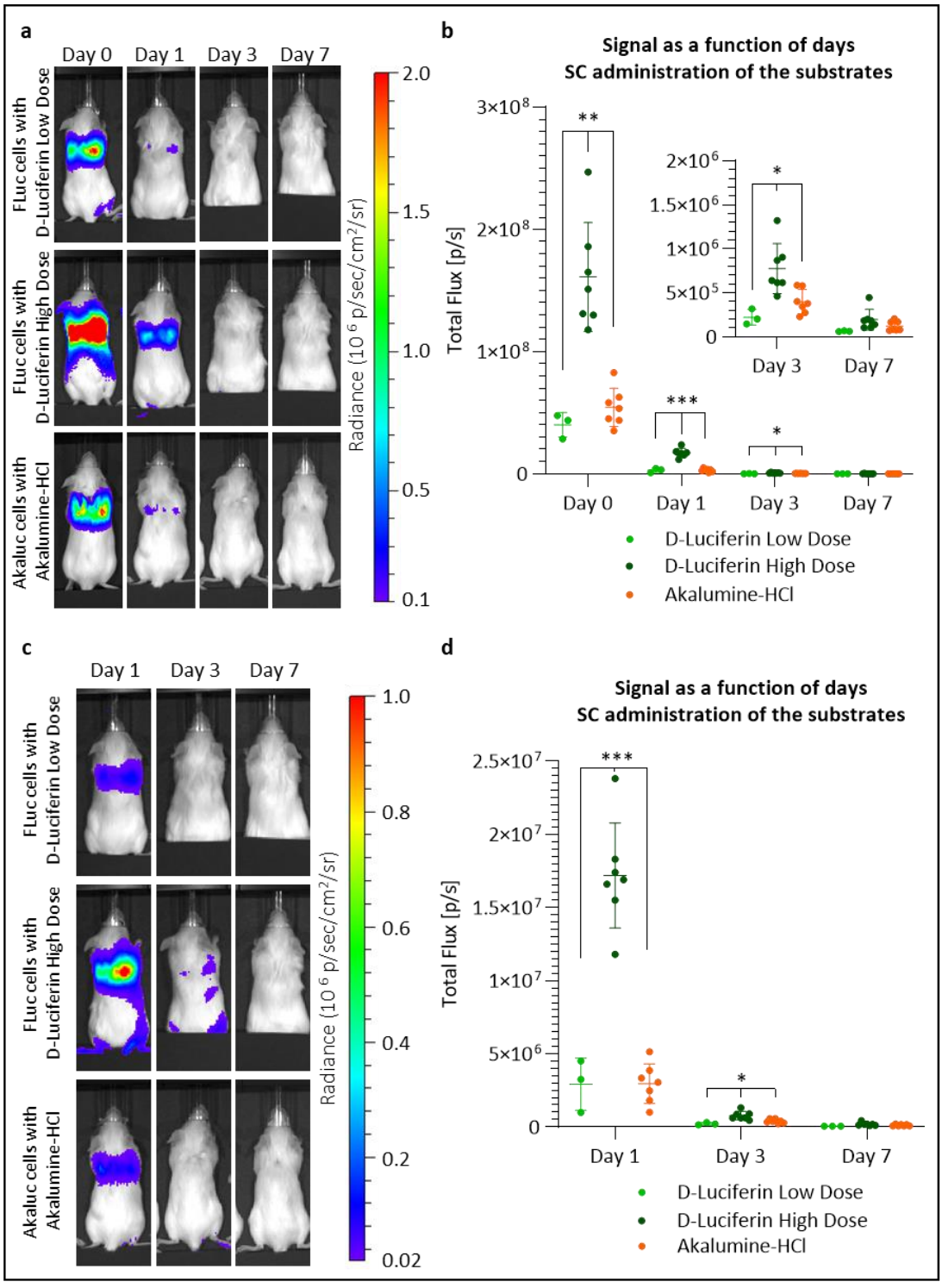

Figure 4.7| Evaluation of FLuc and AkaLuc cells overtime distribution in vivo following SC injection of D-Luciferin and Akalumine-HCl. UC-MSCs ($2.5x10^5$) expressing either the FLuc or the AkaLuc transgene were administered via the tail vein and the mice were imaged using D-Luciferin (low and high dose) or Akalumine-HCl as substrates. **(a)** Representative BLI images of the mice the day of cell injection (day 0), and 1, 3 and 7 days after the injection of the cells, acquired 20 minutes post SC substrate administration (radiance scale from $1x10^5$ to $2x10^6$ p/s/cm^2/sr). **(b)** Light output (flux) as a function of time (days). Data are displayed as mean ± SD from n = 3 (D-Luciferin low dose), n=7 (D-Luciferin high dose and Akalumine-HCl). Statistical analysis performed using a Two-way ANOVA with Tukey's multiple comparison post hoc test. * $p < 0.05$; ** $p < 0.01$; *** $p < 0.001$. **(c)**

Representative BLI images of the mice the from day 1 to day 7 using a lower radiance (from $0.2x10^5$ to $1x10^6$ p/s/cm^2/sr). **(d)** Magnification of the graph in panel a to show the quantification from day 1 to day 7. Data are displayed as mean ± SD from n = 3 (D-Luciferin low dose), n = 7 (D-Luciferin high dose and Akalumine-HCl). Statistical analysis performed using a Two-way Anova with Tukey's multiple comparison post hoc test. * $p < 0.05$; *** $p < 0.001$. Acquisition parameters: open emission filter, 22.8 cm FOV, f-stop of 1 and binning of 8. Exposure time: 45 s for day 0 and day 1, and 180 s for day 3 and day 7.

4.3.3.3 In vivo kinetics following IP administration of Akalumine-HCl and D-Luciferin

Mice administered IV with cells expressing either of the reporters were imaged every minute for 30 minutes after the intraperitoneal injection of the substrates to measure the kinetics of signal generation *in vivo* and to identify the best time window for data acquisition (Figure 4.8). The two BLI systems behaved differently. The FLuc system is similar to SC administration, with a rapid increase in the signal followed by a slightly constant increase up to minute 30 (Figure 4.8b). On the contrary, the AkaLuc system resulted in a peak immediately after the injection of the substrate (min 5, Figure 4.8b) followed by a rapid drop in the signal. Kinetic analysis on day 1, day 3 and day 7 (Figure 4.8c), with data acquisition at min 3, 8, 12, 16 and 20 shows that while FLuc system displayed the same kinetics, the AkaLuc system changed by day 3, with a low signal associated at minute 3 and an increase in flux over time.

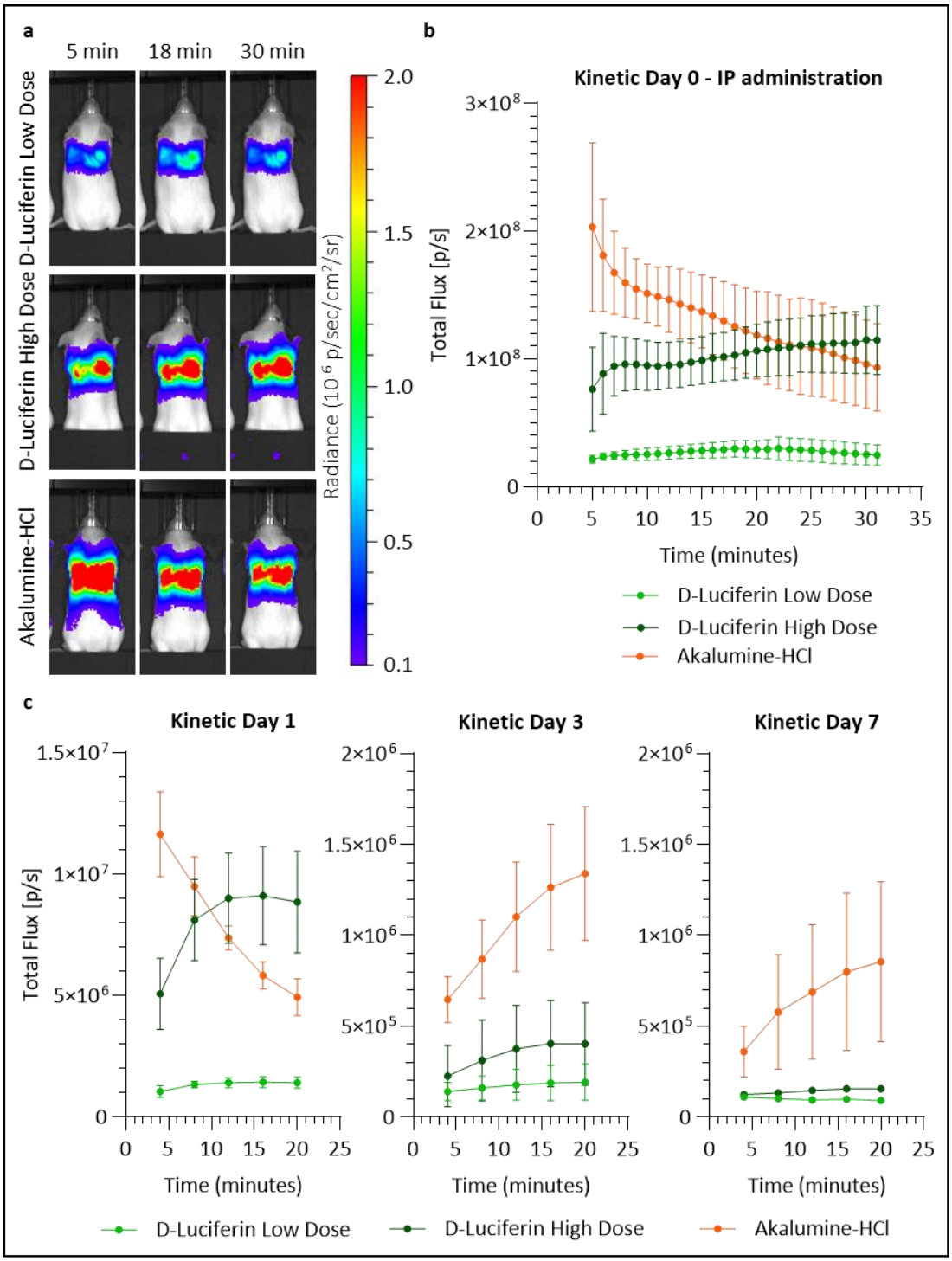

Figure 4.8| FLuc and AkaLuc BLI system kinetics in vivo following IP administration of D-Luciferin and Akalumine-HCl. UC-MSCs ($2.5x10^5$ cells) expressing either the AkaLuc or the FLuc transgene were administered via the tail vein and the mice were imaged every minute for 30 minutes using Akalumine-HCl or D-Luciferin (low and high doses) as substrates. **(a)** Representative BLI images of the mice 5, 18 and 30 minutes post IP substrate administration on the day of cells injection (radiance scale from $1x10^5$ to $2x10^6$ p/s/cm^2/sr). **(b)** Light output (flux) as a function of time, from minute 5 to minute 31, on the day of cell administration. Data are displayed as mean ± SD from n = 4. **(c)** Light output (flux) as a function of time following imaging of mice 3, 8, 12, 16, and 20 minutes post IP administration of the substrate with 180s exposure time 1, 3 and 7 days after the injection of the cells. Data are displayed

as mean ± SD from n = 4. Acquisition parameters: open emission filter, 22.8 cm FOV, f-stop of 1 and binning of 8. Exposure time: 45 s for day 0 and day 1, and 180 s for day 3 and day 7.

4.3.3.4 AkaLuc and FLuc system comparison in vivo following IP administration of substrates

Based on these results, the BLI analysis was performed using the peak signal of each condition. This means that for both low and high dose use D-Luciferin images acquired 20 minutes post IP injection of the substrate were used for all the time points (Figure 4.9a). For AkaLuc cells, images obtained at minute 5 were used for day 0 and minute 3 for days 1, 3 and 7 (Figure 4.9a). On the day of administration of the cells, BLI showed that IV delivery of UC-MSCs expressing FLuc or AkaLuc cells resulted in signals exclusively in the lungs (Figure 4.9a). AkaLuc cells displayed the strongest detectable signal, which was two- and seven-fold stronger than high and low dose of D-Luciferin, respectively (Figure 4.9b). From day 0 to day 1 the signal dropped at least 12-fold in all conditions and almost disappeared by day 3 (Figure 4.9b). Interestingly, the signal coming from the AkaLuc cells moved from the lungs to the liver. This can be clearly observed from the images of the mice in ventral position acquired 3 and 7 days post cell administration and 25 minutes after the administration of the substrates IP (Figure 4.9c).

It is also worth noting that the peak signal produced on the day of cell administration by AkaLuc cells following IP administration of Akalumine-HCl and the one produced by FLuc cells following SC administration of the high dose of D-Luciferin are comparable, with a total flux of $2.0x10^8 \pm 6.6x10^7$ and $1.6x10^8 \pm 4.4x10^7$ (unpaired t-test, $p = 0.23$).

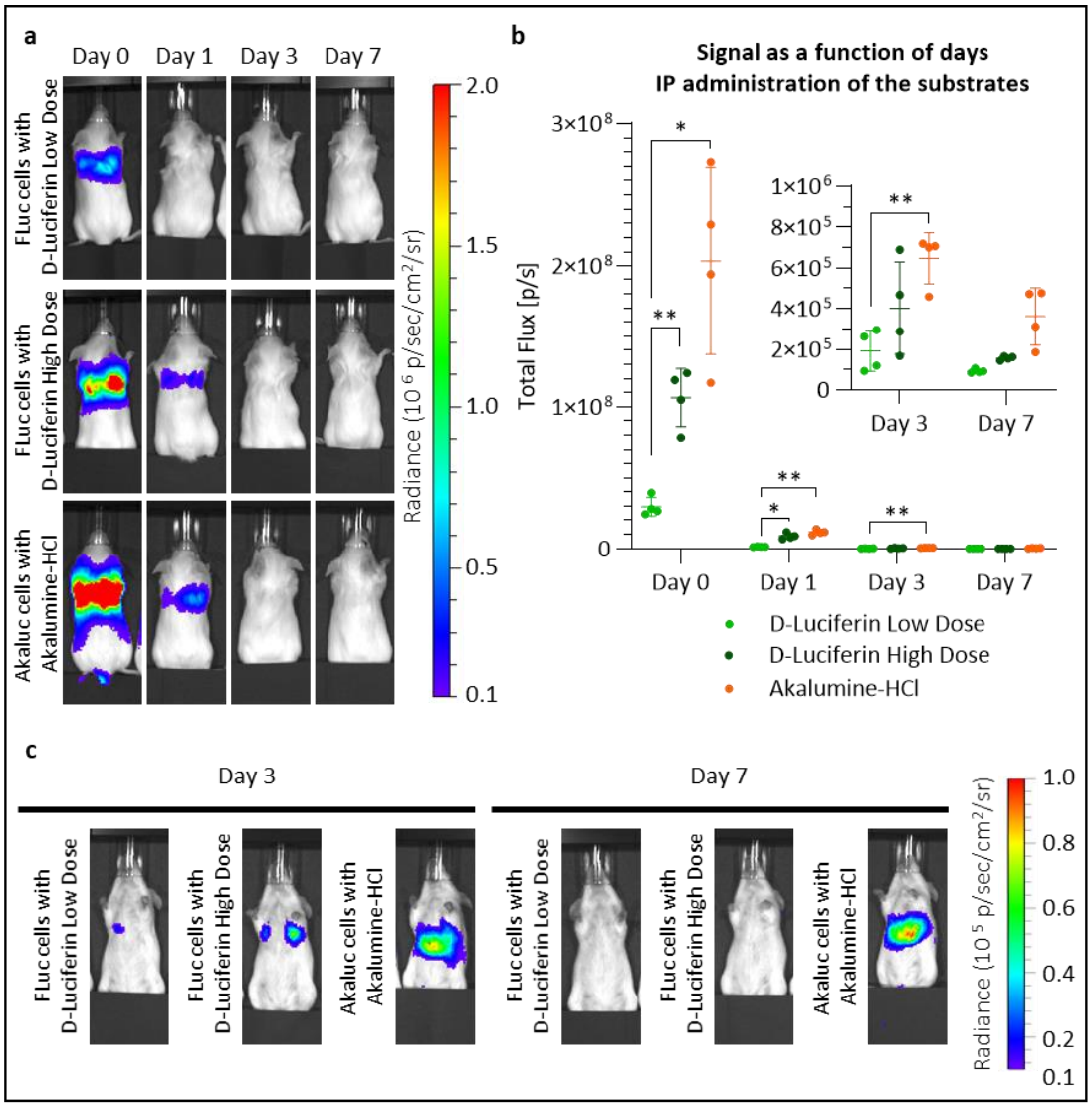

Figure 4.9| Evaluation of FLuc and AkaLuc cells overtime distribution in vivo following IP injection of D-Luciferin and Akalumine-HCl. UC-MSCs ($2.5x10^5$) expressing either the FLuc or the AkaLuc transgene were administered via the tail vein and the mice were imaged using D-Luciferin (low and high doses) or Akalumine-HCl as substrates. **(a)** Representative images of the mice acquired at peak signal of each condition (20 min for D-Luciferin and 5 min (for day 0) or 4 min (for day 1, 3, and 7) for Akalumine-HCl) following IP administration of the substrates (radiance scale from $2x10^4$ to $1x10^6$ p/s/cm^2/sr). **(b)** Light output (flux) as a function of time (days). Data are displayed as mean ± SD from n = 4. Statistical analysis performed using a Two-way ANOVA with Tukey's multiple comparison post hoc test. *p < 0.05; **p < 0.01. **(c)** Representative BLI images of the mice 3 and 7 days after cell injection, acquired 25 minutes post IP substrate administration (radiance scale from $1x10^4$ to $1x10^5$ p/s/cm^2/sr). Acquisition parameters open emission filter, 22.8 cm FOV, f-stop of 1 and a binning of 8. Exposure time: 45 s for day 0 and 180 s for day 1, 3, and 7.

4.3.3.5 AkaLuc and FLuc system unspecific signal in vivo

To investigate the origin of the signal detected 3 days post AkaLuc cells, which appeared to have moved from the lungs to liver during the time course of the experiment, naïve mice that

did not receive any cells were injected with the substrates IP (and also SC in the case of D-Luciferin high dose). Representative images of the mice both in ventral and dorsal position, approximately 20 minutes post IP substrate administration are shown in Figure 4.10a. Akalumine-HCl resulted in a background signal detectable in both positions (Figure 4.10a). The quantitative comparison revealed a statistically significant increase in the total flux emitted by Akalumine-HCl alone compared to the signal detected when injecting D-Luciferin (Figure 4.10b). The signal detected in dorsal position following IP administration of Akalumine-HCl was then compared to the signal obtained in dorsal position 3 days post administration of the AkaLuc cells (1.3.3.4), revealing no differences in flux between these conditions (Figure 4.10c).

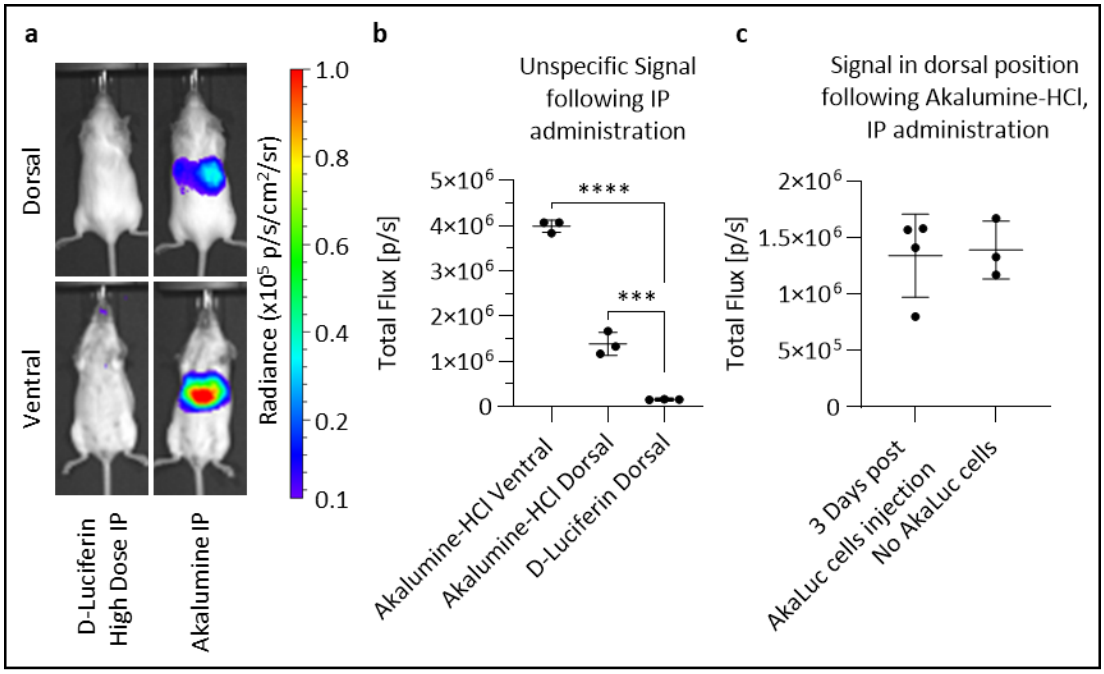

Figure 4.10| In the absence of cells Akalumine-HCl generates a non-specific signal from the liver region when administered IP. High-dose D-Luciferin or Akalumine-HCl was injected IP *in vivo*. The mice were then imaged in dorsal (23 min post substrate administration) and ventral (20 min post administration) positions, with no emission filter, a 22.8 FOV, a f-stop of 1, a binning of 8 and an exposure time of 180 s. **(a)** Representative images of the mice following substrate administration (radiance scale from 1×10^4 to 1×10^5 p/s/cm^2 /sr). **(b)** Quantification of the non-specific signal detected in the liver region of the mice injected with Akalumine-HCl IP, analysed both in ventral and dorsal position, compared with the signal coming from the liver region of mice injected with high dose D-Luciferin IP. Data are displayed as mean ± SD from n = 3. Statistical analysis performed using a ordinary one-way ANOVA with Tukey's multiple comparison post hoc test; **** $p < 0.0001$ and *** $p = 0.0002$. **(c)** Comparison of the signal detected in the liver of mice injected with Akalumine-HCl, three days post administration of 2.5×10^5 AkaLuc expressing cells IV (n = 4) vs. the non-specific luminescence from naive mice that received Akalumine-HCl alone (n = 3), 20 min. There is no statistically significant difference between the two groups (unpaired t-test). Data are displayed as mean ± SD.

4.3.4 Akalumine-HCl *in vivo* reabsorption in the site of injection

To identify which of the BLI system is most adequate for tracking the biodistribution of MSCs, it was also important to consider any possible side-effects. At the end of the 7 days experiment, the mice were culled following schedule 1 procedures (2.4), shaved and the skin was checked for any possible effects of the substrates in the sites of SC injection. Mice administered with Akalumine-HCl displayed scars in the sites of the SC injections with different grades of severity (Figure 4.11). The origin of the scars was not further investigated but could be due to a reaction of the mice to the substrate or to a reduced absorption of Akalumine-HCl, leading to its accumulation onsite. Figure 4.11a shows the pictures of two different mice displaying Akalumine-HCl injection sites with lesions of different severity. The upper panel displays a mouse with a recent injection site, associated with a hard swelling, whereas the lower panel shows a mouse where the scar seems partially recovered and less evident (Figure 4.11a). In contrast, there was no changes to the appearance of the skin of mice treated with D-Luciferin, even when using the high dose (Figure 4.11b). No abnormalities were identified in the peritoneum of mice that received Akalumine-HCl IP. Whether the accumulation of Akalumine-HCl could have a negative effect on the health of the mice is something that should be clarified. Nevertheless, this is another reason that encourages the use of D-Luciferin.

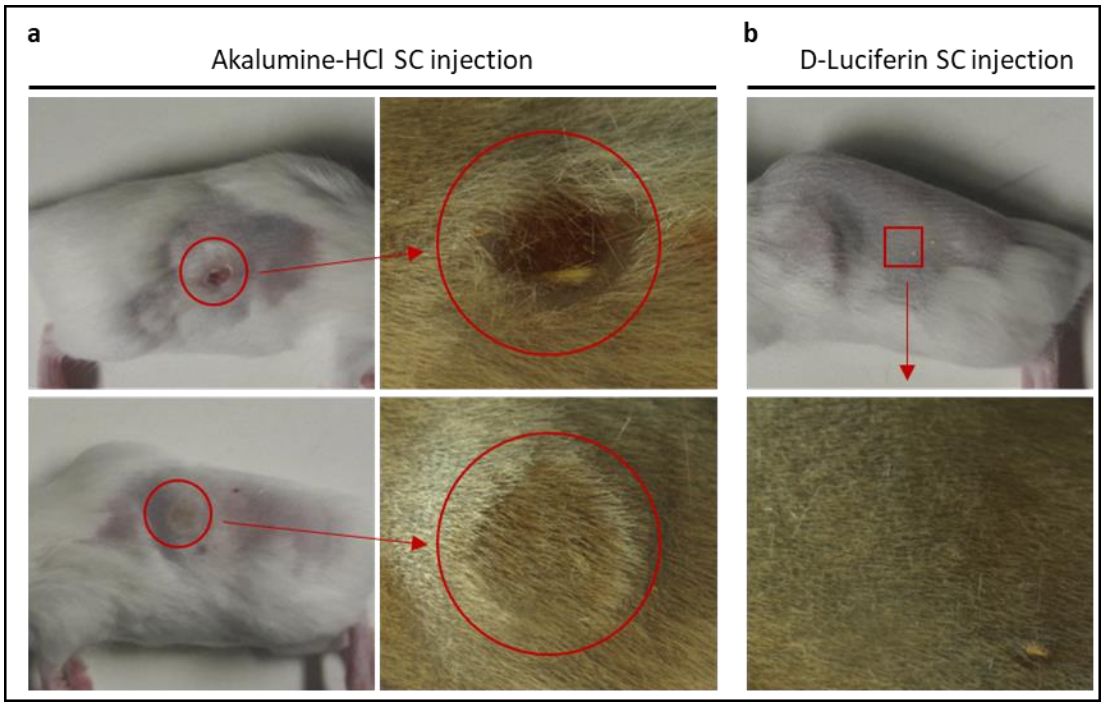

Figure 4.11| Macro analysis performed at day 10 of the substrate injection sites. (a) Images of mice that received SC administration of Akalumine-HCl 30 mM. The pictures on the left show the injection sites of two different mice, each displaying scars of different severities. High magnification images of

the scar, shown on the right, were taken using a stereomicroscope. **(b)** Representative image of a mouse that received SC injections of D-Luciferin high dose. No scars were observed.

4.4 DISCUSSION

The aim of this chapter was to compare two possible BLI systems, the FLuc and the AkaLuc, for the imaging of UC-MSCs *in vivo*.

The AkaLuc-Akalumine-HCl BLI system has a light emission peak around 650 nm, which is an advantage for tissue penetration of the signal. Moreover, Iwano and colleagues [205], recently reported that, after administration of Hela cells in mice, signal generated from an Akalumine-HCl/AkaLuc system yielded a 52-fold stronger signal than with D-Luciferin/FLuc [205]. These data were promising, so UC-MSC populations expressing either AkaLuc or FLuc were generated using the Ps spinoculation methods, one of the protocols identified as suitable for UC MSCs transduction in CHAPTER 3. Then, the two populations were compared to verify whether the Akalumine-HCl/AkaLuc system was superior also with this type of cells. Before doing that, the two population were analysed and compared to untransduced cells in terms of level of common MSC markers expression, proliferation, and morphology. The flow cytometry analysis of the common MSC markers (CD44, CD73, CD90 and CD105) showed similar levels of expression between the reporter UC-MSCs and untransduced cells. Moreover, the doubling time was not affected by the transduction, although at around P10 the engineered cells started to slow down faster than the control cells. Nevertheless, all experiments described in this thesis use cells up to P8. Furthermore, transduced and untransduced cells displayed similar morphological properties, revealing no statistically significant difference in terms of perimeter, area, and circularity. These data suggested that the two reporter cell populations were representative of the untransduced UC-MSCs and can be used for biodistribution analysis.

To compare and characterise the two luciferase systems, transduced cells expressing FLuc and AkaLuc were initially tested *in vitro*. As expected, the Akalumine-HCl/AkaLuc combination resulted in a light emission peak close to 650 nm, while the D-Luciferin/FLuc resulted in a peak close to 600 nm. The wavelengths of light in the visible spectrum are prone to absorption by overlying tissues, with red-shifted wavelengths performing better than those associated with green [271]. Because of this, signal generated by Akalumine-HCl/AkaLuc is expected to penetrate the tissues better than the one produced by D-Luciferin/FLuc.

The *in vitro* BLI analysis revealed that in the AkaLuc system, light emission saturates at relatively low substrate concentrations (40 µM Akalumine-HCl). FLuc, on the other hand, requires higher substrate concentrations to saturate the signal (5.12 mM D-Luciferin). This analysis gave some results that were consistent with the study of Kuchimaru and colleagues [223]. In detail, for substrate concentrations lower than 40 µM, the signal obtained with Akalumine-HCl is greater than that obtained with D-Luciferin, irrespective of the enzyme. Furthermore, the AkaLuc/Akalumine-HCl signal is greater than FLuc/D-Luciferin for substrate concentrations up to 320 µM. The quicker saturation of the AkaLuc and FLuc enzymes mediated by Akalumine-HCl is probably due to a higher affinity of the substrate for the enzymes, associated with a low Michaelis constant (Km) [223]. Although Kuchimaru already reported in his study [223] that the signal of FLuc/D-Luciferin was superior to FLuc/Akalumine-HCl using 250 µM substrates concentration, neither he nor Iwano [205] compared the signal generated by FLuc using a saturating concentration of D-Luciferin to AkaLuc or FLuc signal using saturating concentration of Akalumine-HCl. Here, by further elucidating the saturating properties of the two systems, we reported that the total signal generated by the FLuc/D-Luciferin system at saturation is much stronger than the one produced by AkaLuc cells. In fact, under saturating conditions, D-Luciferin/FLuc combination yielded a signal that was four-fold more intense than the one generated by Akalumine-HCl/AkaLuc. Furthermore, the light output of the cells at 660 nm, when using saturating concentrations of the substrates was similar, with 1346 photons/s/cell and 1139 photons/s/cell for AkaLuc and FLuc cells, respectively.

A critical aspect of this study, however, was determine whether the *in vitro* data is replicated *in vivo*. This is important because the light output is dependent on the bioavailability of the substrate in the model organism. The standard dose of D-Luciferin used for *in vivo* BLI is 0.47 mmol/kg body weight (equivalent to 150 mg/kg) [204, 272-274]. Stock solutions of this substrate are usually prepared in PBS at a concentration of 47 mM and for a typical 20 g mouse, this corresponds to an injection of 200 µL. However, it is not clear if this standard dose saturates FLuc *in vivo*. To test this hypothesis, the injected dose was increased to 2.89 mmol/kg body weight (~6-fold stronger than standard dose). This was achieved by preparing stock solutions of the substrate at its solubility limit (144.5 mM) and by increasing the injection volume to up to 20 mL/kg body weight, which is recognised as maximum when animal welfare is considered [275]. This is equivalent to 400 µL for a 20 g mouse. Akalumine-HCl was injected using the same dose that Iwano and colleagues infused in 7 weeks old C57/b6 albino mice [205]: 100 µL of Akalumine-HCl 30 mM. Following SC injection of the

substrates, both systems were able to show that MSCs were delivered to the lungs after IV administration. However, the signal intensity of cells expressing AkaLuc was not stronger than FLuc when standard substrate doses were used (100 µL of 30 mM Akalumine-HCl and 0.47 mmol/kg body weight). By increasing the D-Luciferin dose to 2.89 mmol/kg body weight, the light output obtained with the FLuc system increased as well, resulting in an average signal 3.2-fold stronger than AkaLuc. However, the signal dropped 10-fold from day 0 to day 1 in all conditions and almost disappeared by day 3. This result is consistent with cell death, and widely reported in the literature [99, 276]. Similarly, following IP administration of the substrates, both systems showed that MSCs were delivered to the lungs. However, this time, the signal intensity of cells expressing AkaLuc was stronger than FLuc with either the high or the low doses of D-Luciferin. Nonetheless, the AkaLuc cells displayed a completely different kinetics of the signal, with a peak immediately following the IP administration of the substrate. This means that for maximum signal intensity, data acquisition needs to proceed quickly after the administration of the substrate. Moreover, due to the rapid decay in signal, the experimental design needs to take into consideration a need for consistent timing between injection of the substrate and data acquisition for each animal. Furthermore, it is well known that IP administration of BLI substrates can lead to unreliable data due to injection failure rate and irregular distribution of the substrate [277]. Also, even following IP administration of the substrate the signal almost disappeared by day 3. At day 3 and day 7 only AkaLuc cells keep displaying some signal, which moved from the lungs of the mice to their liver.

The detection of unspecific signal, following IP administration of Akalumine-HCl, in the liver of mice that did not receive the cells, revealed that the signal observed in the liver of cell treated mice at day 3 and day 7 was not related to the presence of AkaLuc cells. These results are in line with a recent study that reported the presence of unspecific signal in the liver of mice following IP administration of Akalumine-HCl [278]. In contrast, no unspecific signal was reported following the administration of the high dose of D-Luciferin either IP or SC.

Summarising, there are no advantages in using the IP administration route, since Akalumine-HCl peaks immediately after its administration and is not superior to FLuc system SC, and because AkaLuc system is associated with an unspecific signal in the liver of the mice, which can compromise the detection of a small number of cells. On the other hand, following SC administration, not only the high dose of D-Luciferin was associated with the strongest detectable signal, but also the standard dose of D-Luciferin resulted in a signal comparable to the AkaLuc system. Finally, both system following SC and IP administration of the

substrates were associated to a consistent drop in the signal over time, with almost no signal by day 3. Although significant cell death is expected within the time frame of the experiments described here, it is not clear at which time point all injected cells die. Here, some signal was seen in the lungs of mice injected with FLuc cells 3 days post administration, when they were imaged with the high dose of D-Luciferin SC. This indicates that at least some cells are still alive at this time point. Importantly, this was not observed when imaging with the AkaLuc system.

The data obtained in the present study are different from those reported by Iwano and colleagues [205]. Beside the type of cells used, one main difference between the two studies is the number of cells injected. Iwano administered 10^3 cells, while in the present work, $2.5x10^5$ cells were injected. We do not know whether the administration of the high dose of D-Luciferin saturated the enzyme produced by $2.5x10^5$ cells since no *in vivo* saturation study was performed here. Nonetheless, in the presence of the same amount of substrate, using a lower number of cells is expected to lead to a quicker saturation of the signal than using a higher number of cells. After the IV administration of AkaLuc- and FLuc-expressing HeLa cells in mice, Iwano registered that an Akalumine-HCl/AkaLuc combination yielded a 52-fold stronger signal than D-Luciferin/FLuc [205]. Interestingly, the dose of D-Luciferin used by Iwano and co-workers (100 µl of 100 mM D-Luciferin, equal to 0.50 mmol/kg in a 20g mouse) is close to the standard dose that is commonly used. So, it is even more unexpected that in the present study, even though the number of cells was higher, D-Luciferin 47 mM resulted in a similar signal output of Akalumine-HCl *in vivo*.

Akalumine-HCl has been reported to induce cell cytotoxicity when administered in a significant amount to cell culture media [214, 279]. Although toxicity has not been observed in animal experiments by Iwano and colleagues [205], we observed the formation of lesions under the sites of SC injection of Akalumine-HCl with different degrees of severity. To what extent this affects the health of the mice still has to be clarified and investigated.

Concluding, the data in this chapter suggest that the AkaLuc/Akalumine-HCl reporter system is not superior to the FLuc/D-Luciferin system to track the biodistribution of MSCs. Considering also the negative aspects observed (background liver signal and lesions under the skin), FLuc/D-Luciferin combination will be used in the next chapter to track the biodistribution of MSCs.

CHAPTER 5 INVESTIGATING THE FATE, THE SAFETY AND THE INTERACTION OF MSCS WITH THE HOST IMMUNE SYSTEM

5.1 INTRODUCTION

As described in 1.4 mesenchymal stromal cells (MSCs) are multipotent cells identified for the first time in the bone marrow in the 1970s. Since then, several other populations of MSCs have been identified in many other human tissues (e.g. umbilical cord, Warton's jelly, adipose tissue, synovial membrane, tooth pulp, etc) and several of those are currently being investigated in many clinical trials because of the promising properties that these cells have shown in pre-clinical studies [154-156]. MSCs exert several direct and indirect immunomodulatory mechanisms [280] and also display regenerative potential through the secretion of paracrine factors [281]. However, despite that MSCs have been extensively studied, the mechanisms underlying their therapeutic effect have not been fully elucidated. Also, limited data on potential undesired effects associated with the administration of living cells (e.g. tumour formation [169], embolism [173], undesired differentiation [167]). It is also worth noting that MSCs are used in several clinical trials involving patients with an impaired immune system (e.g. people affected by graft versus host disease/GVHD, or patients affected by HIV [clinicaltrials.gov]), further enforcing the need to ensure that these cells do not pose a threat to the health of the patients.

Preclinical models can be used to assess the safety and the biodistribution of injected MSCs by monitoring the fate of the cells following administration. As previously mentioned, intravenous injection of MSCs is one of the most common routes of administration of cells [69], despite being often associate with lung entrapment [103] in animal models. Moreover, while MSCs have reported short survival in the lungs of immunocompetent animals [99, 103], they have also displayed a longer survival in severe combined immunodeficient (SCID) mice [99].

In this part of the thesis, the firefly luciferase expressing UC, BM and A-MSCs produced and characterised in the other chapters of this work will be used to investigate their biodistribution and safety following administration *in vivo* via, BLI techniques. Furthermore, the presence of an ischemia reperfusion injury induced in both kidneys will be used to evaluate whether this affects the biodistribution and the survival of the cells. Finally, any possible influence of the administered UC-MSCs on the hosts' immune cell populations and plasma analytes will be explored. Specifically, this chapter has the following goals:

1. Explore and compare the biodistribution of UC, BM and A-MSCs.
2. Evaluate the biodistribution and the survival of the different MSCs in mice with an ischemia reperfusion injury.
3. Assess the role of the immune system in the clearance of administered UC-MSCs and investigate the safety of the cells, by using immunocompromised animals.
4. Investigate any possible fluctuation in the number of different innate and adaptive immune cells in several organs and tissue following the administration of UC-MSCs *in vivo*.
5. Examine the concentration of different cytokines, chemokines, soluble receptors, and growth factors directly associated with the immune system in the plasma of mice that had received UC-MSCs IV.

5.2 MATERIALS AND METHODS

UC, BM and A-MSCs were transduced and characterised in CHAPTER 3. These cells are used here for the *in vivo* characterisation of their biodistribution, safety and their impact on the mobilisation of the host immune cells.

5.2.1 *In vivo* short term biodistribution analysis

7-9 week old female C57 Black-6 (C57BL/6J.Tyr^{c-2J}, from JAX) albino mice were used to evaluate the biodistribution of the different transduced cells from their administration into the animal (day 0) up to 7 days later.

FLuc^{+} UC-, BM-, and A-MSCs expanded at their optimal seeding density were harvested using trypsin/EDTA, centrifuged, suspended in ice-cold PBS at a concentration of 2.5x10^{5} cells/100 µL and kept on ice until being administered *in vivo*. 4 mice per donor per cell type were anaesthetised with isoflurane and IV injected with 100 µL of cell suspension through the tail vein, followed by SC administration of 200 µL of 47 mM D-Luciferin as identified in CHAPTER 4. The administration of the substrate and the imaging were performed the day of the injection of the cells (day 0) and after 1, 3 and 7 days. Furthermore, based on the results from the kinetics experiments (4.3.3.1), the substrate was administered 20 minutes before imaging the mice in both dorsal and ventral positions with an IVIS Spectrum. Each imaging session was performed using the open filter, a binning of 8, a f-stop of 1, and 60 seconds exposure time at day 0 and 180 seconds exposure time at day 1, 3 and 7.

5.2.2 Biodistribution of MSCs from different sources in an *in vivo* model of ischemia reperfusion injury (IRI)

9-10 week old male C57BL/6J albino mice were used to assess whether the presence of an ischemia reperfusion injury (IRI) induced in the kidney could affect either the biodistribution or the survival of administered MSCs from different sources (1 donor per type of MSC). The IRI model displays strong variability depending on several factors including sex [282]. Here I used male mice because this was the gender in which the model was established at the University of Liverpool.

IRI was induced by Ms. Katherine Trivino, another PhD student from our group. All experimentation was performed under a Project Licence (PPL 7008741) granted by the Home Office under the Animals (Scientific Procedures) Act 1986. In summary, following isoflurane anaesthesia, the mouse kidneys were exposed by two small incisions on the back of the animals. Then both left and right renal vascular pedicles were clamped for 27.5 minutes. At the end of the ischemia induction, the clamps were removed, and the wounds sutured. An intravenous injection of 100 µL of PBS containing either $2.5x10^5$ $FLuc^+$ UC, BM or A-MSCs was then given to each animal via the tail vein immediately after the surgery, under the same anaesthesia session

Because combining the IRI surgery and the BLI on the same day would have been too demanding for the animals, two experimental groups were used:

1. In the first, mice that underwent IRI were imaged immediately after the surgery and culled after the BLI session (n = 3 per cell type).
2. In the second, mice that underwent IRI were allowed to recover after the surgery and then imaged at day 1, day 3 and day 7 (n = 4 per cell type).

A third group of mice (n = 3 per cell type) that did not undergo the IRI procedure but did receive the cells was also included as a control group. The animals used in sections 5.2.1 and 5.2.3 were all females, so this male control group was required in the analysis to exclude any possible difference associated with the sex of the animals. Furthermore, as the back of the IRI animals was shaved due to the procedure, the back of the control animals was shaved as well, to account for the effect of any light attenuation during the imaging due to the presence of the fur.

The BLI sessions were performed as previously explained. All the mice received a SC administration of 200 µL of 47 mM D-Luciferin and were imaged with an IVIS Spectrum in

both ventral and dorsal positions 20 minutes later. An exception was made for the IRI group 1 mice. As those animals underwent a very long anaesthesia, to investigate whether this could have affected the biodistribution of the D-Luciferin following SC administration and to pick the best acquisition time, those animals were imaged every minute for 25 minutes in dorsal position. Each imaging session was performed using the open filter, a binning of 8, a f-stop of 1, and 60 seconds exposure time at day 0 and 180 seconds exposure time from day 1 onwards.

5.2.3 *In vivo* long term biodistribution in immunocompromised mice

7-9 weeks old severe combined immunodeficient (SCID; CB17/lcr-Prkdc^{SCID}/lcrlcoCrl) and Non-obese diabetic SCID (NOD SCID; NOD.CB17-Prkdc^{SCID}/NCrCrl) female mice from Charles River were used to evaluate the biodistribution, the persistence over time and the safety of transduced UC-MSCs up to 31 days from administration. BALB/c immune-competent mice were used as a control group.

FLuc^{+} UC-MSCs (n = 3 different donors) were harvested and administered as described above. Again, 2.5x10^{5} cells/100 µL were administered IV to each strain (n = 5 mice per strain per donor), followed by SC of 200 µL of 47 mM D-Luciferin. During the first week of experiment, the administration of the substrate and the imaging were performed the day of the injection of the cells (day 0) and after 1, 3, 5 and 7 days. From the second week until the end of the experiment, the mice were imaged twice a week. As in the previous chapter, the substrate was administered 20 minutes before imaging the mice in both dorsal and ventral positions with an IVIS Spectrum. Each imaging session was performed using the open filter, a binning of 8, a f-stop of 1, and 60 seconds exposure time at day 0 and 180 seconds exposure time from day 1 onwards.

5.2.4 Analysis of the BLI signal

All the *in vivo* analysis were performed using Living Image (v 4.5.2). The acquired signal was always normalised to radiance (photons/second/centimeter^{2}/steradian) and analysed using the Region of Interest (ROI) tool of the IVIS software to obtain the total number of photons emitted in that specific area, also known as total flux (photons/s). The data were then plotted using GraphPad to generate the final graphs.

5.2.5 Flow cytometry analysis of immune cells from different tissues following MSC administration

7-9 weeks old female C57BL/6J albino mice were used to assess whether the administration of MSCs can have an impact on different immune system cell populations in different organs/tissues. The animals (n = 18) were divided into 3 groups:

- group 1: control naïve mice that did not receive cells,
- group 2: mice culled 2h after the administration of the cells,
- group 3: mice culled 24h after the administration of the cells.

Untransduced UC-MSCs (1 donor) were prepared as previously described. $2.5x10^5$ cells/100 µL were IV injected into anaesthetised 8 weeks old female C57BL/6 mice (n = 12; groups 2 and 3). Either 2 (group 2) or 24 (group 3) hours after the administration of the MSCs, the mice were culled by cardiac exsanguination and 4 different organs/tissues were collected:

I. the whole blood, where both the MSCs and the immune cells are circulating,
II. the lungs, where the administered MSCs are stuck and die in the first 24 hours,
III. the bone marrow, one of the primary lymphoid organs (with the Thymus), where different immune cells are produced, and
IV. the spleen, a secondary lymphoid organ, which contains several immune cells.

5.2.5.1 Whole blood collection and preparation for staining

The whole blood was collected via cardiac puncture under terminal anaesthesia. Immediately after the collection, the blood was incubated with 10 mL of Red Blood Cell (RBC) lysis buffer (eBioscience, #00-4333-57) per 1.0 mL of mice blood for 10 minutes at room temperature, with occasional shaking. After stopping the reaction with 30 mL of PBS, the cells were centrifuged at 400 g for 1 minute at 4°C. The pellet was finally suspended in PEB (PBS, 5mM EDTA and 0.5% w/v bovine serum albumin) buffer.

5.2.5.2 Lungs harvesting and digestion to obtain single-cell suspensions

Lungs were collected and digested to obtain single-cell suspensions following the protocol described by Jungblut M. et al [283]. Briefly, the harvested lung tissue was transferred into a gentleMACS C Tube (Miltenyi Biotec, #130-096-334) containing 4.9 mL of HEPES buffer (10 mM HEPES-NaOH pH 7.4, 150 mM NaCl, 5 mM KCl, 1 mM $MgCl_2$, 1.8 mM $CaCl_2$). Then, 100 µL of Collagenase D (SigmaAldrich, #11088866001; 100 mg/mL stock solution in HEPES

buffer) and 20 µL DNase I solution (SigmaAldrich, #11284932001; 20,000 U/mL stock solution) was added. The C tube was loaded onto the gentleMACS Dissociator and subsequently run with the gentleMACS standard programs "m_lung_01" and "m_lung_02", with a 30 min incubation at 37°C with automated rotation in between. The dissociated tissue was then filtered through a 70 µm cell strainer, centrifuged at 300 g for 10 min and suspended in PEB buffer.

5.2.5.3 Bone marrow harvesting and preparation for staining

Bone marrow was collected from the hind limbs following the protocol described by Amend et al [284]. Briefly, the long bones (femurs and tibias) were carefully dissected from euthanized mice. After the removal of any remaining muscle or connective tissue, the metaphysis of the femurs and the tibias were exposed. An 18 G needle was pushed through the bottom of a 0.5 mL microcentrifuge tube and the long bones were placed into it, with the exposed metaphysis facing the bottom of the tube. The 0.5 mL tube was housed into a 1.5 mL one and centrifuged at ≥10000 g for 15 seconds. After discarding the 0.5 mL tube, the pellet at the bottom of the 1.5 mL tube was incubated for 5 minutes with RBC lysis buffer to remove red blood cells. Following another centrifugation step the cells were suspended into PEB buffer, ready for staining.

5.2.5.4 Spleen harvesting and digestion

To obtain a single cell suspension of splenocytes the spleen was mechanically and enzymatically digested. The freshly harvested spleen was transferred into a gentleMACS C Tube (Miltenyi Biotec, #130-096-334) containing 2 mL of digestion solution, made of 1.8 mL of sterile DMEM, 200 µL of Liberase solution (SigmaAldrich, #5401160001, 3 mg/mL stock solution) and 10 µL DNase I solution (SigmaAldrich, #11284932001; 20,000 U/mL stock solution). The C tube was loaded onto the gentleMACS Dissociator and subsequently run with the gentleMACS standard programs "m_spleen_01" and "m_spleen_02", with a 30 min incubation at 37°C with automated rotation in between. The dissociated tissue was then filtered through a 70 µm cell strainer, centrifuged at 300 g for 10 min and suspended RBC lysis buffer for 5 minutes. At the end of the incubation, the cells were centrifuged again and suspended in PEB for staining.

5.2.5.5 Staining for flow cytometry analysis

Cells isolated from the different organs were suspended in PEB buffer and incubated with Fc blocking agent (#130-092-575, Miltenyi Biotec) at room temperature for 15 minutes. Then,

the cells were divided into individual tubes for each of staining groups, suspended in 100 µL of PEB buffer and stained. Table 5.1 summarises the immune cells investigated and the respective markers, while Table 5.2 presents the antibodies used. All stainings have been performed according to the manufacturer's instructions. FoxP3 and CD68 are intracellular markers so prior to staining with these markers the cells were fixed and permeabilised as suggested by the manufacturer. The flow cytometry data were collected using a FACS Canto II and analysed using the Flowing Software from Perttu Terho [https://bioscience.fi/services/cell-imaging/flowing-software/]. Unstained control cells and single colour stainings were used to set the different gates and to perform the initial compensation for all the immune cells in all the tissue and organs. The gating strategy is based on the study performed by Hensel A. J. et al [285], and is also summarised below:

- Immature myeloid cells (iMCs): population 1 (P1) = singlets; P2 = CD11b VioBlue and Gr-1 APC-Vio770 double positive gate; P3 = F4/80 APC negative and Ly6b FITC negative, F4/80 APC positive and Ly6b FITC negative, F4/80 positive and Ly6b positive gate.
- Neutrophils: P1 = singlets; P2 = CD11b VioBlue and Gr-1 APC-Vio770 double positive gate; P3 = F4/80 APC negative and Ly6b FITC positive gate.
- Macrophages: P1 = singlets; P2 = CD11b VioBlue and F4/80 double-positive gate; P3 = CD68 PE (intracellular staining) positive gate.
- Natural killer (NK) cells: P1 = singlets; P2 = CD3ε APC-Vio770 negative and NKp46 positive gate.
- Myeloid dendritic cells (mDC): P1 = singlets; P2 = CD11b VioBlue and CD11c PE double positive gate.
- Peripheral dendritic cells (pDC): P1 = singlets; P2 = CD11b VioBlue negative and CD11c PE positive gate; P3 = B220 APC-Vio770 and Siglec H FITC double positive gate.
- CD4 T cells: P1 = singlets; P2 = CD3ε APC-Vio770 and CD4 VioBlue double positive gate.
- CD4 T regulatory (Tregs) cells: P1 = singlets; P2 = CD3ε APC-Vio770 and CD4 VioBlue double positive gate; P3 = CD25 and FoxP3 APC (intracellular staining) double positive gate.
- CD8 T cells: P1 = singlets; P2 = CD3ε APC-Vio770 and CD8 FITC double positive gate.
- B cells: P1 = singlets; P2 = B220 APC-Vio770 and CD19 PE double positive gate

Table 5.1: Cell markers used to identify different immune cell populations.

Cell type	Markers			
iMCs	CD11b VioBlue	Gr-1 APC-Vio770	Ly6B^{-} FITC	F4/80$^{-/+}$ APC
			Ly6B^{+} FITC	F4/80^{+} APC
Neutrophils	CD11b VioBlue	Gr-1 APC-Vio770	Ly6B FITC	F4/80 APC[a]
Macrophages	CD11b VioBlue	F4/80 APC	CD68 PE	
NK cells	CD3ε APC-Vio770[a]	NKp46 FITC		
mDC	CD11b VioBlue	CD11c PE		
pDC	CD11b VioBlue	CD11c PE	B220 APC-Vio770	Siglec H FITC
CD4 T cells	CD3ε APC-Vio770	CD4 VioBlue		
CD4 Tregs	CD3ε APC-Vio770	CD4 VioBlue	CD25 PE	FoxP3 APC
CD8 T cells	CD3ε APC-Vio770	CD8 FITC		
B cells	B220 APC-Vio770	CD19 PE		

[a] indicates the absence of a marker

Table 5.2: The antibodies employed for the analysis.

Antibody	Fluorochrome	Supplier	Clone	Dilution Factor
B220	APC-Vio770	Miltenyi	RA3-6B2	1:10
CD3ε	APC-Vio770	Miltenyi	145-2C1	1:50
CD4	VioBlue	Miltenyi	REA604	1:50
CD8	FITC	Miltenyi	53-6.7	1:50
CD11b	VioBlue	Miltenyi	M1/70.15.11.5	1:50
CD11c	PE	Miltenyi	N418	1:50
CD19	PE	Miltenyi	6D5	1:50
CD25	PE	eBioscence	PC61.5	1:200
CD68	PE	Miltenyi	FA-11	1:10
F4/80	APC	Miltenyi	REA126	1:50
FoxP3	APC	Miltenyi	REA788	1:50
Gr-1	APC-Vio770	Miltenyi	REA810	1:50
Ly6b	FITC	Miltenyi	REA115	1:10
NKp46	FITC	Miltenyi	29A1.4.9	1:50
Siglec H	FITC	Miltenyi	551.3D3	1:10

5.2.6 Evaluation of circulating cytokines in the blood of mice administered with UC-MSCs

The experimental design of this set of experiment is the same as 5.2.5. Briefly, 7-9 week old female C57BL/6 albino mice were used to evaluate with a Luminex multiplex analysis the levels of several analytes (Table 5.3) in the blood of animals receiving UC-MSCs. The animals (n = 24) were divided into the same 3 groups as above:

- group 1: control naïve mice that did not receive cells,
- group 2: mice culled 2h after the administration of the cells,
- group 3: mice culled 24h after the administration of the cells.

Untransduced UC-MSCs were prepared and administered as previously described (5.2.5). Blood collection was performed during terminal anaesthesia via cardiac exsanguination. The blood was then collected into tubes containing lithium heparin (BD microtainer tubes, #365966) for plasma separation. Each tube was immediately inverted 10 times and centrifuged at 2000 g for 5 minutes. The plasma was then collected, snap frozen with dry ice (-80 °C) and stored at this temperature until being used for the multiplex assay.

An Immune Monitoring 48-Plex Mouse ProcartaPlex™ Panel (Invitrogen™, EPX480-20834-901) was used to evaluate the presence of 48 different analytes (cytokines, chemokines, soluble receptors, and growth factors) in the plasma of the animals. The multiplexing capabilities of this type of assay are based on the use of magnetic beads internally dyed with red and infrared fluorophores of differing intensities. Each of these beads is associated with a specific number, called bead region, that can be used to differentiate between them. The list of the 48 analytes and the relative bead region are summarised in Table 5.3. The ProcartaPlex 96 well plate and the plasma samples were prepared following the manufacturer's instructions. Each sample was analysed in duplicate as suggested by the manufacturer and a Bio-Plex® Multiplex Immunoassay System (Bio-Rad™) was used to perform the detection and the quantification of multiple analytes. To perform the quantification, a standard curve provided in the kit was used by the instrument as a reference for the calculation of the concentration of each analyte in each sample. When the signal was below the limit of detection and displayed as "OOR< =" (out of range below) it was considered non-available (N/A) and excluded from the dataset. Values below the lower limit of the standard curve but still above the lower detection limit were automatically extrapolated by the system and included in the analysis.

Table 5.3: Details of the analytes. The relative bead regions are shown in brackets.

Analytes			
BAFF [67]	Betacellulin (BTC) [73]	ENA-78 (CXCL5) [57]	Eotaxin (CCL11) [62]
G-CSF (CSF-3) [12]	GM-CSF [42]	Gro-α (CXCL1) [43]	IFN-α [30]
IFN-γ [38]	IL-1α [56]	IL-1β [19]	IL-2 [20]
IL-2R [63]	IL-3 [14]	IL-4 [26]	IL-5 [27]
IL-6 [28]	IL-7 [74]	IL-7Rα [53]	IL-9 [34]
IL-10 [13]	IL-12p70 [39]	IL-13 [35]	IL-15/IL-15R [54]
IL-17A (CTLA-8) [52]	IL-18 [66]	IL-19 [61]	IL-22 [33]
IL-23 [37]	IL-25 (IL-17E) [29]	IL-27 [36]	IL-28 [64]
IL-31 [76]	IL-33 [75]	IL-33R (ST2) [78]	IP-10 (CXCL10) [22]
Leptin [65]	LIF [18]	M-CSF [21]	MCP-1 (CCL2) [51]
MCP-3 (CCL7) [48]	MIP-1α (CCL3) [47]	MIP-1β (CCL4) [72]	MIP-2 [55]
RANKL [46]	RANTES (CCL5) [44]	TNF α [45]	VEGF-A [25]

Abbreviations: BAFF = B cell activating factor; ENA = epithelial-derived neutrophil-activating peptide; CXCL = chemokine (C-X-C motif) ligand; CCL = chemokine (C-C motif) ligand; G-CSF = granulocyte colony stimulating factor; GM-CSF = granulocyte macrophage CSF; IFN = interferon; IL = interleukin; R = receptor; IP = interferon gamma-induced protein; LIF = leukaemia inhibitory factor; MCP = monocyte chemoattractant protein; MIP = macrophage inflammatory protein; RANKL = Receptor activator of nuclear factor kappa-B ligand; RANTES = regulated on activation, normal T cell expressed and secreted; TNF = tumour necrosis factor; VEGF = vascular endothelial growth factor.

5.2.7 Statistical analysis

All values in graphs are represented as mean ± standard deviation. The statistical analysis was performed using the GraphPad software. The type of statistical test and the number of replicates included in the analyses are indicated in the figure legends.

5.3 RESULTS

The MSCs used to produce the data presented in this chapter are those described in CHAPTER 3. As shown there, the transduction process did not change the properties of the cells and their expansion was not associated with any major loss of the transduced genes or a reduction in the percentage of transduced cells. The cells used here are at the same passage used to evaluate the expression of ZsGreen in CHAPTER 3 and 98% of cells in the population expressed the reporter (Table 3.4).

5.3.1 Almost all the administered MSCs die in the first 24 hours *in vivo*

BL images of FLuc$^+$ UC-, BM- and A-MSCs following IV injection into C57BL/6 albino mice show that regardless of the origin of the MSC, all the cells were entrapped in the lungs immediately after the administration (Figure 5.1a). Furthermore, 24h following administration the signal was strongly reduced and there was no sign of migration of the cells from the lung to other body sites. In particular, the signal coming from the BM cells seemed weaker than the signal coming from the two other cell types (Figure 5.1a). Three days after the administration of the cells a weak signal was detectable from mice that receive UC and A-MSCs, while there seemed to be no signal at all coming from the mice that received the BM cells. Finally, 7 days following administration, there was no detectable signal from any of the mice, irrespective of the type of MSC they were injected with (Figure 5.1a). These results are confirmed by the quantitative analysis of the bioluminescent signal (Figure 5.1b). Interestingly, the signal obtained at day 0 was comparable not only between the donors of the same cell type (Figure 5.1b), but also among the different sources of cells ($5.1x10^7 \pm 1.7x10^7$ p/s, $4.1x10^7 \pm 0.91x10^7$ p/s and $2.8x10^7 \pm 0.99x10^7$ p/s for UC, BM and A-MSCs respectively; Figure 5.1c). Furthermore, they all showed a similar reduction in the signal from day 0 to day 1 ($3.6x10^6 \pm 2.5x10^6$ p/s, $0.83x10^6 \pm 0.9x10^6$ p/s and $3.4x10^6 \pm 0.54x10^6$ p/s for UC, BM and A cells respectively, Figure 5.1c) and to day 3 ($2.9x10^5 \pm 1.1x10^5$ p/s, $1.6x10^5 \pm 076x10^5$ p/s and $8.3x10^5 \pm 2.0x10^5$ p/s, Figure 5.1c). By day 7 the detected signal ($0.97x10^5 \pm 0.09x10^5$ p/s, $1.07x10^5 \pm 0.26x10^5$ p/s and $1.04x10^5 \pm 0.11x10^5$ p/s respectively, Figure 5.1c) was not different from the baseline ($1.1x10^5 \pm 0.07x10^5$ p/s), measured on naïve animals that did not receive any cells or substrate. The analysis of the relative bioluminescence intensity normalised to day 0 revealed that in the first 24 hours the signal dropped significantly to 6.3 ± 3.6% for the UC cells, to 2.5 ± 3.1% for the BM-MSCs and to 12.9 ± 3.4% for the A-MSCs (Figure 5.1d). Furthermore, by day 3, only 0.58 ± 0.05%, 0.44 ± 0.31% and 3.47 ± 1.7% of the original signal is detectable from UC, BM and A-MSCs respectively (Figure 5.1d).

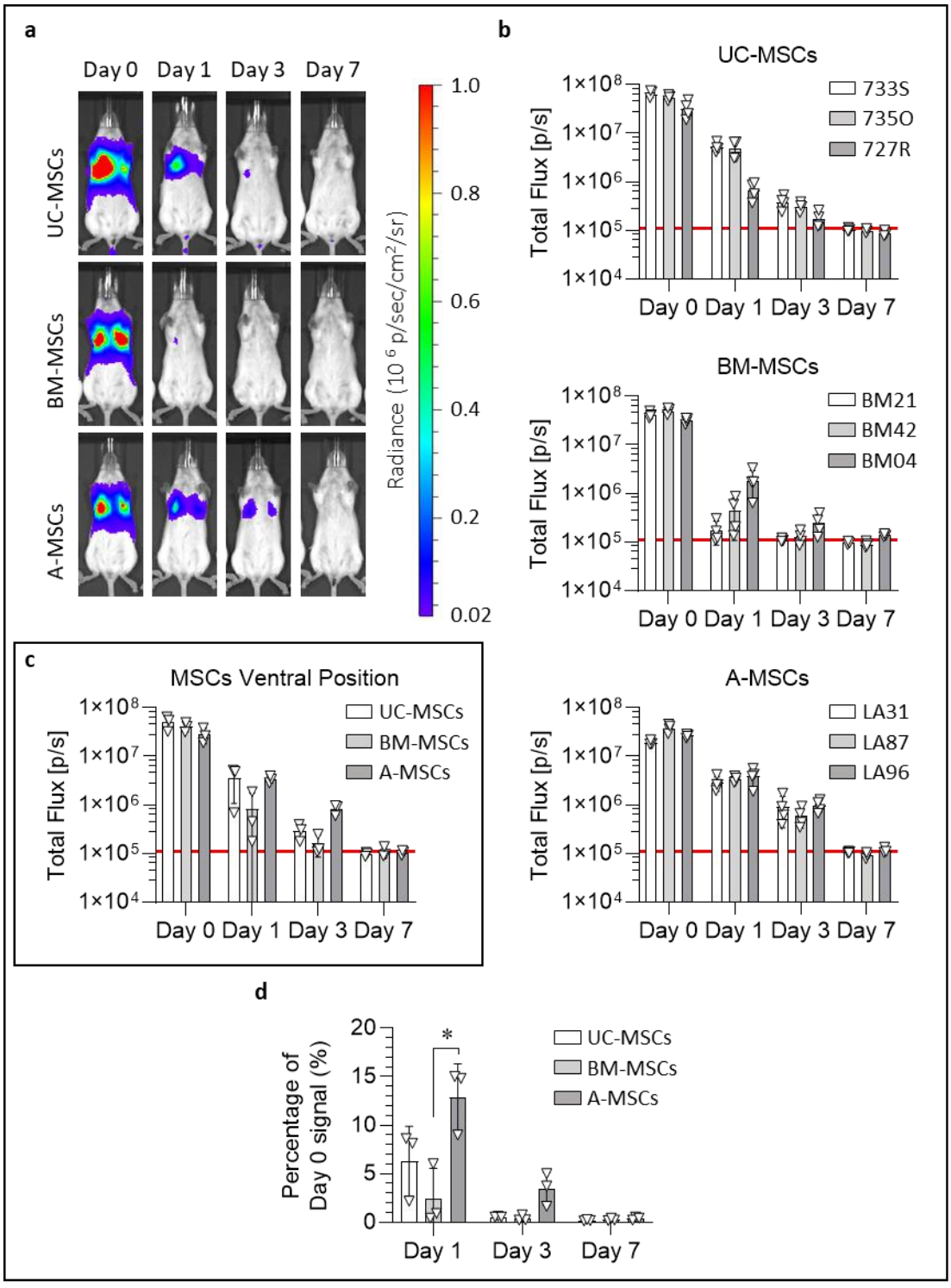

Figure 5.1| All MSCs are entrapped in the lungs and are short-lived following IV administration. **(a)** Representative bioluminescence images of mice administered with FLuc$^+$ UC, BM and A-MSCs on the day of administration of the cells (day 0), and 1, 3 or 7 days after (radiance scale from 0.2x10^5 to 1x10^6 p/s/cm^2/sr). **(b)** Light output (flux) as a function of time (days) coming from three individual donors (shown in legends) for each cell type. Data are displayed as mean ± SD from n = 4 for each donor sample. The red line (1.1x10^5 p/s) is the background BLI signal emitted by naïve animals (n = 4) that did not receive any cells. **(c)** Quantification of the signal originating from the different MSC sources as obtained by averaging the signal from all donors. Data are displayed as mean ± SD from n=3 donor samples. **(d)** Signal at day 1, day 3 and day 7 normalized to the signal at day 0. Data are displayed

as mean ± SD from n=3. Two-way ANOVA with Geisser-Greenhouse correction and Tukey's multiple comparison post-hoc test, * $p < 0.05$.

5.3.2 The presence of an IRI does not affect the lung entrapment of MSCs

An *in vivo* IRI model was used to investigate whether the presence of an ischemia-reperfusion injury in the kidneys could have an impact on the biodistribution and the survival of the cells.

Representative BL images of healthy (CTR) and IRI-induced animals on the day of administration of the cells and after 1, 3 and 7 days, in dorsal position are displayed in Figure 5.2a. This position was chosen for this experiment because the animals were shaven, increasing imaging sensitivity. As previously observed, on the day of administration the cells reach the lungs and get trapped there. After 24 h, the signal was still originating from the lungs in both control and IRI animals for all 3 cell types tested (Figure 5.2a). Interestingly, the signal from all the IRI animals appeared to be stronger than the signal coming from the healthy animals. It is important to recall that the IRI animals imaged on day 0 were terminated on the same day of the surgery and that the animals analysed on day 1, 3 and 7 were different ones. 3 days post administration, the signal from A-MSCs was still clearly detectable and coming from the lungs, while the UC animals displayed a very weak signal and the BM-MSC animals displayed no detectable signal (Figure 5.2a). On day 7 no signal was detectable from any of the cells in any of the conditions (Figure 5.2a).

The quantification of the bioluminescence signal confirmed these qualitative observations (Figure 5.2b). The signal obtained at day 0 was not statistically significant between healthy and IRI animals for UC and A-MSCs ($7.5x10^7 \pm 1.3x10^7$ p/s and $7.3x10^7 \pm 1.3x10^7$ p/s for UC-MSCs, $3.3x10^7 \pm 1.4x10^7$ p/s and $5.9x10^7 \pm 2.4x10^7$ p/s for A-MSCs in healthy and IRI animals respectively (Figure 5.2c), but was statistically different for BM-MSCs ($4.8x10^7 \pm 1.0x10^7$ p/s and $8.5x10^7 \pm 0.5x10^7$ p/s in healthy and IRI animals respectively, Figure 5.2c). Interestingly, differences were observed 24h after the administration of the cells, particularly for A-MSCs where, while the signal in the healthy animals followed the previously observed trend of a strong decay ($3.9x10^6 \pm 1.3x10^6$ p/s, Figure 5.2c), the signal in the IRI animals was still relatively strong ($2.9x10^7 \pm 1.0x10^7$ p/s, Figure 5.2c). A similar result was also observed in animals administered with UC-MSCs ($3.8x10^6 \pm 0.8x10^6$ p/s and $1.4x10^7 \pm 0.5x10^7$ p/s in healthy and IRI animals respectively, Figure 5.2c) and, even if less pronounced, in mice that received BM-MSCs ($1.4x10^6 \pm 0.6x10^6$ p/s and $6.5x10^6 \pm 3.2x10^6$ p/s for BM cells in healthy and IRI animals respectively, Figure 5.2c). At this time point, the difference in signal between healthy and IRI-induced mice was statistically significant for all MSCs. After 3 days from the

administration of the cells the signal coming from healthy and IRI animals was again similar between conditions for all the three cell types ($4.2x10^5 \pm 1.0x10^5$ p/s and $5.8x10^5 \pm 3.2x10^5$ p/s for UC-MSCs, $2.0x10^5 \pm 0.2x10^5$ p/s and $2.3x10^5 \pm 0.9x10^5$ p/s for BM cells, $1.1x10^6 \pm 0.6x10^6$ p/s and $2.9x10^6 \pm 1.6x10^6$ p/s for A-MSCs in healthy and IRI animals respectively, Figure 5.2c). Finally, by day 7 the detected signal for all 3 cell types in both healthy and IRI animals ($1.3x10^5 \pm 0.1x10^5$ p/s and $1.6x10^5 \pm 0.2x10^5$ p/s for UC-MSCs, $1.1x10^5 \pm 0.1x10^5$ p/s and $1.3x10^5 \pm 0.2x10^5$ p/s for BM-MSCs, $1.2x10^5 \pm 0.1x10^5$ p/s and $1.8x10^5 \pm 0.5x10^5$ p/s for A-MSCs in healthy and IRI animals respectively (Figure 5.2c) was very close to the baseline measured in female healthy mice ($1.1x10^5 \pm 0.1x10^5$ p, Figure 5.1), indicating that all injected cells had died.

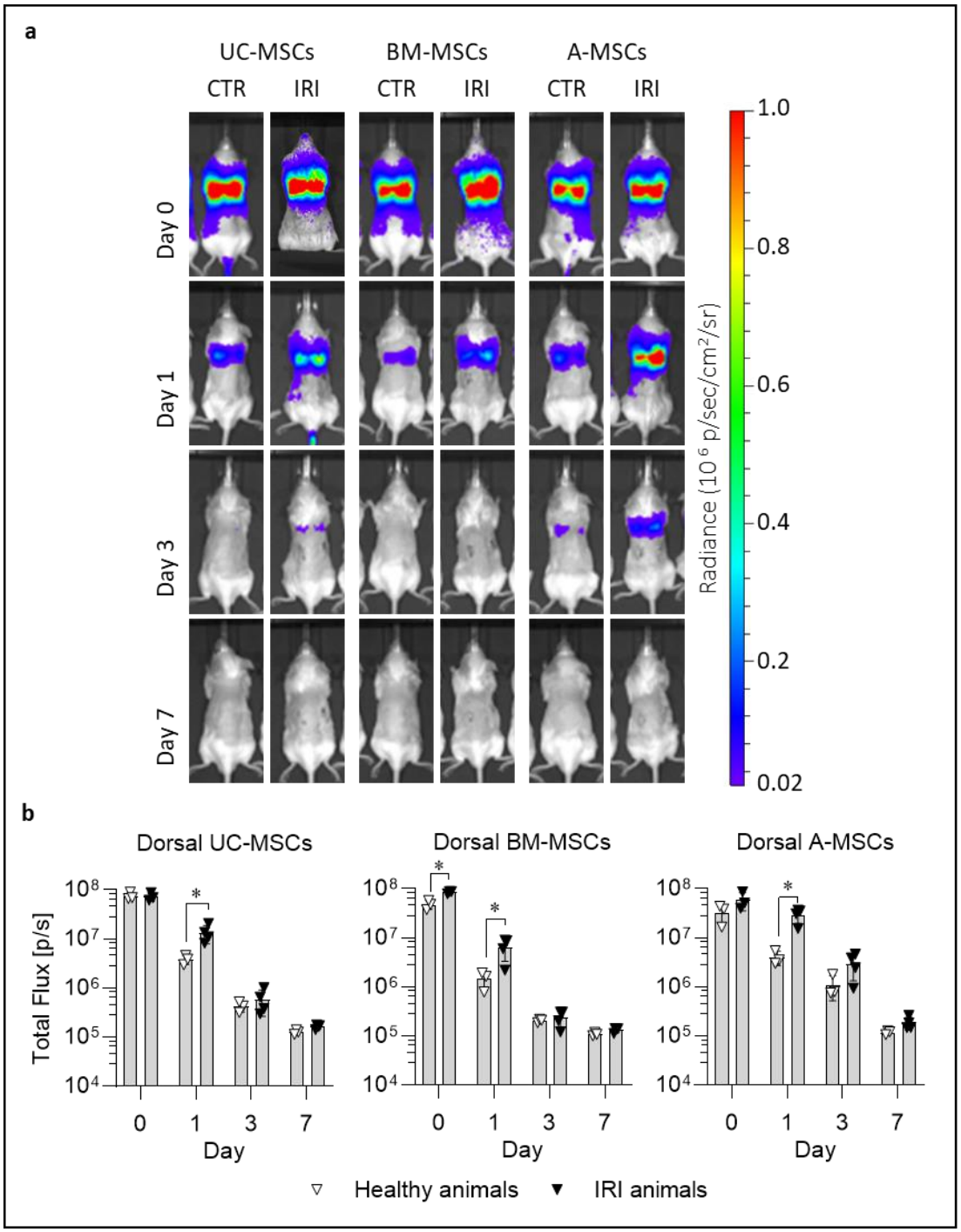

Figure 5.2| MSCs are entrapped in the lungs of healthy and IRI-induced animals and do not migrate to the site of injury. (a) Representative bioluminescence images of control and IRI mice up to 7 days post administration of FLuc$^+$ UC, BM and A-MSCs (radiance scale from 0.2x10^5 to 1x10^6 p/s/cm^2/sr). **(b)** Light output (p/s) as a function of time of the healthy and ischemic animals, separated by cell type. Data are displayed as mean ± SD from n ≥ 3. Day 0 data of the IRI animals comes from animals different from the ones used to perform the day 1, 3 and 7 analysis. Because the IRI animals used at day 0 are different from the ones used at day 1, 3 and 7, a transversal statistical analysis was not possible, and this reduced the strength of the statistical comparison. Welch's t-tests were used to compare the signal from healthy and IRI animals at each time point; * $p < 0.05$.

5.3.3 UC-MSCs are also short-lived in immuno-compromised animals

Two immunocompromised mouse strains (SCID and NOD/SCID) were used to investigate: (a) if the reduction in the intensity of the signal observed in the C57BL/6J albino mice in the first 24 h was associated with an involvement of the immune system and (b) the long-term safety of MSCs in immunocompromised hosts. For this last purpose, the mice were monitored until day 31 from administration, to detect any possible increase in the signal over a long time frame. As no major difference was observed in the biodistribution or the clearance of the signal between the 3 types of MSCs, performing the experiment using 3 different donors of the same cell type (UC-MSCs) was preferred to the testing of just 1 donor from each MSC source. The immunocompetent BALB/c strain was used as a control because both immunocompromised strains shared this genetic background and also to confirm the results obtained in the previous sections with a different immunocompetent strain.

Representative BL images of the 3 strains of mice on the day of administration of the cells, 24h later and 3 days later are displayed in Figure 5.3a. As previously observed for the C57BL/6J albino mice, in this experiment the cells also reached the lungs and got entrapped there, regardless of the immune status of the animals (Figure 5.3a). The drop in signal in the first 24 h was similar for all 3 mouse strains (Figure 5.3a). Then, 3 days post administration, the signal was reduced further (Figure 5.3a). The quantification analysis confirmed that regardless of the donor used, the signal intensity was comparable among the 3 groups of animals. The analysis of the relative bioluminescence intensity normalised to day 0 revealed that at day 1 the signal dropped to 16.3 ± 2.8%, 14.1 ± 4.6% and 8.9 ± 2.1% for BALB/c, SCID and NOD/SCID respectively (Figure 5.3c), showing that the immunocompromised NOD/SCID group is actually the one that displayed the highest signal reduction. At day 3 the signal dropped to 1.1 ± 0.4, 1.3 ± 0.1% and 2.3 ± 1.6%for BALB/c, SCID and NOD/SCID respectively (Figure 5.3c). Interestingly, for 2 out of the 3 donors the signal in the NOD/SCID animals at day 3 was 3.2% and 3.1% of the day 0 signal, while the third one was only 0.4%. On the other hand, all BALB/c and SCID groups behaved similarly regardless of the donor.

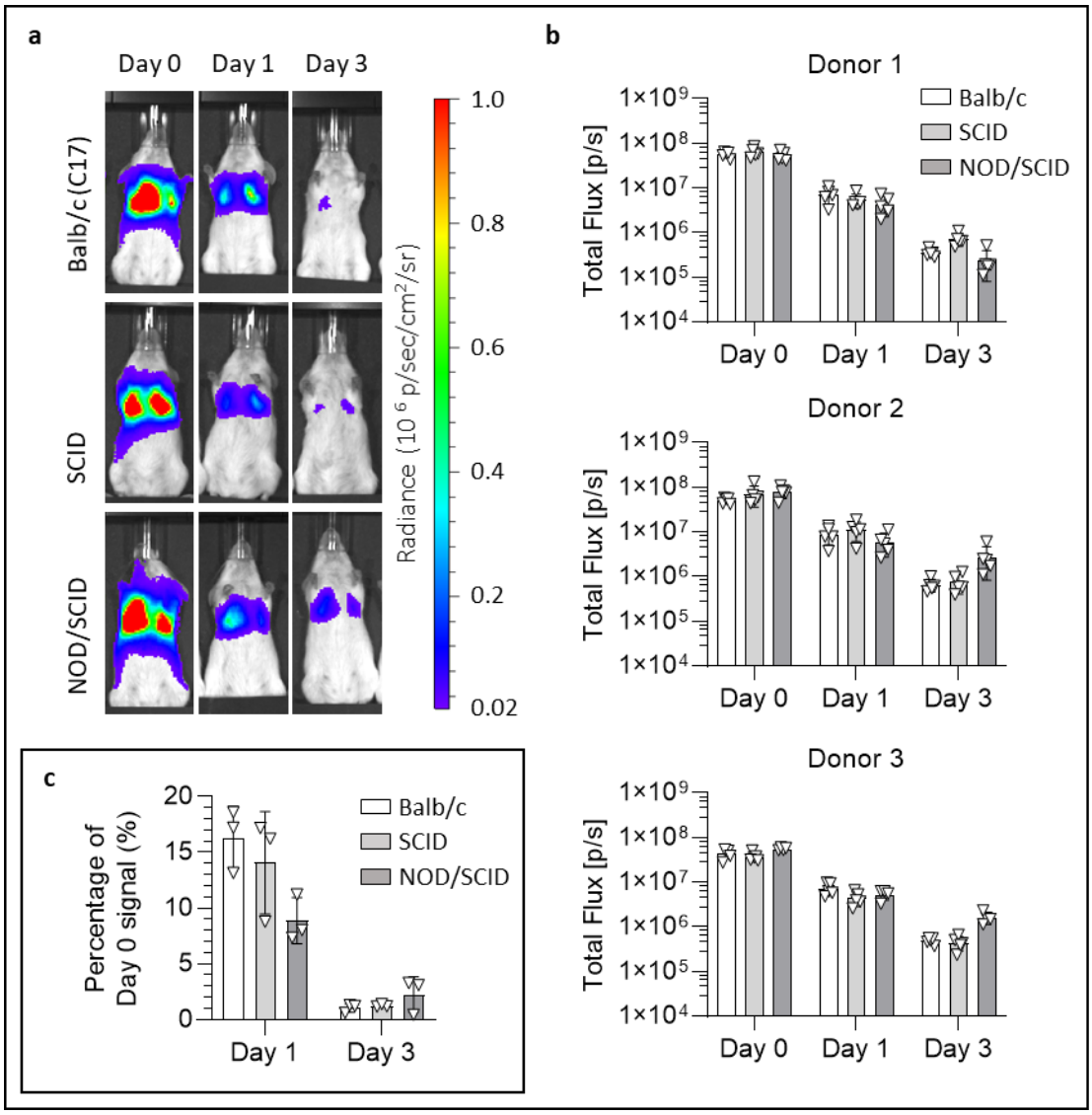

Figure 5.3| Administered UC-MSCs die similarly in immunocompetent and immunocompromised mice. (a) Representative bioluminescence images of BALB/c, SCID and NOD/SCID mice up to 3 days post administration of FLuc$^+$ UC-MSCs (radiance scale from 0.2x10^5 to 1x10^6 p/s/cm^2/sr). **(b)** Light output (flux) as a function of time (days) of each of the 3 UC-MSC donors in the 3 animal strains. Data are displayed as mean ± SD from n ≥ 4 for each donor. **(c)** Day 1 and day 3 flux signal normalised to the respective day 0 signal. Data are displayed as mean ± SD from n = 3.

From day 5 to day 31, no signal originated from the BALB/c group (Figure 5.4a), while some of the SCID and NOD/SCID animals still displayed a weak signal during this period (Figure 5.4a). The general behaviour of the MSCs over time looks comparable between the three donors, with the only exception being the NOD/SCID group that received the donor 1 (727R, Figure 5.4b). While there was no detectable signal from day 5 for donor 1, the NOD/SCID animals that received MSC from the two other donors displayed a weak signal for longer (Figure 5.4b). The details about the number of NOD and NOD/SCID mice displaying a signal from day 5 to day 31 are summarised in Table 5.4 and Table 5.5. Of note, around 27% (4 out

of 15) of the SCID animals that received the UC-MSCs still displayed a detectable signal at day 14, before the signal completely disappeared by day 17 (Table 5.4). Furthermore, while the signal from the NOD/SCID animals of donor 727R disappeared by day 5, the 9 remaining animals displayed a detectable signal until day 10, 7 until day 14 and 3 until day 17 (Table **5.5**). Interestingly, one of the NOD/SCID animals administered with donor 2 (733S) displayed a weak signal until the end of the experiment (Table 5.5, Figure 5.5). The signal coming from this mouse seemed stronger than the other 4 until day 14. Then it stabilised around $2x10^5$ until day 31 (Figure 5.5b).

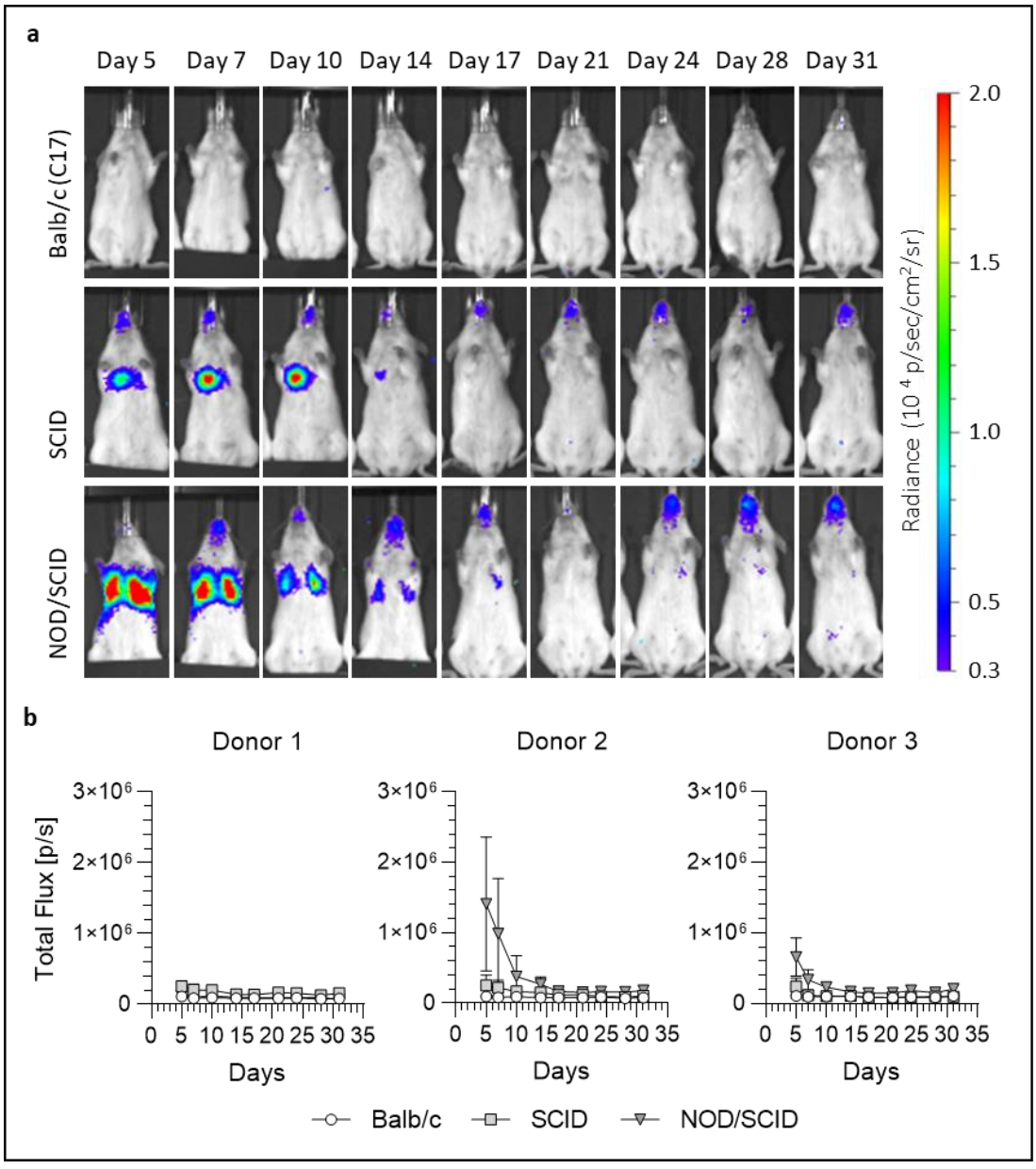

Figure 5.4|SCID and NOD/SCID mice displayed a weak but detectable signal even from 5 days post administration of UC-MSCs. (a) Representative bioluminescence images of BALB/c, SCID and NOD/SCID mice from day 5 to 31 post administration of $FLuc^+$ UC-MSCs (radiance scale from $0.3x10^4$

to 2x10^4 p/s/cm^2/sr). **(b)** Light output (flux) as a function of time (days) for each of the 3 UC-MSC donors in the 3 animal strains. Data are displayed as mean ± SD from n ≥ 4 for each donor.

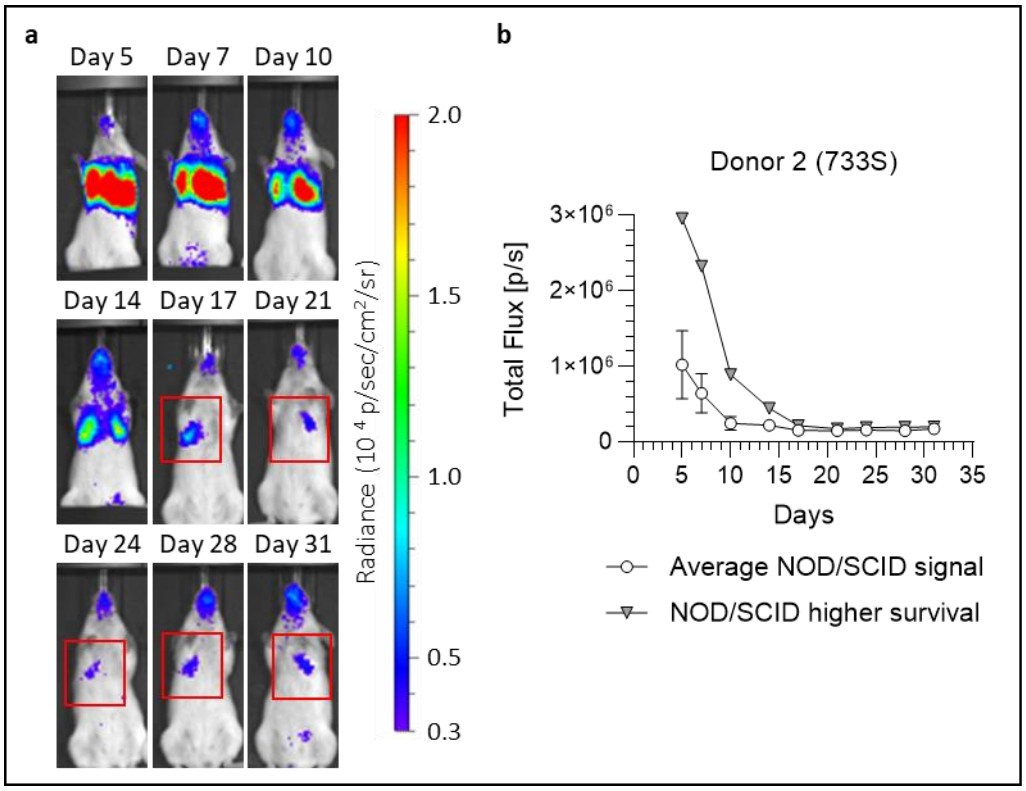

Figure 5.5| Images of the NOD/SCID animal administered with donor 2, which showed reduced cell death after day 5. (a) Representative bioluminescence images of the NOD/SCID mouse from 5 to 31 days post administration of FLuc$^+$ UC-MSCs donor 2 (radiance scale from 0.3x10^4 to 2x10^4 p/s/cm^2/sr). **(b)** Light output (flux) as a function of time (days) of the donor 2 comparing the signal from the animal that displayed signal until the end of the experiment with the average signal obtained from the other 4 NOD/SCID animals administered with the same donor. Data for the average signal are displayed as mean ± SD from n = 4.

Table 5.4: Number of SCID animals displaying detectable signal (n = 5 animals per donor).

Donor	Day 5	Day 7	Day 10	Day 14	Day 17	Day 21	Day 24	Day 28	Day 31
1-727R	5	2	2	2	0	0	0	0	0
2-733S	4	3	3	2	0	0	0	0	0
3-735O	3	1	1	0	0	0	0	0	0

Table 5.5: Number of NOD/SCID animals displaying detectable signal (n = 5 animals per donor)

Donor	Day 5	Day 7	Day 10	Day 14	Day 17	Day 21	Day 24	Day 28	Day 31
727R	0	0	0	0	0	0	0	0	0
733S	5	5	5	5	3	1	1	1	1
735O*	4	4	4	2	0	0	0	0	0

* n = 4

5.3.4 Flow cytometry analysis reveals an upregulation of the circulating neutrophils

C57BL/6 albino mice were used to investigate the impact of UC-MSCs on different immune cells, at 2h and 24h post administration. The percentage of innate (neutrophils, iMCs, macrophages, NK cells, mDC and pDC) and adaptive (CD4 T cells, CD4 Tregs, CD8 T cells and B cells) immune cells was investigated in the blood, the lungs, the spleen and the bone marrow.

The most remarkable results obtained from the data related to the innate immunity concern the neutrophils (Figure 5.6). Two hours after the administration of UC-MSCs increased levels of neutrophils were detected in the blood (25.5 ± 3.9% compared to 8.5 ± 2.1% in naïve mice), in the lungs (6.98 ± 2.74% compared to 1.39 ± 0.37% in naïve mice) and in the spleen (3.9 ± 2.1% compared to 0.72 ± 0.36% in naïve mice) (Figure 5.6a). 24 hours after the administration of the cells, the number of neutrophils returned to normal levels in the blood (7.8 ± 1.2%), the lungs (1.15 ± 0.42%) and the spleen (0.51 ± 0.17%, Figure 5.6a).

On what concerns iMCs, no statistical difference was detected 2 hours after the administration of the cells in any of the tissues or organs (Figure 5.6b). Nonetheless, the number of iMCs decreased significantly in the lungs and in the spleen in the next 22 hours, even if the original increase at 2h was not statistically different to that of naïve mice (Figure 5.6b)

No statistically significant differences were observed between groups for the macrophages (Figure 5.6c), the NK cells (Figure 5.6d) and the pDCs (Figure 5.6f). There was only a difference in the levels of the mDCs in the bone marrow, where the percentage of cells increased from 0.86 ± 0.18% in control mice to 1.50 ± 0.61% 2 hours after the administration of the cells (Figure 5.6e).

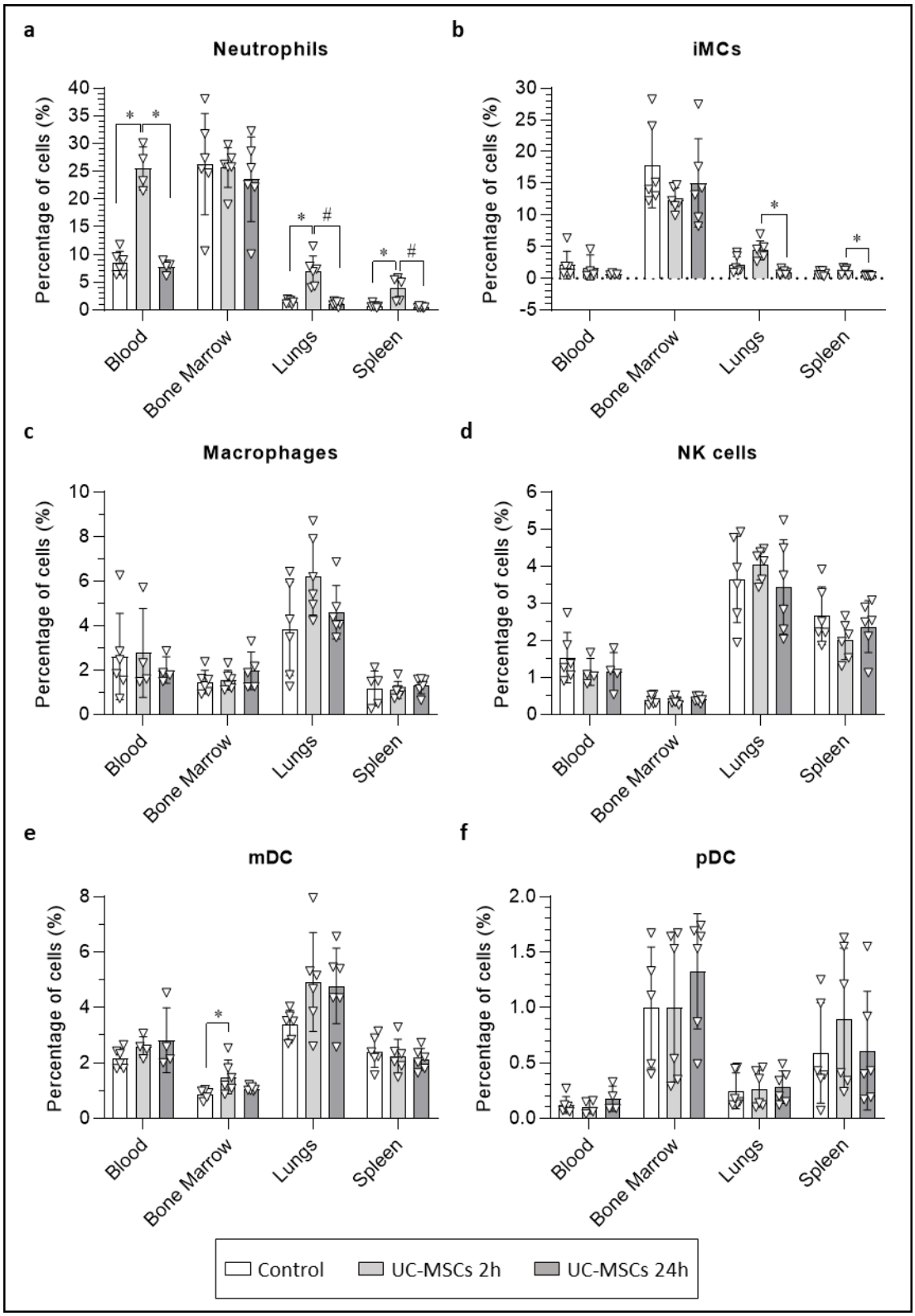

Figure 5.6| Distribution of innate immune cells in the mouse blood, bone marrow, lungs and spleen, 2h and 24h after the administration of UC-MSCs. Evaluation of the levels of **(a)** neutrophils, **(b)** immature myeloid cells, **(c)** macrophages, **(d)** natural killer cells, **(e)** myeloid dendritic and **(f)** plasmacytoid dendritic cells. Data are displayed as mean ± SD from n ≥ 4. Statistical analysis performed using the Kruskal-Wallis test and the Dunn's multiple comparison post hoc test. * $p < 0.05$, # $p < 0.01$

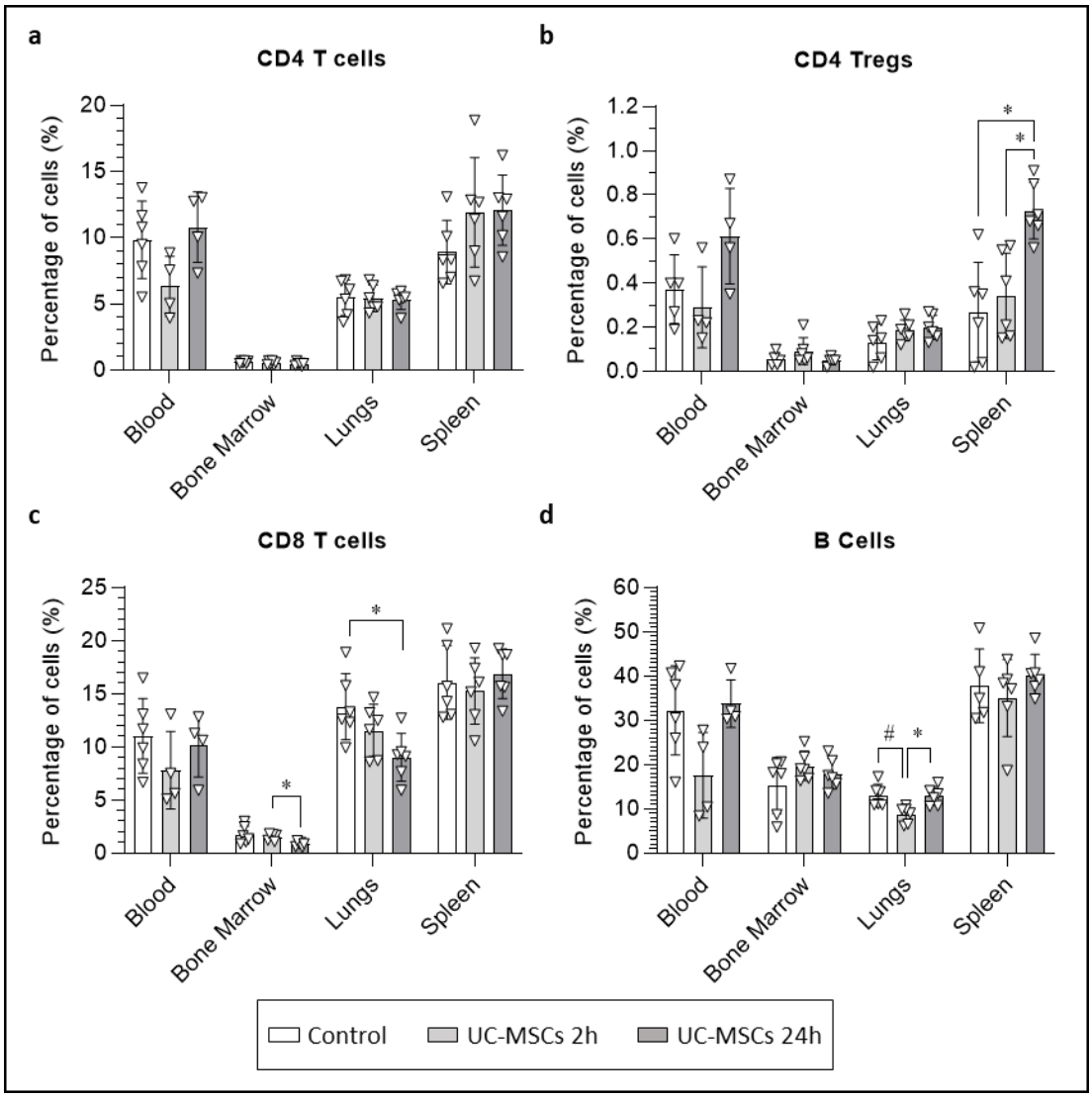

Figure 5.7| Distribution of adaptive immune cells in the mouse blood, bone marrow, lungs and spleen, 2h and 24h after the administration of UC-MSCs. Evaluation of the levels of **(a)** CD4 T cells, **(b)** CD4 T regulatory cells, **(c)** CD8 T cells and **(d)** B cells. Data are displayed as mean ± SD from n ≥ 4. Statistical analysis performed using the Kruskal-Wallis test and the Dunn's multiple comparison post hoc test. * $p < 0.05$, # $p < 0.01$.

The data from the adaptive immunity cells are summarised in Figure 5.7. The administration of the UC-MSCs did not affect the levels of CD4 T cells in any of the sites (Figure 5.7a), although it contributed to a slight increase in the number of CD4 Tregs in the spleen 24 hours after the administration of the cells from 0.27 ± 0.23% in naïve mice and 0.34 ± 0.19% in 2h mice to 0.73 ± 0.13% 24h post administration (Figure 5.7b).

Twenty-four hours post cell administration, the levels of CD8 T cells were statistically significantly reduced in the bone marrow, where they decreased from 1.53 ± 0.31% in 2h

mice to 0.84 ± 0.24% in 24h animals, and in the lungs, where the CD8 T cells decreased from 13.8 ± 3.1% in naïve mice to 9.0 ± 2.3% after 24 hours (Figure 5.7c).

Finally, a reduction in the levels of B cells in the lungs 2 hours after the administration of the cells (from 13.0 ± 2.5% to 8.7 ± 1.9%) was also identified. Their levels returned to basal amounts (12.9 ± 2.1%) after 24 hours (Figure 5.7d).

5.3.5 Multiplex analysis of the plasma of mice receiving UC-MSCs

To further explore the effect of UC-MSCs on the immune system of healthy animals, levels of 48 cytokines, chemokines, soluble receptors, and growth factors were measured in the plasma 2h and 24h after the IV administration of the cells. The levels of the analytes that were detectable in the samples are shown in Figure 5.8. Two hours after infusion, a statistically significant increase in the concentrations of Gro-α (CXCL1) and MCP3 (CCL7) was observed (Figure 5.8a-b). At the 24h time point, Gro-α levels were restored and MCP3 levels dropped to levels below that of controls (Figure 5.8a-b). MCP1 (CCL2) and IP-10 (CXCL10), which were undetectable in controls, increased to detectable levels at the 2h time point, but were again undetectable after 24 hours (Figure 5.8c-d). The levels of the soluble receptors IL-2R and IL-7Rα decreased after UC-MSC administration: IL-2R was significantly reduced after 24 hours (Figure 5.8e), whereas IL-7Rα was only detectable in the control group (Figure 5.8f). The plasma levels of RANKL were significantly reduced 24 h after the administration when compared to control and the 2h time point (Figure 5.8g). IL-18 was also significantly reduced after 24 h when compared to controls (Figure 5.8h). IL-22 level was clearly detectable only in control animals and significantly reduced after 2h (Figure 5.8i). After 24h, the IL-22 signal was detectable in only three animals (Figure 5.8i).

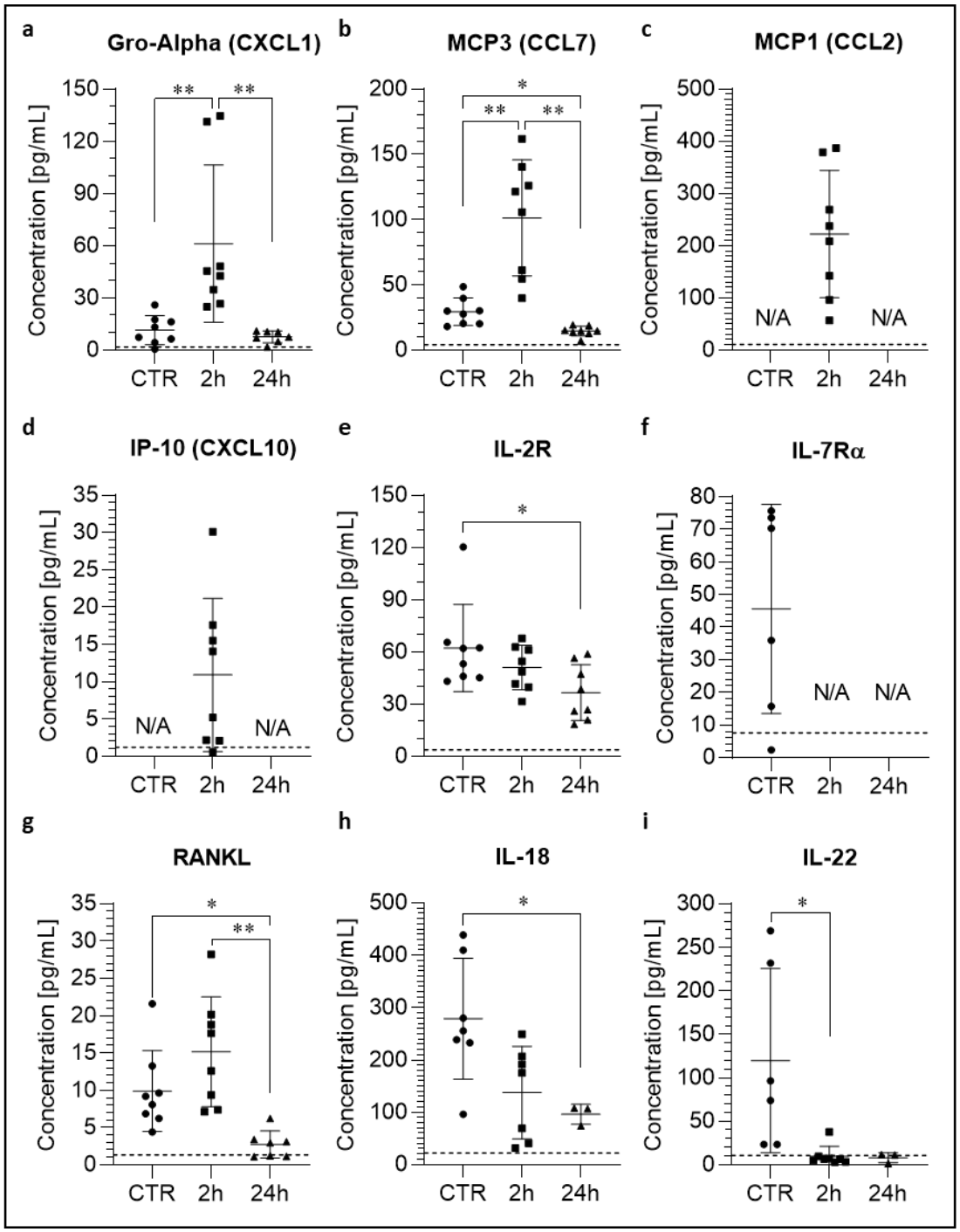

Figure 5.8| Plasma concentrations of cytokines and chemokines after IV infusion of UC-MSCs. Concentrations are expressed as pg/mL. **(a)** Plasma level of Gro-α (CXCL1). Lower limit of quantification (LLOQ) = 1.9 pg/mL. Data are presented as mean ± SD from n = 8 for each group. Kruskal-Wallis test with Dunn's multiple comparison post-hoc test. ** $p < 0.01$. **(b)** Plasma level of MCP3 (CCL7). LLOQ = 4.1 pg/mL. Data are presented as mean ± SD from n = 8 for each group. Brown-Forsythe and Welch ANOVA with Dunnett multiple comparison post-hoc test. * $p < 0.05$, ** $p < 0.01$. **(c)** Plasma level of MCP1 (CCL2). Data from control and 24h were displayed as out of range below (<=OOR, N/A in the graph). Statistical analysis not possible. LLOQ = 11 pg/mL. **(d)** Plasma level of IP-10 (CXCL10). Data from control and 24h N/A (<=OOR). Statistical analysis not possible. LLOQ = 1.2 pg/mL. **(e)** Plasma level of IL-2R. LLOQ = 3.8 pg/mL. Data are presented as mean ± SD from n = 8. Kruskal-Wallis test with Dunn's multiple comparison post-hoc test. * $p < 0.05$. **(f)** Plasma level of IL-7Rα. Data from 2 and 24h N/A

(<=OOR). Statistical analysis not possible. LLOQ = 7.6 pg/mL. **(g)** Plasma level of RANKL. LLOQ = 1.3 pg/mL. Data are presented as mean ± SD from n ≥ 7. Data from one of the 24h not shown (<=OOR). Brown-Forsythe and Welch ANOVA with Dunnett multiple comparison post-hoc test. * $p < 0.05$, ** $p < 0.01$. **(h)** Plasma level of IL-18. LLOQ = 22.2 pg/mL. Data are presented as mean ± SD from n = 7 (CTR and 2h) and n = 3 (24h); missing data points were N/A (<=OOR). Brown-Forsythe and Welch ANOVA with Dunnett multiple comparison post-hoc test. * $p < 0.05$. **(i)** Plasma level of IL-22. LLOQ = 10.5 pg/mL. Data are presented as mean ± SD from n = 6 (CTR), n = 7 (2h) and n = 3 (24h); missing data points were N/A (<=OOR). Kruskal-Wallis test with Dunn's multiple comparison post-hoc test. * $p < 0.05$. The LLOQ are represented in each graph by the dashed line.

No significant changes in plasma concentrations of BAFF, ENA-78 (CXCL5), Eotaxin (CCL11), RANTES (CCL5) and IL-1β were observed (Figure 5.9). The signal from BTC, G-CSF (CSF-3), GM-CSF, IFN-α, IFN-γ, IL-1α, IL-2, IL-3, IL-4, IL-5, IL-6, IL-7, IL-9, IL-10, IL-12p70, IL-13, IL-15/IL-15R, IL-17A (CTLA-8), IL-19, IL-23, IL-25 (IL-17E), IL-27, IL-28, IL-31, IL-33, IL-33R (ST2), leptin, LIF, M-CSF, MIP-1α (CCL3), MIP-1β (CCL4), MIP-2, TNFα and VEGF-A was below the OOR for almost all the animals (data not shown).

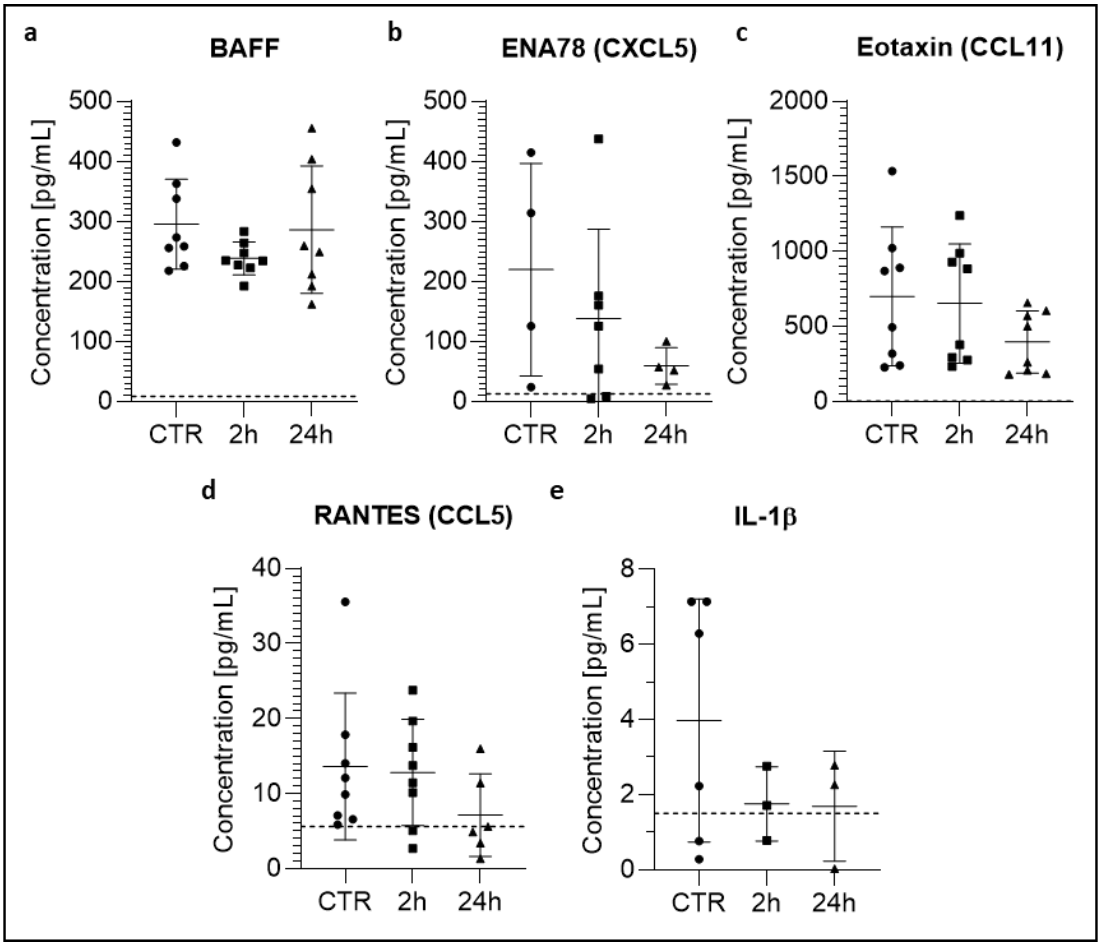

Figure 5.9| Plasma concentrations of cytokines and chemokines after IV infusion of UC-MSCs. Concentrations are expressed as pg/mL. **(a)** Plasma level of BAFF. LLOQ = 8.6 pg/mL. Data are presented as mean ± SD from n = 8 for each group. **(b)** Plasma level of ENA78 (CXCL5). LLOQ = 12.9 pg/mL. Data are presented as mean ± SD from n = 4 (CTR), n = 7 (2h) and n = 4 (24h);

missing data points were N/A (<=OOR) **(c)** Plasma level of Eotaxin (CCL11). LLOQ = 0.8 pg/mL. Data are presented as mean ± SD from n = 8 for each group. The LLOQ are represented in each graph by the dashed line. **(d)** Plasma level of RANTES (CCL5). LLOQ = 5.6 pg/mL. Data are presented as mean ± SD from n = 8 (CTR and 2h), and n = 7 (24h); missing data points were N/A (<=OOR). **(e)** Plasma level of IL-1β. LLOQ = 1.5 pg/mL. Data are presented as mean ± SD from n = 6 (CTR) and n = 3 (2h and 24h); missing data points were N/A (<=OOR). The LLOQ are represented in each graph by the dashed line.

5.4 DISCUSSION

The main aim of this chapter was to characterise the fate and role of MSCs *in vivo*, in terms of biodistribution, safety, survival over time and interaction with the host's immune system. The use of the major types of MSCs, all of which had been cultured, transduced and expanded following the same protocol, enabled the identification of any differences associated with the MSC source.

IV administered MSCs get entrapped in the lungs and are short-lived in healthy animals

Intravenous administration of MSCs is the most common delivery route used in clinical trials [286]. However, the lung entrapment experienced by MSCs following intravenous administration in small animals, also known as pulmonary first pass effect, is something well known and documented in the literature [102, 103, 276, 287]. Here, I started by evaluating the biodistribution of MSCs coming from different tissue sources, cultivated using the same tissue culture conditions, to investigate any possible differences in the behaviour of the cells after their administration *in vivo*. BLI performed immediately after the IV administration of the different MSCs in healthy C57BL/6 albino mice confirmed their entrapment in the lungs, irrespective of their tissue or origin. Also, none of the cells (umbilical cord, bone marrow or adipose tissue) escaped the lungs, neither on the day of administration nor in any of the following days. In fact, when administered to healthy animals, a major drop in the bioluminescence signal coming from the lungs was observed in the first 24h post injection. Furthermore, despite a very small fraction of the signal from A-MSCs being still detectable 3 days post administration, no signal from any of the MSCs was detected 7 days after injection. This result is consistent with various reports in the literature [102, 103, 287] and confirms that this effect is not associated with the origin of the infused MSCs. When cell therapies are considered, the fact that most of the MSCs die in the first 24 hours is not necessarily a bad result. Indeed, it has been proposed, that the apoptosis of IV administered MSCs in the lungs and the subsequent phagocytosis of the cell debris by local macrophages is a mechanism of MSC-mediated immunomodulation [102, 113, 116, 117, 288].

IV administered MSCs do not migrate when administered to IRI mice

It has been claimed in some studies that the presence of an injury can lead to the migration of a proportion of the intravenously administered MSC population toward the site of damage or, at least, an increase in cell-associated signal was detected in the region of injury [289-293]. Jin et al [290] suggested that intravenously infused BM derived MSCs can reach the liver when a chemical injury is induced [290]. Similarly, Jackson et al [294] used MR imaging to track the biodistribution of IV injected BM-MSCs in a model of rat brain lipopolysaccharide (LPS)-induced inflammatory lesions and showed the homing of the cells toward the site of injury [294]. A similar migratory capacity has also been observed in different models of kidney injuries [289, 292, 293, 295]. Some of these studies [289, 290, 295] suffer from the limitation of using lipophilic dyes (e.g. PKH26, CMFDA) to label the MSCs, which have been reported to escape the labelled MSCs and can be internalised by the host cells, leading to false positive results [296]. Due to the discrepancies in the published literature, it was important to investigate if the presence of a kidney injury could induce the migration of any of the MSCs tested in this work.

Here, we used a bilateral ischemia reperfusion injury model on male C57BL/6J albino mice to assess any changes in the biodistribution and survival of the MSCs when compared to healthy animals. Again, immediately after the administration, all the signal was originating from the chest of the animals, in the lung region. No signal was detected from the kidneys neither on the day of cell administration nor on any of the following days. Interestingly, 24 hours after the administration all mice with an injury had a signal slightly higher than the corresponding controls, irrespective of the type of MSCs. The reasons for that are unclear and we did not investigate further, but it could be possible that the inflammatory state induced in the animals by the presence of the injury could somehow help the MSCs to survive in the lungs of the animals. Nonetheless, after seven days from the administration no signal was detected in any of the conditions, confirming that the cells disappear even in the presence of a renal injury. Our data did not reveal any migratory capacity of the different MSCs induced by the presence of the injury, nor any major increase in the survival of the administered cells.

UC-MSCs survive longer in some immunocompromised animals

As previously mentioned, apoptosis of infused MSCs can be a mechanism of action by which the administered cells can exert their immunomodulatory capacity [288]. Dazzi and co-workers have recently identified in a mouse model of graft versus host disease (GVHD) that the apoptosis of the MSCs was directly mediated by $CD56^+$ Natural Killer and $CD8^+$ T cytotoxic

cells [113]. To detect apoptosis, Dazzi evaluated caspase activity in the MSCs following their administration to either GVHD or healthy animals. For that, he applied a BLI strategy to enable the quantification of caspase activity *in vivo*. Interestingly, only MSCs administrated to GVHD mice presented high caspase activation, revealing that perhaps different mechanisms are involved with cell death in healthy animals [113].

Despite Dazzi reporting very little caspase activation in healthy animals, it is important to clarify whether the immune system can have a direct role in the clearance of the cells that is observed in the first 24 hours post-administration and, indeed, in the long-term survival of the MSCs. This is important not only to understand the mechanism that can lead to MSC death after infusion, but also because such cells are currently used to treat patients with impaired or compromised immune systems [297, 298] and the risk of tumorigenicity associated with the use of MSCs has not yet been completely addressed [299]. For this purpose, two different immunocompromised strains, severe combined immunodeficient (SCID) and non-obese diabetic (NOD)/SCID were used here. SCID animals are characterised by a mutation of the Prkdc gene that prevents the maturation of B and T cells, making this strain ideal to investigate the role of the adaptive immunity. Also, the IV administration of UC-MSCs in SCID mice has already been reported to be associated with an increased long-term survival of the cells in around 25% of the animals tested [99]. NOD/SCID mice combine the SCID defects with an impaired natural immunity, which is due to the NOD background, characterised by defective NK-cells, a lack of circulating complement as well as impaired macrophages and antigen presenting cells. Because I did not observe any difference in the clearance of the different type of MSCs when I tested those in healthy BALB/c animals, and the cost/complexity associated with such experiments, I decided to carry out this analysis using 3 different UC-MSCs donors.

As expected, immediately after the administration of the UC-MSCs to SCID and NOD/SCID animals, all the signal detected originated from the lungs, further confirming the pulmonary entrapment. Also, in the first 24 hours post administration, the signal dropped not only in the control immunocompetent BALB/c group, but also in the immunocompromised ones in a comparable way. This trend also continued at day 3 and suggests no direct involvement of either the natural or adaptive immunity in the initial clearance of the cells, indicating that if the cells die due to apoptosis, this is probably not via a mechanism directly induced by the host. On the other hand, while the BALB/c immunocompetent animals behaved like the C57BL/6J albino, showing complete signal loss by day 7, the two immunocompromised groups revealed some variability in MSC survival. It seems that the small fraction of MSCs

that manage to survive the first 72h tend to persist for longer in immunocompromised animals. 10 days post administration, 40% of the SCID animals still displayed some weak detectable signal and on day 14, the last day the signal was detectable before disappearing completely, 27% of them still displayed some cells. These results are in line with what is previously reported in the literature [99], confirming the reproducibility and the consistency of such data. Similar results were obtained with the NOD/SCID animals. Here, while the UC-MSC from one of the donors displayed a decay comparable to that observed in the immunocompetent animals, with no signal detectable by day 7, the MSCs from the two other donors revealed a longer survival in the NOD/SCID animals. After 10 days from administration 100% of the animals that received cells from these 2 donors still displayed some detectable signal. Also, while the signal disappeared after 17 days in most of the animals, some signal was still detectable in 60% of the NOD/SCID animals administered with the MSC from one of the donors, and one of these mice still had a weak signal detectable by the end of experiment, at 31 days post cell administration. These results seem to suggest that the initial death of the cells is unlikely to be associated with an involvement of either the adaptive or the natural immunity. It is possible that the microenvironment of the capillaries of the lungs is not suitable for MSC survival. This can also explain what was observed in the IRI animals. It is indeed well known that acute renal injuries can affect the lungs [300, 301]. It could be possible that the inflammation induced in the lungs by the IRI can increase the local vasodilation, explaining the enhanced survival of the MSCs in the IRI animals. However, the fact that a small percentage of cells can survive longer than 3 days in the two immunocompromised strains tested seems to suggest that both immunological compartments have a role, either direct or indirect, in the clearance of this fraction of infused MSCs. Nonetheless, by the end of experiment only one of the NOD/SCID animals had a detectable signal coming from the lung region and the signal never increased during the study. These data suggest that even in an immunocompromised host, MSCs are safe and do not undergo uncontrolled proliferation. These results are in line with a recent study that revealed the lack of tumorigenesis and pro-tumorigenic potential of human UC-MSCs in NOD/SCID mice [302].

UC-MSCs induce neutrophil migration

Although the death of MSCs is likely unrelated to a direct effect of the host immune system, it is well recognised in the literature that MSCs do interact with the host's immune system, either directly or indirectly, to yield several immunomodulatory mechanisms [280]. In a recent study, Heng and co-workers revealed that preventing the apoptosis of IV-

administered MSCs had a negative impact on their immunomodulatory capacity [288], further reinforcing the hypothesis proposed by Dazzi [113]. Also, efferocytosis, the process by which apoptotic cells are engulfed by local immune cells without triggering a pro-inflammatory response, has been reported to be one of the main immunomodulatory mechanisms exerted by infused MSCs [118, 119, 288]. One important aspect of this chapter is to clarify the interactions between the administered MSCs and the host immune system. Because in all the conditions tested (healthy, injured, immunocompromised) the greatest signal reduction was observed in the first 24 hours post cell administration, I investigated whether the administered MSCs triggered an immunological response in that time window. To do that, the percentage of different immune cell populations was evaluated in several body sites associated with the immune system (bone marrow as primary lymphoid organ, spleen as secondary lymphoid organ) or related to where the cells, both the immune system (IS) cells and the MSCs, are localised (the lungs, where the MSCs are trapped, and the blood, where IS cells are circulating and where the MSCs are infused). 2 hours after the administration of the MSCs, a huge mobilisation of neutrophils was observed in the blood, in the lungs and in the spleen. Neutrophils, as part of the innate immune system, make up a first line host defence. Also, they are major phagocytic cells, which have been reported to be actively involved in the phagocytosis of apoptotic cells [303]. Similar results were recently obtained by Pang et al, where they identified monocytes and neutrophils as the major cell types responsible for the efferocytosis of IV administered BM-MSCs in mice [288]. The increase in the percentage of neutrophils observed via flow cytometry was further strengthened by the multiplex analysis of the plasma of the animals, as several neutrophil chemoattractants (CCL2, CCL7, Gro-α and IP-10) were upregulated (CCL7 and Gro-α) or raised above detectable levels (CCL2 and IP-10) 2 hours after the administration of the cells. The involvement of CCL2 and CCL7 in the recruitment of neutrophils to the lungs has also been reported by Mercer et al who showed this after the intranasal administration of recombinant CCL2 and CCL7 into mice [304]. Gro-α, also known as CXCL1, not only plays an important role in recruiting neutrophils, but also in their activation [305]. These results are in line with a study performed by Hoogduijn et al [306], who also identified an upregulation of the serum levels of MCP-1 (CCL2) and Gro-α (CXCL1) 2 h after the IV administration of mouse adipose derived MSCs in 8–10 week old C57BL/6 mice [306]. Also, he reported that the level of such cytokines went back to normal after 20 hours, in close agreement with my 24h measurements [306].

Although monocytes have also been reported to be responsible for MSC efferocytosis [118, 119, 288], I did not observe any statistically significant upregulation of these cells in the lungs after two hours. This can be either because this time point was not optimal for detecting these changes or because I used pan-monocytes markers, meaning that I couldn't distinguish between different pro- and anti-inflammatory populations. Piraghaj et al [119] revealed an increase in the M2 anti-inflammatory and regulatory phenotype following incubation of macrophages with apoptotic A-MSCs [119]. Similarly, Min et al [307] showed that the efferocytosis of apoptotic cord tissue derived MSCs by macrophages enhanced their immunosuppressive capacity [307].

It is interesting to notice that the presence of MSCs seemed to have an impact on the adaptive immunity in the lungs of the animals. The percentage of B cells reduced after 2 hours, although it went back to the same levels as controls on the day after, and the number of CD8 T cells decreased 24 hours post MSC administration. Despite the levels of B-cell activation factor seems to reduce two hours after the administration of the MSCs, such levels are not statistically different from the control group and from 24h after the administration of the cells. However, it is unclear whether this is directly mediated by the presence of the MSCs, by paracrine mechanisms or by other cells recruited to the lungs.

Among the other analytes investigated, interesting results were observed for IL-18, IL-22, RANKL, sIL-2R and sIL-7Rα.

IL-18 is a pro-inflammatory cytokine of the IL-1 family produced by antigen presenting cells that influences both the innate and adaptive immunity as it can enhance T cell and NK cell maturation [308, 309]. Interestingly, MSCs were reported to reduce the IL-18 signalling pathway in NK cells *in vitro* [310]. Also, in a rat model of sepsis, the intravenous administration of A-MSCs has been shown to reduce the level of IL-18 [311]. Here, it is unclear if the reduction of IL-18 observed in the blood stream can exert a protective effect on the animals, but it would be worth to investigate this cytokine in pathological models.

IL-22 is a cytokine belonging to the IL-10 family with both protective and pro-inflammatory functions. Here I report a downregulation of IL-22 24 hours after the administration of the cells. The MSC-mediated downregulation of IL-22 has already been reported *in vitro* and has been associated with paracrine pathways [312]. Wu et al observed that $CD4^+$ T-Cells isolated from patients with immune thrombocytopenia cocultured with UC-MSCs were associated with reduced IL-22 production [312]. Similar results were obtained by Hyvärinen et al who

showed that both coculture with MSCs and MSC-released EVs increased the polarisation of macrophages toward an anti-inflammatory phenotype [313].

Receptor activator of NFkB ligand (RANKL) is a TNF-family cytokine that is not only required for osteoclast formation but is also important for the development of immune cells, such as dendritic cells, and of lymph nodes [314, 315]. In a recent study by Papadaki et al the overexpression of RANKL in a mouse model of osteoarthritis was associated with a strong increase in the inflammatory response [316]. Also, RANKL has been documented to induce neutrophil degranulation [317], and its inhibition was reported to ameliorate cardiac infarct size and function in mice [318]. Li et al recently published a study where the administration of BM-MSCs in a rat model of collagen-induced arthritis was associated with the reduction of serum RANKL mediated by the reduction of IL-22 [319]. Whether in my study the levels of soluble RANKL are reduced directly or indirectly by the MSCs and what the potential effects could be are unclear.

IL-2 is a cytokine with important roles in both promoting immunological responses and inducing immunological tolerance [320]. In the same way, the soluble form of the IL-2 receptor has a controversial role: it can either function as a decoy-receptor, reducing the availability of the IL-2, or it can mediate the presentation of IL-2 to immune cells expressing dimeric forms of the IL-2R [321]. IL-7, on the other hand, is an important factor promoting the survival of lymphoid precursors and in modulating T and B cell maturation [322]. Soluble cytokine receptors, such as IL-2R and IL-7Rα in this case, can play important roles in regulating inflammation and immunological events. They can indeed function both as agonist and antagonist in cytokine signalling [323]. Soluble IL-2R has been proposed to interfere with the IL-2/IL-2R pathway, exerting an important effect on the balance between immunity and tolerance [321]. Here I observed a statistically significant reduction of soluble IL-2R after 24 h from the administration of the UC-MSCs. In the same way, while I could detect the presence of soluble IL-7Rα in the control mice (6 out of 8), its level was below the detection limit after 2 and 24h from the administration. As I did not observe any increase in the plasma levels of IL-2 or IL-7 it is unclear whether they were exerting any function or if they were simply cleared by the blood stream. Also, it is unclear if the observed reductions have any biological relevance.

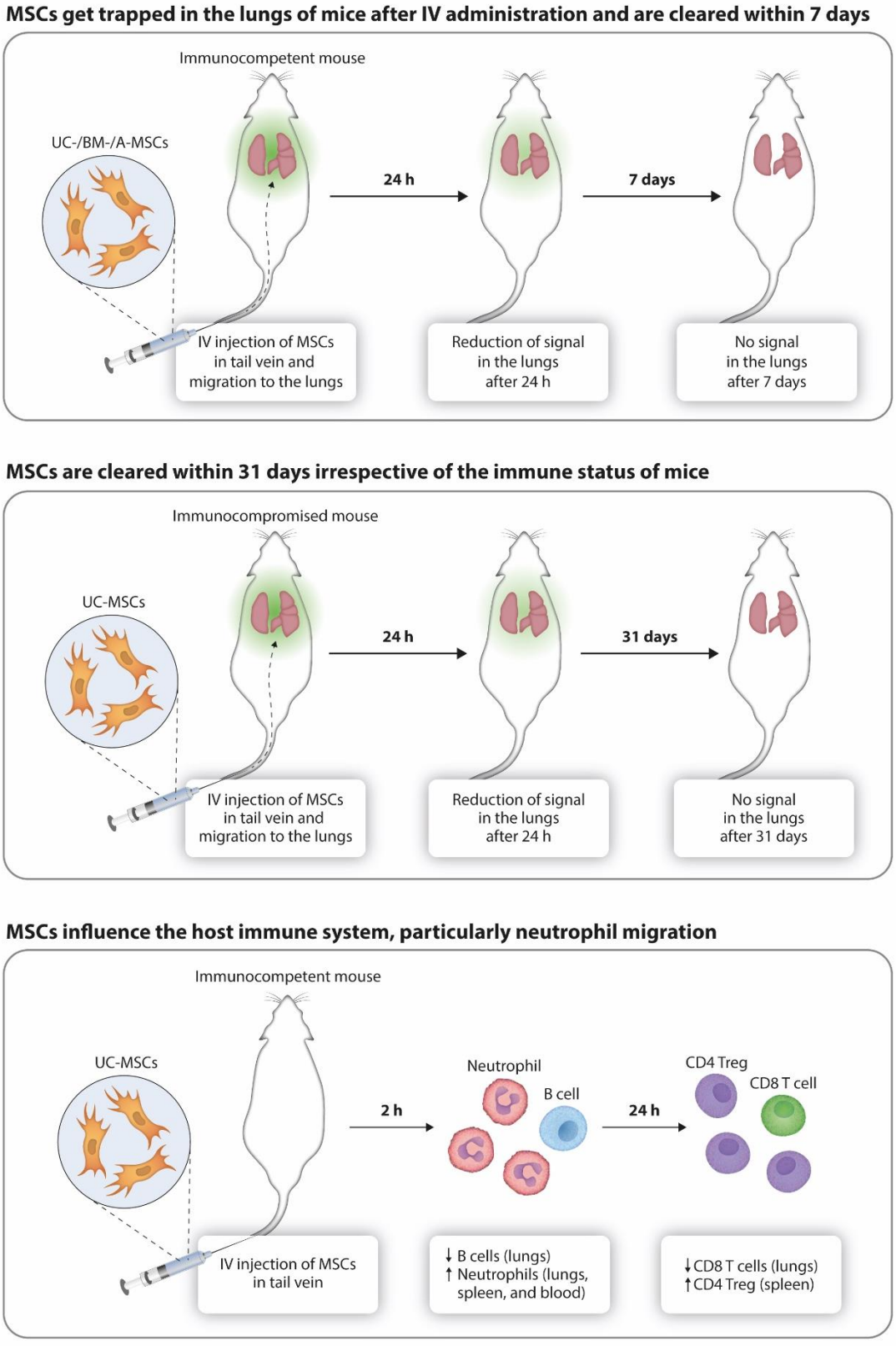

Figure 6.1| Graphical abstract of the main finding achieved in this thesis. Figure produced by Glaze Art for Science.

The experiments performed in this thesis were designed to provide insights into the *in vivo* biodistribution of UC-, BM- and A-MSCs and to evaluate their survival and interactions with the host immune system after IV administration. With these goals in mind, I started by establishing a common protocol for culturing these MSCs, characterising them and optimising a transduction protocol to introduce a reporter gene that enabled me to apply the imaging techniques that were required to perform the *in vivo* experiments. This work led to multiple key findings:

1. **MSCs cultured under the same tissue culture conditions have different characteristics that are associated with the tissue source and the donor.**

BM-, UC- and A-MSCs are the most commonly used MSCs both in pre-clinical studies and clinical trials [clinicaltrial.gov] and this thesis was focused on determining and comparing their biodistribution and safety *in vivo*. Prior to that, they were characterised *in vitro*. To reduce the impact of tissue culture protocols on the outcome of the results, these were standardised and the same medium and batch of serum were used. This is important as batch-to-batch variability of FBS is well known to have an impact on the culture of MSCs [324].

The results revealed that even when using standardised tissue culture protocols, MSCs from different sources display differences that are tissue- and donor-related. BM-MSCs exhibited the longest doubling time and the highest inter-donor variability, whereas UC-MSCs and A-MSCs had less donor-to-donor variability. Also, UC- and A-MSCs displayed a similar doubling time, despite their seeding density being different (3000 cells/cm^2 and 300 cells/cm^2, respectively). The expression of surface markers expected to be negative in MSCs was also different between the three MSC types and between donors of the same MSC type. While all the UC-MSCs were negative for the expression of CD11b, CD19, CD34, CD45 and HLA-DR, A-MSCs displayed small levels of positivity to CD34 and CD45 (2 out of the 3 donors) and BM-MSCs showed some positivity to HLA-DR (2 out of the 3 donors). Although these results are not particularly worrying per se, as discussed in CHAPTER 3, they highlight not only differences between MSCs from different tissues, but also among donors.

The absence of standardised manufacturing processes makes it difficult to optimise MSCs as a therapeutic product [325] and complicates the comparison of results obtained from different pre-clinical and clinical studies. Here, the use of standardised tissue culture conditions still resulted in variability, highlighting the difficulty in developing a single standardised manufacturing process that can be applied universally across all MSCs.

Nonetheless, it is worth underlining that UC- and A-MSCs displayed a comparable doubling time despite being seeded at different densities. Thus, it would be worth exploring other seeding densities for the BM-MSCs, to determine if it is possible to achieve a doubling time comparable to the two other types of MSCs, as there is evidence that doubling time can be dependent on seeding density [326, 327].

To carry out the *in vivo* experiments, all MSCs had to be genetically modified to express a bioluminescence reporter. Because this process could potentially affect the properties of the MSCs, the cells were fully characterised following transduction to determine if there were any significant changes in key properties.

2. DEAE-dextran is an effective polycation to increase the lentiviral transduction efficiency of UC-, BM- and A-MSCs.

Lentiviral infection with the use of polycations as an adjuvant is a method that is commonly used to generate stably transduced cells. However, it is known that some polycations can negatively affect primary MSCs [247-249, 260] and to date, no single study has explored the effect of different polycations on the transduction efficiency and properties of UC-, BM- and A-MSCs. In this thesis, I explored a range of polycations (Pb, Ps and DEAE-dextran), using transduction protocols with and without spinoculation, to produce stably transduced MSCs from these three tissue sources. Overnight incubation of LVs with 6 µg/mL DEAE-dextran was associated with the best transduction efficiency without compromising the viability of the cells and worked consistently with lentiviral particles encoding for different transgenes. Furthermore, transduced and sorted $FLuc^+$ MSC populations revealed no significant changes in proliferation, morphology or expression of MSC markers when compared to naïve MSCs. These $FLuc^+$ MSCs were then used for all the *in vivo* biodistribution and safety studies.

It is worth mentioning that the DEAE-dextran static protocol was not the only suitable protocol to transduce MSCs. The use of Pb together with a spinoculation step was actually the best option to transduce BM-MSCs, and the incubation with Ps coupled with spinoculation was also associated with a good transduction efficiency for UC- and BM-MSCs. It is important to stress the fact that I used consistent tissue culture conditions not only to culture the MSCs, but also to transduce them, which further strengthens the obtained results by reducing the likelihood that the findings from this thesis could be affected by the protocols used to prepare the cells. Nonetheless, alternative protocols can be considered when transducing different types of cells.

3. The use of the novel redshifted AkaBLI reporter system is not superior to the common FLuc system for the tracking of intravenously administered MSCs via bioluminescence.

When D-Luciferin is oxidised by FLuc, the wavelength of ~50% of the emitted photons is below 600 nm [201, 265] which results in them being strongly attenuated by mammalian tissues [328], reducing imaging sensitivity. Several studies have focused on the engineering of luciferase enzyme analogues and in the development of novel substrates in order to shift the emission peak to the near infrared spectrum [204, 265-269]. The AkaBLI is a novel red-shifted BLI system recently developed for cell tracking in preclinical models and claimed to offer superior sensitivity when compared to FLuc [205]. Because this luciferase system had not been used to track the biodistribution of MSCs, it was important to systematically compare the performance of AkaBLI and the standard Firefly luciferase (FLuc) systems with these cells.

In CHAPTER 4 umbilical cord MSCs were transduced to produce two genetically engineered populations, expressing either AkaLuc or the engineered FLuc (luc2). The bioluminescence of $FLuc^+$ and $AkaLuc^+$ cells was assessed both *in vitro* (emission spectra, saturation kinetics and light emission per cell) and *in vivo* (substrate kinetics following intraperitoneal and subcutaneous administration and biodistribution of the cells up to day 7). One of the differences observed between the two systems was associated with the route of administration of the substrates. When the substrates were administered SC, both BLI systems displayed a similar biodistribution kinetics, with the signal reaching a plateau approximately 20 minutes after administration of the substrate, allowing consistent acquisition of data. However, the signal intensity of $AkaLuc^+$ cells was not stronger than $FLuc^+$. On the other hand, when the substrates were administered IP the kinetics were different, with $AkaLuc^+$ cells displaying a peak immediately after administration of the substrate and the FLuc cells showing signal kinetics similar to the SC route. For our experimental procedures, this represented a critical limitation, as a peak shortly after the administration of the substrate and the absence of a plateau can negatively affect the reproducibility and the reliability of the data, especially when long exposure times are required. It is worth noting that the kinetics observed by Iwano et al [205], one of the first reports on the use of AkaBLI, was completely different when imaging cells administered intracranially where the signal after IP administration of the substrate peaked after approximately 15 minutes [205]. These differences in kinetics between organs have never been reported for FLuc and show that AkaBLI results might be inconsistent when doing whole body imaging.

Another AkaBLI limitation observed in CHAPTER 4 was the detection of an unspecific liver signal when the substrate was injected IP, found even in mice that received no MSCs. Although this has been previously reported [196, 278], the quantification of the signal 3 days post administration revealed that the unspecific signal from Akalumine-HCl was actually as strong as the MSC-specific signal from FLuc combined with D-Luciferin, highlighting the potential for inaccuracies when using AkaBLI.

Finally, although Akalumine-HCl has already been reported to be cytotoxic *in vitro* [214, 279], toxicity had not been previously described in animals. The results presented in CHAPTER 4 revealed the formation of lesions in the sites of SC injection of Akalumine-HCl, with different degrees of severity. The nature of these lesions was not investigated here but it is clear that the substrate leads to an abnormal reaction in the animal's skin. On the other hand, administration of substrate IP did not lead to any observable adverse reaction. This could be because the effects are less severe than SC, because the nature of IP delivery makes it more difficult to identify the specific injection area, or because SC administration is associated with a higher local concentration of the substrate compared to IP.

In summary, the data collected revealed no superiority of the AkaBLI to the FLuc system for the experimental set-up used in this thesis. Actually, I found that the FLuc system had a better performance in terms of: (i) stronger signal with SC administration of substrate, which has no bias towards organs of the torso; (ii) signal kinetics, exhibiting a plateau whether the substrate is administered SC or IP, offering a uniform data acquisition window; and (iii) safety, with a non-toxic substrate that is specific to the enzyme of interest.

4. **All MSCs tested, irrespective of the tissue source, are entrapped in the lungs and are short lived when administered intravenously in mice; however, the presence of a kidney injury leads to a minor prolongation of their survival.**

The standardisation of culture and transduction protocols for MSCs enabled my investigation of their biodistribution following IV administration into healthy and injured (IRI) mice. In both groups the cells reached the lungs immediately after their administration, where they became entrapped in the microcapillaries of this organ. Also, the cells died over time and were completely undetectable after 7 days. This was not unexpected and in line with the literature [102, 103, 276, 287].

No migration away from the lungs was observed in either healthy or injured animals, but interestingly, all three types of MSCs displayed a prolonged survival over the first 24 hours in the IRI animals. This was particularly evident for the A-MSCs. As mentioned in CHAPTER 5, I

hypothesised that the inflammatory state induced in the animals by the presence of the injury could somehow help the MSCs to survive in the lungs of the animals. The injury induced in this bilateral renal IRI model is temporary and reported to completely recover within 3 days from the induction of the injury [282]. This is in line with the enhanced cell survival observed, as after 3 days the signal detected in the lungs of healthy and injury animals is similar.

Several mechanisms of action have been proposed for the MSCs, including direct and indirect immunomodulation [329], secretion of extracellular vesicles [330, 331] and the shedding of microRNAs [332, 333]. Whether the cells need to be alive to exert their functions is still under debate, but apoptosis has been proposed as a mechanism whereby the MSCs can interact and prime the host immune system [102, 113, 116, 117].

Because the survival of the cells can have an impact on their possible therapeutic function, it would be interesting to investigate whether this can be further enhanced by inducing a chronic condition in the animals. Also, lipopolysaccharide (LPS) could be utilized to trigger a systemic inflammatory response to investigate whether this can enhance the survival of the cells in the lungs. Exploring how the general health status of the host can influence the survival of the MSCs is important not only for their therapeutic potential, but to possibly improve the patient enrolment criteria when recruiting for a clinical study.

5. **The immune system of the host has no role in the initial cell death observed after the infusion of UC-MSCs, despite an impaired immunological status resulting in an increased cell persistence. UC-MSCs administered in immunocompromised animals are safe and do not proliferate out of control.**

Possible tumorigenicity and uncontrolled differentiation are still concerns on the use of live administered MSCs in the clinic [167, 169, 170, 334]. In CHAPTER 5 I investigated the biodistribution and the survival of UC-MSCs in two different immunocompromised mouse strains, SCID and NOD/SCID, to clarify both the role of the immune system in the cell death observed in immunocompetent animals and the possible proliferation of the administered cells. Because I did not observe any difference between the UC-, BM- and A-MSCs in the previous experiments and the cells were all cultured and transduced following standardised tissue culture procedures, I only used UC-MSCs to investigate the fate in immunocompromised mice.

After confirming that lung entrapment also occurs in immunocompromised strains, I observed a decay in bioluminescence signal from UC-MSCs administered to SCID and

NOD/SCID mice that was comparable to that of immunocompetent animals, both at day 1 and at day 3. Because of this, a direct role of either the innate or the adaptive immunity in the initial death of the cells was excluded. However, while all the immunocompetent animals showed no signs of cells 5 days post administration, this was not the case for the SCID and NOD/SCID animals. Data collected in CHAPTER 5 indicated a prolonged survival of a small fraction of cells in some, but not all the SCID and NOD/SCID animals. This suggests that, despite not being actively involved in the initial cell death, the immune system is likely to have a role, either direct or indirect, in the death of those MSCs that survive beyond day 3. Nonetheless, an impairment of the immune system is not likely to allow the MSCs to proliferate out of control or to migrate and engraft in other tissues, as they eventually completely disappear.

In summary, I observed (i) a reduced cell death when an ischemia injury procedure was induced in immunocompetent mice and (ii) an enhanced persistence of those cells surviving the initial cell death in immunocompromised mice. Although in both cases the cells were cleared by the end of the experiment, it would be interesting to investigate what would be the effect of inducing an inflammatory state in immunocompromised animals on the survival of IV administered MSCs. Patients enrolled for clinical trials may have comorbidities, and some may be immunocompromised, so clarifying if the presence of multiple factors can impact on the survival of the MSCs can help in understanding both their therapeutic potential and their safety.

6. In mice, the presence of UC-MSCs in the lungs triggers a quick neutrophil response 2 hours after their administration.

In CHAPTER 5 I investigated if the administration of UC-MSCs had an influence on plasma cytokines or the presence of several immune cell populations in different organs. As time points for this study, I choose 2 and 24h after MSC injection. The most striking result was the quick upregulation of neutrophils in the blood, in the lungs and in the spleen at 2 h after administration. The neutrophil chemoattractants CCL2, CCL7, Gro-α and IP-10 were also increased in plasma at this time point. It is unclear if these chemoattractants are released by the infused MSCs, by local endothelial cells from the lung capillaries, or by local immune cells that are immediately triggered by the presence of the MSCs. It is worth highlighting that this appears to be a quick and short-lived response by the host, as the levels of neutrophils and the chemoattractants mentioned above are restored after 24 hours. The increase of neutrophils in the spleen is also interesting, as unlike the blood and lungs, no UC-MSCs

reached this organ. As a secondary lymphoid organ, the spleen is connected to the lymphatic system and can be considered analogous to a large lymph node [335]. The reasons why I observed an upregulation of the neutrophils in the spleen immediately after the administration of the UC-MSCs is unclear and should be further investigated, particularly considering that migrating neutrophils could interact with local T- and B-cells in the white pulp. In that aspect, it is interesting to note that I observed a statistically significant increase in the percentage of T regulatory cells in the spleen 24 hours after the administration of the cells. Whether this is directly related to the release of any factors by the MSCs or by neutrophils or other immune cells migrating to the spleen, is unclear and should be investigated.

These results highlight a clear response of the immune system to the presence of the MSCs. The quick response of the neutrophils, as innate immune cells, is not unexpected, but it would be interesting to investigate the behaviour of other immune cells at different time points. It is worth pointing out that B-cells and CD8 T-cells decreased in the lungs 2 and 24 h after the administration of the cells, respectively. This is a quick response of the adaptive immune system, and it would be interesting to investigate what is happening in the spleen at later time points following the administration of the cells. The MSCs are dying in the lungs and the debris is probably removed by recruited phagocytic cells. These cells are likely to migrate to local lymph nodes and to the spleen to exert their antigen presenting cell (APC) functions [335-339]. MSCs are known to exert immunomodulatory functions through different pathways, but nothing is reported in the literature about the interaction of APCs that have engulfed fragments of dead MSCs with B and T naïve cells.

On that concerns the reduced cell death observed in animals that received the IRI, it would be interesting to investigate the response of the immune populations of those animals at different time points and compare it to IRI animals that do not receive cells. Such animals would probably have a systemic inflammatory condition induced by the presence of the injury, so the experiments must be planned with caution. It would also be interesting to investigate the inflammatory populations recruited at the site of the injury. The use of genetic reporter techniques [340] could be used to discriminate between immune cells that have engulfed MSC debris and have migrated there (if this is the case) and inflammatory cells recruited by the injury itself.

6.1 CONCLUSIONS

To conclude, I have shown that the three most common types of MSCs used in clinical trials (UC-, BM- and A-MSCs) reach the lungs following IV administration. Additionally, those cells do not escape the lungs even when an injury is induced in the kidneys, or when the animals are immunocompromised. Most of the cells die shortly after administration, and this is likely because the lung microenvironment isn't suitable for their long-term survival. The immune system is likely responsible for the killing of only those cells that can survive the initial cell death. Finally, despite most of the cells dying in the first 24 hours, they induce an immediate immunological reaction in the host, with a particular involvement of neutrophils. A further comprehension of how the MSCs either directly or, indirectly by paracrine signalling or cell death, can influence the immune system of the host could be key to the successful development of effective MSC-based therapies for different diseases.

REFERENCE LIST

1. Haraldsson, B. and M. Jeansson, *Glomerular filtration barrier.* Curr Opin Nephrol Hypertens, 2009. **18**(4): p. 331-5.
2. Abrahamson, D.R., *Role of the podocyte (and glomerular endothelium) in building the GBM.* Semin Nephrol, 2012. **32**(4): p. 342-9.
3. Miner, J.H., *Glomerular basement membrane composition and the filtration barrier.* Pediatr Nephrol, 2011. **26**(9): p. 1413-7.
4. Reiser, J. and S. Sever, *Podocyte biology and pathogenesis of kidney disease.* Annu Rev Med, 2013. **64**: p. 357-66.
5. Puelles, V.G., R.N. Douglas-Denton, L.A. Cullen-McEwen, J. Li, M.D. Hughson, W.E. Hoy, P.G. Kerr, and J.F. Bertram, *Podocyte Number in Children and Adults: Associations with Glomerular Size and Numbers of Other Glomerular Resident Cells.* J Am Soc Nephrol, 2015. **26**(9): p. 2277-88.
6. Puelles, V.G. and J.F. Bertram, *Counting glomeruli and podocytes: rationale and methodologies.* Curr Opin Nephrol Hypertens, 2015. **24**(3): p. 224-30.
7. Johnson, R.J., J. Feehally, and J. Floege, *Comprehensive clinical nephrology E-Book*. 2014: Elsevier Health Sciences.
8. Tojo, A. and S. Kinugasa, *Mechanisms of glomerular albumin filtration and tubular reabsorption.* Int J Nephrol, 2012. **2012**: p. 481520.
9. Bohrer, M.P., C. Baylis, H.D. Humes, R.J. Glassock, C.R. Robertson, and B.M. Brenner, *Permselectivity of the glomerular capillary wall. Facilitated filtration of circulating polycations.* J Clin Invest, 1978. **61**(1): p. 72-8.
10. Moeller, M.J. and V. Tenten, *Renal albumin filtration: alternative models to the standard physical barriers.* Nat Rev Nephrol, 2013. **9**(5): p. 266-77.
11. Lazzara, M.J. and W.M. Deen, *Model of albumin reabsorption in the proximal tubule.* Am J Physiol Renal Physiol, 2007. **292**(1): p. F430-9.
12. Maunsbach, A.B., *Absorption of I-125-labeled homologous albumin by rat kidney proximal tubule cells. A study of microperfused single proximal tubules by electron microscopic autoradiography and histochemistry.* J Ultrastruct Res, 1966. **15**(3): p. 197-241.
13. Maunsbach, A.B., *Albumin absorption by renal proximal tubule cells.* Nature, 1966. **212**(5061): p. 546-7.
14. Garcia, N.H., C.R. Ramsey, and F.G. Knox, *Understanding the Role of Paracellular Transport in the Proximal Tubule.* News Physiol Sci, 1998. **13**: p. 38-43.
15. Zhuo, J.L. and X.C. Li, *Proximal nephron.* Compr Physiol, 2013. **3**(3): p. 1079-123.
16. Xie, J.X., X. Li, and Z. Xie, *Regulation of renal function and structure by the signaling Na/K-ATPase.* IUBMB Life, 2013. **65**(12): p. 991-8.
17. Wright, E.M., *Renal Na(+)-glucose cotransporters.* Am J Physiol Renal Physiol, 2001. **280**(1): p. F10-8.
18. Nielsen, S., T. Pallone, B.L. Smith, E.I. Christensen, P. Agre, and A.B. Maunsbach, *Aquaporin-1 water channels in short and long loop descending thin limbs and in descending vasa recta in rat kidney.* Am J Physiol, 1995. **268**(6 Pt 2): p. F1023-37.
19. Fenton, R.A. and M.A. Knepper, *Mouse models and the urinary concentrating mechanism in the new millennium.* Physiol Rev, 2007. **87**(4): p. 1083-112.
20. Castrop, H. and I.M. Schiessl, *Physiology and pathophysiology of the renal Na-K-2Cl cotransporter (NKCC2).* Am J Physiol Renal Physiol, 2014. **307**(9): p. F991-F1002.
21. Gamba, G., *The thiazide-sensitive Na+-Cl- cotransporter: molecular biology, functional properties, and regulation by WNKs.* Am J Physiol Renal Physiol, 2009. **297**(4): p. F838-48.

22. Collaboration, G.B.D.C.K.D., *Global, regional, and national burden of chronic kidney disease, 1990-2017: a systematic analysis for the Global Burden of Disease Study 2017.* Lancet, 2020. **395**(10225): p. 709-733.
23. Crews, D.C., A.K. Bello, G. Saadi, and C. World Kidney Day Steering, *Burden, access, and disparities in kidney disease.* J Nephrol, 2019. **32**(1): p. 1-8.
24. Makris, K. and L. Spanou, *Acute Kidney Injury: Definition, Pathophysiology and Clinical Phenotypes.* Clin Biochem Rev, 2016. **37**(2): p. 85-98.
25. Ronco, C., R. Bellomo, and J.A. Kellum, *Acute kidney injury.* Lancet, 2019. **394**(10212): p. 1949-1964.
26. Pickkers, P., M. Ostermann, M. Joannidis, A. Zarbock, E. Hoste, R. Bellomo, J. Prowle, M. Darmon, J.V. Bonventre, L. Forni, S.M. Bagshaw, and M. Schetz, *The intensive care medicine agenda on acute kidney injury.* Intensive Care Med, 2017. **43**(9): p. 1198-1209.
27. Hoste, E.A.J., J.A. Kellum, N.M. Selby, A. Zarbock, P.M. Palevsky, S.M. Bagshaw, S.L. Goldstein, J. Cerda, and L.S. Chawla, *Global epidemiology and outcomes of acute kidney injury.* Nat Rev Nephrol, 2018. **14**(10): p. 607-625.
28. Ostermann, M. and K. Liu, *Pathophysiology of AKI.* Best Pract Res Clin Anaesthesiol, 2017. **31**(3): p. 305-314.
29. Bellomo, R., J.A. Kellum, C. Ronco, R. Wald, J. Martensson, M. Maiden, S.M. Bagshaw, N.J. Glassford, Y. Lankadeva, S.T. Vaara, and A. Schneider, *Acute kidney injury in sepsis.* Intensive Care Med, 2017. **43**(6): p. 816-828.
30. Zarbock, A., H. Gomez, and J.A. Kellum, *Sepsis-induced acute kidney injury revisited: pathophysiology, prevention and future therapies.* Curr Opin Crit Care, 2014. **20**(6): p. 588-95.
31. Sharfuddin, A.A. and B.A. Molitoris, *Pathophysiology of ischemic acute kidney injury.* Nat Rev Nephrol, 2011. **7**(4): p. 189-200.
32. Kane-Gill, S.L. and S.L. Goldstein, *Drug-Induced Acute Kidney Injury: A Focus on Risk Assessment for Prevention.* Crit Care Clin, 2015. **31**(4): p. 675-84.
33. Kellum, J.A. and C. Ronco, *Controversies in acute kidney injury: the 2011 Brussels Roundtable.* Crit Care, 2011. **15**(2): p. 155.
34. Macnider, W.D., *A Study of Acute Mercuric Chloride Intoxications in the Dog with Special Reference to the Kidney Injury.* J Exp Med, 1918. **27**(4): p. 519-38.
35. Bellomo, R., C. Ronco, J.A. Kellum, R.L. Mehta, P. Palevsky, and w. Acute Dialysis Quality Initiative, *Acute renal failure - definition, outcome measures, animal models, fluid therapy and information technology needs: the Second International Consensus Conference of the Acute Dialysis Quality Initiative (ADQI) Group.* Crit Care, 2004. **8**(4): p. R204-12.
36. Mehta, R.L., J.A. Kellum, S.V. Shah, B.A. Molitoris, C. Ronco, D.G. Warnock, A. Levin, and N. Acute Kidney Injury, *Acute Kidney Injury Network: report of an initiative to improve outcomes in acute kidney injury.* Crit Care, 2007. **11**(2): p. R31.
37. Kellum, J.A., N. Lameire, P. Aspelin, R.S. Barsoum, E.A. Burdmann, S.L. Goldstein, C.A. Herzog, M. Joannidis, A. Kribben, and A.S. Levey, *Kidney disease: improving global outcomes (KDIGO) acute kidney injury work group. KDIGO clinical practice guideline for acute kidney injury.* Kidney international supplements, 2012. **2**(1): p. 1-138.
38. Basile, D.P., J.V. Bonventre, R. Mehta, M. Nangaku, R. Unwin, M.H. Rosner, J.A. Kellum, C. Ronco, and A.X.W. Group, *Progression after AKI: Understanding Maladaptive Repair Processes to Predict and Identify Therapeutic Treatments.* J Am Soc Nephrol, 2016. **27**(3): p. 687-97.
39. Ferenbach, D.A. and J.V. Bonventre, *Mechanisms of maladaptive repair after AKI leading to accelerated kidney ageing and CKD.* Nat Rev Nephrol, 2015. **11**(5): p. 264-76.

40. James, S.L., D. Abate, K.H. Abate, S.M. Abay, C. Abbafati, N. Abbasi, H. Abbastabar, F. Abd-Allah, J. Abdela, and A. Abdelalim, *Global, regional, and national incidence, prevalence, and years lived with disability for 354 diseases and injuries for 195 countries and territories, 1990–2017: a systematic analysis for the Global Burden of Disease Study 2017.* The Lancet, 2018. **392**(10159): p. 1789-1858.
41. Foreman, K.J., N. Marquez, A. Dolgert, K. Fukutaki, N. Fullman, M. McGaughey, M.A. Pletcher, A.E. Smith, K. Tang, and C.-W. Yuan, *Forecasting life expectancy, years of life lost, and all-cause and cause-specific mortality for 250 causes of death: reference and alternative scenarios for 2016–40 for 195 countries and territories.* The Lancet, 2018. **392**(10159): p. 2052-2090.
42. Fraser, S.D.S. and P.J. Roderick, *Kidney disease in the Global Burden of Disease Study 2017.* Nat Rev Nephrol, 2019. **15**(4): p. 193-194.
43. Lea, J.P. and S.B. Nicholas, *Diabetes mellitus and hypertension: key risk factors for kidney disease.* J Natl Med Assoc, 2002. **94**(8 Suppl): p. 7S-15S.
44. McClellan, W.M. and W.D. Flanders, *Risk factors for progressive chronic kidney disease.* J Am Soc Nephrol, 2003. **14**(7 Suppl 2): p. S65-70.
45. Ejerblad, E., C.M. Fored, P. Lindblad, J. Fryzek, J.K. McLaughlin, and O. Nyren, *Obesity and risk for chronic renal failure.* J Am Soc Nephrol, 2006. **17**(6): p. 1695-702.
46. Shulman, N.B., C.E. Ford, W.D. Hall, M.D. Blaufox, D. Simon, H.G. Langford, and K.A. Schneider, *Prognostic value of serum creatinine and effect of treatment of hypertension on renal function. Results from the hypertension detection and follow-up program. The Hypertension Detection and Follow-up Program Cooperative Group.* Hypertension, 1989. **13**(5 Suppl): p. I80-93.
47. Ritz, E., G. Bakris, and W.K.D.O. Committee, *World Kidney Day: hypertension and chronic kidney disease.* The Lancet, 2009. **373**(9670): p. 1157-1158.
48. Kazancioglu, R., *Risk factors for chronic kidney disease: an update.* Kidney Int Suppl (2011), 2013. **3**(4): p. 368-371.
49. Gansevoort, R.T., R. Correa-Rotter, B.R. Hemmelgarn, T.H. Jafar, H.J. Heerspink, J.F. Mann, K. Matsushita, and C.P. Wen, *Chronic kidney disease and cardiovascular risk: epidemiology, mechanisms, and prevention.* Lancet, 2013. **382**(9889): p. 339-52.
50. Iseki, K., *Factors influencing the development of end-stage renal disease.* Clin Exp Nephrol, 2005. **9**(1): p. 5-14.
51. Goldstein, S.L. and P. Devarajan, *Acute kidney injury in childhood: should we be worried about progression to CKD?* Pediatr Nephrol, 2011. **26**(4): p. 509-22.
52. Garcia-Esquinas, E., L.F. Loeffler, V.M. Weaver, J.J. Fadrowski, and A. Navas-Acien, *Kidney function and tobacco smoke exposure in US adolescents.* Pediatrics, 2013. **131**(5): p. e1415-23.
53. Hallan, S.I. and S.R. Orth, *Smoking is a risk factor in the progression to kidney failure.* Kidney Int, 2011. **80**(5): p. 516-23.
54. Plantinga, L.C., *Socio-economic impact in CKD.* Nephrol Ther, 2013. **9**(1): p. 1-7.
55. Silbiger, S.R. and J. Neugarten, *The impact of gender on the progression of chronic renal disease.* Am J Kidney Dis, 1995. **25**(4): p. 515-33.
56. Liyanage, T., T. Ninomiya, V. Jha, B. Neal, H.M. Patrice, I. Okpechi, M.-h. Zhao, J. Lv, A.X. Garg, and J. Knight, *Worldwide access to treatment for end-stage kidney disease: a systematic review.* The Lancet, 2015. **385**(9981): p. 1975-1982.
57. Gungor, O., I. Kocyigit, J.J. Carrero, and M.I. Yilmaz, *Hormonal changes in hemodialysis patients: Novel risk factors for mortality?* Semin Dial, 2017. **30**(5): p. 446-452.
58. Zazzeroni, L., G. Pasquinelli, E. Nanni, V. Cremonini, and I. Rubbi, *Comparison of Quality of Life in Patients Undergoing Hemodialysis and Peritoneal Dialysis: a*

Systematic Review and Meta-Analysis. Kidney Blood Press Res, 2017. **42**(4): p. 717-727.
59. Ahmadmehrabi, S. and W.H.W. Tang, *Hemodialysis-induced cardiovascular disease.* Semin Dial, 2018. **31**(3): p. 258-267.
60. *Annual report on kidney transplantation 2020/2021 (1 April 2011 – 31 March 2021)*. Available from: https://nhsbtdbe.blob.core.windows.net/umbraco-assets-corp/24701/kidney-annual-report-2020-21.pdf.
61. Meier-Kriesche, H.-U. and B. Kaplan, *Waiting time on dialysis as the strongest modifiable risk factor for renal transplant outcomes: A Paired Donor Kidney Analysis1.* Transplantation, 2002. **74**(10): p. 1377-1381.
62. Gourlay, W., *Preemptive Kidney Transplantation: What's the Hold Up?* Transplantation, 2018. **102**(7): p. 1035-1036.
63. *Guidelines for Living Donor Kidney Transplantation*. Available from: https://bts.org.uk/wp-content/uploads/2018/07/FINAL_LDKT-guidelines_June-2018.pdf.
64. Veroux, M., G. Grosso, D. Corona, A. Mistretta, A. Giaquinta, G. Giuffrida, N. Sinagra, and P. Veroux, *Age is an important predictor of kidney transplantation outcome.* Nephrol Dial Transplant, 2012. **27**(4): p. 1663-71.
65. Echterdiek, F., V. Schwenger, B. Dohler, J. Latus, D. Kitterer, U. Heemann, and C. Susal, *Kidneys From Elderly Deceased Donors-Is 70 the New 60?* Front Immunol, 2019. **10**: p. 2701.
66. Erez, G., L. Selman, and F.E. Murtagh, *Measuring health-related quality of life in patients with conservatively managed stage 5 chronic kidney disease: limitations of the Medical Outcomes Study Short Form 36: SF-36.* Qual Life Res, 2016. **25**(11): p. 2799-2809.
67. Raspovic, K.M., J. Ahn, J. La Fontaine, L.A. Lavery, and D.K. Wukich, *End-Stage Renal Disease Negatively Affects Physical Quality of Life in Patients With Diabetic Foot Complications.* Int J Low Extrem Wounds, 2017. **16**(2): p. 135-142.
68. Mao, A.S. and D.J. Mooney, *Regenerative medicine: Current therapies and future directions.* Proc Natl Acad Sci U S A, 2015. **112**(47): p. 14452-9.
69. Buzhor, E., L. Leshansky, J. Blumenthal, H. Barash, D. Warshawsky, Y. Mazor, and R. Shtrichman, *Cell-based therapy approaches: the hope for incurable diseases.* Regen Med, 2014. **9**(5): p. 649-72.
70. Sun, R., X. Li, M. Liu, Y. Zeng, S. Chen, and P. Zhang, *Advances in stem cell therapy for cardiovascular disease (Review).* Int J Mol Med, 2016. **38**(1): p. 23-9.
71. Newick, K., S. O'Brien, E. Moon, and S.M. Albelda, *CAR T Cell Therapy for Solid Tumors.* Annu Rev Med, 2017. **68**: p. 139-152.
72. Hansrivijit, P., R.P. Gale, J. Barrett, and S.O. Ciurea, *Cellular therapy for acute myeloid Leukemia - Current status and future prospects.* Blood Rev, 2019. **37**: p. 100578.
73. Stuart, R.K., *Autologous bone marrow transplantation for leukemia.* Semin Oncol, 1993. **20**(5 Suppl 6): p. 40-54.
74. Alessandrini, M., O. Preynat-Seauve, K. De Bruin, and M.S. Pepper, *Stem cell therapy for neurological disorders.* S Afr Med J, 2019. **109**(8b): p. 70-77.
75. Chung, H.C., I.K. Ko, A. Atala, and J.J. Yoo, *Cell-based therapy for kidney disease.* Korean J Urol, 2015. **56**(6): p. 412-21.
76. Thomas, E.D., H.L. Lochte, Jr., W.C. Lu, and J.W. Ferrebee, *Intravenous infusion of bone marrow in patients receiving radiation and chemotherapy.* N Engl J Med, 1957. **257**(11): p. 491-6.
77. Malik, N.N. and M.B. Durdy, *Cell therapy landscape: autologous and allogeneic approaches*, in *Translational Regenerative Medicine*. 2015, Elsevier. p. 87-106.

78. Mamidi, M.K., S. Dutta, R. Bhonde, A.K. Das, and R. Pal, *Allogeneic and autologous mode of stem cell transplantation in regenerative medicine: which way to go?* Med Hypotheses, 2014. **83**(6): p. 787-91.
79. Vertes, A.A., N. Qureshi, A.I. Caplan, and L.E. Babiss, *Stem cells in regenerative medicine: Science, regulation and business strategies*. 2015: John Wiley & Sons.
80. Friedenstein, A.J., K.V. Petrakova, A.I. Kurolesova, and G.P. Frolova, *Heterotopic of bone marrow. Analysis of precursor cells for osteogenic and hematopoietic tissues.* Transplantation, 1968. **6**(2): p. 230-47.
81. Friedenstein, A.J., R.K. Chailakhjan, and K.S. Lalykina, *The development of fibroblast colonies in monolayer cultures of guinea-pig bone marrow and spleen cells.* Cell Tissue Kinet, 1970. **3**(4): p. 393-403.
82. Zuk, P.A., M. Zhu, P. Ashjian, D.A. De Ugarte, J.I. Huang, H. Mizuno, Z.C. Alfonso, J.K. Fraser, P. Benhaim, and M.H. Hedrick, *Human adipose tissue is a source of multipotent stem cells.* Mol Biol Cell, 2002. **13**(12): p. 4279-95.
83. Martin-Rendon, E., D. Sweeney, F. Lu, J. Girdlestone, C. Navarrete, and S.M. Watt, *5-Azacytidine-treated human mesenchymal stem/progenitor cells derived from umbilical cord, cord blood and bone marrow do not generate cardiomyocytes in vitro at high frequencies.* Vox Sang, 2008. **95**(2): p. 137-48.
84. Wang, H.S., S.C. Hung, S.T. Peng, C.C. Huang, H.M. Wei, Y.J. Guo, Y.S. Fu, M.C. Lai, and C.C. Chen, *Mesenchymal stem cells in the Wharton's jelly of the human umbilical cord.* Stem Cells, 2004. **22**(7): p. 1330-7.
85. De Bari, C., F. Dell'Accio, P. Tylzanowski, and F.P. Luyten, *Multipotent mesenchymal stem cells from adult human synovial membrane.* Arthritis Rheum, 2001. **44**(8): p. 1928-42.
86. Gronthos, S., M. Mankani, J. Brahim, P.G. Robey, and S. Shi, *Postnatal human dental pulp stem cells (DPSCs) in vitro and in vivo.* Proc Natl Acad Sci U S A, 2000. **97**(25): p. 13625-30.
87. Covas, D.T., R.A. Panepucci, A.M. Fontes, W.A. Silva, Jr., M.D. Orellana, M.C. Freitas, L. Neder, A.R. Santos, L.C. Peres, M.C. Jamur, and M.A. Zago, *Multipotent mesenchymal stromal cells obtained from diverse human tissues share functional properties and gene-expression profile with CD146+ perivascular cells and fibroblasts.* Exp Hematol, 2008. **36**(5): p. 642-54.
88. Dominici, M., K. Le Blanc, I. Mueller, I. Slaper-Cortenbach, F. Marini, D. Krause, R. Deans, A. Keating, D. Prockop, and E. Horwitz, *Minimal criteria for defining multipotent mesenchymal stromal cells. The International Society for Cellular Therapy position statement.* Cytotherapy, 2006. **8**(4): p. 315-7.
89. Tang, D.Q., Q. Wang, B.R. Burkhardt, S.A. Litherland, M.A. Atkinson, and L.J. Yang, *In vitro generation of functional insulin-producing cells from human bone marrow-derived stem cells, but long-term culture running risk of malignant transformation.* Am J Stem Cells, 2012. **1**(2): p. 114-127.
90. Datta, I., S. Mishra, L. Mohanty, S. Pulikkot, and P.G. Joshi, *Neuronal plasticity of human Wharton's jelly mesenchymal stromal cells to the dopaminergic cell type compared with human bone marrow mesenchymal stromal cells.* Cytotherapy, 2011. **13**(8): p. 918-32.
91. Wang, Y., F. Wang, H. Zhao, X. Zhang, H. Chen, and K. Zhang, *Human adipose-derived mesenchymal stem cells are resistant to HBV infection during differentiation into hepatocytes in vitro.* Int J Mol Sci, 2014. **15**(4): p. 6096-110.
92. Hang, H., Y. Yu, N. Wu, Q. Huang, Q. Xia, and J. Bian, *Induction of highly functional hepatocytes from human umbilical cord mesenchymal stem cells by HNF4alpha transduction.* PLoS One, 2014. **9**(8): p. e104133.
93. Ullah, I., R.B. Subbarao, and G.J. Rho, *Human mesenchymal stem cells - current trends and future prospective.* Biosci Rep, 2015. **35**(2).

94. Weissman, I., *Stem cell therapies could change medicine... if they get the chance.* Cell Stem Cell, 2012. **10**(6): p. 663-665.
95. Shi, Y., Y. Wang, Q. Li, K. Liu, J. Hou, C. Shao, and Y. Wang, *Immunoregulatory mechanisms of mesenchymal stem and stromal cells in inflammatory diseases.* Nat Rev Nephrol, 2018. **14**(8): p. 493-507.
96. Lazarus, H.M., S.E. Haynesworth, S.L. Gerson, N.S. Rosenthal, and A.I. Caplan, *Ex vivo expansion and subsequent infusion of human bone marrow-derived stromal progenitor cells (mesenchymal progenitor cells): implications for therapeutic use.* Bone Marrow Transplant, 1995. **16**(4): p. 557-64.
97. Koc, O.N., S.L. Gerson, B.W. Cooper, S.M. Dyhouse, S.E. Haynesworth, A.I. Caplan, and H.M. Lazarus, *Rapid hematopoietic recovery after coinfusion of autologous-blood stem cells and culture-expanded marrow mesenchymal stem cells in advanced breast cancer patients receiving high-dose chemotherapy.* J Clin Oncol, 2000. **18**(2): p. 307-16.
98. Kabat, M., I. Bobkov, S. Kumar, and M. Grumet, *Trends in mesenchymal stem cell clinical trials 2004-2018: Is efficacy optimal in a narrow dose range?* Stem Cells Transl Med, 2020. **9**(1): p. 17-27.
99. Scarfe, L., A. Taylor, J. Sharkey, R. Harwood, M. Barrow, J. Comenge, L. Beeken, C. Astley, I. Santeramo, C. Hutchinson, L. Ressel, J. Smythe, E. Austin, R. Levy, M.J. Rosseinsky, D.J. Adams, H. Poptani, B.K. Park, P. Murray, and B. Wilm, *Non-invasive imaging reveals conditions that impact distribution and persistence of cells after in vivo administration.* Stem Cell Res Ther, 2018. **9**(1): p. 332.
100. Papazova, D.A., N.R. Oosterhuis, H. Gremmels, A. van Koppen, J.A. Joles, and M.C. Verhaar, *Cell-based therapies for experimental chronic kidney disease: a systematic review and meta-analysis.* Dis Model Mech, 2015. **8**(3): p. 281-93.
101. Assis, A.C., J.L. Carvalho, B.A. Jacoby, R.L. Ferreira, P. Castanheira, S.O. Diniz, V.N. Cardoso, A.M. Goes, and A.J. Ferreira, *Time-dependent migration of systemically delivered bone marrow mesenchymal stem cells to the infarcted heart.* Cell Transplant, 2010. **19**(2): p. 219-30.
102. de Witte, S.F.H., F. Luk, J.M. Sierra Parraga, M. Gargesha, A. Merino, S.S. Korevaar, A.S. Shankar, L. O'Flynn, S.J. Elliman, D. Roy, M.G.H. Betjes, P.N. Newsome, C.C. Baan, and M.J. Hoogduijn, *Immunomodulation By Therapeutic Mesenchymal Stromal Cells (MSC) Is Triggered Through Phagocytosis of MSC By Monocytic Cells.* Stem Cells, 2018. **36**(4): p. 602-615.
103. Eggenhofer, E., V. Benseler, A. Kroemer, F.C. Popp, E.K. Geissler, H.J. Schlitt, C.C. Baan, M.H. Dahlke, and M.J. Hoogduijn, *Mesenchymal stem cells are short-lived and do not migrate beyond the lungs after intravenous infusion.* Front Immunol, 2012. **3**: p. 297.
104. Taylor, A., J. Sharkey, R. Harwood, L. Scarfe, M. Barrow, M.J. Rosseinsky, D.J. Adams, B. Wilm, and P. Murray, *Multimodal Imaging Techniques Show Differences in Homing Capacity Between Mesenchymal Stromal Cells and Macrophages in Mouse Renal Injury Models.* Mol Imaging Biol, 2020. **22**(4): p. 904-913.
105. Saat, T.C., S. van den Engel, W. Bijman-Lachger, S.S. Korevaar, M.J. Hoogduijn, I.J. JN, and R.W. de Bruin, *Fate and Effect of Intravenously Infused Mesenchymal Stem Cells in a Mouse Model of Hepatic Ischemia Reperfusion Injury and Resection.* Stem Cells Int, 2016. **2016**: p. 5761487.
106. Braid, L.R., C.A. Wood, D.M. Wiese, and B.N. Ford, *Intramuscular administration potentiates extended dwell time of mesenchymal stromal cells compared to other routes.* Cytotherapy, 2018. **20**(2): p. 232-244.
107. Spaggiari, G.M., A. Capobianco, S. Becchetti, M.C. Mingari, and L. Moretta, *Mesenchymal stem cell-natural killer cell interactions: evidence that activated NK*

cells are capable of killing MSCs, whereas MSCs can inhibit IL-2-induced NK-cell proliferation. Blood, 2006. **107**(4): p. 1484-90.
108. Selmani, Z., A. Naji, I. Zidi, B. Favier, E. Gaiffe, L. Obert, C. Borg, P. Saas, P. Tiberghien, N. Rouas-Freiss, E.D. Carosella, and F. Deschaseaux, *Human leukocyte antigen-G5 secretion by human mesenchymal stem cells is required to suppress T lymphocyte and natural killer function and to induce CD4+CD25highFOXP3+ regulatory T cells.* Stem Cells, 2008. **26**(1): p. 212-22.
109. Ramasamy, R., H. Fazekasova, E.W. Lam, I. Soeiro, G. Lombardi, and F. Dazzi, *Mesenchymal stem cells inhibit dendritic cell differentiation and function by preventing entry into the cell cycle.* Transplantation, 2007. **83**(1): p. 71-6.
110. Corcione, A., F. Benvenuto, E. Ferretti, D. Giunti, V. Cappiello, F. Cazzanti, M. Risso, F. Gualandi, G.L. Mancardi, V. Pistoia, and A. Uccelli, *Human mesenchymal stem cells modulate B-cell functions.* Blood, 2006. **107**(1): p. 367-72.
111. Glennie, S., I. Soeiro, P.J. Dyson, E.W. Lam, and F. Dazzi, *Bone marrow mesenchymal stem cells induce division arrest anergy of activated T cells.* Blood, 2005. **105**(7): p. 2821-7.
112. Gao, F., S.M. Chiu, D.A. Motan, Z. Zhang, L. Chen, H.L. Ji, H.F. Tse, Q.L. Fu, and Q. Lian, *Mesenchymal stem cells and immunomodulation: current status and future prospects.* Cell Death Dis, 2016. **7**: p. e2062.
113. Galleu, A., Y. Riffo-Vasquez, C. Trento, C. Lomas, L. Dolcetti, T.S. Cheung, M. von Bonin, L. Barbieri, K. Halai, S. Ward, L. Weng, R. Chakraverty, G. Lombardi, F.M. Watt, K. Orchard, D.I. Marks, J. Apperley, M. Bornhauser, H. Walczak, C. Bennett, and F. Dazzi, *Apoptosis in mesenchymal stromal cells induces in vivo recipient-mediated immunomodulation.* Sci Transl Med, 2017. **9**(416).
114. Gonzalez-Pujana, A., M. Igartua, E. Santos-Vizcaino, and R.M. Hernandez, *Mesenchymal stromal cell based therapies for the treatment of immune disorders: recent milestones and future challenges.* Expert Opin Drug Deliv, 2020. **17**(2): p. 189-200.
115. Amadeo, F., K. Trivino Cepeda, J. Littlewood, B. Wilm, A. Taylor, and P. Murray, *Mesenchymal stromal cells: what have we learned so far about their therapeutic potential and mechanisms of action?* Emerg Top Life Sci, 2021. **5**(4): p. 549-562.
116. Gavin, C., S. Meinke, N. Heldring, K.A. Heck, A. Achour, E. Iacobaeus, P. Hoglund, K. Le Blanc, and N. Kadri, *The Complement System Is Essential for the Phagocytosis of Mesenchymal Stromal Cells by Monocytes.* Front Immunol, 2019. **10**: p. 2249.
117. Braza, F., S. Dirou, V. Forest, V. Sauzeau, D. Hassoun, J. Chesne, M.A. Cheminant-Muller, C. Sagan, A. Magnan, and P. Lemarchand, *Mesenchymal Stem Cells Induce Suppressive Macrophages Through Phagocytosis in a Mouse Model of Asthma.* Stem Cells, 2016. **34**(7): p. 1836-45.
118. Cheung, T.S., A. Galleu, M. von Bonin, M. Bornhauser, and F. Dazzi, *Apoptotic mesenchymal stromal cells induce prostaglandin E2 in monocytes: implications for the monitoring of mesenchymal stromal cell activity.* Haematologica, 2019. **104**(10): p. e438-e441.
119. Ghahremani Piraghaj, M., S. Soudi, H. Ghanbarian, Z. Bolandi, S. Namaki, and S.M. Hashemi, *Effect of efferocytosis of apoptotic mesenchymal stem cells (MSCs) on C57BL/6 peritoneal macrophages function.* Life Sci, 2018. **212**: p. 203-212.
120. Arslan, F., R.C. Lai, M.B. Smeets, L. Akeroyd, A. Choo, E.N. Aguor, L. Timmers, H.V. van Rijen, P.A. Doevendans, G. Pasterkamp, S.K. Lim, and D.P. de Kleijn, *Mesenchymal stem cell-derived exosomes increase ATP levels, decrease oxidative stress and activate PI3K/Akt pathway to enhance myocardial viability and prevent adverse remodeling after myocardial ischemia/reperfusion injury.* Stem Cell Res, 2013. **10**(3): p. 301-12.

121. Zhao, J., X. Li, J. Hu, F. Chen, S. Qiao, X. Sun, L. Gao, J. Xie, and B. Xu, *Mesenchymal stromal cell-derived exosomes attenuate myocardial ischaemia-reperfusion injury through miR-182-regulated macrophage polarization.* Cardiovasc Res, 2019. **115**(7): p. 1205-1216.
122. Cui, X., Z. He, Z. Liang, Z. Chen, H. Wang, and J. Zhang, *Exosomes From Adipose-derived Mesenchymal Stem Cells Protect the Myocardium Against Ischemia/Reperfusion Injury Through Wnt/beta-Catenin Signaling Pathway.* J Cardiovasc Pharmacol, 2017. **70**(4): p. 225-231.
123. Gatti, S., S. Bruno, M.C. Deregibus, A. Sordi, V. Cantaluppi, C. Tetta, and G. Camussi, *Microvesicles derived from human adult mesenchymal stem cells protect against ischaemia-reperfusion-induced acute and chronic kidney injury.* Nephrol Dial Transplant, 2011. **26**(5): p. 1474-83.
124. Gu, D., X. Zou, G. Ju, G. Zhang, E. Bao, and Y. Zhu, *Mesenchymal Stromal Cells Derived Extracellular Vesicles Ameliorate Acute Renal Ischemia Reperfusion Injury by Inhibition of Mitochondrial Fission through miR-30.* Stem Cells Int, 2016. **2016**: p. 2093940.
125. Zhang, J., J. Guan, X. Niu, G. Hu, S. Guo, Q. Li, Z. Xie, C. Zhang, and Y. Wang, *Exosomes released from human induced pluripotent stem cells-derived MSCs facilitate cutaneous wound healing by promoting collagen synthesis and angiogenesis.* J Transl Med, 2015. **13**: p. 49.
126. Tan, C.Y., R.C. Lai, W. Wong, Y.Y. Dan, S.K. Lim, and H.K. Ho, *Mesenchymal stem cell-derived exosomes promote hepatic regeneration in drug-induced liver injury models.* Stem Cell Res Ther, 2014. **5**(3): p. 76.
127. Lou, G., X. Song, F. Yang, S. Wu, J. Wang, Z. Chen, and Y. Liu, *Exosomes derived from miR-122-modified adipose tissue-derived MSCs increase chemosensitivity of hepatocellular carcinoma.* J Hematol Oncol, 2015. **8**: p. 122.
128. Wu, H.H. and O.K. Lee, *Exosomes from mesenchymal stem cells induce the conversion of hepatocytes into progenitor oval cells.* Stem Cell Res Ther, 2017. **8**(1): p. 117.
129. Zhang, J., X. Liu, H. Li, C. Chen, B. Hu, X. Niu, Q. Li, B. Zhao, Z. Xie, and Y. Wang, *Exosomes/tricalcium phosphate combination scaffolds can enhance bone regeneration by activating the PI3K/Akt signaling pathway.* Stem Cell Res Ther, 2016. **7**(1): p. 136.
130. Zhang, S., W.C. Chu, R.C. Lai, S.K. Lim, J.H. Hui, and W.S. Toh, *Exosomes derived from human embryonic mesenchymal stem cells promote osteochondral regeneration.* Osteoarthritis Cartilage, 2016. **24**(12): p. 2135-2140.
131. Chew, J.R.J., S.J. Chuah, K.Y.W. Teo, S. Zhang, R.C. Lai, J.H. Fu, L.P. Lim, S.K. Lim, and W.S. Toh, *Mesenchymal stem cell exosomes enhance periodontal ligament cell functions and promote periodontal regeneration.* Acta Biomater, 2019. **89**: p. 252-264.
132. Zhang, S., K.Y.W. Teo, S.J. Chuah, R.C. Lai, S.K. Lim, and W.S. Toh, *MSC exosomes alleviate temporomandibular joint osteoarthritis by attenuating inflammation and restoring matrix homeostasis.* Biomaterials, 2019. **200**: p. 35-47.
133. Reza-Zaldivar, E.E., M.A. Hernandez-Sapiens, B. Minjarez, Y.K. Gutierrez-Mercado, A.L. Marquez-Aguirre, and A.A. Canales-Aguirre, *Potential Effects of MSC-Derived Exosomes in Neuroplasticity in Alzheimer's Disease.* Front Cell Neurosci, 2018. **12**: p. 317.
134. Huang, J.H., X.M. Yin, Y. Xu, C.C. Xu, X. Lin, F.B. Ye, Y. Cao, and F.Y. Lin, *Systemic Administration of Exosomes Released from Mesenchymal Stromal Cells Attenuates Apoptosis, Inflammation, and Promotes Angiogenesis after Spinal Cord Injury in Rats.* J Neurotrauma, 2017. **34**(24): p. 3388-3396.

135. Sengupta, V., S. Sengupta, A. Lazo, P. Woods, A. Nolan, and N. Bremer, *Exosomes Derived from Bone Marrow Mesenchymal Stem Cells as Treatment for Severe COVID-19.* Stem Cells Dev, 2020. **29**(12): p. 747-754.
136. Zhang, S., S.J. Chuah, R.C. Lai, J.H.P. Hui, S.K. Lim, and W.S. Toh, *MSC exosomes mediate cartilage repair by enhancing proliferation, attenuating apoptosis and modulating immune reactivity.* Biomaterials, 2018. **156**: p. 16-27.
137. Qi, H., D.P. Liu, D.W. Xiao, D.C. Tian, Y.W. Su, and S.F. Jin, *Exosomes derived from mesenchymal stem cells inhibit mitochondrial dysfunction-induced apoptosis of chondrocytes via p38, ERK, and Akt pathways.* In Vitro Cell Dev Biol Anim, 2019. **55**(3): p. 203-210.
138. Manning, B.D. and A. Toker, *AKT/PKB Signaling: Navigating the Network.* Cell, 2017. **169**(3): p. 381-405.
139. McCubrey, J.A., L.S. Steelman, W.H. Chappell, S.L. Abrams, E.W. Wong, F. Chang, B. Lehmann, D.M. Terrian, M. Milella, A. Tafuri, F. Stivala, M. Libra, J. Basecke, C. Evangelisti, A.M. Martelli, and R.A. Franklin, *Roles of the Raf/MEK/ERK pathway in cell growth, malignant transformation and drug resistance.* Biochim Biophys Acta, 2007. **1773**(8): p. 1263-84.
140. Merighi, S., A. Benini, P. Mirandola, S. Gessi, K. Varani, E. Leung, S. Maclennan, P.G. Baraldi, and P.A. Borea, *Modulation of the Akt/Ras/Raf/MEK/ERK pathway by A(3) adenosine receptor.* Purinergic Signal, 2006. **2**(4): p. 627-32.
141. Colgan, S.P., H.K. Eltzschig, T. Eckle, and L.F. Thompson, *Physiological roles for ecto-5'-nucleotidase (CD73).* Purinergic Signal, 2006. **2**(2): p. 351-60.
142. Schaefer, K.N. and M. Peifer, *Wnt/Beta-Catenin Signaling Regulation and a Role for Biomolecular Condensates.* Dev Cell, 2019. **48**(4): p. 429-444.
143. Zhang, B., M. Wang, A. Gong, X. Zhang, X. Wu, Y. Zhu, H. Shi, L. Wu, W. Zhu, H. Qian, and W. Xu, *HucMSC-Exosome Mediated-Wnt4 Signaling Is Required for Cutaneous Wound Healing.* Stem Cells, 2015. **33**(7): p. 2158-68.
144. Zhang, B., X. Wu, X. Zhang, Y. Sun, Y. Yan, H. Shi, Y. Zhu, L. Wu, Z. Pan, W. Zhu, H. Qian, and W. Xu, *Human umbilical cord mesenchymal stem cell exosomes enhance angiogenesis through the Wnt4/beta-catenin pathway.* Stem Cells Transl Med, 2015. **4**(5): p. 513-22.
145. Zhang, B., Y. Shi, A. Gong, Z. Pan, H. Shi, H. Yang, H. Fu, Y. Yan, X. Zhang, M. Wang, W. Zhu, H. Qian, and W. Xu, *HucMSC Exosome-Delivered 14-3-3zeta Orchestrates Self-Control of the Wnt Response via Modulation of YAP During Cutaneous Regeneration.* Stem Cells, 2016. **34**(10): p. 2485-2500.
146. Rong, X., J. Liu, X. Yao, T. Jiang, Y. Wang, and F. Xie, *Human bone marrow mesenchymal stem cells-derived exosomes alleviate liver fibrosis through the Wnt/beta-catenin pathway.* Stem Cell Res Ther, 2019. **10**(1): p. 98.
147. Showalter, M.R., B. Wancewicz, O. Fiehn, J.A. Archard, S. Clayton, J. Wagner, P. Deng, J. Halmai, K.D. Fink, G. Bauer, B. Fury, N.H. Perotti, M. Apperson, J. Butters, P. Belafsky, G. Farwell, M. Kuhn, J.A. Nolta, and J.D. Anderson, *Primed mesenchymal stem cells package exosomes with metabolites associated with immunomodulation.* Biochem Biophys Res Commun, 2019. **512**(4): p. 729-735.
148. Liu, H., Z. Liang, F. Wang, C. Zhou, X. Zheng, T. Hu, X. He, X. Wu, and P. Lan, *Exosomes from mesenchymal stromal cells reduce murine colonic inflammation via a macrophage-dependent mechanism.* JCI Insight, 2019. **4**(24).
149. He, X., Z. Dong, Y. Cao, H. Wang, S. Liu, L. Liao, Y. Jin, L. Yuan, and B. Li, *MSC-Derived Exosome Promotes M2 Polarization and Enhances Cutaneous Wound Healing.* Stem Cells Int, 2019. **2019**: p. 7132708.
150. Fan, B., C. Li, A. Szalad, L. Wang, W. Pan, R. Zhang, M. Chopp, Z.G. Zhang, and X.S. Liu, *Mesenchymal stromal cell-derived exosomes ameliorate peripheral neuropathy in a mouse model of diabetes.* Diabetologia, 2020. **63**(2): p. 431-443.

151. Heo, J.S., Y. Choi, and H.O. Kim, *Adipose-Derived Mesenchymal Stem Cells Promote M2 Macrophage Phenotype through Exosomes.* Stem Cells Int, 2019. **2019**: p. 7921760.
152. Lankford, K.L., E.J. Arroyo, K. Nazimek, K. Bryniarski, P.W. Askenase, and J.D. Kocsis, *Intravenously delivered mesenchymal stem cell-derived exosomes target M2-type macrophages in the injured spinal cord.* PLoS One, 2018. **13**(1): p. e0190358.
153. Chamberlain, C.S., A.E.B. Clements, J.A. Kink, U. Choi, G.S. Baer, M.A. Halanski, P. Hematti, and R. Vanderby, *Extracellular Vesicle-Educated Macrophages Promote Early Achilles Tendon Healing.* Stem Cells, 2019. **37**(5): p. 652-662.
154. Perico, L., M. Morigi, C. Rota, M. Breno, C. Mele, M. Noris, M. Introna, C. Capelli, L. Longaretti, D. Rottoli, S. Conti, D. Corna, G. Remuzzi, and A. Benigni, *Human mesenchymal stromal cells transplanted into mice stimulate renal tubular cells and enhance mitochondrial function.* Nat Commun, 2017. **8**(1): p. 983.
155. Cao, J., B. Wang, T. Tang, L. Lv, Z. Ding, Z. Li, R. Hu, Q. Wei, A. Shen, Y. Fu, and B. Liu, *Three-dimensional culture of MSCs produces exosomes with improved yield and enhanced therapeutic efficacy for cisplatin-induced acute kidney injury.* Stem Cell Res Ther, 2020. **11**(1): p. 206.
156. Zou, X., G. Zhang, Z. Cheng, D. Yin, T. Du, G. Ju, S. Miao, G. Liu, M. Lu, and Y. Zhu, *Microvesicles derived from human Wharton's Jelly mesenchymal stromal cells ameliorate renal ischemia-reperfusion injury in rats by suppressing CX3CL1.* Stem Cell Res Ther, 2014. **5**(2): p. 40.
157. Bruno, S., C. Grange, M.C. Deregibus, R.A. Calogero, S. Saviozzi, F. Collino, L. Morando, A. Busca, M. Falda, B. Bussolati, C. Tetta, and G. Camussi, *Mesenchymal stem cell-derived microvesicles protect against acute tubular injury.* J Am Soc Nephrol, 2009. **20**(5): p. 1053-67.
158. Zou, X., D. Gu, G. Zhang, L. Zhong, Z. Cheng, G. Liu, and Y. Zhu, *NK Cell Regulatory Property is Involved in the Protective Role of MSC-Derived Extracellular Vesicles in Renal Ischemic Reperfusion Injury.* Hum Gene Ther, 2016. **27**(11): p. 926-935.
159. Sheashaa, H., A. Lotfy, F. Elhusseini, A.A. Aziz, A. Baiomy, S. Awad, A. Alsayed, A.H. El-Gilany, M.A. Saad, K. Mahmoud, F. Zahran, D.A. Salem, A. Sarhan, H.A. Ghaffar, and M. Sobh, *Protective effect of adipose-derived mesenchymal stem cells against acute kidney injury induced by ischemia-reperfusion in Sprague-Dawley rats.* Exp Ther Med, 2016. **11**(5): p. 1573-1580.
160. Nagaishi, K., Y. Mizue, T. Chikenji, M. Otani, M. Nakano, N. Konari, and M. Fujimiya, *Mesenchymal stem cell therapy ameliorates diabetic nephropathy via the paracrine effect of renal trophic factors including exosomes.* Sci Rep, 2016. **6**: p. 34842.
161. De Martino, M., S. Zonta, T. Rampino, M. Gregorini, F. Frassoni, G. Piotti, G. Bedino, L. Cobianchi, A. Dal Canton, P. Dionigi, and M. Alessiani, *Mesenchymal stem cells infusion prevents acute cellular rejection in rat kidney transplantation.* Transplant Proc, 2010. **42**(4): p. 1331-5.
162. Casiraghi, F., N. Azzollini, M. Todeschini, R.A. Cavinato, P. Cassis, S. Solini, C. Rota, M. Morigi, M. Introna, R. Maranta, N. Perico, G. Remuzzi, and M. Noris, *Localization of mesenchymal stromal cells dictates their immune or proinflammatory effects in kidney transplantation.* Am J Transplant, 2012. **12**(9): p. 2373-83.
163. Sun, Q., Z. Huang, F. Han, M. Zhao, R. Cao, D. Zhao, L. Hong, N. Na, H. Li, B. Miao, J. Hu, F. Meng, Y. Peng, and Q. Sun, *Allogeneic mesenchymal stem cells as induction therapy are safe and feasible in renal allografts: pilot results of a multicenter randomized controlled trial.* J Transl Med, 2018. **16**(1): p. 52.
164. Seifert, M., M. Stolk, D. Polenz, and H.D. Volk, *Detrimental effects of rat mesenchymal stromal cell pre-treatment in a model of acute kidney rejection.* Front Immunol, 2012. **3**: p. 202.

165. McKelvey, M., R.J. Saemundsson, and O. Zaring, *A recent crisis in regenerative medicine: Analyzing governance in order to identify public policy issues.* Science and Public Policy, 2018. **45**(5): p. 608-620.
166. Amariglio, N., A. Hirshberg, B.W. Scheithauer, Y. Cohen, R. Loewenthal, L. Trakhtenbrot, N. Paz, M. Koren-Michowitz, D. Waldman, L. Leider-Trejo, A. Toren, S. Constantini, and G. Rechavi, *Donor-derived brain tumor following neural stem cell transplantation in an ataxia telangiectasia patient.* PLoS Med, 2009. **6**(2): p. e1000029.
167. Yoon, Y.S., J.S. Park, T. Tkebuchava, C. Luedeman, and D.W. Losordo, *Unexpected severe calcification after transplantation of bone marrow cells in acute myocardial infarction.* Circulation, 2004. **109**(25): p. 3154-7.
168. Breitbach, M., T. Bostani, W. Roell, Y. Xia, O. Dewald, J.M. Nygren, J.W. Fries, K. Tiemann, H. Bohlen, J. Hescheler, A. Welz, W. Bloch, S.E. Jacobsen, and B.K. Fleischmann, *Potential risks of bone marrow cell transplantation into infarcted hearts.* Blood, 2007. **110**(4): p. 1362-9.
169. Barkholt, L., E. Flory, V. Jekerle, S. Lucas-Samuel, P. Ahnert, L. Bisset, D. Buscher, W. Fibbe, A. Foussat, M. Kwa, O. Lantz, R. Maciulaitis, T. Palomaki, C.K. Schneider, L. Sensebe, G. Tachdjian, K. Tarte, L. Tosca, and P. Salmikangas, *Risk of tumorigenicity in mesenchymal stromal cell-based therapies--bridging scientific observations and regulatory viewpoints.* Cytotherapy, 2013. **15**(7): p. 753-9.
170. Herberts, C.A., M.S. Kwa, and H.P. Hermsen, *Risk factors in the development of stem cell therapy.* J Transl Med, 2011. **9**: p. 29.
171. Patel, S.A., J.R. Meyer, S.J. Greco, K.E. Corcoran, M. Bryan, and P. Rameshwar, *Mesenchymal stem cells protect breast cancer cells through regulatory T cells: role of mesenchymal stem cell-derived TGF-beta.* J Immunol, 2010. **184**(10): p. 5885-94.
172. Li, J.H., W.S. Fan, M.M. Wang, Y.H. Wang, and Z.G. Ren, *Effects of mesenchymal stem cells on solid tumor metastasis in experimental cancer models: a systematic review and meta-analysis.* J Transl Med, 2018. **16**(1): p. 113.
173. Cui, L.L., E. Kerkela, A. Bakreen, F. Nitzsche, A. Andrzejewska, A. Nowakowski, M. Janowski, P. Walczak, J. Boltze, B. Lukomska, and J. Jolkkonen, *The cerebral embolism evoked by intra-arterial delivery of allogeneic bone marrow mesenchymal stem cells in rats is related to cell dose and infusion velocity.* Stem Cell Res Ther, 2015. **6**: p. 11.
174. Jung, J.W., M. Kwon, J.C. Choi, J.W. Shin, I.W. Park, B.W. Choi, and J.Y. Kim, *Familial occurrence of pulmonary embolism after intravenous, adipose tissue-derived stem cell therapy.* Yonsei Med J, 2013. **54**(5): p. 1293-6.
175. Berglund, A.K., L.A. Fortier, D.F. Antczak, and L.V. Schnabel, *Immunoprivileged no more: measuring the immunogenicity of allogeneic adult mesenchymal stem cells.* Stem Cell Res Ther, 2017. **8**(1): p. 288.
176. Guadix, J.A., J. Lopez-Beas, B. Clares, J.L. Soriano-Ruiz, J.L. Zugaza, and P. Galvez-Martin, *Principal Criteria for Evaluating the Quality, Safety and Efficacy of hMSC-Based Products in Clinical Practice: Current Approaches and Challenges.* Pharmaceutics, 2019. **11**(11).
177. Nguyen, P.K., J. Riegler, and J.C. Wu, *Stem cell imaging: from bench to bedside.* Cell Stem Cell, 2014. **14**(4): p. 431-44.
178. Scarfe, L., N. Brillant, J.D. Kumar, N. Ali, A. Alrumayh, M. Amali, S. Barbellion, V. Jones, M. Niemeijer, S. Potdevin, G. Roussignol, A. Vaganov, I. Barbaric, M. Barrow, N.C. Burton, J. Connell, F. Dazzi, J. Edsbagge, N.S. French, J. Holder, C. Hutchinson, D.R. Jones, T. Kalber, C. Lovatt, M.F. Lythgoe, S. Patel, P.S. Patrick, J. Piner, J. Reinhardt, E. Ricci, J. Sidaway, G.N. Stacey, P.J. Starkey Lewis, G. Sullivan, A. Taylor, B. Wilm, H. Poptani, P. Murray, C.E.P. Goldring, and B.K. Park, *Preclinical imaging*

methods for assessing the safety and efficacy of regenerative medicine therapies. NPJ Regen Med, 2017. **2**: p. 28.
179. Kraitchman, D.L. and J.W. Bulte, *In vivo imaging of stem cells and Beta cells using direct cell labeling and reporter gene methods.* Arterioscler Thromb Vasc Biol, 2009. **29**(7): p. 1025-30.
180. Kosaka, N., T.E. McCann, M. Mitsunaga, P.L. Choyke, and H. Kobayashi, *Real-time optical imaging using quantum dot and related nanocrystals.* Nanomedicine (Lond), 2010. **5**(5): p. 765-76.
181. Li, L., W. Jiang, K. Luo, H. Song, F. Lan, Y. Wu, and Z. Gu, *Superparamagnetic iron oxide nanoparticles as MRI contrast agents for non-invasive stem cell labeling and tracking.* Theranostics, 2013. **3**(8): p. 595-615.
182. Gawne, P.J., F. Man, P.J. Blower, and T.M.d.R. R, *Direct Cell Radiolabeling for in Vivo Cell Tracking with PET and SPECT Imaging.* Chem Rev, 2022. **122**(11): p. 10266-10318.
183. Li, W. and X. Chen, *Gold nanoparticles for photoacoustic imaging.* Nanomedicine (Lond), 2015. **10**(2): p. 299-320.
184. Rodriguez, E.A., G.N. Tran, L.A. Gross, J.L. Crisp, X. Shu, J.Y. Lin, and R.Y. Tsien, *A far-red fluorescent protein evolved from a cyanobacterial phycobiliprotein.* Nat Methods, 2016. **13**(9): p. 763-9.
185. Ziv, K., G. Meir, A. Harmelin, E. Shimoni, E. Klein, and M. Neeman, *Ferritin as a reporter gene for MRI: chronic liver over expression of H-ferritin during dietary iron supplementation and aging.* NMR Biomed, 2010. **23**(5): p. 523-31.
186. Vandsburger, M., *Cardiac Cell Tracking with MRI Reporter Genes: Welcoming a New Field.* Curr Cardiovasc Imaging Rep, 2014. **7**: p. 9250.
187. Ward, K.M., A.H. Aletras, and R.S. Balaban, *A new class of contrast agents for MRI based on proton chemical exchange dependent saturation transfer (CEST).* J Magn Reson, 2000. **143**(1): p. 79-87.
188. Yaghoubi, S.S., D.O. Campbell, C.G. Radu, and J. Czernin, *Positron emission tomography reporter genes and reporter probes: gene and cell therapy applications.* Theranostics, 2012. **2**(4): p. 374-91.
189. Contag, C.H. and M.H. Bachmann, *Advances in in vivo bioluminescence imaging of gene expression.* Annu Rev Biomed Eng, 2002. **4**: p. 235-60.
190. Baklaushev, V.P., A. Kilpelainen, S. Petkov, M.A. Abakumov, N.F. Grinenko, G.M. Yusubalieva, A.A. Latanova, I.L. Gubskiy, F.G. Zabozlaev, E.S. Starodubova, T.O. Abakumova, M.G. Isaguliants, and V.P. Chekhonin, *Luciferase Expression Allows Bioluminescence Imaging But Imposes Limitations on the Orthotopic Mouse (4T1) Model of Breast Cancer.* Sci Rep, 2017. **7**(1): p. 7715.
191. Haddock, S.H., M.A. Moline, and J.F. Case, *Bioluminescence in the sea.* Ann Rev Mar Sci, 2010. **2**: p. 443-93.
192. Yeh, H.W. and H.W. Ai, *Development and Applications of Bioluminescent and Chemiluminescent Reporters and Biosensors.* Annu Rev Anal Chem (Palo Alto Calif), 2019. **12**(1): p. 129-150.
193. Yang, X., R. Sun, L. Ci, N. Wang, S. Yang, J. Shi, H. Yang, M. Zhang, and J. Fei, *Tracing the dynamic expression of the Nfkappab2 gene during inflammatory processes by in vivo bioluminescence imaging in transgenic mice.* Biochem Biophys Res Commun, 2018. **501**(1): p. 41-47.
194. Zagozdzon, A.M., P. O'Leary, J.J. Callanan, J. Crown, W.M. Gallagher, and R. Zagozdzon, *Generation of a new bioluminescent model for visualisation of mammary tumour development in transgenic mice.* BMC Cancer, 2012. **12**: p. 209.
195. Dragulescu-Andrasi, A., C.T. Chan, A. De, T.F. Massoud, and S.S. Gambhir, *Bioluminescence resonance energy transfer (BRET) imaging of protein-protein*

interactions within deep tissues of living subjects. Proc Natl Acad Sci U S A, 2011. **108**(29): p. 12060-5.
196. Yeh, H.W., T. Wu, M. Chen, and H.W. Ai, *Identification of Factors Complicating Bioluminescence Imaging.* Biochemistry, 2019. **58**(12): p. 1689-1697.
197. Vieira, J., L. Pinto da Silva, and J.C. Esteves da Silva, *Advances in the knowledge of light emission by firefly luciferin and oxyluciferin.* J Photochem Photobiol B, 2012. **117**: p. 33-9.
198. Larionova, M.D., S.V. Markova, and E.S. Vysotski, *Bioluminescent and structural features of native folded Gaussia luciferase.* J Photochem Photobiol B, 2018. **183**: p. 309-317.
199. Sadikot, R.T. and T.S. Blackwell, *Bioluminescence imaging.* Proc Am Thorac Soc, 2005. **2**(6): p. 537-40, 511-2.
200. Raghuram, A., *Determining the depth limit of bioluminescent sources in scattering media*. 2020, Rice University.
201. Zhao, H., T.C. Doyle, O. Coquoz, F. Kalish, B.W. Rice, and C.H. Contag, *Emission spectra of bioluminescent reporters and interaction with mammalian tissue determine the sensitivity of detection in vivo.* J Biomed Opt, 2005. **10**(4): p. 41210.
202. Horecker, B.L., *The absorption spectra of hemoglobin and its derivatives in the visible and near infra-red regions.* Journal of biological chemistry, 1943. **148**(1): p. 173-183.
203. Kaskova, Z.M., A.S. Tsarkova, and I.V. Yampolsky, *1001 lights: luciferins, luciferases, their mechanisms of action and applications in chemical analysis, biology and medicine.* Chem Soc Rev, 2016. **45**(21): p. 6048-6077.
204. Evans, M.S., J.P. Chaurette, S.T. Adams, Jr., G.R. Reddy, M.A. Paley, N. Aronin, J.A. Prescher, and S.C. Miller, *A synthetic luciferin improves bioluminescence imaging in live mice.* Nat Methods, 2014. **11**(4): p. 393-5.
205. Iwano, S., M. Sugiyama, H. Hama, A. Watakabe, N. Hasegawa, T. Kuchimaru, K.Z. Tanaka, M. Takahashi, Y. Ishida, J. Hata, S. Shimozono, K. Namiki, T. Fukano, M. Kiyama, H. Okano, S. Kizaka-Kondoh, T.J. McHugh, T. Yamamori, H. Hioki, S. Maki, and A. Miyawaki, *Single-cell bioluminescence imaging of deep tissue in freely moving animals.* Science, 2018. **359**(6378): p. 935-939.
206. Jones, K.A., W.B. Porterfield, C.M. Rathbun, D.C. McCutcheon, M.A. Paley, and J.A. Prescher, *Orthogonal Luciferase-Luciferin Pairs for Bioluminescence Imaging.* J Am Chem Soc, 2017. **139**(6): p. 2351-2358.
207. Rathbun, C.M., W.B. Porterfield, K.A. Jones, M.J. Sagoe, M.R. Reyes, C.T. Hua, and J.A. Prescher, *Parallel Screening for Rapid Identification of Orthogonal Bioluminescent Tools.* ACS Cent Sci, 2017. **3**(12): p. 1254-1261.
208. Wood, K.V., Y.A. Lam, and W.D. McElroy, *Introduction to beetle luciferases and their applications.* J Biolumin Chemilumin, 1989. **4**(1): p. 289-301.
209. Hall, M.P., C.C. Woodroofe, M.G. Wood, I. Que, M. Van't Root, Y. Ridwan, C. Shi, T.A. Kirkland, L.P. Encell, K.V. Wood, C. Lowik, and L. Mezzanotte, *Click beetle luciferase mutant and near infrared naphthyl-luciferins for improved bioluminescence imaging.* Nat Commun, 2018. **9**(1): p. 132.
210. Teranishi, K. and O. Shimomura, *Solubilizing coelenterazine in water with hydroxypropyl-β-cyclodextrin.* Bioscience, biotechnology, and biochemistry, 1997. **61**(7): p. 1219-1220.
211. Yeh, H.W., Y. Xiong, T. Wu, M. Chen, A. Ji, X. Li, and H.W. Ai, *ATP-Independent Bioluminescent Reporter Variants To Improve in Vivo Imaging.* ACS Chem Biol, 2019. **14**(5): p. 959-965.
212. Jiang, T., L. Du, and M. Li, *Lighting up bioluminescence with coelenterazine: strategies and applications.* Photochem Photobiol Sci, 2016. **15**(4): p. 466-80.

213. Hall, M.P., J. Unch, B.F. Binkowski, M.P. Valley, B.L. Butler, M.G. Wood, P. Otto, K. Zimmerman, G. Vidugiris, T. Machleidt, M.B. Robers, H.A. Benink, C.T. Eggers, M.R. Slater, P.L. Meisenheimer, D.H. Klaubert, F. Fan, L.P. Encell, and K.V. Wood, *Engineered luciferase reporter from a deep sea shrimp utilizing a novel imidazopyrazinone substrate.* ACS Chem Biol, 2012. **7**(11): p. 1848-57.
214. Yeh, H.W., O. Karmach, A. Ji, D. Carter, M.M. Martins-Green, and H.W. Ai, *Red-shifted luciferase-luciferin pairs for enhanced bioluminescence imaging.* Nat Methods, 2017. **14**(10): p. 971-974.
215. Shakhmin, A., M.P. Hall, T. Machleidt, J.R. Walker, K.V. Wood, and T.A. Kirkland, *Coelenterazine analogues emit red-shifted bioluminescence with NanoLuc.* Org Biomol Chem, 2017. **15**(40): p. 8559-8567.
216. Pfleger, K.D. and K.A. Eidne, *Illuminating insights into protein-protein interactions using bioluminescence resonance energy transfer (BRET).* Nat Methods, 2006. **3**(3): p. 165-74.
217. Sun, S., X. Yang, Y. Wang, and X. Shen, *In Vivo Analysis of Protein-Protein Interactions with Bioluminescence Resonance Energy Transfer (BRET): Progress and Prospects.* Int J Mol Sci, 2016. **17**(10).
218. Chu, J., Y. Oh, A. Sens, N. Ataie, H. Dana, J.J. Macklin, T. Laviv, E.S. Welf, K.M. Dean, F. Zhang, B.B. Kim, C.T. Tang, M. Hu, M.A. Baird, M.W. Davidson, M.A. Kay, R. Fiolka, R. Yasuda, D.S. Kim, H.L. Ng, and M.Z. Lin, *A bright cyan-excitable orange fluorescent protein facilitates dual-emission microscopy and enhances bioluminescence imaging in vivo.* Nat Biotechnol, 2016. **34**(7): p. 760-7.
219. Schaub, F.X., M.S. Reza, C.A. Flaveny, W. Li, A.M. Musicant, S. Hoxha, M. Guo, J.L. Cleveland, and A.L. Amelio, *Fluorophore-NanoLuc BRET Reporters Enable Sensitive In Vivo Optical Imaging and Flow Cytometry for Monitoring Tumorigenesis.* Cancer Res, 2015. **75**(23): p. 5023-33.
220. Suzuki, K., T. Kimura, H. Shinoda, G. Bai, M.J. Daniels, Y. Arai, M. Nakano, and T. Nagai, *Five colour variants of bright luminescent protein for real-time multicolour bioimaging.* Nat Commun, 2016. **7**: p. 13718.
221. de Wet, J.R., K.V. Wood, M. DeLuca, D.R. Helinski, and S. Subramani, *Firefly luciferase gene: structure and expression in mammalian cells.* Mol Cell Biol, 1987. **7**(2): p. 725-37.
222. Seliger, H.H. and W.D. McElroy, *Quantum yield in the oxidation of firefly luciferin.* Biochemical and Biophysical Research Communications, 1959. **1**(1): p. 21-24.
223. Kuchimaru, T., S. Iwano, M. Kiyama, S. Mitsumata, T. Kadonosono, H. Niwa, S. Maki, and S. Kizaka-Kondoh, *A luciferin analogue generating near-infrared bioluminescence achieves highly sensitive deep-tissue imaging.* Nat Commun, 2016. **7**: p. 11856.
224. Nakajima, Y., T. Yamazaki, S. Nishii, T. Noguchi, H. Hoshino, K. Niwa, V.R. Viviani, and Y. Ohmiya, *Enhanced beetle luciferase for high-resolution bioluminescence imaging.* PLoS One, 2010. **5**(4): p. e10011.
225. Lorenz, W.W., R.O. McCann, M. Longiaru, and M.J. Cormier, *Isolation and expression of a cDNA encoding Renilla reniformis luciferase.* Proc Natl Acad Sci U S A, 1991. **88**(10): p. 4438-42.
226. Loening, A.M., T.D. Fenn, A.M. Wu, and S.S. Gambhir, *Consensus guided mutagenesis of Renilla luciferase yields enhanced stability and light output.* Protein Eng Des Sel, 2006. **19**(9): p. 391-400.
227. Loening, A.M., A.M. Wu, and S.S. Gambhir, *Red-shifted Renilla reniformis luciferase variants for imaging in living subjects.* Nat Methods, 2007. **4**(8): p. 641-3.
228. Verhaegent, M. and T.K. Christopoulos, *Recombinant Gaussia luciferase. Overexpression, purification, and analytical application of a bioluminescent reporter for DNA hybridization.* Anal Chem, 2002. **74**(17): p. 4378-85.

229. Kim, S.B., H. Suzuki, M. Sato, and H. Tao, *Superluminescent variants of marine luciferases for bioassays.* Anal Chem, 2011. **83**(22): p. 8732-40.
230. Degeling, M.H., M.S. Bovenberg, G.K. Lewandrowski, M.C. de Gooijer, C.L. Vleggeert-Lankamp, M. Tannous, C.A. Maguire, and B.A. Tannous, *Directed molecular evolution reveals Gaussia luciferase variants with enhanced light output stability.* Anal Chem, 2013. **85**(5): p. 3006-12.
231. Shimomura, O., T. Masugi, F.H. Johnson, and Y. Haneda, *Properties and reaction mechanism of the bioluminescence system of the deep-sea shrimp Oplophorus gracilorostris.* Biochemistry, 1978. **17**(6): p. 994-8.
232. Wilson, T. and J.W. Hastings, *Bioluminescence.* Annu Rev Cell Dev Biol, 1998. **14**: p. 197-230.
233. Berebichez-Fridman, R., R. Gomez-Garcia, J. Granados-Montiel, E. Berebichez-Fastlicht, A. Olivos-Meza, J. Granados, C. Velasquillo, and C. Ibarra, *The Holy Grail of Orthopedic Surgery: Mesenchymal Stem Cells-Their Current Uses and Potential Applications.* Stem Cells Int, 2017. **2017**: p. 2638305.
234. Majka, M., M. Sulkowski, B. Badyra, and P. Musialek, *Concise Review: Mesenchymal Stem Cells in Cardiovascular Regeneration: Emerging Research Directions and Clinical Applications.* Stem Cells Transl Med, 2017. **6**(10): p. 1859-1867.
235. Yun, C.W. and S.H. Lee, *Potential and Therapeutic Efficacy of Cell-based Therapy Using Mesenchymal Stem Cells for Acute/chronic Kidney Disease.* Int J Mol Sci, 2019. **20**(7).
236. Rodriguez-Fuentes, D.E., L.E. Fernandez-Garza, J.A. Samia-Meza, S.A. Barrera-Barrera, A.I. Caplan, and H.A. Barrera-Saldana, *Mesenchymal Stem Cells Current Clinical Applications: A Systematic Review.* Arch Med Res, 2021. **52**(1): p. 93-101.
237. Seo, Y., T.H. Shin, and H.S. Kim, *Current Strategies to Enhance Adipose Stem Cell Function: An Update.* Int J Mol Sci, 2019. **20**(15).
238. Selich, A., K. Zimmermann, M. Tenspolde, O. Dittrich-Breiholz, C. von Kaisenberg, A. Schambach, and M. Rothe, *Umbilical cord as a long-term source of activatable mesenchymal stromal cells for immunomodulation.* Stem Cell Res Ther, 2019. **10**(1): p. 285.
239. Heo, J.S., Y. Choi, H.S. Kim, and H.O. Kim, *Comparison of molecular profiles of human mesenchymal stem cells derived from bone marrow, umbilical cord blood, placenta and adipose tissue.* Int J Mol Med, 2016. **37**(1): p. 115-25.
240. Wolff, J.H. and J.G. Mikkelsen, *Delivering genes with human immunodeficiency virus-derived vehicles: still state-of-the-art after 25 years.* J Biomed Sci, 2022. **29**(1): p. 79.
241. Seiden, D., *Specific granules of the rat atrial muscle cell.* Anat Rec, 1979. **194**(4): p. 587-602.
242. Cornetta, K. and W.F. Anderson, *Protamine sulfate as an effective alternative to polybrene in retroviral-mediated gene-transfer: implications for human gene therapy.* J Virol Methods, 1989. **23**(2): p. 187-94.
243. Denning, W., S. Das, S. Guo, J. Xu, J.C. Kappes, and Z. Hel, *Optimization of the transductional efficiency of lentiviral vectors: effect of sera and polycations.* Mol Biotechnol, 2013. **53**(3): p. 308-14.
244. Davis, H.E., J.R. Morgan, and M.L. Yarmush, *Polybrene increases retrovirus gene transfer efficiency by enhancing receptor-independent virus adsorption on target cell membranes.* Biophys Chem, 2002. **97**(2-3): p. 159-72.
245. Davis, H.E., M. Rosinski, J.R. Morgan, and M.L. Yarmush, *Charged polymers modulate retrovirus transduction via membrane charge neutralization and virus aggregation.* Biophys J, 2004. **86**(2): p. 1234-42.
246. Seitz, B., E. Baktanian, E.M. Gordon, W.F. Anderson, L. LaBree, and P.J. McDonnell, *Retroviral vector-mediated gene transfer into keratocytes: in vitro effects of*

polybrene and protamine sulfate. Graefes Arch Clin Exp Ophthalmol, 1998. **236**(8): p. 602-12.
247. Lin, P., D. Correa, Y. Lin, and A.I. Caplan, *Polybrene inhibits human mesenchymal stem cell proliferation during lentiviral transduction.* PLoS One, 2011. **6**(8): p. e23891.
248. Griukova, A., P. Deryabin, M. Sirotkina, A. Shatrova, N. Nikolsky, and A. Borodkina, *P38 MAPK inhibition prevents polybrene-induced senescence of human mesenchymal stem cells during viral transduction.* PLoS One, 2018. **13**(12): p. e0209606.
249. Lin, P., Y. Lin, D.P. Lennon, D. Correa, M. Schluchter, and A.I. Caplan, *Efficient lentiviral transduction of human mesenchymal stem cells that preserves proliferation and differentiation capabilities.* Stem Cells Transl Med, 2012. **1**(12): p. 886-97.
250. O'Doherty, U., W.J. Swiggard, and M.H. Malim, *Human immunodeficiency virus type 1 spinoculation enhances infection through virus binding.* J Virol, 2000. **74**(21): p. 10074-80.
251. Guo, J., W. Wang, D. Yu, and Y. Wu, *Spinoculation triggers dynamic actin and cofilin activity that facilitates HIV-1 infection of transformed and resting CD4 T cells.* J Virol, 2011. **85**(19): p. 9824-33.
252. Yan, R., Y. Zhang, D. Cai, Y. Liu, A. Cuconati, and H. Guo, *Spinoculation Enhances HBV Infection in NTCP-Reconstituted Hepatocytes.* PLoS One, 2015. **10**(6): p. e0129889.
253. Ren, J., H. Wang, K. Tran, S. Civini, P. Jin, L. Castiello, J. Feng, S.A. Kuznetsov, P.G. Robey, M. Sabatino, and D.F. Stroncek, *Human bone marrow stromal cell confluence: effects on cell characteristics and methods of assessment.* Cytotherapy, 2015. **17**(7): p. 897-911.
254. Quirici, N., C. Scavullo, L. de Girolamo, S. Lopa, E. Arrigoni, G.L. Deliliers, and A.T. Brini, *Anti-L-NGFR and -CD34 monoclonal antibodies identify multipotent mesenchymal stem cells in human adipose tissue.* Stem Cells Dev, 2010. **19**(6): p. 915-25.
255. Yoshimura, K., T. Shigeura, D. Matsumoto, T. Sato, Y. Takaki, E. Aiba-Kojima, K. Sato, K. Inoue, T. Nagase, I. Koshima, and K. Gonda, *Characterization of freshly isolated and cultured cells derived from the fatty and fluid portions of liposuction aspirates.* J Cell Physiol, 2006. **208**(1): p. 64-76.
256. Lin, C.S., H. Ning, G. Lin, and T.F. Lue, *Is CD34 truly a negative marker for mesenchymal stromal cells?* Cytotherapy, 2012. **14**(10): p. 1159-63.
257. Yeh, S.P., J.G. Chang, C.L. Lin, W.J. Lo, C.C. Lee, C.Y. Lin, and C.F. Chiu, *Mesenchymal stem cells can be easily isolated from bone marrow of patients with various haematological malignancies but the surface antigens expression may be changed after prolonged ex vivo culture.* Leukemia, 2005. **19**(8): p. 1505-7.
258. Grau-Vorster, M., A. Laitinen, J. Nystedt, and J. Vives, *HLA-DR expression in clinical-grade bone marrow-derived multipotent mesenchymal stromal cells: a two-site study.* Stem Cell Res Ther, 2019. **10**(1): p. 164.
259. Tandon, N., K.N. Thakkar, E.L. LaGory, Y. Liu, and A.J. Giaccia, *Generation of Stable Expression Mammalian Cell Lines Using Lentivirus.* Bio Protoc, 2018. **8**(21).
260. Deryabin, P., A. Griukova, A. Shatrova, A. Petukhov, N. Nikolsky, and A. Borodkina, *Optimization of lentiviral transduction parameters and its application for CRISPR-based secretome modification of human endometrial mesenchymal stem cells.* Cell Cycle, 2019. **18**(6-7): p. 742-758.
261. Nanbakhsh, A., B. Best, M. Riese, S. Rao, L. Wang, J. Medin, M.S. Thakar, and S. Malarkannan, *Dextran Enhances the Lentiviral Transduction Efficiency of Murine and Human Primary NK Cells.* J Vis Exp, 2018(131).

262. Kumar, M., B. Keller, N. Makalou, and R.E. Sutton, *Systematic determination of the packaging limit of lentiviral vectors.* Hum Gene Ther, 2001. **12**(15): p. 1893-905.
263. Cante-Barrett, K., R.D. Mendes, W.K. Smits, Y.M. van Helsdingen-van Wijk, R. Pieters, and J.P. Meijerink, *Lentiviral gene transfer into human and murine hematopoietic stem cells: size matters.* BMC Res Notes, 2016. **9**: p. 312.
264. Taylor, A., J. Sharkey, A. Plagge, B. Wilm, and P. Murray, *Multicolour In Vivo Bioluminescence Imaging Using a NanoLuc-Based BRET Reporter in Combination with Firefly Luciferase.* Contrast Media Mol Imaging, 2018. **2018**: p. 2514796.
265. Adams, S.T., Jr. and S.C. Miller, *Beyond D-luciferin: expanding the scope of bioluminescence imaging in vivo.* Curr Opin Chem Biol, 2014. **21**: p. 112-20.
266. Liang, Y., P. Walczak, and J.W. Bulte, *Comparison of red-shifted firefly luciferase Ppy RE9 and conventional Luc2 as bioluminescence imaging reporter genes for in vivo imaging of stem cells.* J Biomed Opt, 2012. **17**(1): p. 016004.
267. Reddy, G.R., W.C. Thompson, and S.C. Miller, *Robust light emission from cyclic alkylaminoluciferin substrates for firefly luciferase.* J Am Chem Soc, 2010. **132**(39): p. 13586-7.
268. Iwano, S., R. Obata, C. Miura, M. Kiyama, K. Hama, M. Nakamura, Y. Amano, S. Kojima, T. Hirano, and S. Maki, *Development of simple firefly luciferin analogs emitting blue, green, red, and near-infrared biological window light.* Tetrahedron, 2013. **69**(19): p. 3847-3856.
269. Miura, C., M. Kiyama, S. Iwano, K. Ito, R. Obata, T. Hirano, S. Maki, and H. Niwa, *Synthesis and luminescence properties of biphenyl-type firefly luciferin analogs with a new, near-infrared light-emitting bioluminophore.* Tetrahedron, 2013. **69**(46): p. 9726-9734.
270. Jathoul, A.P., H. Grounds, J.C. Anderson, and M.A. Pule, *A dual-color far-red to near-infrared firefly luciferin analogue designed for multiparametric bioluminescence imaging.* Angew Chem Int Ed Engl, 2014. **53**(48): p. 13059-63.
271. Lyons, S.K., P.S. Patrick, and K.M. Brindle, *Imaging mouse cancer models in vivo using reporter transgenes.* Cold Spring Harb Protoc, 2013. **2013**(8): p. 685-99.
272. Khalil, A.A., M.J. Jameson, W.C. Broaddus, T.D. Chung, S.E. Golding, S.M. Dever, E. Rosenberg, and K. Valerie, *Subcutaneous administration of D-luciferin is an effective alternative to intraperitoneal injection in bioluminescence imaging of xenograft tumors in nude mice.* ISRN Mol Imaging, 2013. **2013**.
273. Aswendt, M., J. Adamczak, S. Couillard-Despres, and M. Hoehn, *Boosting bioluminescence neuroimaging: an optimized protocol for brain studies.* PLoS One, 2013. **8**(2): p. e55662.
274. Simonyan, H., C. Hurr, and C.N. Young, *A synthetic luciferin improves in vivo bioluminescence imaging of gene expression in cardiovascular brain regions.* Physiol Genomics, 2016. **48**(10): p. 762-770.
275. *GOOD PRACTICE GUIDELINES Administration of Substances (Rat, Mouse, Guinea Pig, Rabbit)*. Available from: https://researchanimaltraining.com/wp-content/uploads/2021/05/lasa_administration.pdf.
276. Fischer, U.M., M.T. Harting, F. Jimenez, W.O. Monzon-Posadas, H. Xue, S.I. Savitz, G.A. Laine, and C.S. Cox, Jr., *Pulmonary passage is a major obstacle for intravenous stem cell delivery: the pulmonary first-pass effect.* Stem Cells Dev, 2009. **18**(5): p. 683-92.
277. Inoue, Y., S. Kiryu, K. Izawa, M. Watanabe, A. Tojo, and K. Ohtomo, *Comparison of subcutaneous and intraperitoneal injection of D-luciferin for in vivo bioluminescence imaging.* Eur J Nucl Med Mol Imaging, 2009. **36**(5): p. 771-9.
278. Su, Y., J.R. Walker, Y. Park, T.P. Smith, L.X. Liu, M.P. Hall, L. Labanieh, R. Hurst, D.C. Wang, L.P. Encell, N. Kim, F. Zhang, M.A. Kay, K.M. Casey, R.G. Majzner, J.R. Cochran, C.L. Mackall, T.A. Kirkland, and M.Z. Lin, *Novel NanoLuc substrates enable*

bright two-population bioluminescence imaging in animals. Nat Methods, 2020. **17**(8): p. 852-860.
279. Saito, R., T. Kuchimaru, S. Higashi, S.W. Lu, M. Kiyama, S. Iwano, R. Obata, T. Hirano, S. Kizaka-Kondoh, and S.A. Maki, *Synthesis and luminescence properties of near-infrared N-heterocyclic luciferin analogues for in vivo optical imaging.* Bulletin of the Chemical Society of Japan, 2019. **92**(3): p. 608-618.
280. Weiss, A.R.R. and M.H. Dahlke, *Immunomodulation by Mesenchymal Stem Cells (MSCs): Mechanisms of Action of Living, Apoptotic, and Dead MSCs.* Front Immunol, 2019. **10**: p. 1191.
281. Chang, C., J. Yan, Z. Yao, C. Zhang, X. Li, and H.Q. Mao, *Effects of Mesenchymal Stem Cell-Derived Paracrine Signals and Their Delivery Strategies.* Adv Healthc Mater, 2021. **10**(7): p. e2001689.
282. Harwood, R., J. Bridge, L. Ressel, L. Scarfe, J. Sharkey, G. Czanner, P.A. Kalra, A. Odudu, S. Kenny, B. Wilm, and P. Murray, *Murine models of renal ischemia reperfusion injury: An opportunity for refinement using noninvasive monitoring methods.* Physiol Rep, 2022. **10**(5): p. e15211.
283. Jungblut, M., K. Oeltze, I. Zehnter, D. Hasselmann, and A. Bosio, *Standardized preparation of single-cell suspensions from mouse lung tissue using the gentleMACS Dissociator.* J Vis Exp, 2009(29).
284. Amend, S.R., K.C. Valkenburg, and K.J. Pienta, *Murine Hind Limb Long Bone Dissection and Bone Marrow Isolation.* J Vis Exp, 2016(110).
285. Hensel, J.A., V. Khattar, R. Ashton, and S. Ponnazhagan, *Characterization of immune cell subtypes in three commonly used mouse strains reveals gender and strain-specific variations.* Lab Invest, 2019. **99**(1): p. 93-106.
286. Moll, G., J.A. Ankrum, J. Kamhieh-Milz, K. Bieback, O. Ringden, H.D. Volk, S. Geissler, and P. Reinke, *Intravascular Mesenchymal Stromal/Stem Cell Therapy Product Diversification: Time for New Clinical Guidelines.* Trends Mol Med, 2019. **25**(2): p. 149-163.
287. Patrick, P.S., K.K. Kolluri, M. Zaw Thin, A. Edwards, E.K. Sage, T. Sanderson, B.D. Weil, J.C. Dickson, M.F. Lythgoe, M. Lowdell, S.M. Janes, and T.L. Kalber, *Lung delivery of MSCs expressing anti-cancer protein TRAIL visualised with (89)Zr-oxine PET-CT.* Stem Cell Res Ther, 2020. **11**(1): p. 256.
288. Pang, S.H.M., J. D'Rozario, S. Mendonca, T. Bhuvan, N.L. Payne, D. Zheng, A. Hisana, G. Wallis, A. Barugahare, D. Powell, J. Rautela, N.D. Huntington, G. Dewson, D.C.S. Huang, D.H.D. Gray, and T.S.P. Heng, *Mesenchymal stromal cell apoptosis is required for their therapeutic function.* Nat Commun, 2021. **12**(1): p. 6495.
289. Jang, H.R., J.H. Park, G.Y. Kwon, J.E. Lee, W. Huh, H.J. Jin, S.J. Choi, W. Oh, H.Y. Oh, and Y.G. Kim, *Effect of preemptive treatment with human umbilical cord blood-derived mesenchymal stem cells on the development of renal ischemia-reperfusion injury in mice.* Am J Physiol Renal Physiol, 2014. **307**(10): p. F1149-61.
290. Jin, S.-Z., B.-R. Liu, J. Xu, F.-L. Gao, Z.-J. Hu, X.-H. Wang, F.-H. Pei, Y. Hong, H.-Y. Hu, and M.-Z. Han, *Ex vivo-expanded bone marrow stem cells home to the liver and ameliorate functional recovery in a mouse model of acute hepatic injury.* Hepatobiliary & Pancreatic Diseases International, 2012. **11**(1): p. 66-73.
291. Kidd, S., E. Spaeth, J.L. Dembinski, M. Dietrich, K. Watson, A. Klopp, V.L. Battula, M. Weil, M. Andreeff, and F.C. Marini, *Direct evidence of mesenchymal stem cell tropism for tumor and wounding microenvironments using in vivo bioluminescent imaging.* Stem Cells, 2009. **27**(10): p. 2614-23.
292. Schubert, R., J. Sann, J.T. Frueh, E. Ullrich, H. Geiger, and P.C. Baer, *Tracking of Adipose-Derived Mesenchymal Stromal/Stem Cells in a Model of Cisplatin-Induced Acute Kidney Injury: Comparison of Bioluminescence Imaging versus qRT-PCR.* Int J Mol Sci, 2018. **19**(9).

293. Burks, S.R., B.A. Nguyen, P.A. Tebebi, S.J. Kim, M.N. Bresler, A. Ziadloo, J.M. Street, P.S. Yuen, R.A. Star, and J.A. Frank, *Pulsed focused ultrasound pretreatment improves mesenchymal stromal cell efficacy in preventing and rescuing established acute kidney injury in mice.* Stem Cells, 2015. **33**(4): p. 1241-53.
294. Jackson, J.S., J.P. Golding, C. Chapon, W.A. Jones, and K.K. Bhakoo, *Homing of stem cells to sites of inflammatory brain injury after intracerebral and intravenous administration: a longitudinal imaging study.* Stem Cell Res Ther, 2010. **1**(2): p. 17.
295. Xing, L., R. Cui, L. Peng, J. Ma, X. Chen, R.J. Xie, and B. Li, *Mesenchymal stem cells, not conditioned medium, contribute to kidney repair after ischemia-reperfusion injury.* Stem Cell Res Ther, 2014. **5**(4): p. 101.
296. Li, P., R. Zhang, H. Sun, L. Chen, F. Liu, C. Yao, M. Du, and X. Jiang, *PKH26 can transfer to host cells in vitro and vivo.* Stem Cells Dev, 2013. **22**(2): p. 340-4.
297. Wang, L., Z. Zhang, R. Xu, X. Wang, Z. Shu, X. Chen, S. Wang, J. Liu, Y. Li, L. Wang, M. Zhang, W. Yang, Y. Wang, H. Huang, B. Tu, Z. Liang, L. Li, J. Li, Y. Hou, M. Shi, and F.S. Wang, *Human umbilical cord mesenchymal stem cell transfusion in immune non-responders with AIDS: a multicenter randomized controlled trial.* Signal Transduct Target Ther, 2021. **6**(1): p. 217.
298. Trujillo-Rodriguez, M., P. Viciana, I. Rivas-Jeremias, A.I. Alvarez-Rios, A. Ruiz-Garcia, O. Espinosa-Ibanez, S. Arias-Santiago, J. Martinez-Atienza, R. Mata, O. Fernandez-Lopez, E. Ruiz-Mateos, A. Gutierrez-Valencia, and L.F. Lopez-Cortes, *Mesenchymal stromal cells in human immunodeficiency virus-infected patients with discordant immune response: Early results of a phase I/II clinical trial.* Stem Cells Transl Med, 2021. **10**(4): p. 534-541.
299. Neri, S., *Genetic Stability of Mesenchymal Stromal Cells for Regenerative Medicine Applications: A Fundamental Biosafety Aspect.* Int J Mol Sci, 2019. **20**(10).
300. Altmann, C., A. Andres-Hernando, R.H. McMahan, N. Ahuja, Z. He, C.J. Rivard, C.L. Edelstein, L. Barthel, W.J. Janssen, and S. Faubel, *Macrophages mediate lung inflammation in a mouse model of ischemic acute kidney injury.* Am J Physiol Renal Physiol, 2012. **302**(4): p. F421-32.
301. Faubel, S. and C.L. Edelstein, *Mechanisms and mediators of lung injury after acute kidney injury.* Nat Rev Nephrol, 2016. **12**(1): p. 48-60.
302. He, J., X. Yao, P. Mo, K. Wang, Z.L. Yang, N.N. Tian, X.Q. Zhu, J. Zhao, R.Q. Pang, G.P. Ruan, and X.H. Pan, *Lack of tumorigenesis and protumorigenic activity of human umbilical cord mesenchymal stem cells in NOD SCID mice.* BMC Cancer, 2022. **22**(1): p. 307.
303. Esmann, L., C. Idel, A. Sarkar, L. Hellberg, M. Behnen, S. Moller, G. van Zandbergen, M. Klinger, J. Kohl, U. Bussmeyer, W. Solbach, and T. Laskay, *Phagocytosis of apoptotic cells by neutrophil granulocytes: diminished proinflammatory neutrophil functions in the presence of apoptotic cells.* J Immunol, 2010. **184**(1): p. 391-400.
304. Mercer, P.F., A.E. Williams, C.J. Scotton, R.J. Jose, M. Sulikowski, J.D. Moffatt, L.A. Murray, and R.C. Chambers, *Proteinase-activated receptor-1, CCL2, and CCL7 regulate acute neutrophilic lung inflammation.* Am J Respir Cell Mol Biol, 2014. **50**(1): p. 144-57.
305. Sawant, K.V., K.M. Poluri, A.K. Dutta, K.M. Sepuru, A. Troshkina, R.P. Garofalo, and K. Rajarathnam, *Chemokine CXCL1 mediated neutrophil recruitment: Role of glycosaminoglycan interactions.* Sci Rep, 2016. **6**: p. 33123.
306. Hoogduijn, M.J., M. Roemeling-van Rhijn, A.U. Engela, S.S. Korevaar, F.K. Mensah, M. Franquesa, R.W. de Bruin, M.G. Betjes, W. Weimar, and C.C. Baan, *Mesenchymal stem cells induce an inflammatory response after intravenous infusion.* Stem Cells Dev, 2013. **22**(21): p. 2825-35.
307. Min, H., L. Xu, R. Parrott, C.C. Overall, M. Lillich, E.M. Rabjohns, R.R. Rampersad, T.K. Tarrant, N. Meadows, A. Fernandez-Castaneda, A. Gaultier, J. Kurtzberg, and

A.J. Filiano, *Mesenchymal stromal cells reprogram monocytes and macrophages with processing bodies.* Stem Cells, 2021. **39**(1): p. 115-128.
308. Biet, F., C. Locht, and L. Kremer, *Immunoregulatory functions of interleukin 18 and its role in defense against bacterial pathogens.* J Mol Med (Berl), 2002. **80**(3): p. 147-62.
309. Neyestani, T., *Immune alterations in metabolic syndrome: the old story of chicken and egg.* Bioactive Food as Dietary Interventions for Arthritis and Related Inflammatory Diseases: Bioactive Food in Chronic Disease States, 2012: p. 431.
310. Chatterjee, D., N. Marquardt, D.M. Tufa, T. Hatlapatka, R. Hass, C. Kasper, C. von Kaisenberg, R.E. Schmidt, and R. Jacobs, *Human Umbilical Cord-Derived Mesenchymal Stem Cells Utilize Activin-A to Suppress Interferon-gamma Production by Natural Killer Cells.* Front Immunol, 2014. **5**: p. 662.
311. Wang, H., P. Xuan, H. Tian, X. Hao, J. Yang, X. Xu, and L. Qiao, *Adiposederived mesenchymal stem cellderived HCAR1 regulates immune response in the attenuation of sepsis.* Mol Med Rep, 2022. **26**(3).
312. Wu, M., H. Ge, S. Li, H. Chu, S. Yang, X. Sun, Z. Zhou, and X. Zhu, *Mesenchymal Stem Cells Immunosuppressed IL-22 in Patients with Immune Thrombocytopenia via Soluble Cellular Factors.* J Immunol Res, 2015. **2015**: p. 316351.
313. Hyvarinen, K., M. Holopainen, V. Skirdenko, H. Ruhanen, P. Lehenkari, M. Korhonen, R. Kakela, S. Laitinen, and E. Kerkela, *Mesenchymal Stromal Cells and Their Extracellular Vesicles Enhance the Anti-Inflammatory Phenotype of Regulatory Macrophages by Downregulating the Production of Interleukin (IL)-23 and IL-22.* Front Immunol, 2018. **9**: p. 771.
314. Anderson, D.M., E. Maraskovsky, W.L. Billingsley, W.C. Dougall, M.E. Tometsko, E.R. Roux, M.C. Teepe, R.F. DuBose, D. Cosman, and L. Galibert, *A homologue of the TNF receptor and its ligand enhance T-cell growth and dendritic-cell function.* Nature, 1997. **390**(6656): p. 175-9.
315. Kong, Y.Y., H. Yoshida, I. Sarosi, H.L. Tan, E. Timms, C. Capparelli, S. Morony, A.J. Oliveira-dos-Santos, G. Van, A. Itie, W. Khoo, A. Wakeham, C.R. Dunstan, D.L. Lacey, T.W. Mak, W.J. Boyle, and J.M. Penninger, *OPGL is a key regulator of osteoclastogenesis, lymphocyte development and lymph-node organogenesis.* Nature, 1999. **397**(6717): p. 315-23.
316. Papadaki, M., V. Rinotas, F. Violitzi, T. Thireou, G. Panayotou, M. Samiotaki, and E. Douni, *New Insights for RANKL as a Proinflammatory Modulator in Modeled Inflammatory Arthritis.* Front Immunol, 2019. **10**: p. 97.
317. Quercioli, A., F. Mach, M. Bertolotto, S. Lenglet, N. Vuilleumier, K. Galan, S. Pagano, V. Braunersreuther, G. Pelli, V. Pistoia, G. Bianchi, G. Cittadini, G.L. Viviani, A. Pende, P. Roux-Lombard, A. Thomas, C. Staub, O. Ratib, F. Dallegri, T.H. Schindler, and F. Montecucco, *Receptor activator of NF- kappaB ligand (RANKL) increases the release of neutrophil products associated with coronary vulnerability.* Thromb Haemost, 2012. **107**(1): p. 124-39.
318. Carbone, F., L.A. Crowe, A. Roth, F. Burger, S. Lenglet, V. Braunersreuther, K.J. Brandt, A. Quercioli, F. Mach, J.P. Vallee, and F. Montecucco, *Treatment with anti-RANKL antibody reduces infarct size and attenuates dysfunction impacting on neutrophil-mediated injury.* J Mol Cell Cardiol, 2016. **94**: p. 82-94.
319. Li, F., X. Li, G. Liu, C. Gao, and X. Li, *Bone Marrow Mesenchymal Stem Cells Decrease the Expression of RANKL in Collagen-Induced Arthritis Rats via Reducing the Levels of IL-22.* J Immunol Res, 2019. **2019**: p. 8459281.
320. Malek, T.R. and I. Castro, *Interleukin-2 receptor signaling: at the interface between tolerance and immunity.* Immunity, 2010. **33**(2): p. 153-65.
321. Damoiseaux, J., *The IL-2 - IL-2 receptor pathway in health and disease: The role of the soluble IL-2 receptor.* Clin Immunol, 2020. **218**: p. 108515.

322. Dias, S., H. Silva, Jr., A. Cumano, and P. Vieira, *Interleukin-7 is necessary to maintain the B cell potential in common lymphoid progenitors.* J Exp Med, 2005. **201**(6): p. 971-9.
323. Levine, S.J., *Mechanisms of soluble cytokine receptor generation.* J Immunol, 2004. **173**(9): p. 5343-8.
324. Zheng, X., H. Baker, W.S. Hancock, F. Fawaz, M. McCaman, and E. Pungor, Jr., *Proteomic analysis for the assessment of different lots of fetal bovine serum as a raw material for cell culture. Part IV. Application of proteomics to the manufacture of biological drugs.* Biotechnol Prog, 2006. **22**(5): p. 1294-300.
325. Liu, S., L.F. de Castro, P. Jin, S. Civini, J. Ren, J.A. Reems, J. Cancelas, R. Nayak, G. Shaw, T. O'Brien, D.H. McKenna, M. Armant, L. Silberstein, A.P. Gee, D.J. Hei, P. Hematti, S.A. Kuznetsov, P.G. Robey, and D.F. Stroncek, *Manufacturing Differences Affect Human Bone Marrow Stromal Cell Characteristics and Function: Comparison of Production Methods and Products from Multiple Centers.* Sci Rep, 2017. **7**: p. 46731.
326. Neuhuber, B., S.A. Swanger, L. Howard, A. Mackay, and I. Fischer, *Effects of plating density and culture time on bone marrow stromal cell characteristics.* Exp Hematol, 2008. **36**(9): p. 1176-85.
327. Bhat, S., P. Viswanathan, S. Chandanala, S.J. Prasanna, and R.N. Seetharam, *Expansion and characterization of bone marrow derived human mesenchymal stromal cells in serum-free conditions.* Sci Rep, 2021. **11**(1): p. 3403.
328. Dawson, J.B., D.J. Barker, D.J. Ellis, E. Grassam, J.A. Cotterill, G.W. Fisher, and J.W. Feather, *A theoretical and experimental study of light absorption and scattering by in vivo skin.* Phys Med Biol, 1980. **25**(4): p. 695-709.
329. Zhou, Y., Y. Yamamoto, Z. Xiao, and T. Ochiya, *The Immunomodulatory Functions of Mesenchymal Stromal/Stem Cells Mediated via Paracrine Activity.* J Clin Med, 2019. **8**(7).
330. Skovronova, R., C. Grange, V. Dimuccio, M.C. Deregibus, G. Camussi, and B. Bussolati, *Surface Marker Expression in Small and Medium/Large Mesenchymal Stromal Cell-Derived Extracellular Vesicles in Naive or Apoptotic Condition Using Orthogonal Techniques.* Cells, 2021. **10**(11).
331. Almeria, C., S. Kress, V. Weber, D. Egger, and C. Kasper, *Heterogeneity of mesenchymal stem cell-derived extracellular vesicles is highly impacted by the tissue/cell source and culture conditions.* Cell Biosci, 2022. **12**(1): p. 51.
332. Phinney, D.G., M. Di Giuseppe, J. Njah, E. Sala, S. Shiva, C.M. St Croix, D.B. Stolz, S.C. Watkins, Y.P. Di, G.D. Leikauf, J. Kolls, D.W. Riches, G. Deiuliis, N. Kaminski, S.V. Boregowda, D.H. McKenna, and L.A. Ortiz, *Mesenchymal stem cells use extracellular vesicles to outsource mitophagy and shuttle microRNAs.* Nat Commun, 2015. **6**: p. 8472.
333. Eleuteri, S. and A. Fierabracci, *Insights into the Secretome of Mesenchymal Stem Cells and Its Potential Applications.* Int J Mol Sci, 2019. **20**(18).
334. Thate, C., C. Woischwill, G. Brandenburg, M. Muller, S. Bohm, and J. Baumgart, *Non-clinical assessment of safety, biodistribution and tumorigenicity of human mesenchymal stromal cells.* Toxicol Rep, 2021. **8**: p. 1960-1969.
335. Hyun, Y.M. and C.W. Hong, *Deep insight into neutrophil trafficking in various organs.* J Leukoc Biol, 2017. **102**(3): p. 617-629.
336. Randolph, G.J., J. Ochando, and S. Partida-Sanchez, *Migration of dendritic cell subsets and their precursors.* Annu Rev Immunol, 2008. **26**: p. 293-316.
337. Meinderts, S.M., G. Baker, S. van Wijk, B.M. Beuger, J. Geissler, M.H. Jansen, A. Saris, A. Ten Brinke, T.W. Kuijpers, T.K. van den Berg, and R. van Bruggen, *Neutrophils acquire antigen-presenting cell features after phagocytosis of IgG-opsonized erythrocytes.* Blood Adv, 2019. **3**(11): p. 1761-1773.

338. Takashima, A. and Y. Yao, *Neutrophil plasticity: acquisition of phenotype and functionality of antigen-presenting cell.* J Leukoc Biol, 2015. **98**(4): p. 489-96.
339. Vono, M., A. Lin, A. Norrby-Teglund, R.A. Koup, F. Liang, and K. Lore, *Neutrophils acquire the capacity for antigen presentation to memory CD4(+) T cells in vitro and ex vivo.* Blood, 2017. **129**(14): p. 1991-2001.
340. Raymond, M.H., A.J. Davidson, Y. Shen, D.R. Tudor, C.D. Lucas, S. Morioka, J.S.A. Perry, J. Krapivkina, D. Perrais, L.J. Schumacher, R.E. Campbell, W. Wood, and K.S. Ravichandran, *Live cell tracking of macrophage efferocytosis during Drosophila embryo development in vivo.* Science, 2022. **375**(6585): p. 1182-1187.